A Search for the Production of a Single Top Quark in association with a Z Boson at the LHC

Alexander D. J. Morton

High Energy Physics Group
Department of Electronic and Computer Engineering
Brunel University London

A thesis submitted in fulfilment of the requirements for the degree of Doctor of Philosophy

Abstract

A search for the production of a single top quark in association with a Z boson and an additional jet using data from proton-proton collisions at $\sqrt{s} = 13\,\text{TeV}$ collected by the Compact Muon Solenoid (CMS) experiment at the Large Hadron Collider is presented. This is a rare process that is predicted by the Standard Model. This search focussed on identifying the final state containing two leptons from the Z boson decay, two jets from the decay of the W boson produced by the top quark decay, a b-jet from the top quark decay and a recoil jet. The signal was dominated by backgrounds involving a real Z boson or two promptly produced leptons consistent with a Z boson decay, primarily Z+jet and top quark pair production. As such, a Boosted Decision Tree was used to enhance the separation between the signal and background processes. Using a dataset corresponding to $35.9\,\text{fb}^{-1}$, signal strengths of $6.21^{+2.34}_{-2.67}$ and $4.73^{+1.92}_{-2.02}$ were measured for this process when the Z boson decays into a pair of electron or muons, respectively, and the W boson decay hadronically. These measurements correspond to an observed (expected) signal significance of 2.72σ (0.46σ) and 2.50σ (0.54σ), respectively, when compared to the background-only hypothesis. These measurements are consistent within two standard deviations of the Standard Model prediction.

The CMS experiment's new tracking detector at the High-Luminosity Large Hadron Collider will require the ability to reconstruct all charged tracks with transverse momentum greater than 2-3 GeV within $4\,\mu$s so that they can be used in the Level-1 trigger decision. One of the proposed track finders is an FPGA-based based solution using a fully time-multiplexed architecture, where track candidates are reconstructed using a projective binning algorithm based on the Hough Transform. Studies into the suitability of a linearised χ^2 algorithm for fitting track parameters were undertaken and it was found that its performance was inferior compared to that of a combinatorial Kalman Filter fitter. The impact of reducing the minimum track transverse momentum from 3 GeV to 2 GeV on the proposed system was also evaluated. The resulting degradation of performance was found to be recoverable by improving the handling of multiple scattering in the track finding and fitting algorithms.

Declaration of Authorship

The work described in this thesis was conducted solely by the author, except where collaboration with others occurred as stated within the text, during their time as a candidate for a research degree at this University.

Figures from CMS publications are labelled "CMS" or "CMS Simulation", when the material only includes simulated events. Figures labelled "CMS Preliminary" are from an unpublished or preliminary public CMS publication. All figures taken from external sources are referenced throughout this thesis.

The work described in Chapter 4 formed part of the author's contributions to *TMTT* project's development of the proposed track finding system described within that chapter. To produce the results presented in Chapter 4, the author worked in collaboration with other members of the *TMTT* project who were predominantly based at the University of Bristol, Brunel University London, Imperial College London, STFC Rutherford Appleton Laboratory and the Karlsruhe Institute of Technology. In addition to the studies described in that chapter, the author's other contributions to the *TMTT* project included various robustness studies and the development of the software framework used to integrate and evaluate the performance of track fitting algorithms

The author has collaborated with other members of the High Energy Physics group at Brunel University London to produce the physics analysis presented in this thesis. The principle contributions the author made towards the analysis are described in Chapters 5, 6, and 7. The work involving the development and optimisation of the multivariate analysis technique and statistical analysis technique that was used was principally undertaken by other members of the High Energy Physics group and is described in Chapters 7 and 8, respectively.

No work contained within this thesis has been submitted to this or any other university as part of the requirement for any qualification. When the published work of others has been consulted, it has been clearly attributed within the text.

Acknowledgements

This thesis would not have been possible without the time, help, thoughts, and advice of many people.

First and foremost, I would like to thank my principal supervisor *Joanne Cole* for her continual support, guidance and advice over the course of the last four years. I am not sure how I can ever express my gratitude for her ability to always find time for me and for the uncountable number of times she has corrected this thesis. I would also like to thank my second supervisor *Peter Hobson* and my research development advisor *David Smith* for their help and guidance through the past four years.

My thanks go to *Catherine Mackay* and *Corin Hoad* in particular for their work on the statistical analysis of the tZq measurement presented in this thesis. Without both of their efforts, I suspect that the analysis would not be in such a mature state. My thanks also go to *Ivan Reid* whose timely technical support and tolerance of my high bandwidth usage on the HEP group's computing resources made the work presented in this thesis possible.

I would also like to thank all those I've worked with throughout the UK CMS Collaboration and during my time at CERN, especially those from the CMS Single Top Physics community and the *TMTT* collaboration. In particular I would like to thank *Andrew Rose* and *Mark Pesaresi* not only for their advice throughout the last four years, but also for introducing me to *High Energy Physics* in the first place. Special thanks are warranted for *Douglas Burns*, *Fionn Ball*, *Rachel Hyneman*, *Thomas James*, *Sioni Summers*, and *Seth Zenz* for the many enjoyable (and educational) lunches and cups of coffee we've had from across the globe.

I would like to thank all of my friends and family for their support through the years. *Darije Čustović*, *Diana Lucaci*, *Reuben Hill*, *Thore Bucking* and *Annabel Shaw*; for providing me with a place to stay when I needed it and whose interest in my work, no matter how seemingly banal, re-motivated me when I needed it most. I am incredibly grateful to my Mother and Father. Without their constant support and encouragement throughout the years, especially during the writing of this thesis, I doubt I would have made it this far.

Finally, but most importantly, I would like to thank *Peter Hobson* and the *Science and Technologies Facilities Council*. Without them, I would not have had the privilege of being able to embark on this work.

Contents

List of Figures

List of Tables

Chapter 1

Introduction

"If I have seen further it is by standing on the shoulders of giants" Letter to Robert Hooke FRS, February 15th 1676, by Sir Isaac Newton FRS (1643-1727)

The idea that nature can be explained through rational explanations, such as the ancient philosophical concepts of *Atomism* and the Ancient Greek's *Classical Elements*, is one that stretches back into time immemorial.

Following the scientific revolution of the 17th century the scientific method replaced such philosophical reasoning as the basis for exploring the nature of reality. By formulating hypotheses whose predictions can tested by empirical evidence, successive generations of scientists have built upon and improved on the ideas of those before them. By amending existing theories or proposing new theories supported by new and more precise measurements, unified descriptions of seemingly unrelated phenomena have emerged, such as James Clark Maxwell's theory of electromagnetism. This process has taken us from John Dalton's atomic theory and Sir Isaac Newton's laws of motion to the Standard Model (SM) of Particle Physics in the present day, describing all known elementary particles and three of the four fundamental forces of nature.

The SM is one of the greatest and most powerful scientific theories, making remarkably accurate predictions that have withstood incredible experimental scrutiny. Despite the completion of the SM with the discovery of the Higgs Boson in 2012 [1, 2] at the Large Hadron Collider (LHC), it is clear that the SM cannot be a complete description of reality for a number of reasons; including the following:

- Gravity is not accounted for within the SM and at high energy densities it is fundamentally irreconcilable with the classical theory of General Relativity [3].
- There is strong experimental evidence that the observed rotation curves of galaxies and gravitational lensing cannot be accounted for by SM particles alone and that

there must therefore be a large weakly interacting *Dark Matter* component to the Universe [4].

- The presence of so-called *Dark Energy* has also been inferred from astronomical and cosmological observations to account for the observed rate of expansion of the Universe [5].
- Neutrinos have been observed to oscillate between different flavours, implying that they have non-zero masses in contrast to SM expectations [6, 7].
- There is currently no explanation that accounts for the clear abundance of matter over anti-matter in the observable universe.

In addition to these, many scientists are uncomfortable with the fact that the SM contains a large number of finely tuned experimentally derived parameters, preferring a theory from which these values would emerge naturally, resulting in a more "complete" description of reality [8].

One of the approaches to study these issues is to investigate increasingly higher energy scales to test our existing theories and to look for new physics beyond them. The LHC at CERN is the most powerful and luminous particle accelerator built to date and provides physicists the capability to study an unprecedented number of events. In addition to discovering the Higgs boson, the unprecedented collision energies and number of events produced provide physicists the capability to probe the consistency of the SM through precision measurements and to search for new physics at the and above the TeV level.

As the heaviest known fundamental particle, the top quark provides a unique means to probe multiple aspects of the SM. The top quark's mass of $173.0 \pm 0.4\,\text{GeV}$ [9] not only places it near the electroweak symmetry breaking scale, but has the consequence of the top quark having a lifetime shorter than the strong force's characteristic time. Consequently, the top quark decays before it can be confined into a hadron, thus making measurements of its properties more accessible compared to the other quarks. As such, studying the top quark provides unique opportunities to probe the electroweak force and the properties of individual quarks.

This thesis presents a search for an as yet unobserved SM process in which a single top quark is produced in association with a Z boson, known as *tZq*, in the file state containing two leptons based on proton-proton collision data at $\sqrt{s} = 13\,\text{TeV}$ collected by the Compact Muon Solenoid (CMS) experiment at the LHC during 2016. tZq is a process which is a particularly sensitive probe of the electroweak sector as not only is the top quark produced through electroweak interactions, but also the Z boson coupling to both the top quark and W boson.

This thesis also presents studies relating to the future upgrade of the CMS silicon tracker for the High Luminosity (HL-LHC). The High Luminosity LHC will be capable of providing

an instantaneous luminosity up to an order of magnitude greater than the LHC today. Consequently, the CMS experiment's tracking detector will require a track finder to provide information to the online trigger in order to discriminate in favour of potentially interesting physics against increasingly large backgrounds. During the development of one possible track finder, studies were undertaken regarding various track fitting algorithm would best find tracks down to transverse momenta of just 3 GeV and precisely fit track helix parameters to them. The studies presented in this thesis detail the development of a linearised χ^2 fitter and the impact on the proposed system of reducing the minimum track transverse momenta requirement from the baseline specification of 3 GeV to 2 GeV.

Chapter 2

An Introduction to the Standard Model and Top Quark Physics

2.1 The Standard Model

The Standard Model (SM) of particle physics describes all the known elementary matter particles and their interactions with the weak, strong, and electromagnetic forces using renormalisable Quantum Field Theory (QFT). QFT describes particles as excitations of quantum fields, whose dynamics are typically described using the Lagrangian formalism [10].

This chapter introduces and briefly describes the theoretical framework of the SM, the shortcomings of the SM and the physics of the top quark. The second section of the chapter discusses the motivations and context of the search for a single top quark produced in association with a Z boson presented in this thesis.

Throughout this thesis *natural units*, where the fundamental constants c, $\hbar$ and k_B (Boltzmann constant) are set to unity, and Einstein's summation convention are used.

2.1.1 Fundamental Particles

The SM describes all matter as being made up of spin-$\frac{1}{2}$ particles known as fermions that interact through the fundamental forces, which are mediated by spin-1 gauge bosons. The spin-0 Higgs boson arises as a consequence of the breaking of the electroweak symmetry, imbuing the massive weak force gauge bosons with mass and providing an explanation for how fermions acquire their mass.

Matter consists of six quarks, fundamental particles that interact through the strong, electromagnetic and weak forces, and six leptons, fundamental particles that do not experience the strong force [10]. Each fermion has an associated anti-matter equivalent, which has

identical mass but opposite charge. Both types of fermion are subdivided into three "generations" of particles where each subsequent generation of particles is identical, except for their quantum number and mass [11]. Table 2.1 lists the charges, weak isospins and masses of the quarks and leptons for each of the three generations.

The "up-type" and "down-type" quarks have an electrical charges of $+\frac{2}{3}$ and $-\frac{1}{3}$, respectively, and *colour charges* (or anti-colour charges) of red, blue or green. As the phenomena of *colour confinement* (described in Section 2.1.4) only allows for colourless states, quarks form composite particles collectively called hadrons. Typically hadrons are composed of a quark anti-quark pair, known as mesons, or of groups of three quarks, referred to as baryons. Exotic hadrons formed of larger groupings of quarks can be also formed, with both tetraquark and pentaquark states having been observed by the LHCb detector [12, 13] and elsewhere [9].

Each generation of leptons consists of a charged lepton that interacts through the electromagnetic and weak forces, and a corresponding neutral near massless lepton, known as a neutrino, that interacts solely through the weak force. As with the quarks, the charged lepton of each subsequent generation is more massive than the last. Initially, it was assumed that neutrinos were massless, but the discovery of neutrino flavour oscillation implies that they must have non-zero masses. The hierarchy of the neutrino mass eigenstates is currently unknown [14].

Table 2.1: The Standard Model fermions and their properties [9].

	Generation	**Particle**	**Mass [MeV]**	**Electric Charge**	**Weak Isospin**
Quarks	I	up (u)	$2.2^{+0.5}_{-0.4}$	$+\frac{2}{3}$	$+\frac{1}{2}$
		down (d)	$4.8^{+0.5}_{-0.3}$	$-\frac{1}{3}$	$-\frac{1}{2}$
	II	charm (c)	$1.275^{+0.025}_{-0.035} \times 10^3$	$+\frac{2}{3}$	$+\frac{1}{2}$
		strange (s)	95^{+9}_{-3}	$-\frac{1}{3}$	$-\frac{1}{2}$
	II	top (t)	$(173.1 \pm 0.9) \times 10^3$	$+\frac{2}{3}$	$+\frac{1}{2}$
		bottom (b)	$(4.18^{+0.04}_{0.03}) \times 10^3$	$-\frac{1}{3}$	$-\frac{1}{2}$
Leptons	I	electron (e)	0.511	-1	$-\frac{1}{2}$
		electron neutrino (ν_e)	$< 2 \times 10^{-6}$	0	$+\frac{1}{2}$
	II	muon (μ)	106	-1	$-\frac{1}{2}$
		muon neutrino (ν_μ)	< 0.19	0	$+\frac{1}{2}$
	II	tau (τ)	1777	0	$-\frac{1}{2}$
		tau neutrino (ν_τ)	< 18.2	0	$+\frac{1}{2}$

The SM contains five integer spin gauge bosons, shown in Table 2.2, along with their corresponding masses, charges, and weak isospins. The four spin-1 vector bosons mediate the electromagnetic, weak and strong forces. The massless photon, γ, mediates the electromagnetic force, while the massive neutral Z^0 and charged $W^\pm$ bosons mediate the weak force. Massless gluons mediate the strong force and have one of eight colour states [10]. The spin-0 Higgs boson originates from the breaking of the electroweak symmetry, accounting for

the massive gauge bosons' masses and providing a mechanism for how other fundamental particles acquire their mass.

Table 2.2: The fundamental forces of nature and the SM bosons which mediate them [9].

Bosons	**Mass [GeV]**	**Electrical Charge**	**Colour Charge**	**Weak Isospin**
Photon (γ)	0	0	0	0
W ($W^{\pm}$)	80.385 ± 0.015	± 1	0	± 1
Z (Z^0)	91.1876 ± 0.0021	0	0	0
Higgs (h^0)	125 ± 0.24	0	0	$-\frac{1}{2}$
Gluon (g)	0	0	$r\bar{g},\ r\bar{b}, g\bar{r}, g\bar{b}, b\bar{r}, b\bar{g},$ $\frac{1}{\sqrt{2}}(r\bar{r} - g\bar{g}), \frac{1}{\sqrt{6}}(r\bar{r} + g\bar{g} - 2b\bar{b})$	0

2.1.2 Gauge Symmetries

The idea that the laws of physics are consistent for all observers, even if the measurements differ between observers, is a fundamental component of all modern physical theories [15]. Systems that are unchanged or *invariant* under a given transformation are considered to possess a corresponding *symmetry*.

As shown by Noether's theorem, the generator(s) of any such symmetry conserve a corresponding quantity [16]. Examples of such quantities include the conservation of energy-momentum from space-time symmetry or electrical charge from the $U(1)$ symmetry in electromagnetism. If a symmetry transformation has no space-time dependence it is said to have a *global symmetry* and conversely, if it has a space-time dependence it is said to have a *local* or *gauge symmetry* [17].

These concepts can be demonstrated by considering applying the $U(1)$ gauge symmetry of Quantum Electrodyanmics, the theory of electromagnetism, to the Lagrangian of a relativistic spin-$\frac{1}{2}$ free-fermion field (e.g. electrons) with a wavefunction $\psi(x)$ and mass m [18]:

$$\mathcal{L} = \bar{\psi}(x)(i\gamma^{\mu}\partial_{\mu} - m)\psi(x) \tag{2.1}$$

where ∂_{μ} is the partial derivative operator γ^{μ} are the Dirac matrices, defined in Appendix A.

If we consider this Lagrangian to have a global $U(1)$ symmetry, then $\psi(x)$ transforms as:

$$\psi(x) \rightarrow \psi'(x) = e^{-iq\alpha}\psi(x) \tag{2.2}$$

which leaves the Lagrangian in Equation (2.1) unchanged as q is a constant and α is an arbitrary phase.

If Equation (2.1) has a local $U(1)$ symmetry, then $\psi(x)$ transforms according to:

$$\psi(x) \rightarrow \psi'(x) = \psi(x)e^{-iq\alpha(x)} \tag{2.3}$$

As such a local transformation involves α being dependent on x, the derivative term in Equation (2.1) now transforms as:

$$\begin{aligned} \bar{\psi}(x)\partial_\mu\psi(x) \rightarrow \bar{\psi}'(x)\partial_\mu\psi'(x) &= \bar{\psi}(x)e^{iq\alpha(x)}\partial_\mu\big(e^{-iq\alpha(x)}\psi(x)\big) \\ &= \bar{\psi}(x)\partial_\mu\psi(x) - i\bar{\psi}(x)\partial_\mu\alpha(x)\psi(x) \end{aligned} \tag{2.4}$$

which consequently results in the Lagrangian no longer being invariant:

$$\mathcal{L} \rightarrow \mathcal{L}' = \mathcal{L} + \bar{\psi}(x)\big(i\gamma^\mu\partial_\mu\alpha(x)\big)\psi(x) \tag{2.5}$$

For the Lagrangian to remain invariant under local transformations, a vector or *gauge* field, $A_\mu(x)$, associated with the $\psi(x)$ field, can be introduced, which transforms as follows:

$$A_\mu(x) \rightarrow A_\mu(x)' + \frac{1}{q}\partial_\mu\alpha(x) \tag{2.6}$$

This field can be simply introduced by replacing the derivative ∂_μ with the *gauge covariant derivative* [18], which is defined as $D_\mu = \partial_\mu - iA_\mu(x)$. As D_μ transforms as:

$$D_\mu\psi(x) \rightarrow e^{-iq\alpha(x)}D_\mu\psi(x) \tag{2.7}$$

the non-invariant term in Equation (2.5) cancels out and ensures that the Lagrangian remains invariant under the local $U(1)$ gauge transformations.

The presence of this gauge field allows for the inclusion of a gauge invariant term containing a field strength tensor $F_{\mu\nu}$, that describes the geometry of $A_\mu(x)$, in the Lagrangian. The general form of $F_{\mu\nu}$ is given by:

$$F^a_{\mu\nu} = \partial_\mu A^a_\nu - \partial_\nu A^a_\mu + gf^{abc}A^b_\mu A^c_\nu \tag{2.8}$$

where g is the self-coupling constant and f^{abc} are the structure constants of the symmetry group.

For the case of QED, as $U(1)$ has only one generator, which self-commutes, g is zero.

Therefore, with the addition of the simplest gauge invariant term for incorporating $F_{\mu\nu}$, the QED Lagrangian is given by:

$$\mathcal{L}_{QED} = \bar{\psi}(i\gamma^\mu D_\mu - m)\psi - \frac{1}{4}F_{\mu\nu}F^{\mu\nu} \tag{2.9}$$

where excitations of the gauge field A_μ correspond to the massless photon and q represents the electric charge of the electron.

Similarly, by requiring the SM Lagrangian to be gauge invariant under the $SU(3)_C$ gauge symmetry of the strong force and under the $SU(2)_L \times U(1)_Y$ gauge symmetry of the electroweak force, the gauge fields and their associated gauge bosons for the electromagnetic, weak and strong forces naturally emerge.

The resultant SM Lagrangian is constructed of four terms:

$$\mathcal{L}_{SM} = \mathcal{L}_{Gauge} + \mathcal{L}_{Fermion} + \mathcal{L}_{Higgs} + \mathcal{L}_{Yukawa} \tag{2.10}$$

where $\mathcal{L}_{Gauge}$ describes the spin-1 gauge boson fields that arise from requiring that the Lagrangian is invariant under local transformations of the symmetry group and $\mathcal{L}_{Fermion}$ describes the fermion fields. The $\mathcal{L}_{Higgs}$ and $\mathcal{L}_{Yukawa}$ terms arise as a consequence of the breaking of electroweak symmetry and describe the scalar spin-0 Higgs field and the interactions between the Higgs field and fermions and gauge bosons, respectively.

2.1.3 Electroweak Theory

2.1.3.1 Quantum Electrodynamics

Quantum Electrodynamics (QED) is the Abelian gauge theory that describes how the electromagnetic force interacts with electrically charged particles. QED is based on the $U(1)_{EM}$ gauge group, which describes the conservation of electrical charge, q, and the mediation of the force by the massless and chargeless photon. The massless nature of the photon results in the electromagnetic force having an infinite range.

In contrast to the featureless void of the classical vacuum, in QFT the vacuum is the ground state of the quantum field. Given that neither the position nor the momentum of the photon field can be precisely known as a consequence of Heisenberg's uncertainty principle, the field experiences random fluctuations. These fluctuations are interpreted as virtual electron-anti-electron pairs that are continually materalising out of the vacuum before annihilating [19]. During their brief existence, these virtual electrons and anti-electrons interact with the electromagnetic fields of real particles - being attracted to oppositely signed and repelled by same signed particles. This results in the vacuum acting as a dielectric medium which partially screens the strength of a charged particle's field. At shorter distances however, the effective strength of a charged particle's field increases as the impact of screening is reduced.

2.1.3.2 Weak Interactions

The weak force acts upon *weak isospin*, T, and is mediated by the massive electrically charged $W^{\pm}$ and electrically neutral Z^0 gauge bosons [11]. The weak force conserves weak

isospin along the z-axis, T_3.

Given that the chirality of a fermion determines the value of T_3, $\mathrm{W}^{\pm}$ bosons, which have $T_3 = \pm 1$, can only interact with left-handed fermions, which have $T_3 = \pm\frac{1}{2}$ [17]. This property makes charged weak interactions unique in being the only interactions during which fermion flavour can change and violate parity (P) [20, 21] and charge-parity (CP) symmetries [22]. The violation of CP symmetry results in weak interactions involving matter and anti-matter occurring at different rates. Such processes have a bias towards matter production, which partially accounts for the observed matter-anti-matter asymmetry in the universe. As Z^0 bosons have $T_3 = 0$, they interact with both left and right handed fermions and conserve fermion flavour and CP symmetry.

2.1.3.3 Electroweak Unification

The theory of *electroweak* interactions, formulated by Glashow, Salam and Weinberg [23, 24, 25], is described by the $SU(2)_L \times U(1)_Y$ gauge group and describes the two seemingly disparate constituent forces - weak and electromagnetic - as a single unified electroweak force above some threshold energy.

The $U(1)_Y$ component of the theory has a single generator and an associated gauge field B_μ with coupling constant g'. This field acts on, and conserves, weak hypercharge, Y_W, which is related to electrical charge, Q, and the z-projection of weak isospin, T_3, by $Q = T_3 + \frac{1}{2}Y_W$.

The $SU(2)_L$ component of the theory has three generators, $T_i = \frac{\sigma_i}{2}$, which manifest as the gauge fields W^i_μ with coupling constant g, where $i = 1, 2, 3$ and $\boldsymbol{\sigma}$ are the Pauli spin matrices (defined in Appendix A). As $SU(2)$ transformations are non-Abelian, W^i_μ are able to interact with themselves.

The B_μ and W^i_μ gauge fields are related to the four physically observed gauge bosons as follows:

$$\begin{aligned} \mathrm{A}_\mu &= sin(\theta_W)W^3_\mu + cos(\theta_W)B_\mu \\ \mathrm{Z}_\mu &= cos(\theta_W)W^3_\mu - sin(\theta_W)B_\mu \\ \mathrm{W}^{\pm}_\mu &= \frac{1}{\sqrt{2}}(W^1_\mu \mp iW^2_\mu) \end{aligned} \tag{2.11}$$

where θ_W is the weak mixing or *Weinberg* angle, which is defined as:

$$\theta_W = \frac{g}{g^2 + g'^2} \tag{2.12}$$

The $\mathrm{W}^{\pm}$ gauge bosons only interact with the left-handed components of the fermion field, ψ_L. The left- and right-handed components of the fermion field ψ are obtained using the

projection operators, $P_{L/R}$, as follows:

$$\psi_{L/R} = P_{L/R}\psi \tag{2.13}$$

where $P_{L/R} = \frac{1}{2}(1 \pm \gamma^5)$ and $\gamma^5 = i\gamma^0\gamma^1\gamma^2\gamma^3$.

Under the $SU(2)_L$ group of transformations, ψ_L transforms as doublets, and ψ_R as a singlet. The ψ_L doublet consists of either a left-handed pair of up-type and down-type quarks of the same generation or a charged lepton and its associated neutrino. As no right-handed neutrinos have been observed, the ψ_R singlet consists of a right-handed up- or down-type quark or a charged lepton.

As the weak flavour eigenstates of the down-type quarks do not coincide with their mass eigenstates, charged weak interactions allow for flavour changing interactions. The Cabibbo-Kobayashi-Maskawa (CKM) matrix, in Equation (2.14), is a unitary matrix that describes the proportion of the mass eigenstates d, s, and b that are present in the weak flavour eigenstates d', s', and b' [9]. The individual elements of the CKM matrix describe the strength of the couplings for charged weak interactions.

$$\begin{pmatrix} d' \\ s' \\ b' \end{pmatrix} = \begin{pmatrix} V_{ud} & V_{us} & V_{ub} \\ V_{cd} & V_{cs} & V_{cb} \\ V_{td} & V_{ts} & V_{tb} \end{pmatrix} \begin{pmatrix} d \\ s \\ b \end{pmatrix} \tag{2.14}$$

The current best estimates of the elements of the CKM matrix, which have been determined by a global fit of the measurements various experiments have performed, are [9].

$$V_{CKM} = \begin{pmatrix} 0.97420 \pm 0.00021 & 0.2243 \pm 0.0005 & 0.00394 \pm 0.00036 \\ 0.218 \pm 0.004 & 0.997 \pm 0.017 & 0.0422 \pm 0.0008 \\ 0.0081 \pm 0.0005 & 0.0394 \pm 0.0023 & 1.019 \pm 0.025 \end{pmatrix} \tag{2.15}$$

2.1.3.4 Spontaneous symmetry breaking

Originally, the SM lacked a mechanism to include massive gauge fields in its Lagrangian, without breaking the gauge invariance of weak isospin rotations [26]. The inclusion of gauge invariant mass terms in the electroweak Lagrangian was achieved through the spontaneous symmetry breaking *Higgs mechanism* proposed by Brout, Engler, Higgs, Guralnik, Hagen and Kibble [27, 28, 29].

The Higgs mechanism introduces a complex scalar field with four degrees of freedom, ϕ. As the symmetrical potential of ϕ, $V(\phi)$, has a non-zero vacuum expectation value (VEV), it has an infinite number of degenerate ground states. Figure 2.1 shows that while the

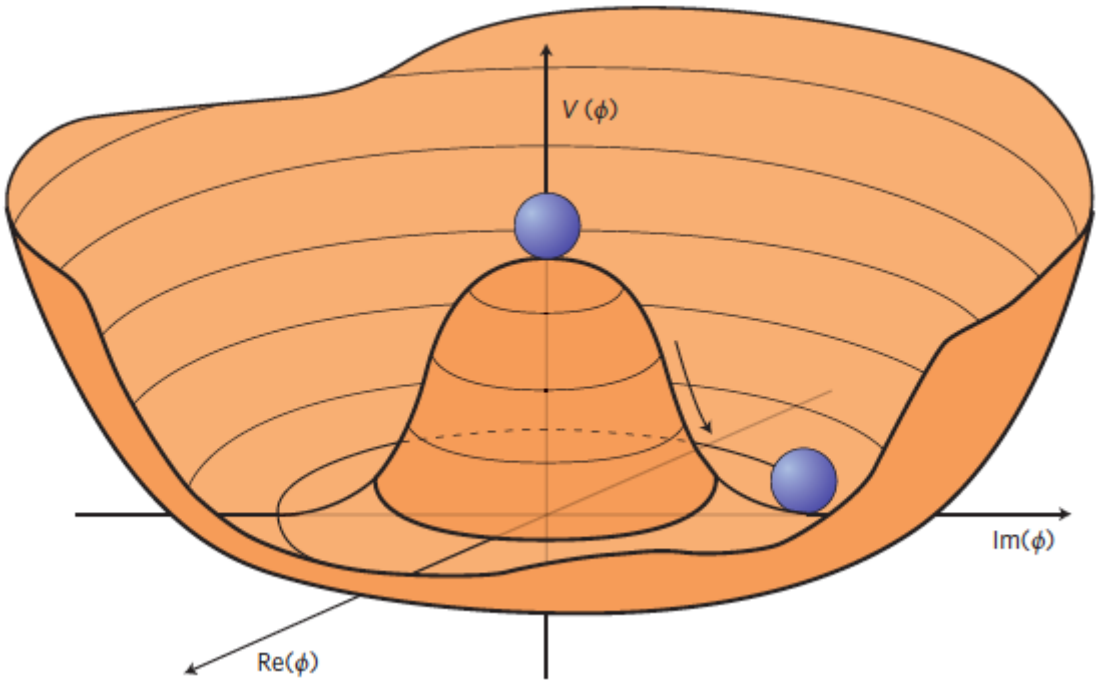

Figure 2.1: The potential of the Higgs field as a function of its real and imaginary components [30]. The infinite number of degenerate ground states form a circle in phase space.

potential $V(\phi)$ is symmetrical, the rotational symmetry of the field is spontaneously broken when a single ground state for the vacuum is chosen.

Through the spontaneous symmetry breaking of the Higgs potential, three of the four degrees of freedom of the Higgs field couple to and provide mass terms for the weak gauge bosons. The remaining degree of freedom manifests as a single massive scalar field excitatation known as the *Higgs boson* [17]. Both the CMS and ATLAS experiments at CERN have independently confirmed the existence of a Higgs boson with a mass of $125 \pm 0.24\,\text{GeV}$ [1, 2].

While the introduction of a Higgs field was motivated to explain the broken electroweak symmetry, it has allowed for of gauge invariant *Yukawa* mass terms for fermions to be added to the SM Lagrangian. In these terms, the strength of a fermion's Yukawa coupling to the Higgs results in the fermions gaining a non-zero mass [17]. The experimental evidence for the Higgs coupling to fermions include the recent observations of $t\bar{t}H$ production [31] and of the Higgs boson decaying a $\tau\overline{\tau}$ pair [32] and $b\bar{b}$ pairs [33].

2.1.4 Quantum Chromodynamics

The strong force and its interactions is described by Quantum Chromodynamics (QCD). QCD is based on the non-Abelian $SU(3)_{colour}$ gauge group, which describes strong interactions through eight massless spin-1 gauge bosons called *gluons* that act upon the *colour*

charge, C, carried by quarks [11]. Quarks carry either a red, green or blue colour charge, with anti-quarks possessing equivalent anti-colour charges. Given the non-Abelian nature of QCD, gluons can self-couple as they themselves carry both a colour and and anti-colour charge, unlike the photon, for example, which is electrically neutral.

The self-coupling nature of gluons results in the phenomenon known as *asymptotic freedom* [11, 19, 34], whereby the strength of the strong coupling constant, α_s, decreases with decreasing distance (increasing momenta). This occurs as, like the QED vacuum of a sea of virtual e^+e^- pairs, QCD considers the vacuum to be occupied by a virtual *sea* of gluons and $q\bar{q}$ pairs. In contrast to photons in QED however, as gluons self-couple, the virtual gluons have an attractive effect greater than the screening effect of virtual $q\bar{q}$ pairs. Therefore, while α_s is sufficiently small inside a hadron for partons to behave as free particles, increasingly large amounts of energy are required to pull a hadron apart. This results in the *colour confinement* of partons [11, 26, 34]. This behaviour of α_s means that when partons are liberated from hadrons, such as in the high energy hadron collisions of the LHC, the resultant shower of partons form new hadrons in a process known as hadronisation [35].

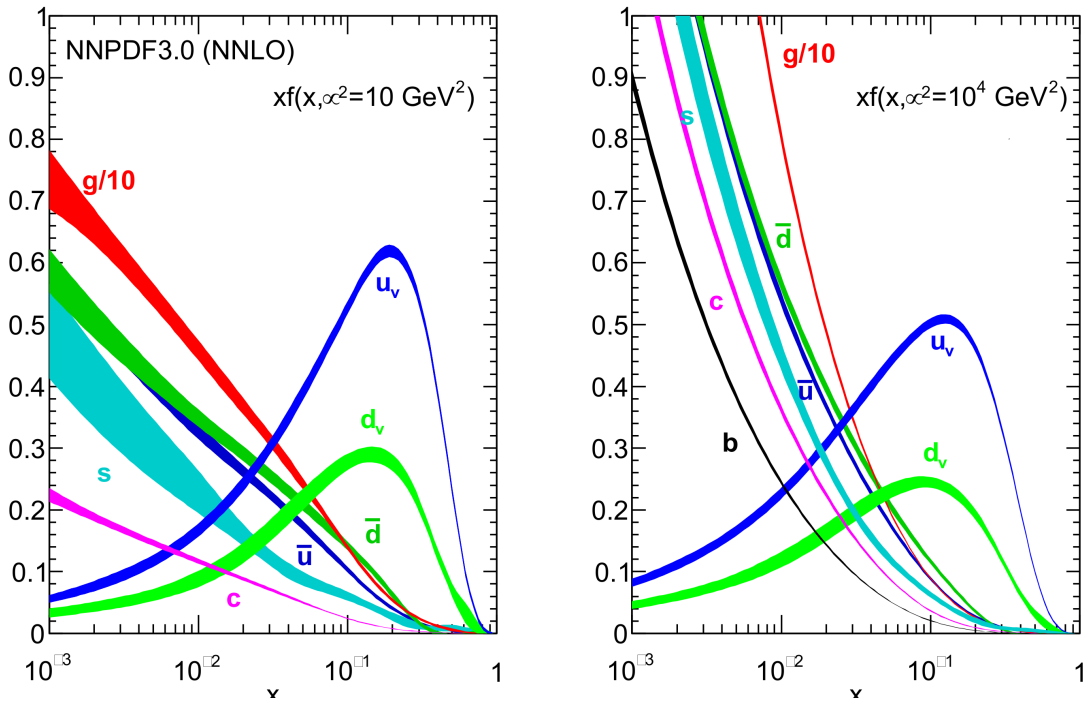

Figure 2.2: The proton parton distribution functions $xf(x)$ as a function of the momentum fraction determined by the NNPDF3.0 fit for factorisation scales of $\mu_F = 10\,\mathrm{GeV}^2$ (left) and $\mu_F = 10^4\,\mathrm{GeV}^2$ [36].

In QED, the contribution to the calculation of the Matrix Element for a process decreases with increasing order of the diagram considered due to the electromagnetic coupling constant being considerably smaller than one. In contrast however, higher order contributions in

QCD become increasingly important as α_s increases, making higher order QCD calculations more and more difficult to perform. It has been demonstrated that QCD calculations can be temporally split (factorised) into components that describe the long and short distance behaviours. This allows the short distance components to be described using perturbation theory, such as the hard scattering of hadrons, while the long distance components are described using non-perturbative phenomenological models, such as Parton Distribution Functions (PDFs). For a given hadron, PDFs describe the number density of each parton flavour as a function of the fraction of the hadron's momentum (Bjorken x) at a given energy scale. PDFs are constrained by fits made to measurements made by a variety of different experiments [34, 36]. Figure 2.2 shows the results of one the fit known as NNPDF3.0 which was used for the generation of the simulation samples considered in this thesis [36].

2.2 Top Physics

The existence of a third generation of quarks was first hypothesised in 1973 by Makoto Kobayashi and Toshihide Maskawa as the CP violation observed in kaon decays was not possible with only two generations of quarks [37]. This hypothesis was reinforced with the discovery of a third generation (tau) lepton in 1975 and a third generation down-type (bottom) quark in 1977 [38], which strongly implied the existence of a weak isospin partner to the bottom quark. As the top quark was more massive than initially assumed, it would remain unobserved until a sufficiently powerful collider was built. Finally in 1995 the top quark was observed at the Tevatron at the Fermi National Accelerator Laboratory by the CDF and DØ experiments [39, 40].

The top quark's mass, m_{top}, of $173.0 \pm 0.4\,\text{GeV}$ [9] makes it the most massive known fundamental particle and is responsible for imbuing it with properties that have no equivalent for the other five quarks [9]. Unlike the other five quarks, the top quark is massive enough to decay into an on-shell W boson, giving it a much shorter lifetime than the other quarks. This lifespan of 5×10^{-25} seconds is several orders of magnitude smaller than the characteristic timescale of the strong interaction [41]. Consequently, the top quark is the only quark that decays before it can hadronise, making it a unique probe into the nature of a "bare" quark, such as its spin and polarisation, through studying the angular distributions of its decay products [42]. This also makes it possible to determine the helicity of the W boson involved in the decay. Measurements of the Wtb vertex allows for the $|V_{tb}|$ element of the Cabibbo-Kobayashi-Maskawa (CKM) matrix to be directly measured and thus test whether the CKM matrix is unitary, as presumed, or otherwise [43].

The top quark predominantly decays into a bottom quark and a W boson, as shown in Figure 2.3. Currently, the most precise measurement of the branching ratio for this decay mode has been measured to be $1.014 \pm 0.003(\text{stat}) \pm 0.032(\text{syst})$ by the CMS Collaboration [44].

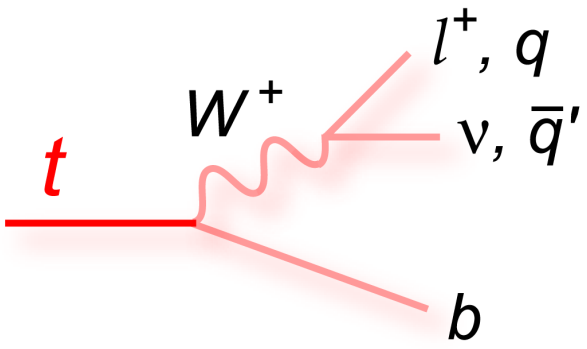

Figure 2.3: The main decay mode of the top quark into a b-quark and W boson, where the W boson decays either leptonically or hadronically [45].

Given all these properties, the top quark makes an excellent probe of the Wtb vertex and is sensitive to any anomalous couplings that would impact it. Additionally, with the top mass being greater than that of any other fundamental particle, it has the strongest Yukawa coupling to the Higgs field. Consequently, many believe that the top quark has a special role to play in electroweak symmetry breaking and Beyond the Standard Model (BSM) Physics [46]

2.2.1 Top quark pair production

At hadron colliders, top quarks are predominantly produced by pair production ($t\bar{t}$) through strong interactions. As illustrated in the Feynman diagrams in Figure 2.4, at Leading Order (LO) $t\bar{t}$ events are produced by either gluon fusion or quark-anti-quark annihilation.

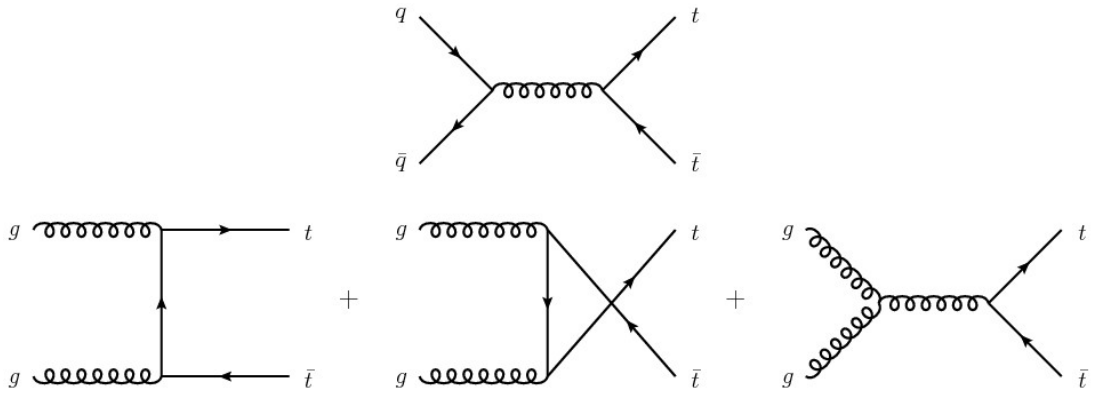

Figure 2.4: The three Leading Order Feynman diagrams for top quark pair production at hadron colliders. Quark-anti-quark annihilation is illustrated on the top row and gluon fusion on the bottom.

While approximately 85% of $t\bar{t}$ events produced at the Tevatron occured via quark fusion, 80-90% of $t\bar{t}$ events at the LHC are produced by gluon fusion for $\sqrt{s} = 8 - 14\,\text{TeV}$ [9, 47]. These differences in production rates occur for two reasons:

- Higher centre-of-mass energies results in smaller Bjorken x, resulting in a much larger fraction of the proton's energy being carried by gluons.
- The Tevatron was a proton-anti-proton collider, both quarks involved in quark fusion could be valance quarks, unlike the LHC where one would have to be a sea quark.

As the top quark predominately decays into a W boson and a b-quark, the three different decay modes of pair produced top quarks are characterised by the manner in which the two W bosons decay:

- **hadronic** decays occur when both W bosons decay into a quark and anti-quark.
- **lepton + jets** decays occur when one W boson decays into a lepton and its associated anti-neutrino, while the other W boson decays hadronically.
- **dilepton** decays occur when both W bosons decay into a lepton and its associated anti-neutrino.

Top quark pair production can also occur in association with a vector boson ($t\bar{t}V$), albeit at relatively small cross sections compared to both $t\bar{t}$ and single top production.

2.2.2 Single top quark production

Top quarks can also be produced singly through weak interactions, albeit with smaller cross sections than that for $t\bar{t}$ production given the relative weakness of the electroweak coupling compared to the strong coupling. There are three main SM single top production mechanisms, which are categorised by the virtuality of the W boson involved in the interaction.

Figure 2.5(a) shows the first of these mechanisms, which is known as s-channel production. This is quark-anti-quark annihilation producing an off-shell W boson that decays into a top and anti-b quark. This process has the lowest production cross section of the three at the LHC due to the charge-asymmetric initial state. Given its low cross section and a final state topology similar to larger background processes, the s-channel has yet to be observed at the LHC [48].

The t-channel production mechanism, as shown in Figure 2.5(b), is the dominant single top prodution mechanism at the LHC. The process involves the scattering of a W boson off a sea b quark or produced a b quark produced by gluon splitting. Initially observed at the

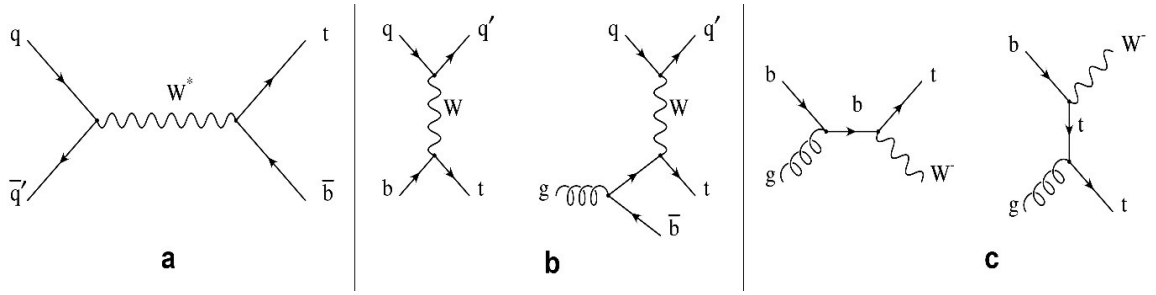

Figure 2.5: The leading order diagrams for each of the three single top production mechanisms: (a) s-channel, (b) t-channel and (c) single top production in association with a W boson (tW production).

Tevatron [49, 50], the t-channel process has since been studied at higher energies at the LHC, with all results to date remaining consistent with the SM [51, 52].

The tW production mechanism, as shown in Figure 2.5(c), is the process in which a top quark is produced in association with an on-shell W boson. In contrast to having a negligible cross section at the Tevatron, the tW cross section at the LHC is sufficiently large to make it accessible, resulting in it being discovered in 2014 [53].

Single top production processes are a powerful probe of the electroweak interactions of the top quark. In contrast to $t\bar{t}$, these processes allow for the Wtb vertex involved in top quark production to be probed in addition to providing complimentary measurements of the Wtb vertex in top quark decays.

Understanding single top quark production processes is also important from an experimental viewpoint as:

- These processes form backgrounds for not only SM processes such as $t\bar{t}$, but also for Higgs and BSM physics searches, such those which introduce new electroweak couplings.
- Precision measurements of these processes can be used to compliment measurements of $t\bar{t}$ processes in constraining Parton Distribution Functions [54].

2.2.3 Single top production in association with a Z boson

The analysis presented in this thesis is the search for the production of a single top quark in association with a Z boson with an additional jet, known as tZq production, using the dilepton final state.

The high centre-of-mass energies and integrated luminosities available at the LHC have made it possible to not only perform precision studies of $t\bar{t}$ and single top quark process, but also to make measurements of processes involving the tZ vertex. Such measurements provide not

only the ability to perform precision tests of SM predictions, but are also sensitive to new physics such as the existence of new electroweak bosons, new fermions or Flavour Changing Neutral Currents (FCNC).

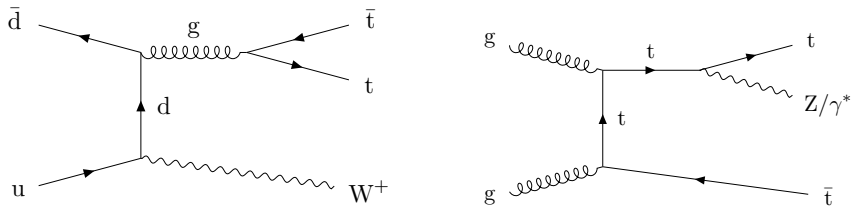

Figure 2.6: Leading order $t\bar{t}W$ (left) and $t\bar{t}Z$ (right) production diagrams [55]. Unlike $t\bar{t}Z$ and $t\bar{t}H$ production, the gauge boson in $t\bar{t}W$ is not radiated from the top quark, but from the initial state quarks.

It may initially assumed that given the larger production cross section for $t\bar{t}$ compared to single top processes that $t\bar{t}$ processes would provide the best conditions to probe the electroweak interactions with the top quark. The tW coupling however, can only be probed through the single top tW process as the W boson couples to the initial state quarks for $t\bar{t}W$ processes, as illustrated in figure 2.6. tH has yet to be observed [56] as it is much more difficult to access than $t\bar{t}H$ due to the destructive interference between the tH and HW vertices [57]. This destructive interference occurs due to the large matrix element contributions from both tH and HW Feynman diagrams being of the same order of magnitude but having opposite signs.

In contrast, $t\bar{t}Z$ has a lower production cross section than the combined tZ and $\bar{t}Z$ production cross sections [58] as tZq contains fewer particles in the final state and thus is easier to produce. CMS has made measurements of $t\bar{t}H$, $t\bar{t}W$, and $t\bar{t}Z$, all with signifiances in excess of five standard deviations and consistent with their SM predictions [31, 55].

tZq production is a rare SM process where a single top quark is produced in association with a Z boson with an additional jet. Unlike $t\bar{t}Z$ where the Z boson is radiated from one of the top quarks, tZq involves the Z boson being radiated off one of the quark legs, as shown in the top two rows of Figure 2.7, or from the exchanged W boson, as shown shown in the bottom left diagram in Figure 2.7. As tZq production is sensitive the WWZ coupling, unlike $t\bar{t}Z$ production, and is expected to be as sensitive to this coupling as WZ production, this process provides a unique precision probe of electroweak interactions with the top quark [58].

In addition, tZq production needs to be well understood as it forms one of the irreducible backgrounds for other rare SM processes, such as tH production, as well as BSM processes such as Flavour Changing Neutral Currents (FCNC) [59].

As the top quark predominately decays into a W boson and a b-quark, the four possible

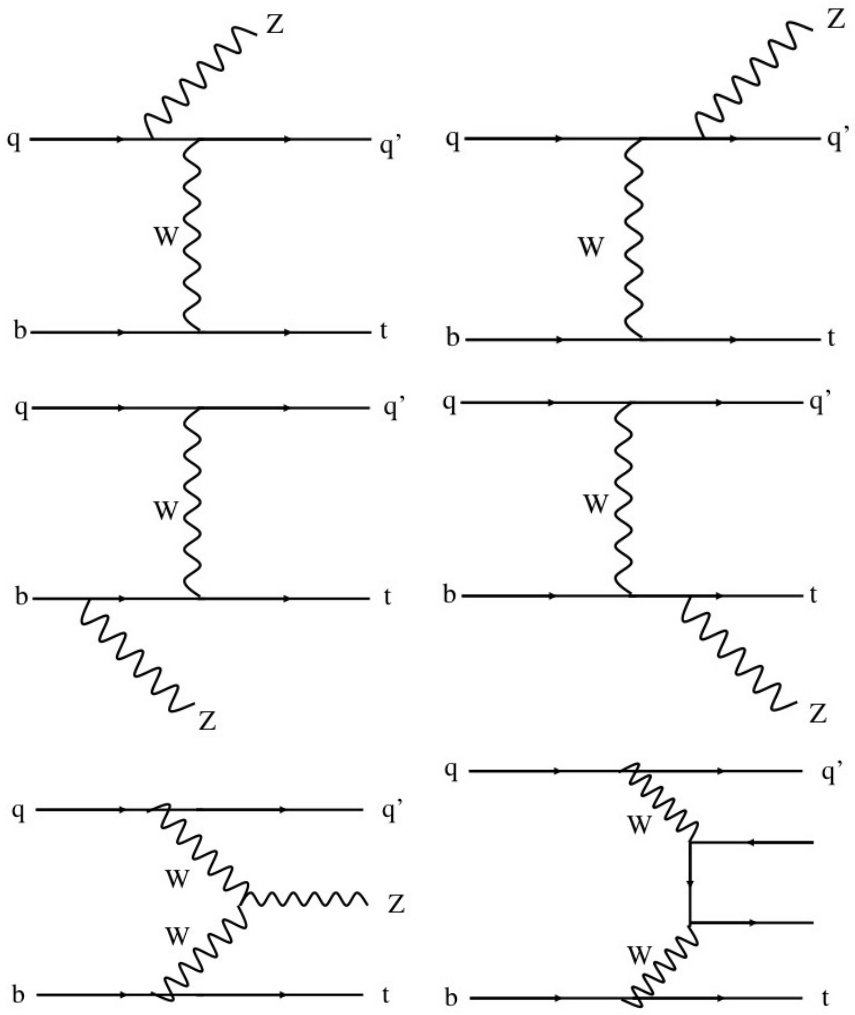

Figure 2.7: Leading order tZq production diagrams, where the Z boson is radiated off one of the quark lines in the diagrams in the top two rows, where the Z boson is radiated off the exchanged W in the lower left diagram and from the non-resonant contribution to the tZq process in the bottom right diagram.

final states are characterised by the decay mode of the Z boson and W boson:

- **trilepton:** when the W boson decays into a lepton and neutrino and the Z boson decays into a lepton and anti-lepton.
- **dilepton:** when the Z boson decays into a pair of leptons and the W boson into a quark and anti-quark.
- **single lepton:** where the W boson decays into a lepton and neutrino and the Z boson decays into a quark and anti-quark.
- **hadronic:** both the W boson and Z boson decay into a quark and anti-quark.

The physics analysis presented in this thesis is the first search at CMS for tZq using the dilepton final state. The initial searches for tZq however, used the trilepton final state as despite it having a smaller production cross section than either of the dilepton or hadronic final states, it is the easiest to separate from background processes.

The first search for tZq however, was unable to observe the process, making a measurement with an observed significance of 2.9 σ [60]. Both ATLAS and CMS have since been able to observe the trilepton final state for tZq at $\sqrt{s} = 13\,\text{TeV}$ as a result of the tZ and $\bar{\text{t}}$Z cross sections increasing with the centre-of-mass energy at a similar rate to $\text{t}\bar{\text{t}}$Z and the large integrated luminosity delivered by the LHC at $\sqrt{s} = 13\,\text{TeV}$ [61, 62]. This increase in the tZq production cross section and the large integrated luminosity being delivered by the LHC at $\sqrt{s} = 13\,\text{TeV}$ has also made it possible to perform searches for the other tZq final states, including the dilepton final state, allowing for complimentary measurements of this process to be made.

The observed results presented in this work and the previous CMS searches for tZq using the trilepton final state at $\sqrt{s} = 13\,\text{TeV}$ use the reference next-to-leading order production cross section for tZq where the Z boson decays leptonically, for $m_{ll} > 30\,\text{GeV}$ [62]:

$$\sigma(\text{tZq}, Z \to l^+l^-) = 94.2^{+1.9}_{-1.8}\text{scale} \pm 2.5\ \text{(PDF)}\ \text{fb} \tag{2.16}$$

The analysis strategy and full event selection requirements used in the analysis of this process is discussed in detail in Chapter 6, the modelling of the backgrounds in Chapter 7 and the statistical methodology used to perform the measurement of this process in Chapter 8.

2.3 Beyond the Standard Model Physics

The SM has been incredibly successful at accurately predicting the majority of the properties of the known fundamental particles up to the electroweak scale. However, given the inability of the SM to incorporate gravity and to fully address a number of experimental observations, such as massive neutrinos, it is apparent that there must be new physics beyond the Standard Model.

2.3.1 Shortcomings of the Standard Model Physics

One of the major and most apparent shortcomings of the SM is its inability to explain why there is an asymmetry between matter and anti-matter in the universe. While CP symmetry violation does occur within the SM, it is insufficient to account for the amount of matter observed in the universe.

Gravity is currently described by the extremely successful classical theory of General Relativity (GR). GR however, is fundamentally incompatible with the SM and has produced contradictory results, such as their predictions for the cosmological constant differing by 120 orders of magnitude [63]. While attempts have been made to reconcile the two theories, no successful quantum theory of gravity has yet been produced [3].

One of the other serious theoretical issues with the SM is the *hierarchy problem* concerning the lack of explanation for the vast differences observed between the electroweak scale and the Grand Unified Theory and Plank scales where gravity becomes strong [8]. The mass of the Higgs boson presents a related hierarchy problem. As the vacuum expectation value of the Higgs field determines the mass of the weak bosons, for the observed masses of these bosons, one would expect a vacuum expectation value of approximately 246 GeV. Given that the loop corrections for the Higgs mass are quadratically divergent, this would imply that the Higgs vacuum expectation value would be either zero or at the mass scale of any new physics. Therefore, in order to obtain the observed Higgs mass of 125 GeV, the cancellations required from the radiative corrections must be extremely "fine tuned". While there is nothing fundamentally wrong with this, many scientists find such fine tuning to be *unnatural*.

Perhaps the greatest inconsistency experimentally observed with the SM is the fact that neutrinos are not massless. The first indication of massive neutrinos was made by the Homestake experiment, which found that the fraction of electron neutrinos arriving from the Sun was at most half what was expected [64]. While this observation could be explained by neutrinos experiencing flavour oscillations, this would require neutrinos to have mass in contrast to the expectations of the SM in order for their flavour eigenstates to mix with their mass eigenstates. Further experiments have confirmed however, that neutrinos do undergo flavour oscillations and thus must have mass [6, 7, 65].

Chapter 3

The LHC accelerator and the CMS experiment

3.1 The Large Hadron Collider

The Large Hadron Collider (LHC) at the European Organisation for Nuclear Research (CERN) [66], in Geneva, Switzerland is the highest-energy particle accelerator constructed to date. It is designed to operate at a centre-of-mass energy of 14 TeV at a design instantaneous luminosity of $10^{34}\,\mathrm{cm}^{-2}\,\mathrm{s}^{-1}$ [67]. The LHC is also capable of accelerating heavy-ions, which is usually done for one month a year with lead ions with up to 2.76 TeV per nucleon being used for lead-lead or lead-proton collisions.

The beams collide at four interaction points around the LHC, with one of the four major experiments being based at each of them. The experiments are: A Toroidal LHC Apparatus (ATLAS) [68] and the Compact Muon Solenoid (CMS) [69] detectors, which are the two multi-purpose experiments; the Large Hadron Collider beauty (LHCb) experiment [70], which specialises in b-physics and A Large Ion Collider Experiment (ALICE) [71], which, as the name suggests, specialises in heavy ion physics. Three smaller experiments are situated close to one of the four main experiments and use the same collision points. Both the TOTal Elastic and diffractive cross section Measurement (TOTEM) [72] and LHC-forward (LHCf) [73] experiments study diffractive physics in the very-forward regions of collisions at the CMS and ATLAS experiments' collision points, respectively. Monopole and Exotics Detector At the LHC (MoEDAL) [74] shares the LHCb experiment's cavern and performs direct searches for magnetic monopoles and highly ionising stable and pseudo-stable massive particles.

Currently there are three planned phases of operation for the LHC: "Phase-0" will see the preparations for 14 TeV operations; "Phase-I" will see the accelerator prepared for high luminosity operations; and "Phase-II" will see modifications for very high luminosity oper-

ations [75]. Figure 3.1 illustrates the timescales of the current plans for the operation and shutdown periods of the LHC. Any proposed upgrades of the detectors will naturally have to coincide with the shutdowns of the LHC.

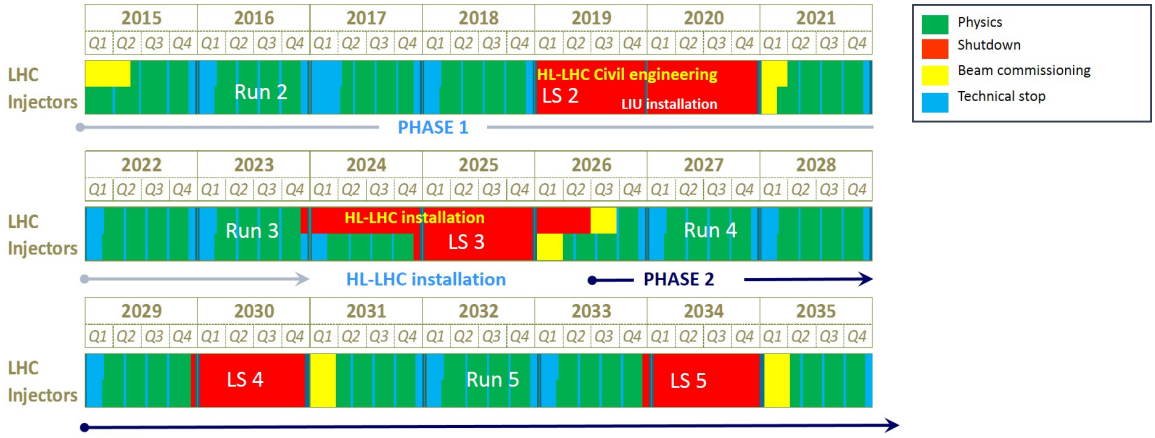

Figure 3.1: Overview of the plan for the LHC and its injectors from 2015 to 2035 [76]. Data taking for physics is indicated in green, long shutdowns in red, beam commissioning in yellow and technical stops in blue.

3.1.1 Accelerator Complex

When operating in proton-proton mode, the preparation of the LHC beams starts at Linear accelerator 2 (Linac2). Protons from a hydrogen gas source are accelerated to 50 MeV and are injected into the Proton Synchrotron Booster (PSB) which accelerates the protons to 1.4 GeV before injection into the Proton Synchrotron (PS). In the PS, the protons are accelerated to 26 GeV and are injected into the Super Proton Synchrotron (SPS) where they are accelerated to 450 GeV before finally entering the LHC, as illustrated in Figure 3.2.

Sixteen Radio Frequency (RF) cavities (eight per beam), each operating at frequency of 400 MHz, delivering a maximum of 2 MV at an operational temperature of 4.5K, are used to accelerate the two beams up to their designed operational energies of 7 TeV over the course of about twenty minutes. Each of the two beams are accelerated in separate beam pipes, circulating in opposite directions. The beams requires 1232 dipole magnets to bend them along their circular path and 392 quadrupole magnets to focus them, with each magnet producing a 8.3T field whilst operating at 1.9K. A more detailed description of the LHC accelerator chain at CERN can be found in [78].

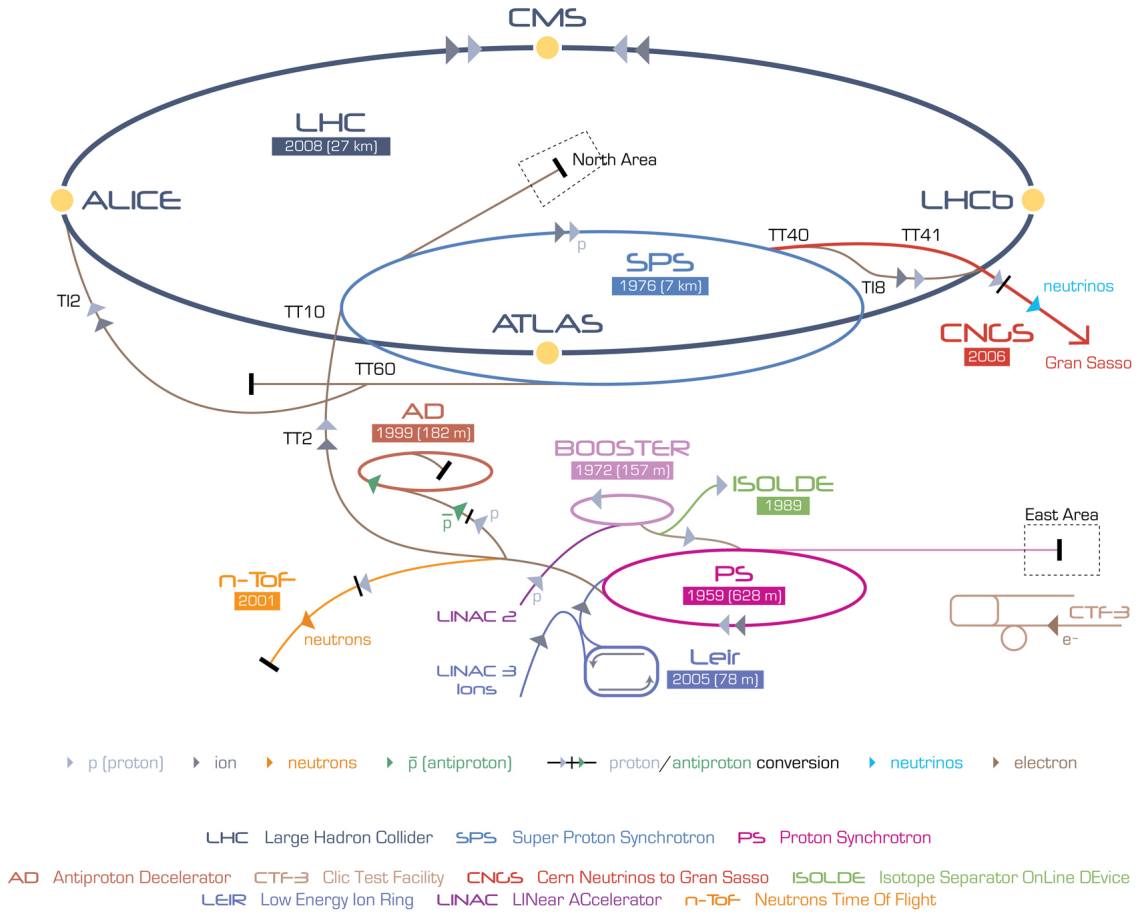

Figure 3.2: CERN complex, including the various linear accelerators, synchrotrons, LHC, LHC detectors and other aspects of the complex [77].

3.1.2 Motivation

The core motivations behind the LHC are to shed light on the nature of the electroweak symmetry breaking, for which the Higgs was presumed and found to be responsible, and to probe the consistency of the SM above the TeV level through precision measurements of SM parameters and the Higgs mechanism. Extensions of the SM, such as SUSY theories, additional dimensions or new fundamental forces and particles are expected to emerge at and above the TeV level, giving the potential to ascertain whether these theories have any basis beyond mere conjecture [67]. As shown in Figure 3.3, the production cross section of the Higgs boson and hypothesised SUSY particles, if they have TeV masses (and exist), are predicted to be many orders of magnitude smaller than both their associated backgrounds and the total inelastic cross section.

Consequently, in order to perform measurements of such processes, as well as precision measurements of SM parameters, the LHC was designed to be capable of achieving an instantaneous beam luminosity of up to $10^{34}\,\mathrm{cm}^{-2}\,\mathrm{s}^{-1}$. Such a high instantaneous luminosity

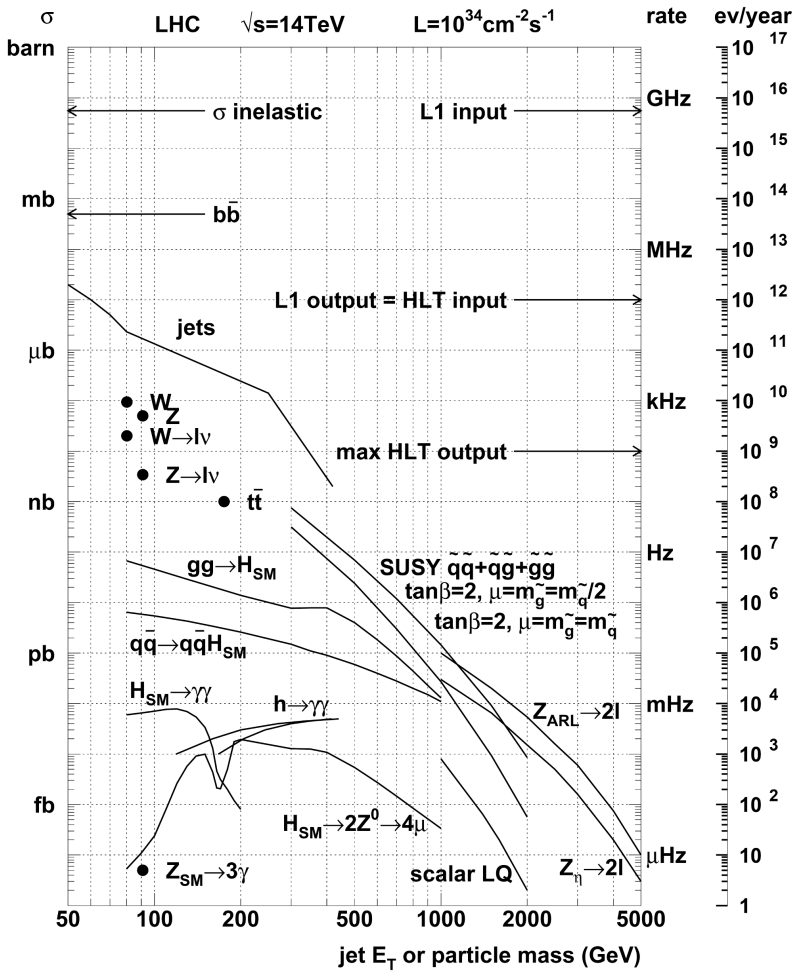

Figure 3.3: The inclusive proton-proton cross sections at $\sqrt{s} = 14\,\text{TeV}$ and the production frequency for various physics processes, as a function of jet E_T or mass, expected at the LHC at a luminosity of $10^{34}\,\text{cm}^{-2}\,\text{s}^{-1}$ [79].

was achieved by delivering protons in 2808 bunches per beam, with each bunch containing up to 1.15×10^{11} protons, which at design luminosity will separated by 25ns to provide a bunch collision rate of up to 40 MHz. The instantaneous luminosity is further increased by squeezing the proton bunches to enhance the number of simultaneous inelastic proton-proton interactions during each bunch crossing. These multiple simultaneous collisions are named pile-up (PU) interactions and usually consist of soft QCD interactions [66, 80]. PU can occur both within and adjacent to an event's bunch crossing, known as *in-time* and *out-of-time* PU respectively.

This high event rate presents the experiments' data acquisition and readout challenges, whilst retaining excellent signal-to-background resolution and sufficient radiation hardness in order to withstand the expected fluence.

3.2 The Compact Muon Solenoid

3.2.1 Overview

The Compact Muon Solenoid (CMS) [69] is a large, general purpose, hermetic particle detector and the smaller of the two multi-purpose experiments operating at the LHC. Figure 3.4 illustrates how the experiment and its sub-detectors are divided into a central cylindrical barrel section and two endcap disk sections at each end of the barrel. A superconducting solenoid encompasses, moving from the interaction point at the centre of the detector outwards, an all-silicon tracking detector, a homogeneous lead tungstate ($PbWO_4$) electromagnetic calorimeter (ECAL) and a hadronic calorimeter (HCAL) comprised of plastic scintillating tiles interspaced with brass absorbers. Beyond the solenoid there is an outer hadronic calorimeter (HO) and interspaced between the iron return yoke are three different types of Muon Detectors. There is also a pair of very-forward calorimeters (HF) to further extend the hadronic calorimetry coverage to ensure good dijet mass and $E_{\mathrm{T}}^{\mathrm{miss}}$ resolutions.

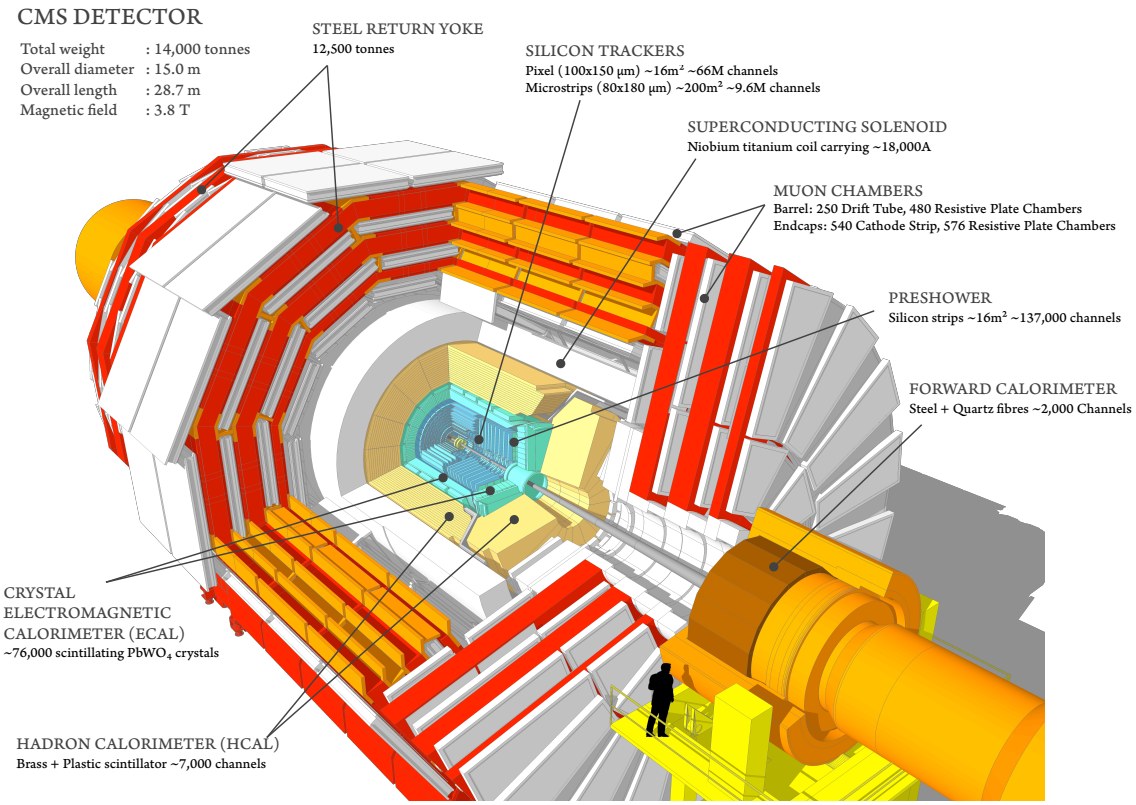

Figure 3.4: Cutaway diagram of CMS's layers, illustrating its onion-like nature and the location of the detecting technologies within [81].

These detectors were designed to investigate the wide range of physics phenomena in the LHC's physics program, resulting in the accurate and precise identification and measurement

of electrons, photons, jets and muons over both a large energy and momenta range.

The coordinate system adopted by the CMS experiment has its origin at the nominal interaction point at the centre of the detector. The z-axis is parallel to the anti-clockwise proton beam, the x-axis points towards the centre of the LHC, and the y-axis points vertically upwards. The azimuthal angle, ϕ, is the angle measured from the x-axis in the x-y plane and the polar angle, θ, is the angle measured clockwise relative to the positive z-axis. Pseudorapidity, defined as $\eta \equiv -ln\tan(\theta/2)$, is usually used in lieu of θ, as η is Lorentz invariant along the z-axis and is approximately equivalent to rapidity, $y \equiv \frac{1}{2}ln(E + p_z/E - p_Z)$, for highly relativistic particles.

3.2.2 Tracker

The tracker, measuring 5.8m with a 2.5m radius over a pseudorapidity range of $|\eta| < 2.5$, surrounds the interaction point. The tracker is designed to provide precision trajectory measurements of charged particles emerging from collisions and precise reconstruction of vertices at high efficiencies, whilst operating in a harsh radiation environment (maximum flux $\approx 10^7/s$) and minimising the number charged particles interacting with the tracker.

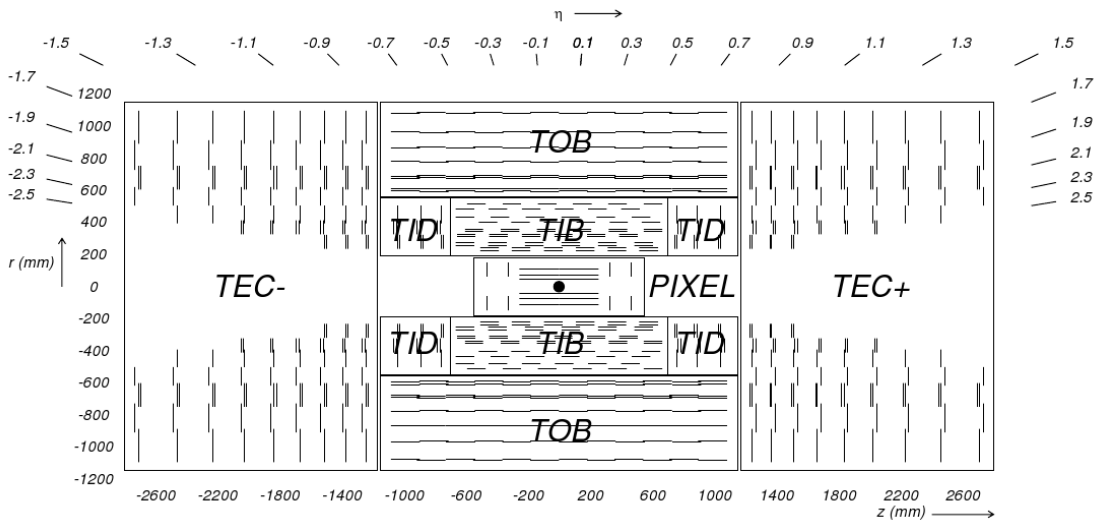

Figure 3.5: Schematic of the CMS tracking detector, displaying the interaction point in the centre and the location of the sub-detectors and, through the arrangement of the lines, their modules. The double lines present in the microstrip tracker denote modules with double-sided sensors [82].

Silicon fulfils these requirements and is used in both the inner pixel and microstrip detectors. Figure 3.5 illustrates how the various parts of the silicon microstrip detector surround the inner pixel detector. The high particle multiplicity expected closest to the interaction point requires high granularity pixels provide in order to ensure a low channel occupancy ($< 1\%$).

For radii above 20 cm however, the particle flux is sufficiently low enough that microstrips can be used without compromising track reconstruction efficiency. The low occupancy of the tracker results in a tracking efficiency of greater than 99% for charged particles with $p_{\mathrm{T}} > 1\,\mathrm{GeV}$. In the presence of the solenoid's magnetic field, the tracking system has an impact parameter resolution of approximately $10\,\mu\mathrm{m}$ and momentum resolutions between 1.5% and 3.0% for charged particles with $p_{\mathrm{T}} = 100\,\mathrm{GeV}$ and $1 < p_{\mathrm{T}} < 100\,\mathrm{GeV}$ respectively [83, 84].

3.2.2.1 Silicon Pixel Tracker

The original silicon pixel detector for the CMS experiment was comprised of three 53.3 cm-long barrel layers at mean radii of 4.4 cm, 7.3 cm and 10.2 cm respectively, and two endcap disks either side of the barrel at $|z| = 34.5$ and 46.5 cm respectively, that extend from $r = 6.0$ to 15 cm. Figure 3.6 shows an installed pixel detector endcap disk and a half disk being reinstalled around the LHC beam pipe before the start of Run 2 operations. The pixel sensors consist of n^{+}-type implants on n-type silicon which are connected by indium bump-bonds to highly integrated ReadOut Chips (ROCs). Each of the 66 million pixels measures $100 \times 150\,\mu\mathrm{m}^2$, covering a total surface area of 1.06 m^2, resolutions of $10\,\mu\mathrm{m}$ in $r - \phi$ and $20\,\mu\mathrm{m}$ in z, providing the granularity required to have a high track reconstruction efficiency and to be able to precisely calculate the track impact parameters and vertex position.

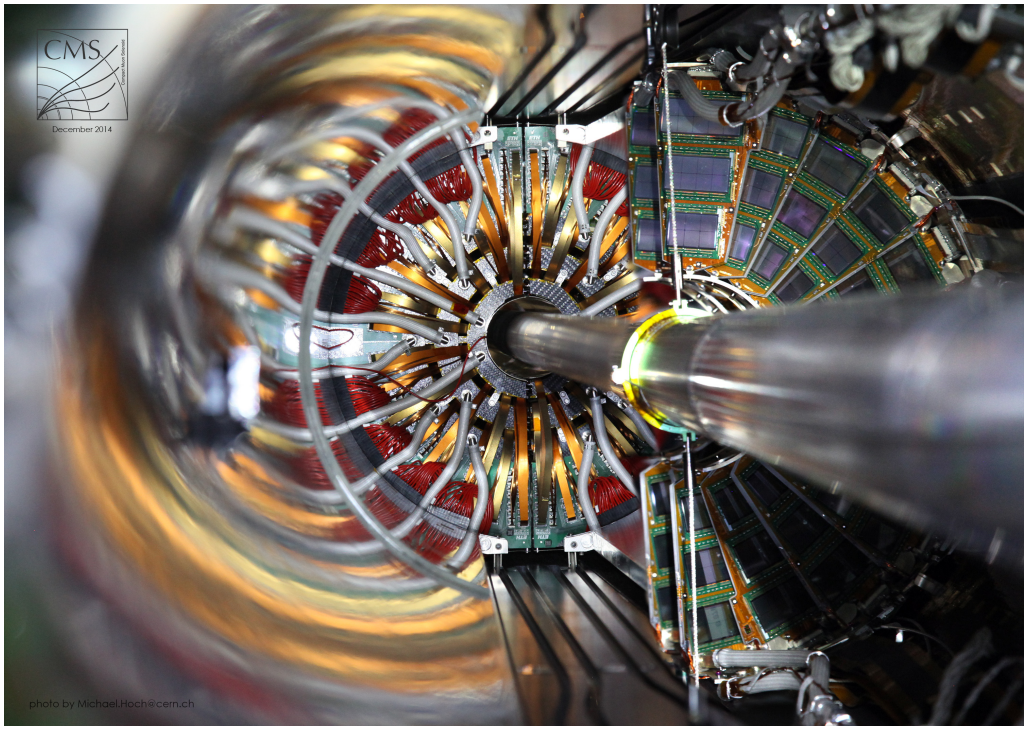

Figure 3.6: The pixel detector endcap disks being reinstalled around the beam pipe in December 2014 following Long Shutdown 1 [85].

The original detector was designed to operate under a nominal instantaneous luminosity of $1 \times 10^{34}\,\mathrm{cm}^{-2}\,\mathrm{s}^{-1}$. With the LHC planning to deliver higher instantaneous luminosities with the same 25 ns bunch spacing following LS1, if no action was taken, the radiation damage from the increased PU environment would result in the pixel tracker experiencing an unacceptable degradation in track reconstruction efficiency. As such, it has been long recognised that the original pixel detector would require replacing at least once during LHC operations [86]. Consequently, the original pixel tracker was completely replaced during the End of Year Technical Stop that took place between data taking in 2016 and 2017. A detailed description of the Phase-I Pixel detector is given in [87] as none of the results presented in this thesis involve data collected by the CMS experiment after 2016.

3.2.2.2 Silicon Microstrip Tracker

As illustrated in Figure 3.5, the silicon microstrip detector is comprised of four parts: the Tracker Inner Barrel (TIB), Tracker Inner Disks (TID), Tracker Outer Barrel (TOB) and Tracker EndCaps (TEC). The sensors are rectangular in the barrel region and trapezoid in the endcaps and all consist of single-sided strips of p^{+}-type implants on n-type silicon, which are connected to ROCs by aluminium strips. A total of 9.3 million sensors are used across all four parts, covering a total area of 198 m^2.

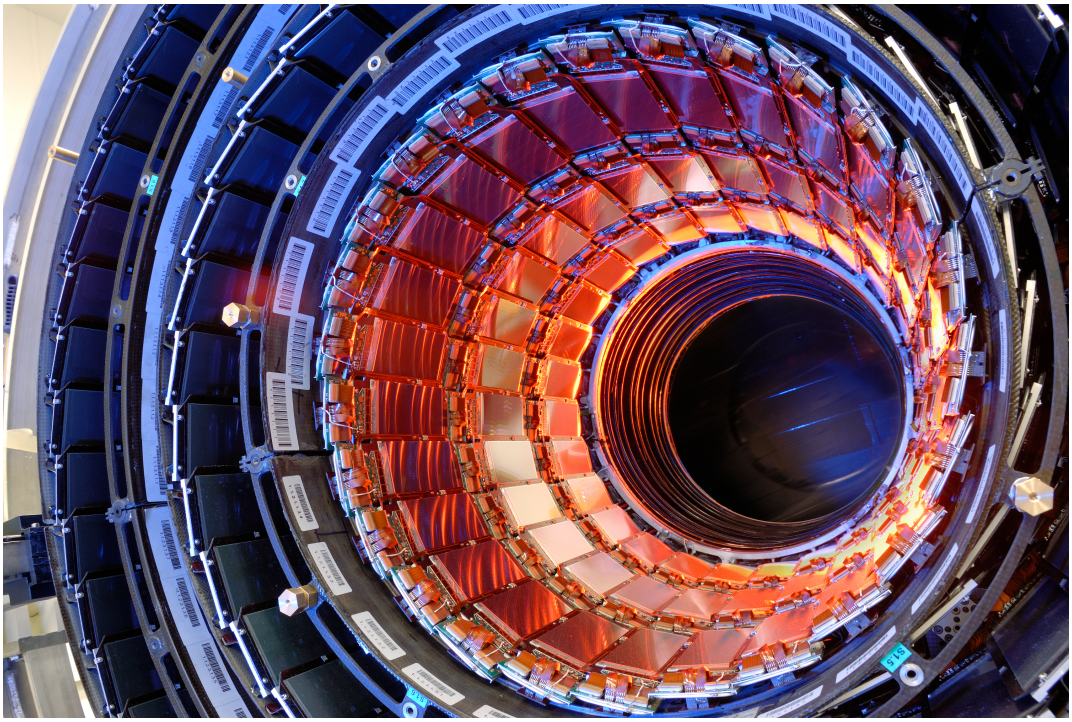

Figure 3.7: The first half of the Tracker Inner Barrel (TIB) containing three layers of silicon strip modules [88].

The TIB, shown in Figure 3.7, provides coverage in the range $20\,\text{cm} < r < 55\,\text{cm}$ and up to $|z| = 65\,\text{cm}$ and is comprised of four layers. The strips have a pitch of $80\,\mu\text{m}$ for the inner two layers and $120\,\mu\text{m}$ for the outer two layers, and a thickness of $320\,\mu\text{m}$ and a typical length of 10 cm in each of the four layers. The three disks on each side of the TIB form the TID, extends the inner microstrip tracker's coverage from $|z| = 65\,\text{cm}$ to $|z| = 120\,\text{cm}$. Each disk is formed of three rings and the sensor pitches across the rings vary between 81-158 μm, but have a thickness of $320\,\mu\text{m}$ throughout.

The TOB surrounds the TIB and TID and is comprised of six layers that provide coverage up to $|z| = 110\,\text{cm}$. In the outer microstrip tracker, increased strip thickness, length and pitch are used where the radiation levels are lower so that a similar occupancy and signal-to-noise ratio to that in the inner microstrip tracker can be maintained. The pitch of the strips vary from $183\,\mu\text{m}$ for the inner four layers to $122\,\mu\text{m}$ for the outer two layers, with all having a thickness of $500\,\mu\text{m}$ and a typical length of 25 cm. The TEC's nine disks per endcap extend coverage from $|z| = 120\,\text{cm}$ to $|z| = 280\,\text{cm}$, with the number of rings per disk varying from four to seven, depending on the disk's position in z. The thickness of the sensors in the TEC are $320\,\mu\text{m}$ in the three innermost rings and $500\,\mu\text{m}$ in the rest respectively.

A number of "stereo" modules consisting of two back-to-back sensors are used in the inner two layers of the TIB and TOB, the inner two rings of the TID and rings one, two and five of the TEC. These sensors are aligned at an angle of 100 mrad to each other, allowing measurements of both the $r - \phi$ and r-z coordinates, to a resolution of 23-34 μm in $r - \phi$ and $23\,\mu\text{m}$ in z and 35–$52\,\mu\text{m}$ in $r - \phi$ and $52\,\mu\text{m}$ in z in the TIB and TOB, respectively.

3.2.3 Electromagnetic Calorimeter

Beyond the tracker, the ECAL [89, 90], a homogeneous calorimeter, measures the energies of electrons and photons using lead tungstate ($PbWO_4$) scintillating crystals. The choice of detector technology was motivated by the need for the ECAL to be sufficiently compact to fit inside the solenoid along with the HCAL, while containing the EM showers' energy within the ECAL. Therefore, lead tungstate crystals were chosen due to their short radiation length (0.89 cm) and small Molieré radius (2.2 cm). The crystals also have a high radiation tolerance and have a short scintillation delay time, with 80% of the scintillated light being emitted within one 25 ns bunch crossing.

The ECAL barrel and each of the ECAL endcaps contain 61,200 and 7,324 crystals, respectively, with each crystal having a granularity of 0.0174 in the $\eta - \phi$ plane. As the $PbWO_4$) crystals emit a relatively low light yield, photodetectors are required to amplify this light. Avalanche photodiodes are used in the barrel and the more radiation hard vacuum phototriodes in the endcap disks, respectively, to amplify the light and convert it into an electrical current that is directly proportional to the energy of the induced electromagnetic showers.

These signals are digitised on-detector and buffered until a Level-1 Trigger decision has been made.

The layout of the ECAL system is displayed in Figure 3.8, illustrating the layout of both the barrel (EB) and endcap (EE) cystal systems, the gap between the EB and EE, and the Preshower (ES) [91] device located in front of the ECAL endcaps.

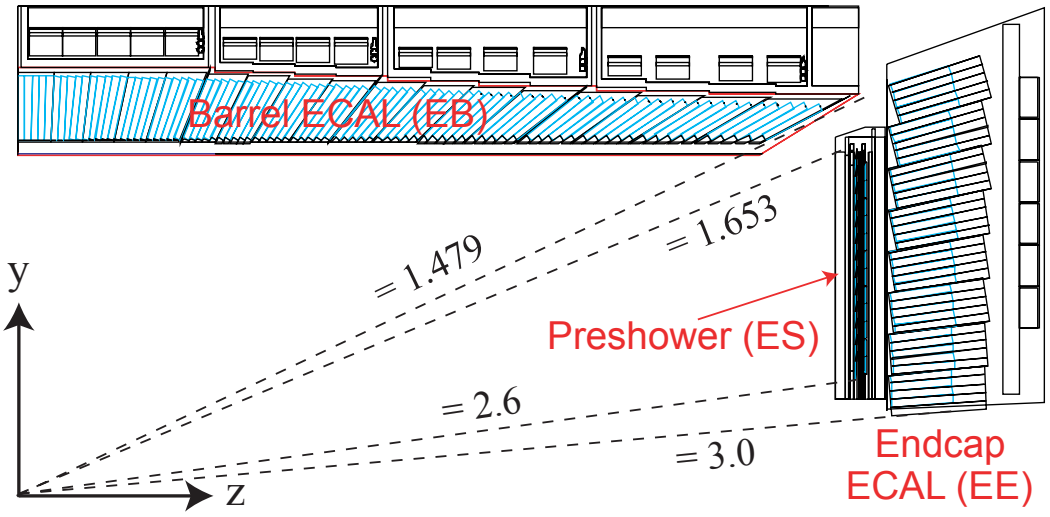

Figure 3.8: Layout of one quadrant of the ECAL system, illustrating the locations of the barrel ECAL (EB), endcap ECAL (EE) and ECAL Preshower (ES) device [92].

The ES aids the EE system in discriminating between neutral pions and photons within the fidicial region $1.653 < |\eta| < 2.6$. For each ES, two lead radiators initiate the electromagnetic showers and two silicon strip sensors, orthogonal to one another to provide fine resolution, are placed after the radiators. The thickness of the radiators was chosen to be two and one radiation lengths for the first and second lead radiators, respectively, in order to ensure that 95% of incident photons shower before reaching the second silicon strip sensor.

ECAL test beam measurements [93] of the $PbWO_4$ crystals in the absence of a magnetic field have determined the energy resolution, σ_E, to be,

$$(\frac{\sigma_E}{E})^2 = (\frac{2.8\%}{\sqrt{E}})^2 + (\frac{12\%}{E})^2 + (0.3\%)^2 \ . \tag{3.1}$$

where E is the energy of the incident electron in GeV. The first term is the stochastic term representing the statistical fluctuations in the amount of photo-electrons produced, the second term is the nosie term which represents the noise from the electronics and digitisation, and the third term is the constant term which covers any non-uniform longitudinal response and shower containment losses [93].

3.2.4 Hadronic Calorimeter

Hadronic particles pass through the ECAL and enter the HCAL [94]. The HCAL measures the energies of the resulting hadronic jets and contains them for the accurate determination of the missing transverse energy [94]. As such, the HCAL was designed to have as much absorber material within the solenoid coil as practical.

The barrel (HB) and endcaps (HE) both use plastic scintillator tiles which are interspersed between brass and steel absorber plates. Steel is used for the innermost and outermost HB and HE absorber plates for structural strengthening. The HB covers the rapidity range $|\eta| < 1.4$, with the HE providing coverage over the range $1.3 < |\eta| < 3.0$. Both the HB and HE are segmented in $\eta - \phi$ by 0.087×0.087 for $|\eta| < 1.6$ and up to 0.17×0.17 for $|\eta| >= 1.6$. Wavelength shifting fibres embedded in the tiles are used convert the scintillation light and channel it to hybrid photodiodes.

The forward hadronic calorimeters (HF) extends coverage up to $\eta < 5.2$ region [95]. As the very forward region experiences the highest radiation dose, quartz fibres, interspaced between steel absorbers, are used instead due to their radiation hardness and fast response time. The quartz fibres produce Cherenkov radiation above a certain energy threshold (thus ignoring low energy particles) and are able to give directional information due to the light being strongly correlated with the showers' trajectories. The Cherenkov light is transmitted down the fibres to individually shielded photomultiplier tubes contained in readout boxes.

Due to space constraints within the solenoid, the 5.8 to 10.6 interactions lengths of absorber material within the HB is insufficient to fully contain highly penetrating jets. Therefore, the HB is supplemented by an additional calorimeter in the barrel region outside the coil known as the HO [96]. With the solenoid's coil, which acts as an additional absorber, the HO increases the effective absorber thickness to at least 11.8 interaction lengths.

Using test beam measurements using electrons, muons and pions, the combined energy resolution of the ECAL and HCAL together, in terms of the stochastic and constant terms, was determined to be

$$(\frac{\sigma_E}{E})^2 = (\frac{84.4 \pm 1.6\%}{\sqrt{E}})^2 + (7.4 \pm 0.8\%)^2 \ . \tag{3.2}$$

for the HB and HE [97], and

$$(\frac{\sigma_E}{E})^2 = (\frac{198\%}{\sqrt{E}})^2 + (9\%)^2 \ . \tag{3.3}$$

for the HF [98].

3.2.5 The Superconducting Solenoid

One of the defining features of the CMS detector is the superconducting solenoid, that encompasses the silicon tracker and calorimetry [99, 100]. The cylindrical coil measures 13 m long, has a 5.9 m inner diameter, is situated inside a vacuum tank where it is cooled to its operating temperature of 4.5 K using liquid helium, and operates at magnetic field of 3.8 T. While the solenoid was designed to operate at 4 T, the CMS Collaboration chose to operate it at 3.8 T in order maximise the lifetime of the apparatus.

As shown in Figure 3.9, the solenoid provides a strong homogenous magnetic field within its volume. This large bending power not only provides excellent momentum resolution for charged particles within the tracking detector, but it also prevents low transverse momentum charged particles from reaching the calorimetry and negatively impacting on energy resolution and isolation efficiency. Outside the solenoid, an iron return yoke guides and contains the return magnetic field. The return magnetic field is approximately 1.7 T in the barrel and outermost endcap disks which is sufficiently strong to enable accurate momentum resolution for tracking and charge identification of high momentum, i.e. ≥ 1 TeV, muons.

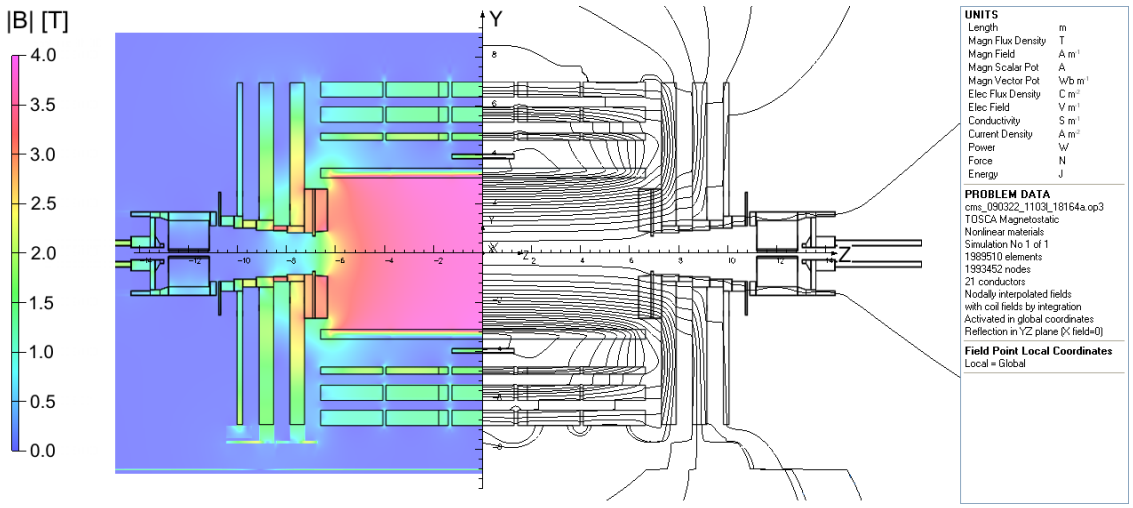

Figure 3.9: Longitudinal section of the CMS detector, illustrating the predicted magnetic field strength (left) and field lines (right) for the operational central magnetic flux density of 3.8 T [101].

3.2.6 Muon Detectors

As implied by the experiment's name, the detection and measurement of muons is incredibly important for CMS, as many of the signatures of interesting events involve them. As muons are Minimum Ionising Particles (MIPs), they pass through the inner detectors and the solenoid with minimal interaction. Consequently, the muon chambers [102] are placed

outside the solenoid and are interspaced between the iron return yoke rings and disks.

Figure 3.10 shows the layout of the gas detectors which make up the muon system. As the magnetic field outside the solenoid is non-uniform and the radiation levels vary, the muon system is comprised of three different types of detectors that use different technologies in order to provide a high performance system.

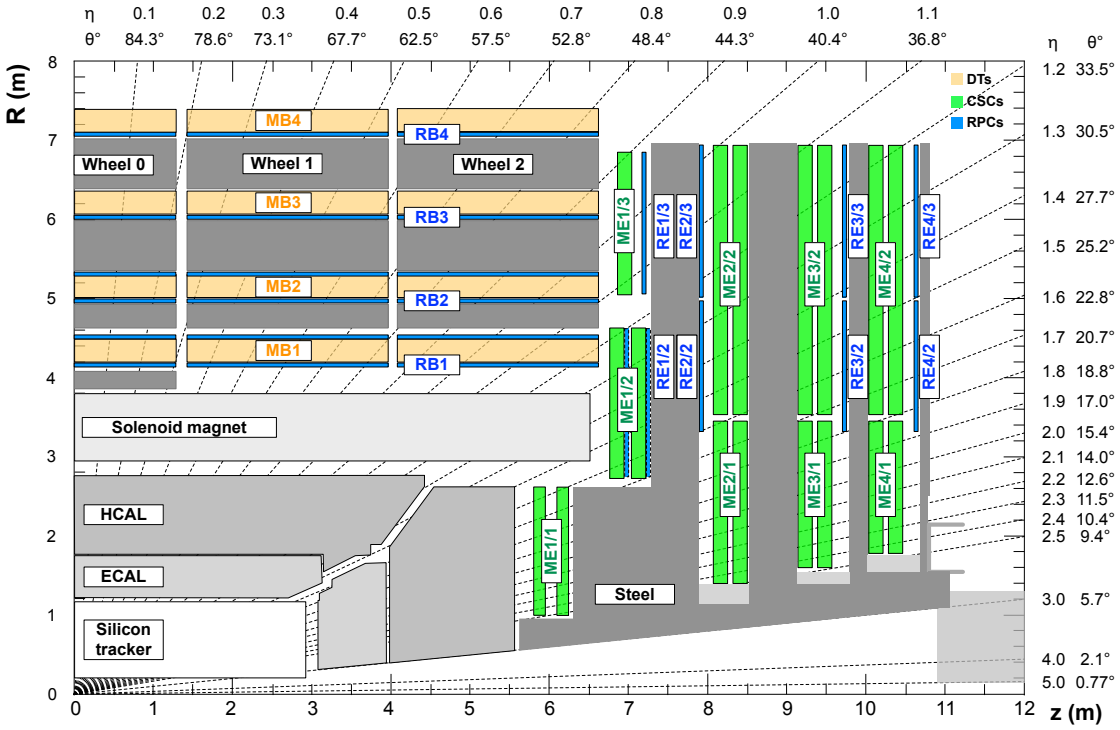

Figure 3.10: Layout of one quadrant in $\mathring{z}$ of the CMS muon detectors in their current configuration. The DTs are marked in yellow, the CSCs in green and the RPCs in blue [103].

Drift Tubes (DTs) operate in the barrel region covering $|\eta| < 1.2$, where the magnetic field strength is low as most of the return field is contained within the return yoke. Each tube is a 4.2 cm × 1.3 cm cell that contains an anode wire surrounded by a mixture of Ar (85%) and CO_2 (15%). As a muon passes through the chamber it ionises the gas within, with the resultant free electrons drifting towards the positively charged wire and inducing an electrical signal that is read out.

As shown in Figure 3.11, the DT chambers are comprised of twelve layers of DTs that are grouped into three *superlayers* (SLs) of DTs. Each SL is comprised of four layers of DTs, with each layer being offset from the other by half the width of half a DT in order to improve angular resolution. The outer SLs are orientated to measure coordinates in the $r - \phi$ plane and the innermost SL is orientated to measure coordinates in the r-z plane (which the outermost station lacks). A honeycomb spacing structure separates SL3 from the other SLs to increase the lever arm length for measuring the track direction in the bending plane. This

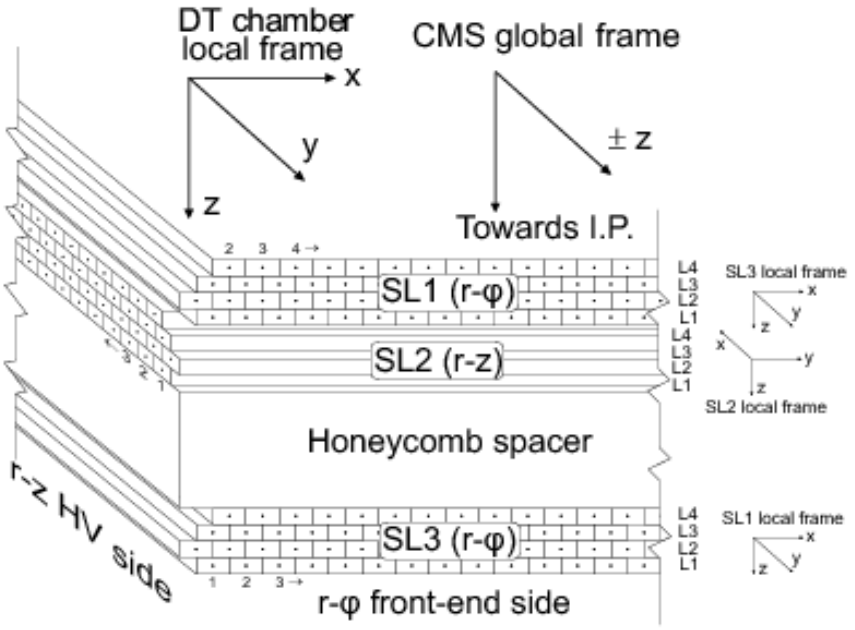

Figure 3.11: A schemeatic layout of a DT chamber, illustrating the half DT width offset between the adjacent layers and the $r-\phi$ plane orientation of the outer SLs and the r-z plane orientation of the inner layer [104].

arrangement allows for a high muon track identification efficiency and provides resolutions of about 200 μm and a ϕ angular resolution of approximately 1 mrad.

Cathode Strip Chambers (CSCs) are employed across four endcap disks which cover the region $0.9 < \eta < 2.4$. SCS are used in the endcaps as they are more suited to the higher muon rate and non-uniform magnetic field environment of the forward regions. While only the innermost ring of the outermost (fourth) disk was originally installed, an outer ring for the outermost disk was installed during LS1 during 2013-2015 [105].

Each CSC, as shown in Figure 3.12, is composed of seven trapezoidal panels. The six gaps between the panels are filled with planes of anode wires that run almost perpendicular to a planes of cathode strips which are surrounded by a gas mixture of Ar, CO_2 and CF_4 [106]. This provides six position measurements per chamber with a resolution in the $r-\phi$ plane of 75 μm for the two innermost rings of the first disk and 150 μm for the other disks [102].

Resistive Plate Chambers (RPCs) provide complimentary coverage in the range $|\eta| < 1.8$ [105]. The barrel contains six layers of RPCs, with a layer either side of the first two DT layers and one in each of the outer stations, and the endcaps have 4 RPC disks each, one for each CSC disk.

Each RPC is formed of two parallel resistive plates, separated by a gas filled gap of a few millimetres, with a large electric field applied across it. In contrast to the DTs and CSCs,

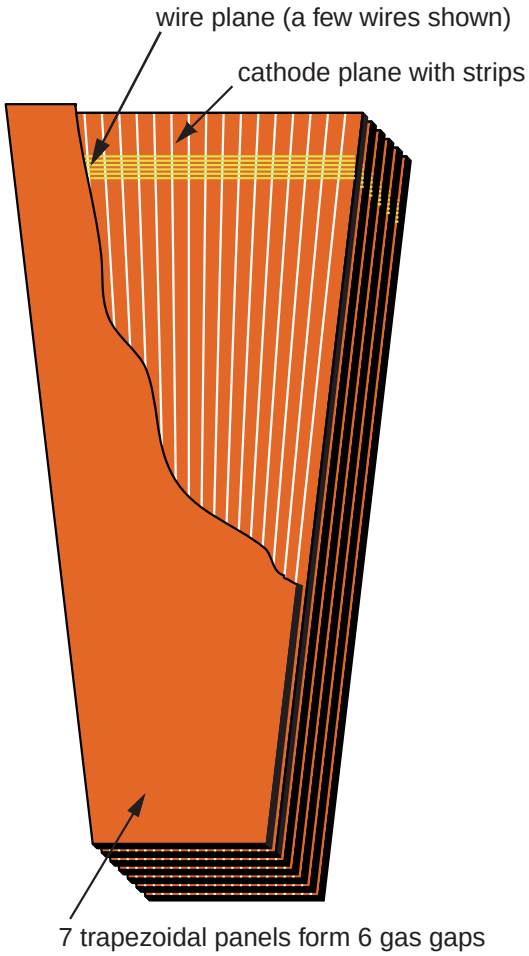

Figure 3.12: A schemeatic overview of a CSC, illustrating a plane of anode wires between two of the trapezoidal panels and the plane of cathode strips which run almost perpendicular to them [92].

RPCs have a coarser position resolution of about 1 cm but have faster response times and a superior excellent time resolution of approximately 2 ns. Consequently, the RPCs are used by trigger system to identify muons and to accurately determine which bunch crossing they originated from. Their coarser spatial resolution is also used to supplement information from the DTs and CSCs in track reconstruction.

When the information from the muon and tracker systems are combined, as described in Chapter 5, the CMS detector is able to measure momentum resolutions of 1.3% to 2.0% in the barrel and up to 6% in the endcaps and a charge misidentification rate of less than 0.1% for muons with p_{T} less than 100 GeV [107, 108].

3.2.7 Trigger and Data Acquisition Systems

At design luminosity, the LHC has a bunch crossing (BX) rate of 40 MHz, i.e. of the order of 10^9 inelastic events per second. With each proton-proton collision event having a size of about 1.5MB [92], even if there was processing power and sufficient bandwidth available to reconstruct the read-out of all the sub-detectors for every event, there would be insufficient storage capacity to save them.

The vast majority of events however, are uninteresting from a physics perspective, with the cross sections of interesting processes being at least a factor of 10^7 smaller than the total proton-proton cross section of 110.6 ± 3.4 mb [109]. Consequently, the CMS trigger system is designed to reject these background events and select events in a manner that allows all possible new physics signatures to be detected whilst keeping acceptance thresholds sufficiently as low as reasonably possible.

The CMS trigger system is comprised of two stages, the Level-1 (L-1) Trigger and the High Level Trigger (HLT), as it is not feasible to reduce the data rate in a single processing stage without compromising on physics performance. Since initial operations of the CMS experiment, the original event storage rate of 100 Hz has been increased to 0.5-1 kHz [79, 110].

3.2.7.1 Level-1 Trigger

The Level-1 trigger reduces the input 40 MHz rate to about 100 kHz and consists of FPGAs (Field Programmable Gate Arrays) and ASICs (Application Specific Integrated Circuits), which have to be highly efficiency at identifying interesting physics signals. As the trigger decision cannot be made before the subsequent BX, the L-1 Trigger uses a pipelined approach that is capable of buffering the detector for about 3.8 μs (limited by the tracker and ES buffers) before a decision has to be made on whether to read-out an event or discard it. This latency precludes both the reading out of events in full and of the use of iterative reconstruction algorithms. While the calorimeters and muon detectors contribute to the L-1 Trigger decision, tracking information does not as as when CMS was designed it was not possible to read out every event from the tracker.

The current L-1 trigger, the *Phase-I Trigger*, was developed to ensure that the 100 kHz L1 trigger limit would be maintained following the increase in the instantaneous luminosity and centre-of-mass energy of the LHC following LS1 [110]. The Phase-I Calorimeter Trigger is based on a *time-multiplexed* architecture which uses large FPGAs on a small number of general-purpose boards with fast optical links that allow for full granularity data to be used. The previous calorimeter trigger architecture reduced the volume of input data by identifying the best trigger candidates at a regional level and forwarding them to a global stage where a L-1 acceptance decision would be made [110]. In contrast, time-multiplexed trigger concept processes full granularity data from across the calorimetry systems for every

nth bunch crossing on one of n identical processors. Such a system requires at least two layers, linked by a switching network which buffers and transmits data from the multiple sources to a single processor, as illustrated in Figure 3.13.

A time-multiplexed architecture was used as it provided a number of advantages compared to traditional trigger architectures, including:

- minimised boundary issues and data sharing between processors, saving time and resources and allowing for data from the entire calorimeter for a bunch crossing to be considered on a single processor and thus consider candidates that would have been discarded by the previous regional triggers;
- synchronisation being only required within each processor instead of the entire system;
- system demonstration with a single processor as each processor is identical and fully pipelined (no sideways connections);
- validation only requiring one processor as each is identical and has no sideways communication;
- the loss of a processor resulting in the loss of a bunch crossing instead of a region of the detector;
- the use of spare processors to test new algorithms online in parallel with the nominal trigger without affecting the current system and as backup processors in case of the failure of another.

The electronics of the Phase-I Trigger were installed during LS1 and ran using the legacy trigger system during 2015 with the new trigger system running in parallel for validation prior to commissioning and usage during 2016 [112].

Given the operational successes of this architecture, a similar time-multiplexed approach for a proposed track finding system for the Phase-II Outer Tracker has been developed. This proposed system and the studies presented in this thesis relating to it are discussed in Chapter 4.

3.2.7.2 High Level Trigger and Data Acquisiation

Upon receipt of a L1 trigger, the Data Acquisition (DAQ) system reads out the buffered data from the detector front-end electronics and collates it into a complete event to be processed by the HLT [113].

The HLT is a high performance computing farm comprised of commercially available processors running the CMS Software (known as CMSSW) which reduces the L1 rate of about

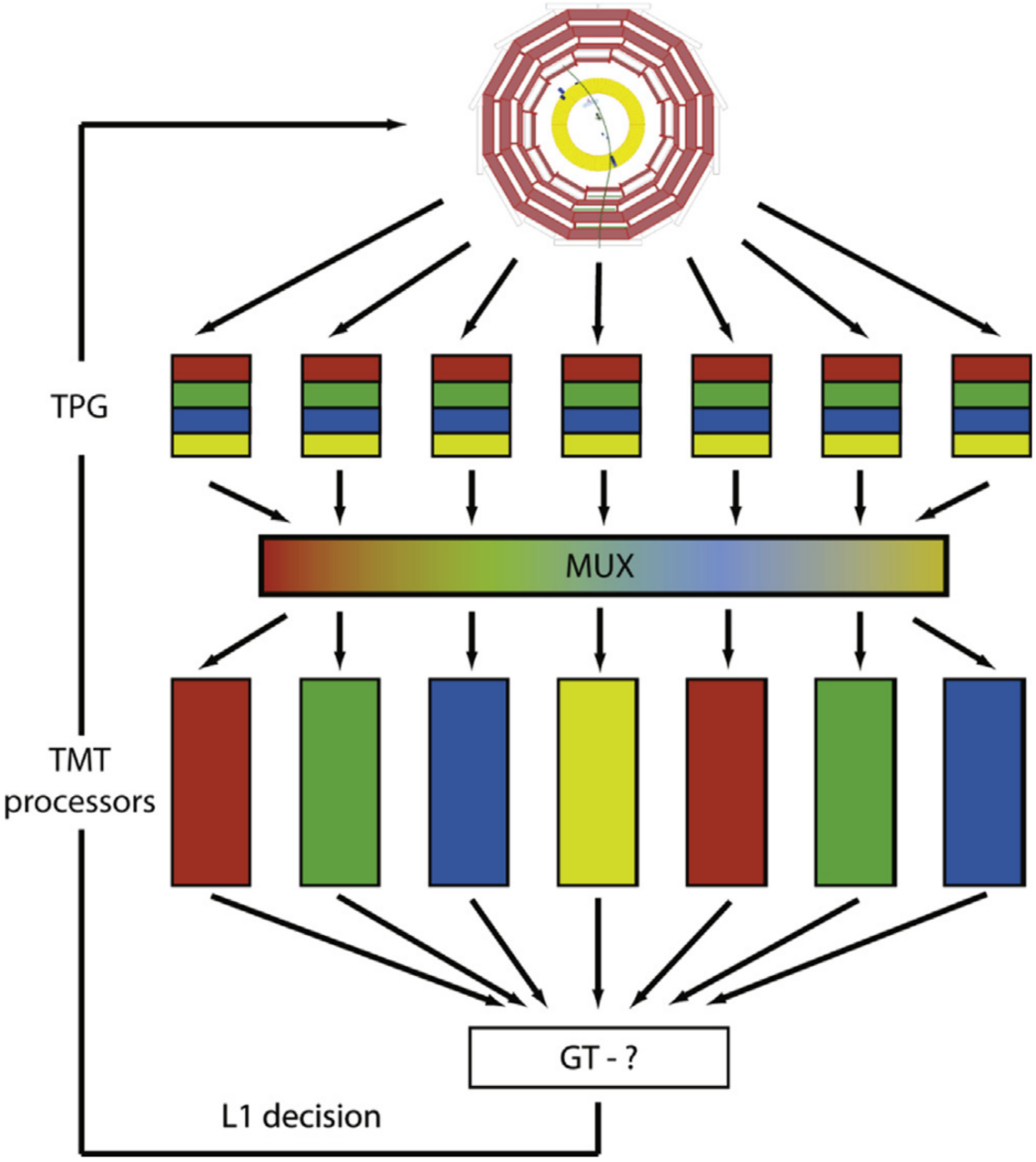

Figure 3.13: In a time-multiplexed trigger, all data from the Trigger Primitive Generators (TPG) covering the entire detector are transmitted to one of "n" identical processors after passing through the multiplexing fabric (MUX), a serial interconnection linking each TPG to each TMT processor, before being passed to the Global Trigger (GT) where the decision of whether or not to issue a L1 receipt to the HLT is determined [111].

100 kHz to an output rate of approximately 1 kHz. In contrast to the L1 trigger, the HLT has a larger latency budget and is able to make use of the full detector readout (including the Tracker and ES), allowing for more sophisticated reconstruction and selection algorithms to be used to select events for storage. This however, does not mean that the full event is reconstructed, as such a task is too CPU intensive to be done online within the latency constraints. Events accepted by the HLT are forwarded to the offline Tier-0 computing centre for offline processing and reconstruction and are also passed to the online detector monitoring systems.

3.2.8 LHC and CMS Performance

During 2016, the LHC operated at $\sqrt{s} = 13\,\text{TeV}$ up to a maximum instantaneous luminosity of $15.3 \times 10^{33}\ \text{cm}^{-2}\,\text{s}^{-1}$. As shown in Figure 3.14, the LHC delivered a total integrated luminosity of $40.82\,\text{fb}^{-1}$ during stable beams to the CMS detector, of which $37.76\,\text{fb}^{-1}$ was recorded [114, 115].

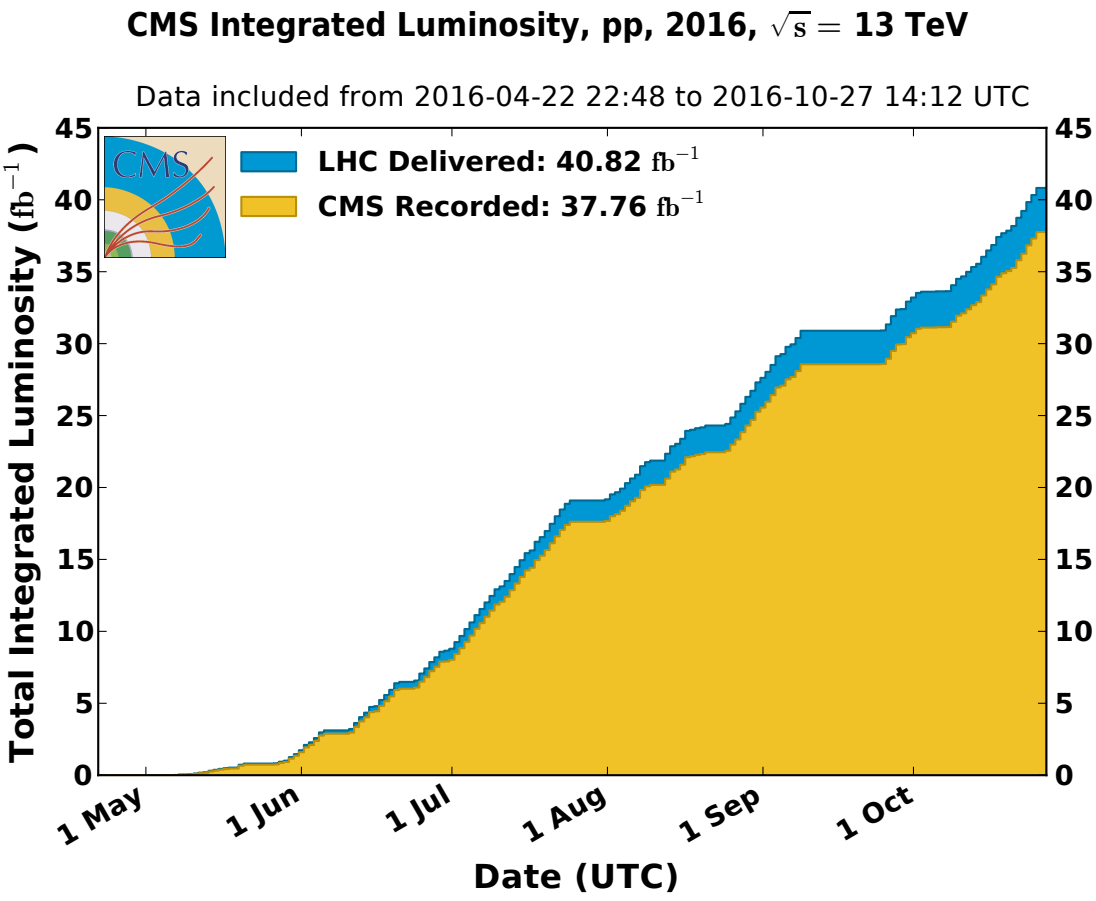

Figure 3.14: The total integrated luminosity delievered to and recorded by the CMS experiment during 2016 [115].

The CMS experiment monitors and measures the instantaneous and integrated luminosity delivered by the LHC using the pixel detector, DTs, HF, the Fast Beam Conditions Monitor and Pixel Luminosity Telescope. During Run 2 of the LHC, the primary offline luminosity measurements made by the CMS Luminosity Group used the pixel detector using the Pixel Cluster Counting (PCC) method due its stability over time for up an average PU of 150 and the high precision results obtained with it during Run 1. The PCC algorithm is able to achieve such a precision by measuring the instantaneous luminosity through the number of pixels present. This is possible as the probability of pixel hit belonging to multiple tracks is very small due to the very low occupancy of the detector, inferring that the number of pixel hits are linearly proportional to the number of interactions during a bunch crossing [115].

Van der Meer (VdM) scans during dedicated LHC runs were used to calibrate the absolute luminosity scale calibrations of the detectors [116]

Chapter 4

Development of a Level-1 Track Trigger for the CMS Phase 2 Upgrade

Before the start of these higher luminosity operations, the then life-expired CMS tracker will need replacing. The new tracker will not only need to have increased radiation hardness to withstand the increased PU environment, but also the capability to provide limited tracking information to the L-1 trigger in order to keep the L-1 acceptance rate below 750 kHz.

This chapter introduces the motivations behind the high luminosity upgrade of the LHC, the planned upgrade of the CMS tracker and the studies undertaken for one of the proposed track finding systems for the upgrade tracker.

4.1 The High-Luminosity Large Hadron Collider

In order to fully exploit the physics discovery potential of the LHC, it is planned to increase the instantaneous luminosity the accelerator can deliver by up to an order of magnitude greater than the nominal design.

The High-Luminosity Large Hadron Collider (HL-LHC) upgrade is intended to increase the instantaneous luminosity of the LHC up to $7.5 \times 10^{34}\,\mathrm{cm}^{-2}\,\mathrm{s}^{-1}$. This corresponds to an average number of proton-proton interactions (PU) per 40 MHz bunch crossing of between 140 and 200 and a total integrated luminosity of up to of $3000\,\mathrm{fb}^{-1}$ being provided to both the ATLAS and CMS experiments during the 10 year planned lifetime of the HL-LHC.

The installation of the HL-LHC upgrade is planned to take occur during Long Shutdown 3 (LS3), which is currently expected to start during 2024 [117]. The timing of LS3 is motivated in part by the need to replace the inner triplet quadrupole magnets that focus the beams at

the ATLAS and CMS collision regions are expected to be near life-expired due to radiation exposure [118, 119].

The instantaneous luminosity, L, of an accelerator and its beam parameters are related by [117]:

$$L \propto \frac{n_b N_p^2}{\beta^*} R \tag{4.1}$$

where n_b is the number of bunches, N_p^2 is the number of protons per bunch, β^* is the focal length (beam β value) at the collision point, and R is a crossing-angle-dependent luminosity geometrical reduction factor.

As it is not practical to increase the number of proton bunches due to the resultant heat loads induced by electron clouds, the increase in the machine's luminosity will be achieved by increasing the number of protons per bunch and by reducing β^* [117]. Replacing Linac2 with the new Linear accelerator 4 (Linac4) [120] during the Long Shutdown 2 (2019-2020) will allow for the number of protons per bunch to be increased by a factor of two compared to the nominal LHC design (and to increase the injection energy by a factor of three). The new, more radiation tolerant, quadrupole magnets to be installed during LS3 will provide the higher magnetic field strength and the aperture needed to provide the lower β^* required to increase the instantaneous luminosity.

4.2 The Phase-II Outer Tracker Upgrade

To meet the significant challenges of, and exploit, the increased instantaneous luminosity delivered by the HL-LHC, the CMS detector will be substantially upgraded. This upgrade will take place during LS3 and will not only deliver the improved radiation hardness to handle the increase in radiation from the increased PU but also greater detector granularity to reduce occupancy and enhanced bandwidth and triggering capabilities to avoid compromising physics potential [76, 119].

The Phase-II upgrade will see the entire silicon tracking detector being replaced with one comprised of a pixel Inner Tracker and pixel and strip Outer Tracker that have the following properties:

- **Improved radiation hardness** is required so that the tracker is able to withstand the increased fluence of the HL-LHC (up to $2.3 \times 10^{16} n_{eq}/cm^2$ for the innermost layers) and operate efficiently up to the target luminosity. A margin of about 50% will be required to accommodate the target luminosity being exceeded and the uncertainties in the anticipated radiation exposure.

- **Increased sensor granularity** is required to ensure that the channel occupancy is kept at or below the per cent (per mille) level for the Outer (Inner) Tracker to ensure that a high track reconstruction efficiency and a low misidentification rate is maintained under the increased PU conditions. This will also enable improved track separation in dense environments, such as high p_{T} jets, compared to the current pixel detector.

- **Reduced material in the tracking volume** will significantly enhance the performance of the detector.

- **Level-1 trigger contributions** are required in order to maintain L-1 trigger performance. It has been shown that the performance of the L-1 trigger will deteriorate in the high luminosity environment from both the rate increase and the reduced efficiencies of the L-1 selection algorithms [119]. Raising the upgraded calorimeters' and muon chambers' trigger thresholds would have minimal impact on the rate, and would negatively impact sensitivity to BSM physics that predicts new low mass particles [119]. Therefore the L-1 bandwidth and latency will be increased (from 100 kHz to 750 kHz and from 3.2 μs to 12.5 μs respectively) and tracking information will be included in the L-1 decision process to preserve and improve trigger performance.

- **An extended tracking acceptance** of up to $|\eta| = 4$ in the forward region will greatly improve the overall physics capabilities of the CMS experiment as the density of jets associated with vector boson increases with pseudorapidity [119]. By extension, measurements of missing transverse energy, total energy and jet b-tagging acceptance will also be improved.

Therefore, the Inner Tracker is designed to cover the range up to $|\eta| = 4$ using $100 - 150\,\mu$m thick planar silicon pixel sensors, measuring either $25 \times 100\,\mu\mathrm{m}^2$ or $50 \times 50\,\mu\mathrm{m}^2$. These sensors provide the low (per mille) occupancy and track separation with the negligible inefficiencies required.

As with the previous pixel detectors, the Inner Tracker is also designed for easy installation and removal to facilitate repairs and replacement of degraded parts. Further discussion of the Inner Tracker can be found in the Phase-II Technical Design Report [76].

As tracking information is required to make L-1 decisions at the HL-LHC, the design of the Outer Tracker has been driven by the need to provide tracking information to the L-1 trigger. Given that it will not be possible to read out the entire Outer Tracker for the L-1 trigger for every bunch crossing, a novel design of a pair of closely-spaced silicon sensor layers, separated by a few mm, that are capable of rejecting low transverse momentum tracks has been proposed [121, 122]. These sensors, known as the p_{T}-*modules*, are able to discriminate against low transverse momentum charged particle tracks.

As the bend angle of a charged particle in a magnetic field depends on its transverse momentum, a p_{T}-module is able to reject tracks below a configurable p_{T} threshold by comparing the distance between clusters of hits between its two sensor layers, as demonstrated in Figure 4.1(a). The p_{T} threshold is designed to be configurable as the separation between the clusters increases with a module's distance from the beam if the sensor spacing remain unchanged, as illustrated in Figure 4.1(b). The sensor spacing however, is increased for the endcap disks, where the p_{T}-modules are orientated perpendicular to the beam line, in order to maintain comparable discrimination due to projective effects, as shown in Figure 4.1(c).

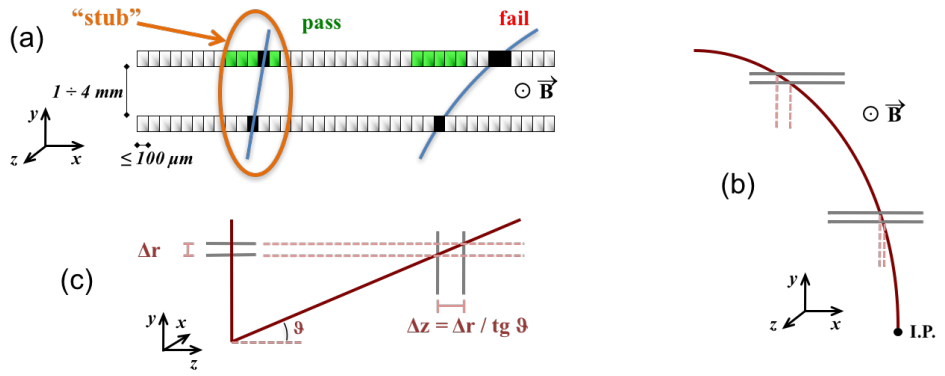

Figure 4.1: Cluster matching in the p_{T}-modules proposed for the Outer Tracker [76] as described in the text; (a) demonstrates how correlating pairs of closely-spaced clusters between the two sensor layers allows for the discrimination of a track candidate's transverse momentum; (b) shows that if the sensor spacing remains unchanged, that the separation between the two clusters increases the further a module is away from the beam line; and (c) illustrates that the sensor spacing of modules in the endcap disks, which are perpendicular to the beam line, is required to be larger because of projective effects.

By correlating pairs of clusters on-detector that are consistent with a track with a transverse momentum of about 2 GeV or greater, an effective data rate reduction of approximately a factor of 10 is achieved before the resultant *stubs* are transferred to the L-1 trigger [123, 124].

Two p_{T}-modules are being developed for the Outer Tracker upgrade: 2S *strip-strip* modules and PS *pixel-strip* modules. The 2S modules, are designed to be used at radii $r > 60$ cm from the beam line, where the hit occupancies are lower and each sensor has an active area of 0.05 cm $\times$ 9.14 cm. Both 2S module strip layers have a pitch of 90 μm in the transverse plane (r-φ) and a strip length of 5.03 cm along the direction of the beam axis, z. Each PS module sensor layer has an active area of 4.69 cm $\times$ 9.60 cm and will be used at radii in the range $20 < r < 60$ cm where the occupancies are highest. The upper PS module layers consist of a silicon strip sensor and a silicon pixel sensor, both with a pitch of 100 μm in r-φ, and a strip length in z of 2.35 cm for the strips and 1.47 mm for the pixels. The finer granularity provided by the pixel layer affords better resolution along the z axis, which is crucial for vertex identification in the high PU environment of the HL-LHC. Further details

on the two p_{T}-modules can be found in [76, 119].

The current proposed layout of the Phase-II Outer Tracker, referred to as the *tilted barrel* geometry, is depicted in the upper diagram in Figure 4.2, and a previous proposal, referred to as the *flat barrel* geometry, is shown in the lower diagram [119]. Both plots illustrate the PS and 2S module positions in the six barrel layers and the five endcap disks on either side of the barrel, with only modules located at $|\eta| < 2.4$ being configured to send stub data off-detector. The geometries are so named as they were inspired by whether or not the modules in the three innermost barrel layers are tilted so that their normals point towards the interaction region. The advantages of the tilted geometry over the original flat barrel are that it not only improves stub-finding efficiency for tracks with large incident angles but that it also reduces the overall cost of the system [76]. Due to the maturity of the preparations for the review between the three competing proposed track finder systems, discussed later in Section 4.3, at the time the tilted barrel geometry was adopted for the Phase-II Outer Tracker TDR it was decided to use the flat barrel geometry for results produced for the review.

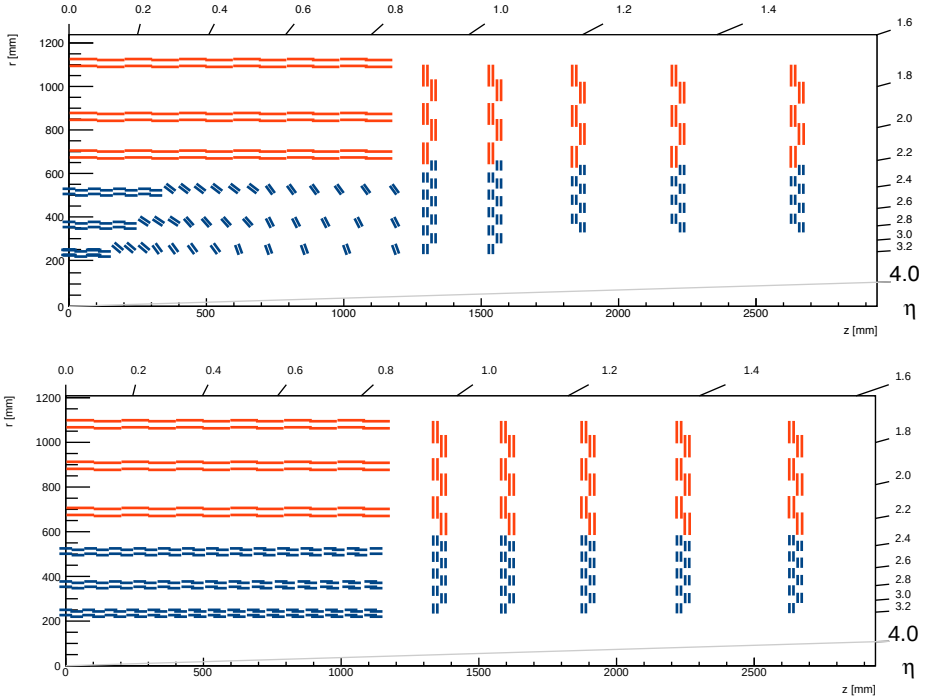

Figure 4.2: One quadrant of the Phase-II Outer Tracker layout, showing the placement of the the PS (blue) and 2S (red) modules. The upper diagram shows the currently proposed *tilted barrel* geometry [76, 125], and the lower diagram shows an older proposal for the layout, known as the *flat barrel* geometry [119].

Figure 4.3 illustrates the data flow and latency requirements from the p_{T}-modules to the off-detector electronics for the upgraded tracker. Out of the total L-1 latency of 12.5 μs, about 1 μs is required for generation, packaging and transmission of stubs from the tracker

front-end (FE) electronics to the Data, Trigger and Control (DTC) system. Approximately 4 μs is available for the reconstruction of tracks from data arriving at the DTC. The rest of the available latency is allocated for the correlation of tracks with trigger primitives from the calorimeters and muon systems (3.5 μs), the propagation of the L-1 decision to the hardware/firmware buffers (1 μs) and an additional safety margin (3 μs) [126].

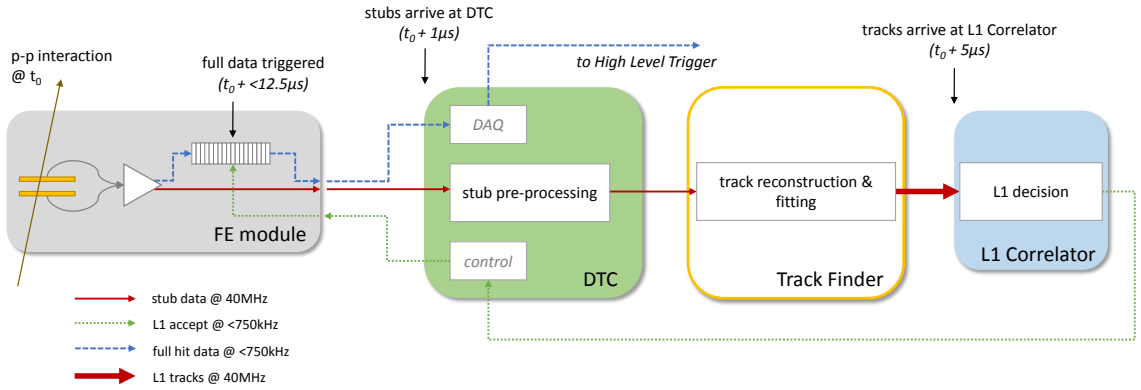

Figure 4.3: Illustration of data flow and latency requirements starting from the p_{T}-modules and front-end (FE) electronics and running through to the off-detector electronics dedicated to forming the L-1 trigger decision [126].

The architecture of any Track Finder system proposed, which will take the pre-processed stubs as input and output fully reconstructed tracks for the L-1, will be constrained by the system's latency budget and how the detector is cabled to the DTC system. The 4 μs latency constraint will limit the amount of processing that can be done for the finding and fitting of tracks and the choice of cabling scheme for the detector will determine how data is distributed and processed throughout the Track Finder system.

4.3 A Time-Multiplexed Track Finder

Three different L-1 track finders have been explored by the CMS Collaboration. One of the proposals uses Associative Memory (AM) ASICs for track finding and FPGAs for track fitting [76, 127]. The other two proposasls are all-FPGA approaches, one using a fully Time-Multiplexed Track ($TMTT$) finder which uses the Hough Transform to identify track candidates [126] and one using a "road search" (*tracklet*) algorithm to reconstruct tracks [76, 128]. Hardware demonstrators for each of these proposed L-1 track finders were constructed to prove the feasibility of each approach, which were reviewed in 2016.

In rest of this section the architecture and components of the $TMTT$ Track Finding Processor are discussed.

4.3.1 The Track Finding Architecture

The proposed FPGA-based Hough Transform Track Finder is a scalable, flexible and redundant design based on a fully time-multiplexed architecture for implementation on commercially available FPGAs, as previously demonstrated by the Phase-I Calorimeter Trigger Upgrade [110] discussed in Section 3.2.7.1. As discussed in Section 3.2.7.1, a time-multiplexed design has a number of advantages, including that only a single Track Finding Processor (TFP) is required to demonstrate the full system as each processor is identical in every respect.

Unlike the Phase-I Calorimeter Trigger, it is not feasible to process the entire output of the Phase-II Outer Tracker in a single processor for a given time slice. This is because of the limits imposed on the system by the total data and latency bandwidth a single FPGA-based processor can handle.

The number of independent track finding processors was determined by how the DTC system was connected to the tracker. At the time of the 2016 review it was assumed that the detector would be cabled to the DTC system such that each DTC board would process all data from a i.e. 45 degree φ-sector, known as a *detector octants*, in the tracker. Consequently, the proposed track finding system was divided into *processor octants* that were offset from the detector octants by about 22.5 degrees in ϕ, as shown in Figure 4.4, in order to handle data duplication across hardware boundaries. The detector octants are not uniform as the geometry of the tracker does not have an exact eight-fold symmetry.

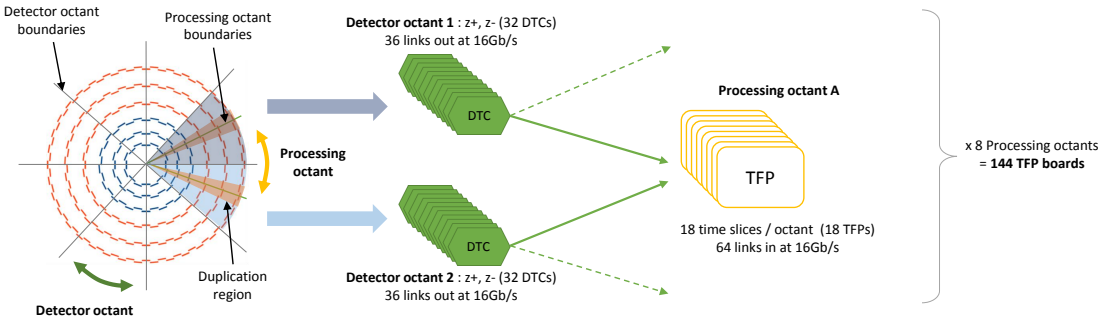

Figure 4.4: An illustration of the baseline system architecture described in the text, demonstrating how two neighbouring DTCs time-multiplex and duplicate stub data across processing octants and how it transmits the processed data to two neighbouring TFPs [126]

This baseline track finding system architecture, illustrated in Figure 4.4, uses two neighbouring DTC boards to time-multiplex and duplicate stub data across processing octant boundaries before each DTC transmits 50% of its data to one TFP and 50% to the neighbouring TFP. Based on current electronics and the high speed links available, the data

requires 18 TFPs per processing octant (one for each time slice, resulting in a full system requiring 144 TFPs).

A hardware demonstrator of the baseline system consisting of five Master Processor Virtex-7 (MP7) cards [129], capable of processing one phi-octant of the tracker with a time-multiplexing factor of 36, was used to validate the feasibility of the proposed full system using hardware available at the time of the 2016 review. All of the results achieved, and a complete description of the system, are given in [126].

4.3.2 The Track Finding Processor

The Track Finding Processor shown in Figure 4.5 consists of four self-contained components:

- **Geometric Processor (GP):** Responsible for pre-processing the stubs from the DTC.
- **Hough Transform (HT):** A highly parallelised initial coarse track finding that identifies track candidates that are consistent with a track in the r-φ plane, greatly reducing the data volume and combinatorics that have to be considered by the subsequent stages.
- **Kalman Filter (KF):** A track filtering and fitting stage which removes incorrectly reconstructed tracks, stubs that are incorrectly associated to a track and precisely fits helix parameters.
- **Duplicate Removal (DR):** A final pass filter that uses the precise fit information to remove duplicate tracks generated by the Hough Transform.

Each of these components is described in more detail below.

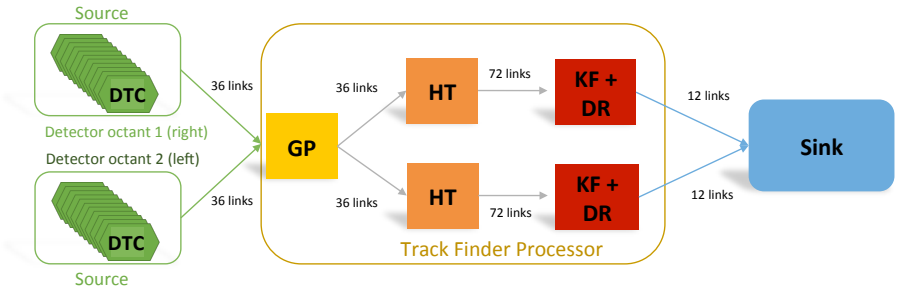

Figure 4.5: The four self-contained logical components of the Track Finding Processor, where each box (block) in the diagram represents a single FPGA. The two FPGAs for the two detector octant sources and the sink FPGA and the optical links between all components are also shown.

4.3.2.1 Geometric Processor

Each GP performs two tasks: the conversion of the 48-bit DTC stubs into a 64-bit format extended format that is used to reduce the HT processing load and assignment of the stubs in each sector into a subsector. Each sector is composed of 2 sub-sectors in ϕ and 18 in η.

This division of the processing octants simplifies the task of the downstream logic, allowing the track finding to be carried out independently and in parallel within each sub-sector. The chosen η binning is sufficiently fine to ensure that any track found by the r-φ HT is consistent with a straight line in the r-z plane, despite the fact the Hough Transform itself only searches for tracks in the r-φ plane, thus rejecting incompatible track candidates.

Stubs that are compatible with more than one sub-sector, usually due to track curvature in ϕ, are duplicated.

Stubs are assigned to sub-sectors occurs in a three stage process:

- A rough η sorting into six bins;
- A subsequent fine η sorting into three bins and;
- A ϕ sorting into two bins.

Each of the TFP's logic blocks shown in Figure 4.5 has been designed to be highly reconfigurable and can easily be adapted to any alternative sub-sector definition.

4.3.2.2 Hough Transform

The Hough Transform algorithm is a widely used method of detecting geometric features in digital image processing [130]. While the Hough Transform can be used to find any shape that can be parametrised, its simplest form of detecting straight lines is the most relevant for the proposed track finder. In this case, the Hough Transform describes a point (x, y) in real space as a straight line with a gradient and intercept (m, c) in the parameter space known as *Hough*-space. Conversely, a point in Hough-space corresponds to a straight line in real space. Therefore, a straight line corresponding to a set of points in real-space is given by the intersect of a set of lines corresponding to the real-space points in Hough-space.

The Hough Transform is used by the TFP to find the tracks of charged particles with $p_{\mathrm{T}} > 3\,\mathrm{GeV}$ in the r-φ plane, which has a better resolution than the r-z plane, independently for each η-ϕ sub-sector within each processing octant.

The radius of curvature, R (cm), for a charged particle's trajectory can be described as a function of the particle's p_{T}, charge q and of the homogeneous magnetic field, B, in which it is travelling:

$$R = \frac{p_{\mathrm{T}}}{0.003\,qB} \tag{4.2}$$

A stub associated with such a charged particles' trajectory and which has coordinates (r,φ) is related to R by:

$$\frac{r}{2\,R} = \sin\left(\varphi - \phi\right) \tag{4.3}$$

where ϕ is the angle of the track in the transverse plane at the origin [122].

From Equation (4.2), it can be seen that tracks with large p_{T} ($> 2-3\,\mathrm{GeV}$) have a large R. This allows for the use of the small angle approximation to simplify the right-hand side of Equation (4.3). If energy losses are neglected from processes such as multiple scattering and Bremsstrahlung, the position of the stubs will be compatible with the trajectory described by Equation (4.3) (i.e. R can be assumed to be constant).

Therefore, Equations (4.2) and (4.3) can be combined to describe how a stub's position in (r, φ) can be transformed into a line in (q/p_{T},ϕ) Hough-space where:

$$\phi = \varphi - \frac{0.0015\,qB}{p_{\mathrm{T}}} \cdot r \tag{4.4}$$

If a particle produces multiple stubs, such as those represented by the six dots in the left-hand side of Figure 4.6, they can be used to identify a track candidate through their intersection point, which is also shown in the figure (right-hand side). The coordinates of the intersection point in Hough-space also provides an initial estimate of the track's p_T and ϕ helix parameters, as defined in Section 4.4.1.

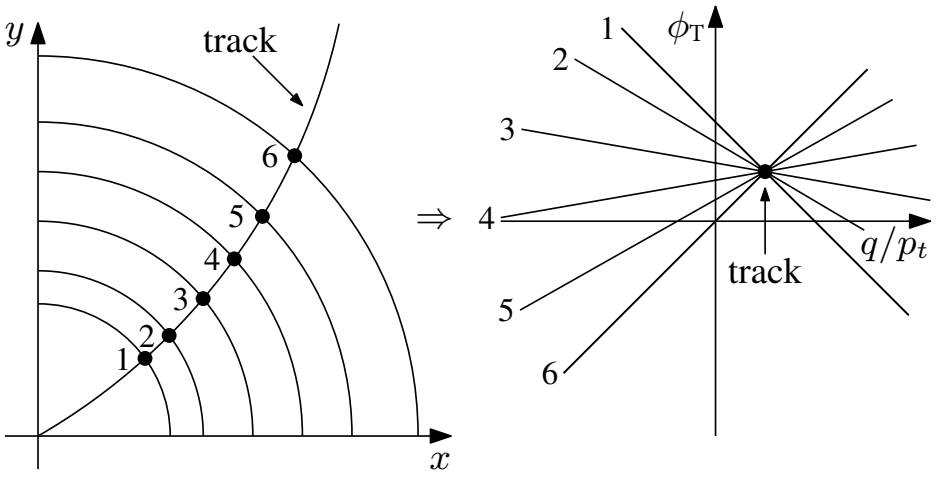

Figure 4.6: Illustration of the Hough Transform. The left-hand side shows the trajectory of a single charged particle in one quarter of the tracker barrel in the $x-y$ plane. The right-side illustrates the six lines in Hough-Space which correspond to the six dots in real space.

As the radii of the stubs gives the line gradients in Hough-space, they will always be positive. Therefore, it is preferable to measure the stub coordinates relative to the point where the

corresponding track crosses a cylinder in the $x - y$ plane of radius T. By choosing an appropriate value of T, the transformation of $r \to r_T$ and $\phi \to \phi_T$ increases the size of Hough Transform phase space used. This allows more precise measurements of the intersection point to be made and consequently fewer fake tracks and duplicates are found. The optimal value of T was determined to be 58 cm [126].

As the R for the lowest p_{T} track (3 GeV) to be considered is greater than the outer radius of the tracking detector ($r = 1.2$ m), all relevant particles are expected to traverse at least six barrel layers or endcap disks. The threshold for the identification of a track candidate however, is set at a minimum of five detector layers or disks in order to allow for detector or readout inefficiencies. This threshold can be further reduced to four layers to account for the reduced geometric coverage between $0.89 < \eta < 1.16$ or for dead detector layers or disks without significantly increasing the volume of data considered.

A detailed description of the firmware implementation of the Hough Transform for the demonstrator system is given in [126, 131].

4.3.2.3 Kalman Filter

While the Hough Transform is highly efficient at finding genuine tracks, it was found in simulation that over half of the genuine tracks found contain at least one incorrectly associated stub. If ignored, the presence of such incorrectly associated stubs would degrade the resolution of the helix parameters fitted to reconstructed tracks that are associated with a particle. In addition, simulation studies indicated that approximately half of the track candidates created by the Hough Transform did not have stubs associated to the same particle in at least four tracker layers/disks (i.e. were fake). Therefore, a Kalman Filter was developed to precisely fit the track parameters given its ability to simultaneously remove these incorrectly associated stubs and "fake" tracks while obtaining the best possible estimate of the reconstructed track's helix parameters.

While the Kalman Filter is the optimal filter for linear systems and, the optimal linear filter for non-linear systems, it also has several aspects that make it suitable for FPGA implementation compared to global track fitting methods [132], namely:

- The matrices involved are small and their size is independent of the number of measurements, minimising the logic required to implement them;
- The only matrix inversion involved is for a small matrix.

Figure 4.7 illustrates the Kalman Filter filtering and fitting process for a track candidate in the r-z plane of the barrel, where each line segment represents the predicted track trajectory at a given stage in the fitting process. The Kalman Filter begins with an estimate of the

track parameters and their covariance matrix (containing the measurement uncertainties) from the Hough Transform array, which along with the η-ϕ segment assignment, is known as the *state*. Stubs are iteratively added to the predicted state in order to produce an updated state estimate formed of the weighted combination of the predicted state and the measurement. This weighting, known as the *Kalman gain*, is derived from the relative uncertainties of the predicted state and measurement and is used to control how the state's track parameters are updated. Therefore, with every additional measurement added to the state, the uncertainty of the state's estimate decreases. This is illustrated in Figure 4.7 by the size of the shaded area around the line segments decreasing with every stub added [126].

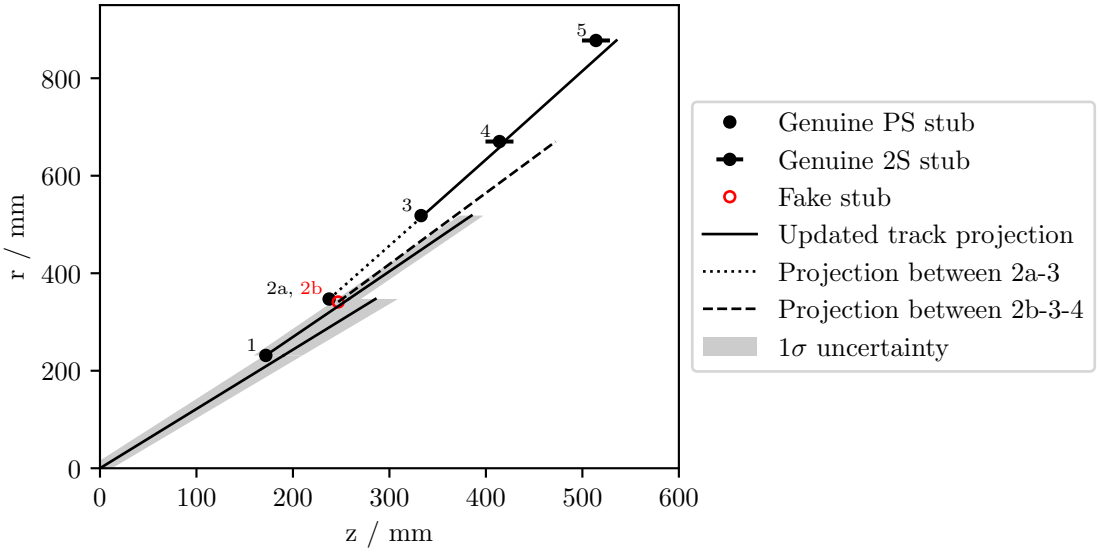

Figure 4.7: An illustrated example of the Kalman Filter filtering procedure for a track candidate in the r-z plane of the barrel as described in the text [126].

The filtering of state following each update makes use number of configurable criteria, including p_{T}, χ^2, and the minimum number of stubs from PS modules. It can also be configured to take into account and skip missing layers when the expected stub is either missing or deemed to be incorrectly associated with the track.

In the event multiple stubs are found on the same layer, each can be propagated with up to the four best states being kept and presented to a final state selector. Preference is given to states with the fewest missing layers and the smallest χ^2. An example of this is shown in Figure 4.7, where the two dashed line segments correspond to the projected trajectories of the track from the stubs labelled 2a and 2b. As each stub is compatible with the expected track trajectory at that stage, both are propagated. The track associated to stub 2b however, is rejected after stub 4 has been added to the track propagated from stub 2a, due to failing a χ^2 cut in two consecutive layers.

A full description of the Kalman formalism is given in [132]. The details of the *TMTT*

project's implementation of the Kalman Filter using FPGAs for online track reconstruction is given in [126, 133].

4.3.2.4 Duplicate Removal

Over half of the track candidates at input to the DR are duplicate tracks created by the HT. Instead of comparing pairs of tracks to see if they are the same, a more elegant and subtle DR algorithm is used which takes into account how the Hough Transform produces these duplicate tracks. This approach is illustrated in Figure 4.8. In this example, the Hough Transform has produced candidates in the yellow cell and two green HT cells from the five stubs, which correspond to the blue lines in Hough Space, that have been produced by a single particle. As all three candidates however, contain the same stubs, they will be fitted by the Kalman Filter with identical helix parameters in the same (yellow) cell regardless of the original HT cell. By comparing a track's fitted parameters with the Hough Transform cell in which they were initially found, any track whose fitted parameters does not correspond to the same HT cell in which the Hough Transform found the track in is rejected.

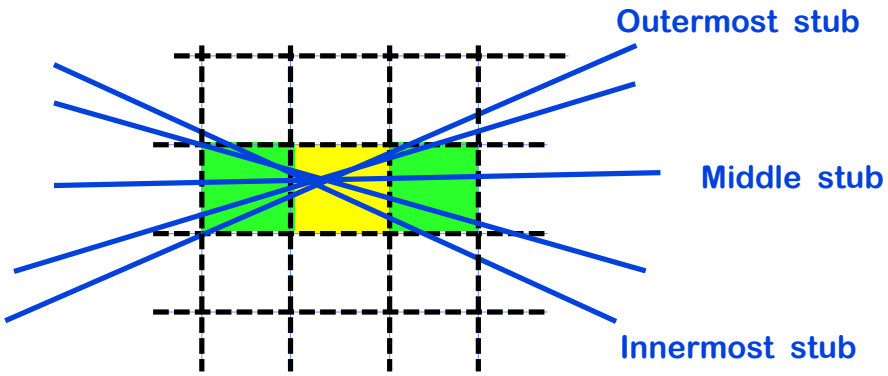

Figure 4.8: Illustration of how duplicates are formed by the r-φ Hough Transform, as discussed in the text [126].

There is however, a small subtlety, as the DR algorithm rejects a small number of non-duplicated tracks due to resolution effects resulting from the discretised implementation of Hough Transform arrays, , the algorithm performs second pass through the rejected tracks. This second pass looks for tracks which have fitted parameters that do not correspond to the HT cell of a track from the first pass. As such tracks are probably not duplicates, they are recovered.

A more detailed description of the firmware implementation of the Duplicate Removal for the demonstrator system is discussed in [126].

4.4 Simulation Studies

This section presents a number of simulation studies that were undertaken as part of the development of the *TMTT* finder demonstrator system both before and following the 2016 review. All of the results discussed were obtained using simulated $t\bar{t}$ events with an average PU ($<$ PU $>$) of 200 interactions and use digitised output from the Hough Transform. The set of metrics used to evaluate the performance of the proposed track finder systems in the 2016 review are used for the results presented. These are defined below in Section 4.4.1.

As mentioned in Section 4.2, at the time of the review the flat barrel geometry described earlier was used for all the studies undertaken, as depicted in the lower diagram in Figure 4.2. As such, unless stated otherwise, the results discussed below use the flat barrel geometry instead of the current tilted geometry.

The results presented in Section 4.4.2 for the linearised χ^2 track fitting algorithm involve the use of a *Seed Filter* (SF) stage that was run after the Hough Transform stage. The SF removes stubs in a Hough Transform cell that are inconsistent with a straight line in the $r - z$ plane. This process filters out incorrectly reconstructed tracks and stubs that were incorrectly assigned to tracks. It was found that using a SF stage before the Kalman Filter stage did not improve the overall performance of the system due to the effectiveness of the Kalman Filter's filtering.

4.4.1 Definitions

A common set of parameters and metrics are used throughout the next sections of this chapter to describe tracks and how well the track fitters have reconstructed them. They are defined as below in Sections 4.4.1.1- 4.4.1.2.

4.4.1.1 Helix Parameters

The helical trajectory of a charged particle at the impact point is described by five helix parameters. In the CMS these parameters are defined as:

- $\boldsymbol{p_T}$ - the transverse momentum of the track;
- $\boldsymbol{\phi_0}$ - the track angle in the transverse plane;
- $\boldsymbol{z_0}$ - the *longitudinal* impact parameter, i.e. the distance in z from the point of closest approach to the interaction point;
- $\boldsymbol{\cot(\theta)}$ - the cotangent of the *dip* (polar) angle, related to η by $\cot(\theta) = \sinh(\eta)^{-1}$;

- $\boldsymbol{d_0}$ - the *transverse* impact parameter, i.e. the distance of the track vertex from the interaction point in the $x - y$ plane.

As the Hough Transform and track fitting algorithms discussed all assume that all tracks originate at the interaction point, d_0 is not given in the results below as it is fixed to zero.

4.4.1.2 Reconstructed Tracks

The common definitions of track reconstruction efficiency [126] used for the three proposed L-1 Track Finder systems are used for the results presented in this chapter:

- The reconstruction efficiency (ϵ) is measured relative to all generated charged particles from the primary interaction that produce a track that satisfies the following definition: produces stubs in at least four layers/disks of the tracker, $p_{\mathrm{T}} > 3\,\mathrm{GeV}$, $|\eta| < 2.4$, $|z_0| < 30\,\mathrm{cm}$ and $d_{xy} < 1\,\mathrm{cm}$, where d_{xy} is the distance in the $x - y$ plane from the point of closest approach to the interaction point.
- A track is defined as being correctly reconstructed or *matched* if the reconstructed track has stubs associated to the particle in at least four tracker layers/disks. Tracks which fail this matching criteria are known either as *unmatched* or *fake* tracks.
- If the reconstruction of a charged particle produces more than one track, these additional tracks are considered to be *duplicates*.
- If all a reconstructed track's stubs originated from the same particle, the track is defined as being *perfectly* reconstructed (ϵ_P).

This stricter definition of *perfect* track reconstruction efficiency is typically used in quoting results from the entire chain (i.e. all four components of the TFP discussed in Section 4.3.2). Otherwise, the nominal definition of track reconstruction efficiency is used as the presence of stubs incorrectly associated with a track is to be expected if only part of the TFP chain has been run. Where appropriate, the results for both definitions are given.

Similarly, the common definitions for the resolution of the track parameters used for both the three proposed L-1 Track Finder systems and in the Phase-II Upgrade of the CMS tracker Technical Design Report [76] are used for the results discussed below. For all of the track parameters quoted, the resolution was defined as the difference between the reconstructed track's helix parameter and the matched simulated track's helix parameter.

4.4.2 Linearised χ^2 Track Fitting Studies

Three different track fitting algorithms were explored for the track fitter component of the TFP used in the 2016 hardware demonstrator review: a Kalman Filter, a Linear Regression (LR) algorithm and a Linearised χ^2 Fit algorithm.

The development of a Kalman Filter was motivated by its ability to filter incorrectly assigned stubs from tracks and the remove fake track candidates at the same time as precisely fitting track parameters. As the Kalman Filter provided the best perfect track reconstruction efficiency and fake track candidate rejection rate out of the three fitting algorithms explored, it was selected as the baseline fitter for the TFP in the 2016 review.

A Linear Regression (LR) track fitting algorithm was developed as an alternative to the KF [134]. As high p_{T} tracks should form a straight line in the r-φ and r-z planes, the linear nature of the LR fit's mathematics makes it well suited to perform independent fits in each plane using minimal latency and resources. This algorithm also required the use of the SF in order for it to deliver optimal performance.

A linearised χ^2 track fit was the first fitting algorithm to be studied by the *TMTT* project. Given the limited time and resource constraints at the start of the *TMTT* project, there was the urgent need to quickly evaluate potential track fitting algorithms so that the optimal one could be implemented in a complete track finder system for the 2016 review. Following discussions with both the *tracklet* and *AM* projects, it was decided a linearised χ^2 fit based on the algorithm proposed by the *tracklet* project would be investigated. A linearised χ^2 fit determines improved helix parameters for the track candidate by calculating the residuals between the stubs and the seeded track that minimise the χ^2 of the fit. The general form of the χ^2 fit and the derivation of the track derivatives used by the algorithm were provided in a private communication [135] and were used to produce a *TMTT* implementation of it.

In Section 4.4.2.1, the general form of the χ^2 fit is described, detailing how these hit residuals were used to obtain a fit of a track's helix parameters. Following this, a discussion of the development and outcomes for the χ^2 fit algorithm is given in Section 4.4.2.2.

4.4.2.1 General Form of a χ^2 Fit

For the general form of a χ^2 fit for a track, f, described by its helix parameters, $\overrightarrow{h}$, and the position of its hits (i.e. stubs), s_i, where i labels the different measurements, the expected trajectory of the track, f_i, is initially linearly expanded around the estimate of the helix parameters $\overline{h}$:

$$f_i(\overrightarrow{h}) = f_i(\overrightarrow{h} + \delta\overrightarrow{h}) \; = f_i(\overline{h}) + \delta\overrightarrow{h}\frac{\partial f_i}{\partial \overrightarrow{h}} + \mathcal{O}(\delta\overrightarrow{h}^2) \tag{4.5}$$

The χ^2 of such a track is expressed as:

$$\begin{aligned}\chi^2 &= \sum_{ij} \big(f_i(\overrightarrow{h}) - s_i\big) V_{ij}^{-1} \big(f_j(\overrightarrow{h}) - s_j\big) \\ &= \sum_{ij} \big(f_i(\overline{h}) - s_i + \delta\overrightarrow{h}\frac{\partial f_i}{\partial \overrightarrow{h}}\big) V_{ij}^{-1} \big(f_j(\overline{h}) - s_j + \delta\overrightarrow{h}\frac{\partial f_j}{\partial \overrightarrow{h}}\big) \\ &= \sum_{ij} \big(\delta f_i + \delta\overrightarrow{h}\frac{\partial f_i}{\partial \overrightarrow{h}}\big) V_{ij}^{-1} \big(\delta f_j + \delta\overrightarrow{h}\frac{\partial f_j}{\partial \overrightarrow{h}}\big)\end{aligned} \tag{4.6}$$

where $\delta f_i \equiv f_i(\overline{h}) - s_i$ are the residuals between the expected position of the track (given by the seed helix parameters) and the position of the track given by the stub, and $V_{ij}^{-1} = diag(\sigma_{ii}^2)$ is the variance matrix that describes the uncertainty associated with the measurement of the stubs.

By minimising the χ^2, δh can be determined:

$$0 = \frac{\partial \chi^2}{\partial \delta \overrightarrow{h_k}} = \sum_{ij} \frac{\partial f_i}{\partial \delta \overrightarrow{h_k}} V_{ij}^{-1} (\delta f_j + \delta\overrightarrow{h}\frac{\partial f_j}{\partial \overrightarrow{h}}) + \sum_{ij} (\delta f_i + \delta\overrightarrow{h}\frac{\partial f_i}{\partial \overrightarrow{h}}) V_{ij}^{-1} \frac{\partial f_j}{\partial \delta \overrightarrow{h_k}} \tag{4.7}$$

By defining the matrices $D_{ij} = \frac{\partial f_i}{\partial h_k}$ and $M = D^T V^{-1} D$, Equation (4.7) can be rewritten and solved for δh:

$$0 = D^T V^{-1} \delta f + M \delta h \Rightarrow \delta h = -M^{-1} D^T \delta f \tag{4.8}$$

Therefore Equation (4.8) provides a simple linear form for how the track helix parameters should be updated for a set of residuals with respect to the seed track candidate.

Similarly the χ^2 of the fit can also be expressed in a linear form:

$$\begin{aligned}\chi^2 &= (\delta f + D\delta h)^T (\delta f + D\delta h) \\ &= (\delta f - DM^{-1}D^T \delta f)^T (\delta f - DM^{-1}D^T \delta f) \\ &= \delta f^T (1 - DM^{-1}D^T)(1 - DM^{-1}D^T)\delta f \\ &= \delta f^T (1 - DM^{-1}D^T)\delta f \\ &= \delta f^T \delta f - \delta f^T DM^{-1}D^T \delta f \\ &= \chi^2_{seed} + \delta f^T D \delta \overrightarrow{h}\end{aligned} \tag{4.9}$$

As the linear forms of Equations (4.8) and (4.9) consist of repeated addition and multiplication operations of the matrices involved, they are naturally suitable for implementation on an FPGA.

This is because while FPGAs can easily perform such operations, potential complications arise when considering the calculation of the track derivatives that form the elements of D. Determining these elements would not be trivial given the presence of a large number of division operations and trigonometric functions for the endcaps' derivatives. Therefore, any implementation in firmware for an FPGA will require the use of lookup tables containing the precomputed values of the derivatives in order to quickly update a track's helix parameters without exceeding latency requirements.

4.4.2.2 χ^2 Track Fitter Software Implementation

From Equations (4.8) and (4.9) and the track derivatives derived in [135], a software implementation of the linearised χ^2 track fit algorithm was developed.

Initially the algorithm was implemented using floating point calculations in order to both debug and optimise its performance. This process involved confirming that the track derivatives and stub residuals were correctly calculated and the track finding efficiencies and parameter resolution of the χ^2 were comparable to the *tracklet* project's software implementation at the time.

Using the exact expressions for the track derivatives with floating point precision and calculating each derivative as required however, would not be feasible to implement in any future FPGA based firmware given the system's resources and constraints. Therefore, the lowest order approximations of the track derivatives (containing the fewest possible number of free parameters) were determined in order to develop a version of the algorithm that used tabulated track derivatives and digitised variables and calculations that gave performance comparable to the original derivatives with floating point precision The performance of both of the versions of the algorithm is discussed below in terms of their track reconstruction efficiencies and the resolution of the fitted track parameters.

Following the development of the "discretised" mathematics version of the algorithm, an iterative filtering process based on the residuals of the stubs was explored. Stubs that were incorrectly associated with a track or were associated with an incorrectly reconstructed track were expected to have larger residuals than those which don't. Multiple iterations of the fitting algorithm were run, where stubs that have a residual above a threshold value being discarded after each iteration prior to the track being refit. The performance of differing numbers of fitting iterations were compared against each other and the Kalman Filter in terms of the purity of the matched tracks, the fraction of fake tracks found, and the impact on the track parameter resolutions.

Table 4.1 compares the tracking performance between the floating point and "discretised" mathematics implementations of the χ^2 track fitting algorithm and the raw track finding output from the Hough Transform. It can be seen that whilst the Hough Transform finds

Table 4.1: Track finding performance on simulated $t\bar{t}$ events with a $<$ PU $>$ of 200 events, after the Hough Transform and the full chain for both the exact floating point and discretised calculations of the track derivatives used by the χ^2 track fit.

Stage	ϵ [%]	ϵ_P [%]	$< N_{tracks} >$	**Fakes** [%]	**Duplicates** [%]
HT	97.0	43.1	351.2	43.9	37.0
χ^2+DR (floating point)	95.0	85.8	86.4	15.7	9.5
χ^2+DR (discretised)	94.9	85.6	87.4	15.5	10.9

tracks with high efficiency, over half have at least one incorrectly associated stub and a significant number of the tracks found were fake or duplicated tracks. Both floating point and discretised mathematics implementations give comparable results, indicating that the approximations made were acceptable. The χ^2 track fit increases the purity of the reconstructed tracks by a factor of two and eliminates the majority of the fake tracks, while the Duplicate Removal algorithm removes the majority of the duplicates.

Figure 4.9 shows that resolutions of the four track parameters as a function of η for primary tracks in $t\bar{t}$ events with a $<$ PU $>$ of 200 events for both the floating point and discretised implementations of the algorithm. The resolution of each of the helix parameters compares well not just between the two implementations of the algorithm's mathematics, but also with those obtained for the barrel region by the offline track reconstruction which is able to use all information from the detector with more sophisticated reconstruction techniques [76], guaranteeing their usefulness to the L-1 trigger. The increasing degradation of the track parameters with increasing pseudorapidity results from combined effects of the reduced hit precision in the endcap disks, shorter effective lever arm available and the increasing amount of material that particles pass through.

In order to filter out these incorrectly assigned stubs from matched tracks, and also remove fake tracks, the residuals calculated for each stub following the fit were considered. These "fake" stubs were expected have large residuals compared to stubs correctly associated to genuine tracks or stubs belonging to a fake track.

Therefore, in order to decrease the fake rate and increase the matched track purity the stub with the worst/largest residual was compared against a configurable threshold. If the residual failed to meet the threshold criteria, it would be removed from the track and the track would be refitted using only its remaining stubs. This process was repeated until the latency budget was exceeded/no further stubs were removed, with no further consideration of the remaining stubs' residuals following the final threshold.

During the optimisation of this stub quality check it was found that a track could end up

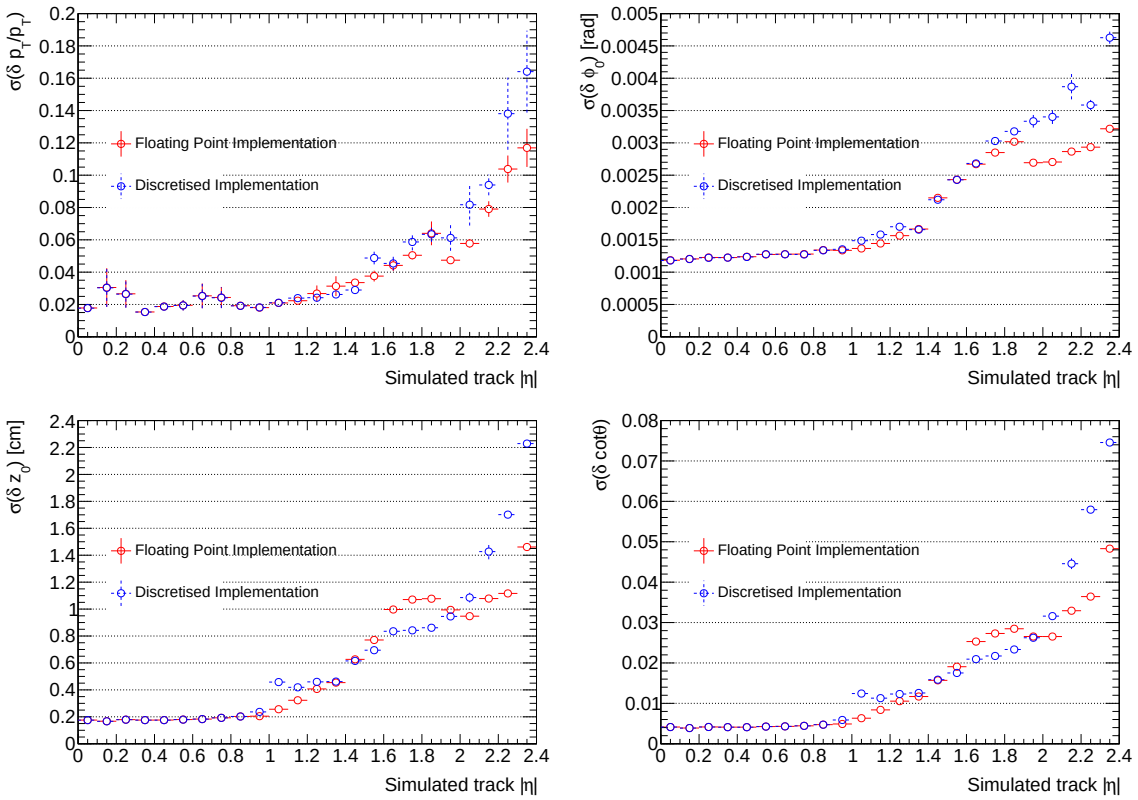

Figure 4.9: Relative p_{T} resolution, ϕ_0 resolution, z_0 resolution and $cot(\theta)$ resolution measured for primary reconstructed tracks in simulated $t\bar{t}$ events with a $<$ PU $>$ of 200 events for the floating point (red) and discretised mathematics (blue) implementations of the linearised χ^2 fit algorithm for a single fitting iteration.

having fewer than the minimum of four stubs required to be considered track candidate - thus potentially discarding a matched track by mistake. To avoid this while still retaining the improved matched track purity and reduced fake rate, a looser residual threshold was applied for tracks only containing four stubs.

Table 4.2 illustrates how the tracking performance of the linearised χ^2 fitting algorithm improves over successive fitting iterations and how it compares to the Kalman Filter. Performing one additional fitting iteration considerably improved the performance of the χ^2 track fit, as the removal of incompatible stubs reduced the fraction of fake tracks by over a half and considerably increased the purity of the fitted matched tracks. Further successive fitting iterations however, yield diminishing returns, with no further improvements seen following four iterations of the χ^2 fitting algorithm. This was not unexpected, as with the mean number of hits associated to a track being seven, only up to three stubs (across four fitting iterations) can be removed for the majority of tracks. In contrast, the Kalman Filter achieves a tracking efficiency comparable to the χ^2 fitter after two fitting iterations but with none of the matched tracks containing any incorrect stubs. This suggests that if a more

Table 4.2: Track finding performance on simulated $t\bar{t}$ events with a $<$ PU $>$ of 200 events, for one to four fitting iterations, N_{It}, of the χ^2 track fit and for the Kalman Filter. Further fitting iterations are not shown as further improvement was observed.

Track Fitter	N_{It}	$\boldsymbol{\epsilon}$ [%]	$\boldsymbol{\epsilon_P}$ [%]	$< \boldsymbol{N_{tracks}} >$	**Fakes** [%]	**Duplicates** [%]
χ^2+DR	1	94.9	85.6	87.4	15.5	10.9
	2	93.8	91.0	73.8	6.6	7.7
	3	93.1	91.0	71.4	5.3	6.9
	4	93.0	91.0	71.1	5.2	6.8
KF+DR	-	94.1	94.1	82.1	21.1	4.5

sophisticated method of removing bad quality stubs were used in the linearised χ^2 fitter, very few matched tracks would be discarded with improved purity.

Figure 4.10 compares the the helix parameter resolutions obtained by the χ^2 track fit after one and four fitting iterations with those achieved by the Kalman Filter. It can be seen that the additional fitting iterations performed by the χ^2 fitting algorithm considerably improved each of the track parameter's resolution obtained in the forward regions. While the χ^2 fitter's p_{T} relative and ϕ_0 resolutions were comparable to those achieved by the Kalman Filter, its z_0 and $cot(\theta)$ resolutions at high pseudorapidity were considerably less precise than those obtained with the Kalman Filter. It was found that the Kalman Filter fitter's z_0 and $cot(\theta)$ resolutions in the forward regions were improved with the inclusion of higher order terms in the relevant track derivatives. These additional terms were not considered in the"discretised" mathematics implementation of the χ^2 track fitting algorithm as they introduced additional free parameters that would have resulted in their associated lookup tables being too large to implement on existed FPGAs.

Following the parallel development of both the linearised χ^2 track fit and the Kalman Filter algorithms, it was decided that development of the former would be discontinued. This decision was made as the Kalman Filter was capable of achieving both a higher track finding efficiency with 100.0% purity for matched tracks and superior z_0 and $cot(\theta)$ resolutions in the forward regions. In addition, considerable progress had been made with a firmware implementation of the Kalman Filter.

In contrast, the linearised χ^2 track was not competitive in terms of track resolution and reconstruction ability, especially with respect to the stricter tracking efficiency definition. There were also concerns over the potential feasibility of tabulating all (or the most frequently used) track derivatives in the endcap disks for FPGAs that were commercially available at the time.

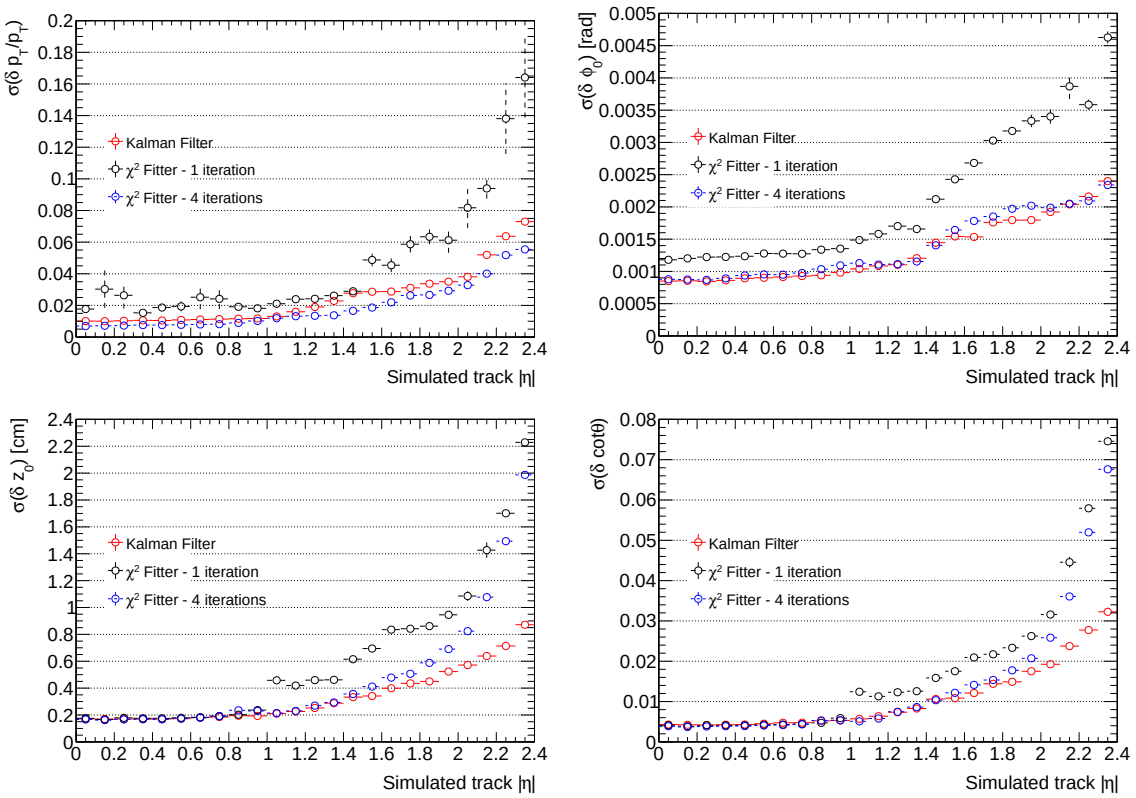

Figure 4.10: Relative p_{T} resolution, ϕ_0 resolution, z_0 resolution and $cot(\theta)$ resolution measured for primary reconstructed tracks in simulated $t\bar{t}$ events with a $<$ PU $>$ of 200 events for the discretised mathematics implementation of the linearised χ^2 fit algorithm for one (black) and four (blue) fitting iterations. The Kalman Filter (red) is also included for comparison.

4.4.3 Tracking at low transverse momenta studies

The flexibility to reconstruct tracks down to a lower p_{T} threshold of 2 GeV is potentially desirable and so the impact of this potential requirement on the performance of the proposed track-finder system was studied.

These studies were initially undertaken as part of the robustness studies required for the 2016 demonstrator review, which investigated the impact that lowering the track reconstruction p_{T} threshold had on the Hough Transform. Therefore, the results for these studies were produced using the flat barrel geometry.

Following the 2016 review, the studies into tracking at lower transverse momenta were further developed by optimising the Kalman Filter algorithm . These results were produced with the preferred tilted barrel geometry.

As the number and width of q/p_{T} Hough Transform columns used varies from the standard fixed number and size of columns typically used, thus varying the p_{T} resolution available, results in the following subsections are expressed as a function of $1/p_{\mathrm{T}}$ instead of p_{T}.

4.4.3.1 Hough Transform Optimisation and Results

Lowering the p_{T} threshold from 2 GeV required modifying the GP and HT configuration parameters to ensure adequate duplication in ϕ and increasing the number of q/p_{T} columns by 50% to take into account the increased p_{T} range whilst maintaining the same precision. The increased number of q/p_{T} columns increases the required FPGA resources by 50% and the output data rate from the Hough Transform by a factor of 2.2.

Without applying further modifications, there was a considerable degradation in the track reconstruction efficiency in the range $2\,\mathrm{GeV} < p_{\mathrm{T}} \leq 2.7\,\mathrm{GeV}$, due to these low momenta tracks being dominated by multiple scattering. This results in a significant fraction of stubs not intersecting within a single Hough Transform cell and thus failing to exceed the threshold criteria and generate track candidates. To mitigate against these efficiency losses, the precision of the Hough Transform cells along q/p_{T} and ϕ_T for the range $2\,\mathrm{GeV} < p_{\mathrm{T}} \leq 2.7\,\mathrm{GeV}$ was reduced by a factor of two (i.e. 2×2 cells were merged) The concept of a variable precision Hough Transform had been implemented in firmware as part of another series of studies.

In addition, the Kalman Filter state χ^2 cuts for tracks with $p_{\mathrm{T}} \leq 2.7\,\mathrm{GeV}$ were optimised to reflect the increased hit position uncertainty from the decreased precision of the hits in these Hough Transform cells. The optimisation of the Kalman Filter state χ^2 cut was done to reduce the number of duplicate and fake tracks as far as possible without negatively impacting on the Hough Transform track reconstruction efficiency. Figure 4.11 shows how the tracking efficiency improves following the use of the variable precision Hough Transform with and without optimised Kalman Filter state cuts after both the Hough Transform and the full demonstrator chain.

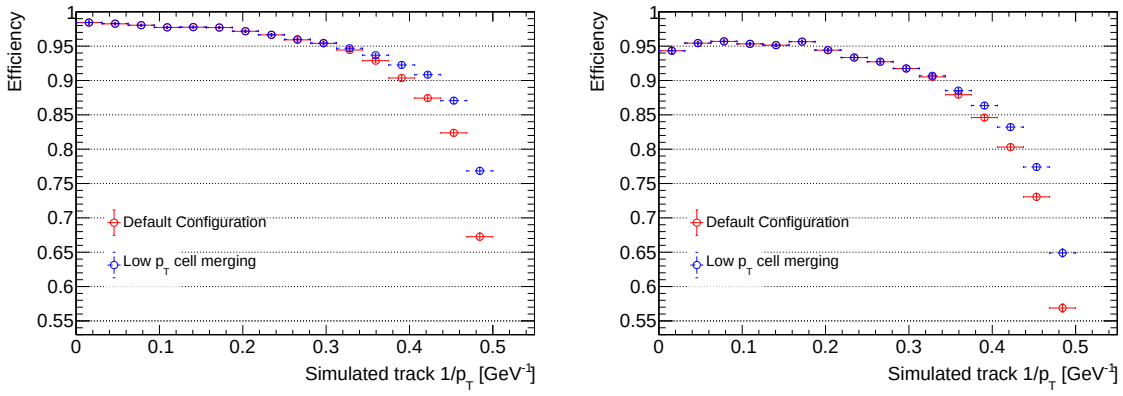

Figure 4.11: The post-Hough Transform (left) and post-Kalman Filter (right) tracking efficiency for tracks with $p_{\mathrm{T}} > 2\,\mathrm{GeV}$ for $t\bar{t}$ events with a $<$ PU $>$ of 200 events. The default configuration where only the number of q/p_{T} columns were increased are shown in red and the configuration with the increased number of columns, HT cell merging and Kalman Filter state cuts optimisation shown in blue).

Table 4.3 shows the impact that the decreased precision Hough Transform cells and optimised Kalman Filter state cuts have on tracking performance both following the Hough Transform and after the full chain has been run. It was clear that whilst the merging of adjacent Hough Transform cells recovers tracks that did not previously intersect within a single Hough Transform cell, the tracking efficiency following running the full chain was significantly less than that post-Hough Transform. As can be seen in Figure 4.11, these losses occur for tracks where the particle's p_{T} ($\frac{1}{p_{\mathrm{T}}}$) is less (greater) than 3 GeV (0.33/ GeV), as the Kalman Filter does not take the effects of multiple scattering into account. This shortcoming of the Kalman Filter also accounts for it not being as efficient at removing fake tracks, with an observed increase of 5% in the fraction of fakes reconstructed. The duplicate removal algorithm however, remains effective at removing almost all the duplicates.

Table 4.3: Track finding performance on simulated $t\bar{t}$ events with a $<$ PU $>$ of 200 events, after the Hough Transform and the full chain have been considered for the configurations of only increasing just the number of q/p_{T} columns (*Default*),and also applying Hough Transform cell merging and the optimised Kalman Filter state cuts (*Optimised*).

Configuration	**Stage**	ϵ [%]	$< N_{tracks} >$	**Fakes** [%]	**Duplicates** [%]
Default	**HT**	93.6	713.2	34.0	44.5
	Full chain	89.2	193.9	21.1	5.1
Optimised	**HT**	94.6	799.2	40.5	39.7
	Full chain	90.0	210.4	26.3	3.8

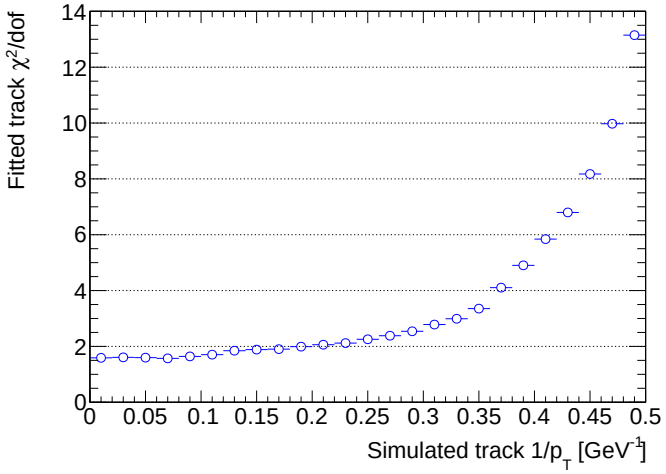

Figure 4.12: $\frac{\chi^2}{ndf}$ as a function of $\frac{1}{p_{\mathrm{T}}}$ for genuine tracks produced by the Kalman Filter.

The impact of the Kalman Filter not considering the impact of multiple scattering increasing the uncertainty in a hit's position at lower lower transverse momenta is further illustrated by Figure 4.12, which shows the distributions of χ^2 per number of degree of freedom ($\frac{\chi^2}{ndf}$) as a function of $\frac{1}{p_{\mathrm{T}}}$ for genuine tracks produced by the Kalman Filter. If all sources of uncer-

tainties were accounted for, the ideal distribution of $\frac{\chi^2}{ndf}$ would be unity for all values of p_{T} ($\frac{1}{p_{\mathrm{T}}}$), in contrast to the observed dramatic increase above approximately 3 GeV (0.33/ GeV).

Figure 4.13 shows that the resolutions of the track parameters fitted by the Kalman Filter were comparable for $p_{\mathrm{T}}(frac1p_{\mathrm{T}}) < 3\,\mathrm{GeV}(0.33/\,\mathrm{GeV})$ both before and after the Hough Transform and associated Kalman Filter optimisation for tracks originating from the primary interaction. The slight degradation in the ϕ_0 resolution results from the decreased precision coordinates from the Hough Transform and the small improvement observed in the z_0 resolution is due to the Kalman Filter being able to consider genuine stubs that were not previously found by the Hough Transform.

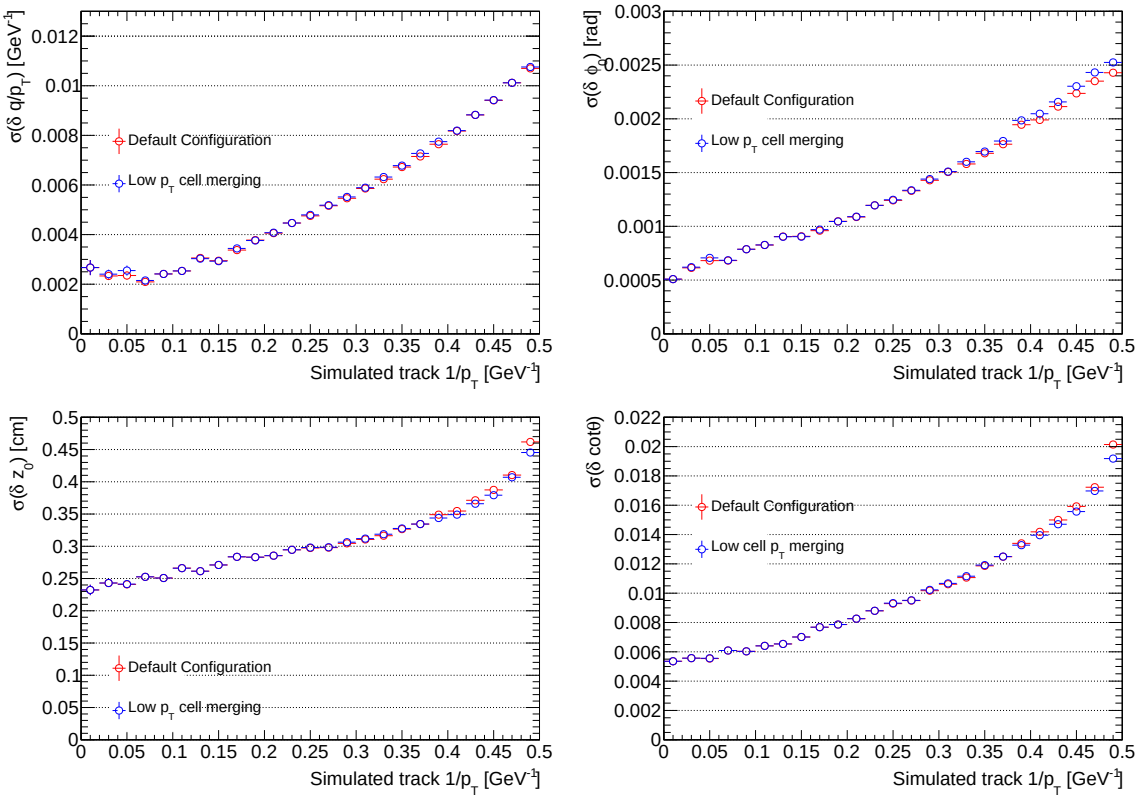

Figure 4.13: $\frac{q}{p_{\mathrm{T}}}$ resolution, ϕ_0 resolution, z_0 resolution and cotθ resolution measured for both the default configuration where only the number of Hough Transform q/p_{T} columns have been increased (red) and after the Hough Transform and Kalman Filter optimisations have been applied (blue) for primary reconstructed tracks in simulated $t\bar{t}$ events with a $<$ PU $>$ of 200 events for tracks with $p_{\mathrm{T}} > 2\,\mathrm{GeV}$.

4.4.3.2 Kalman Filter Optimisation and Results

Incorporation of multiple scattering into the Kalman Filter involved including a *process noise* term, namely, the variance of the multiple scattering angles, to the *measurement noise* (i.e. measurement error) term already present in the Kalman Filter covariance matrix. In this updated form, the Kalman Filter now can consider stubs that are compatible with those that have undergone multiple scattering, allowing tracks with previously discarded stubs to be reconstructed and resulting in more accurate χ^2 values which can be used to better discriminate against fake tracks.

For small deflection angles and relativistic particles, the standard deviation of the distribution of deflection angles, σ_θ, for any layer is given by [136] :

$$\sigma_\theta = \frac{13.6\,\text{MeV}}{\beta c p} q \sqrt{\frac{x}{X_0}} [1 + 0.088 \log_{10} \frac{x}{X_0}] \tag{4.10}$$

where the momentum, velocity, electrical charge of the incident particle and thickness of the scattering medium in radiation lengths are given by p, βc, q and $\frac{x}{X_0}$, respectively. The result from this equation has been found to have an accuracy no greater than 11% [136].

With the particles involved having relativistic velocities (i.e. $\beta c \cong 1$) and scattering in the r-z plane ignored as the impact of multiple scattering is considerably smaller hit position resolution in r-z, the multiple scattering contribution in the r-φ plane can be expressed as:

$$\sigma_\theta = \frac{k}{p_\text{T}} \tag{4.11}$$

where k is the coefficient of proportionality that describes the constant terms of Equation (4.11) in the relativistic limit.

From the simplified form of Equation (4.11), two alternative forms of the coefficient k, which should require minimal resources and latency, were investigated:

- **constant coefficient:** a constant coefficient of the order of the average anticipated scattering angle is used. The typical scattering angle for $2 - 3\,\text{GeV}$ tracks is of the order of a milliradian.
- **layer-dependent coefficient:** the coefficient used depends on the layer ID (i.e. the layer/disk of the stub used to update the Kalman state) in order to take into account the impact of repeated scattering from passing through multiple layers increasing the uncertainty associated with the hit position.

The initial layer-dependent coefficients were obtained through experimentally determining, using simulation, the multiple scattering contribution to the observed variance in ϕ. Both

these initial-layer dependent coefficients and the initial constant coefficient of a milliradian were subsequently further optimised in order to recover as much tracking efficiency as possible. Similarly, the Kalman Filter state χ^2 cuts for both approaches were also tuned in order to reject the optimal number of fake and duplicate tracks without compromising on tracking efficiency.

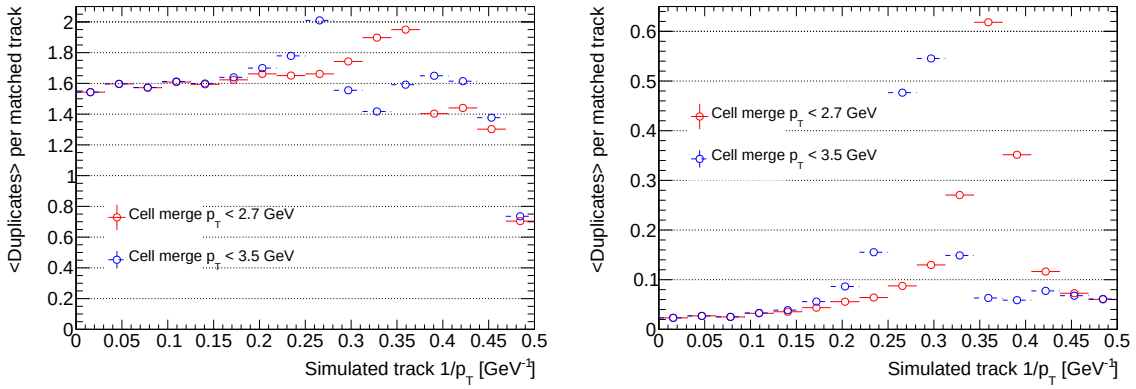

Figure 4.14: The average number duplicate tracks per matched track as a function of $\frac{1}{p_{\mathrm{T}}}$ following reconstruction by the Hough Transform (left) and fitting and filtering by the Kalman Filter and Duplicate Removal (right) for where the Hough Transform cell merging p_{T} threshold is set to 2.7 GeV (red) and 3.5 GeV (blue). The constant coefficient for the multiple scattering contribution was used for these Kalman Filter results.

During the comparative studies of the two multiple scattering coefficients, it was found that the average number of duplicate tracks per matched track did not remain constant as a function of the simulated track's $p_{\mathrm{T}}(\frac{1}{p_{\mathrm{T}}})$. As shown in Figure 4.14, there was an increase in the number of duplicates produced near the 2×2 merging of Hough Transform cells threshold of $p_{\mathrm{T}} = 3\,\mathrm{GeV}(\frac{1}{p_{\mathrm{T}}} = 0.331/\,\mathrm{GeV}$ following both the Hough Transform and Duplicate Removal stages, implying that the Hough Transform produces more duplicates at low p_{T} in the full precision cells. Given that the number of duplicate tracks produced in the decreased precision Hough Transform cells were well controlled, the p_{T} $(\frac{1}{p_{\mathrm{T}}})$ threshold for the 2×2 merging of Hough Transform cells was increased from 2.7 GeV $(0.37/\,\mathrm{GeV})$ to 3.5 GeV $(0.29/\,\mathrm{GeV})$. Despite this change decreasing the number of duplicates below the p_{T} $(\frac{1}{p_{\mathrm{T}}})$ threshold of 3.5 GeV $(0.29/\,\mathrm{GeV})$, an increase in the number of duplicates produced per matched track near the Hough Transform cell merging threshold was still present. While these increases in the duplicate rate have yet to be fully understood, they are suspected to have arisen from resolution effects at the boundaries between the differently sized Hough Transform cells given their proximity to the p_{T} threshold for merging Hough Transform cells. As the p_{T} threshold of 3.5 GeV recovered a further 0.2% of the tracks that were previously lost to multiple scattering and reduced the overall duplicate rate by 2.8%, this change was adopted by the project and all the results presented below use this increased threshold.

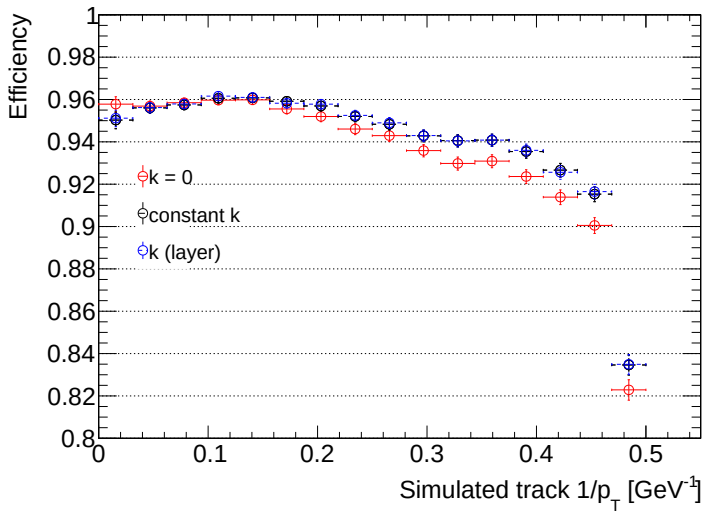

Figure 4.15: Tracking efficiency as a function of $\frac{1}{p_{\mathrm{T}}}$ for $t\bar{t}$ events with a $<$ PU $>$ of 200 events after the full chain has been run, where the Kalman Filter has not been modified to take multiple scattering into account (red), a constant coefficient for multiple scattering is used (black) and a layer dependent coefficient for multiple scattering is used (blue).

Figure 4.15 and Table 4.4 illustrate that tracking efficiency improves when the Kalman Filter's covariance matrix accounts for multiple scattering. At high p_{T} (low $\frac{1}{p_{\mathrm{T}}}$) however, the tracking efficiencies of both Kalman Filter configurations incorporating multiple scattering were up to 1% worse than the configuration where the effects of multiple scattering are not considered. This degraded performance results from the process noise term not considering the impact of the density effect, which becomes more important at increasing energies, reducing the effect stopping power of the material being traversed. In addition, Table 4.4 shows that compared to just the Hough Transform optimisations alone, for both multiple scattering coefficients, the Kalman Filter was more effective at rejecting incorrectly reconstructed tracks by up to an additional 3-4%. In contrast, the fraction of duplicates increases

Table 4.4: Track finding performance on simulated $t\bar{t}$ events with a $<$ PU $>$ of 200 events, after the full demonstrator chain for the three differing Kalman Filter configurations where multiple scattering is not considered ($k = 0$), a constant multiple scattering coefficient (const k) is used and a layer dependent multiple scattering coefficient ($k(layer)$)is used. The track finding efficiencies, ϵ, following each stage are given along with the mean number of tracks, $< N_{tracks} >$, and the fraction of those tracks which are either fake or duplicate tracks.

Scattering coefficient	ϵ [%]	$< N_{tracks} >$	**Fakes** [%]	**Duplicates** [%]
$k = 0$	93.6	216.0	13.3	9.4
const k	94.2	216.3	10.3	11.2
$k(layer)$	94.2	222.1	10.8	12.3

for both coefficients by 3-5% for the full chain. As illustrated in Figure 4.14, this increase occurs between 3.2 GeV and 5 GeV - near the $p_{\mathrm{T}} = 3.5\,\mathrm{GeV}(\frac{1}{p_{\mathrm{T}}} = 0.291/\,\mathrm{GeV})$ threshold for merging adjacent Hough Transform cells. Currently it is not understood how incorporating multiple scattering into the Kalman Filter causes this, but it is suspected to be related to the use of the reduced precision of Hough Transform cells.

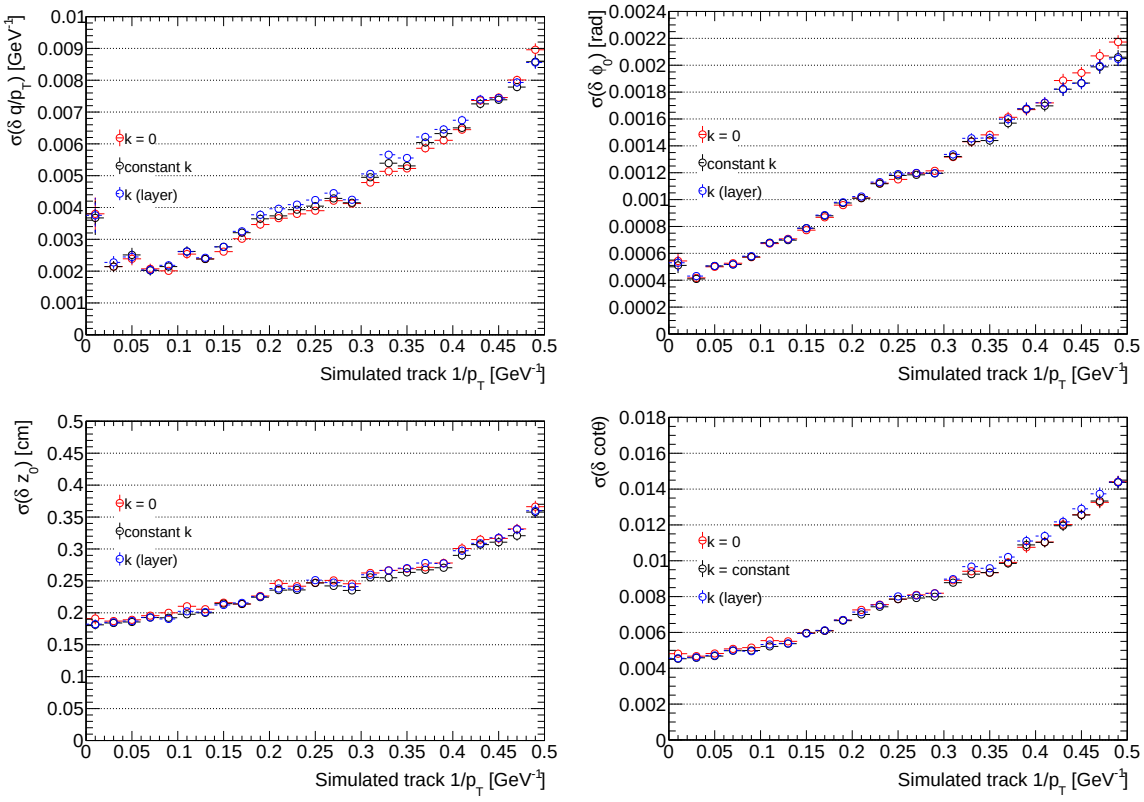

Figure 4.16: $\frac{q}{p_{\mathrm{T}}}$ resolution, ϕ_0 resolution, z_0 resolution and cotθ resolution determined for primary reconstructed tracks in simulated $t\bar{t}$ events with a $<$ PU $>$ of 200 events. The distribution for when the Kalman Filter has not been modified to take multiple scattering into account is given in red, for a constant multiple scattering coefficient in black and a layer-dependent multiple scattering coefficient in blue.

Figure 4.16 shows the resolutions of the helix parameters for primary reconstructed tracks as a function of track $\frac{1}{p_{\mathrm{T}}}$ in simulation for both of the multiple scattering coefficients considered and for when multiple scattering was not accounted for at all in the Kalman Filter covariance matrix. As effects of multiple scattering only dominate at low p_{T}, there was no improvement observed in the resolutions of the helix parameters for high p_{T} tracks. The $\frac{q}{p_{\mathrm{T}}}$ resolution however, was noticeably worse in the range $0.181/\,\mathrm{GeV} < frac1p_{\mathrm{T}} < 0.331/\,\mathrm{GeV}$ for both of the multiple scattering noise terms considered. While the cause of this degradation in the $\frac{q}{p_{\mathrm{T}}}$ resolution is as yet to be determined, it is suspected, like the increased duplicate rate in the same p_{T} range, to be related to the reduced precision of Hough Transform cells. The ϕ_0 precision at low p_{T} was found to be improved as the increased uncertainty in the

position each successive ϕ measurement resulted in the Kalman Filter giving greater weight to the innermost and more precise measurements. Similarly, the $\frac{q}{p_{\mathrm{T}}}$ resolution was more precise at low p_{T} for $frac1p_{\mathrm{T}} > 0.4$. Only minor differences were observed for the z_0 and cotθ resolutions as the multiple scattering terms did not degrade the z measurement error.

Incorporating a noise term to account for the effects multiple scattering is further justified by considering the reconstructed tracks' $\frac{\chi^2}{ndf}$ as a function of $\frac{1}{p_{\mathrm{T}}}$ in Figure 4.17. In contrast to when the Kalman Filter lacks a noise term accounting for multiple scattering, the distributions of the Kalman Filter's performance for both multiple scattering coefficients considered implies that multiple scattering was the dominant source of uncertainty in the track measurements and that it has been well accounted for.

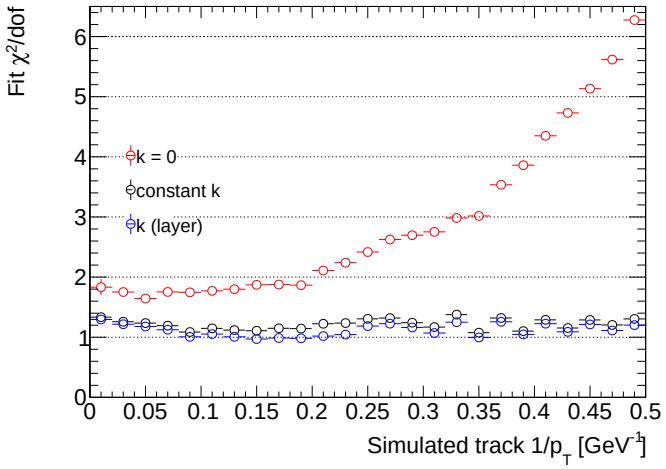

Figure 4.17: $\frac{\chi^2}{ndf}$ as a function of $\frac{1}{p_{\mathrm{T}}}$ for $t\bar{t}$ events with a $<$ PU $>$ of 200 events after the full chain has been run. The distribution for when the Kalman Filter has not been modified to take multiple scattering into account is given in red, for a constant multiple scattering coefficient in black and a layer-dependent multiple scattering coefficient in blue.

As shown in Figures 4.15 and 4.16 and Table 4.4, there were only small differences in the performance of the two multiple scattering coefficients. This is due the amount of material traversed by a track not being constant for a single layer given that the amount of material contributions in the Inner and Outer Trackers, between the Inner and Outer Trackers and services varies as a function of pseudorapidity [76].

Following the improved performance considering the impact of multiple scattering on the Hough Transform and Kalman Filter discussed in these studies, these optimisations have been incorporated into the firmware for both TFP components. The constant multiple scattering term was chosen for inclusion into the Kalman Filter as it demonstrated the best performance and required the least resources to implement.

4.4.4 Summary

Software studies were undertaken as part of the development of the *TMTT* collaboration's proposed track finding system for the CMS Phase-II Outer Tracker in order to evaluate the performance of different aspects of the system. These studies included the development and evaluation of a linearised χ^2 track fitting algorithm and determining the robustness of the system if the minimum track reconstruction p_{T} threshold was reduced from 3 GeV to 2 GeV.

The development of the linearised χ^2 track fitting algorithm initially involved validating the algorithm using floating point calculations prior to producing a version that produced comparable results using tabulated track derivatives and digitised variables and calculations. It was demonstrated that by performing multiple iterations, the algorithm was capable of removing both incorrectly associated stubs from genuine tracks and unmatched tracks, resulting in 100% track purity for more than 97% of all matched tracks and helix parameter resolutions comparable to the expected offline resolution in the barrel region.

Following the parallel development of the linearised χ^2 track fit and the Kalman Filter algorithms, it was decided to discontinue development of the former, as the latter was capable of reconstructing all genuine tracks with no incorrectly associated stubs and fitting z_0 and $cot(\theta)$ more precisely at high $/eta$. In addition, whilst substantial progress had been made with a firmware implementation of the Kalman Filter, there were concerns over the feasibility of tabulating the linearised χ^2 track fit's most frequently used track derivatives for the endcap disks for commercially available FPGAs.

Reducing the minimum track reconstruction p_{T} threshold from 3 GeV to 2 GeV required modifying the TFP's configuration parameters to ensure adequate duplication in ϕ and increasing the number of q/p_{T} columns by 50% to maintain the same Hough Transform cell precision over the larger q/p_{T} range considered. As tracks with $p_{\mathrm{T}} < 3$ GeV are increasingly dominated by multiple scattering, a significant fraction of stubs did not intersect within a single Hough Transform cell which resulted in a reduced track reconstruction efficiency below 2.7 GeV. These reconstruction efficiency losses were mitigated against by reducing the precision of the Hough Transform cells along q/p_{T} and ϕ_T by a factor of two for $2 < p_{\mathrm{T}} \leq 2.7$ GeV. A process noise term was added to the Kalman Filter to describe the effect of multiple scattering increasing the uncertainty in the hit position in the r-φ plane. Two noise terms were evaluated, one that described the effect as a function of the track's p_{T} and the other as a function of the track's p_{T} and the layer/disk of the stub added to the Kalman state. Both noise terms produced comparable results and were shown to not only improve the track reconstruction efficiency of the system, but also to account for the dominant source of uncertainty in the track measurements. This performance could be further improved by constructing a process noise term that better accounts for the amount of material traversed and by establishing the cause behind the increased production of duplicate tracks observed near the boundary between normal and reduced precision Hough Transform cells.

Chapter 5

Event Simulation and Object Reconstruction

After triggered events from the CMS experiment have been read out, the reconstruction of the particles produced by the proton-proton collision is performed. Monte Carlo (MC) simulation is used in physics analyses to optimise searches and in the statistical analysis of the measurements that are made. It is therefore essential that MC provides a detailed, precise and realistic description of the expected physics processes.

The event simulation and object reconstruction algorithms which are relevant to the single top physics search presented in this thesis are discussed in this chapter.

5.1 Event Simulation

As MC simulation is meant to provide a realistic description of physics processes, both accurate modelling of these processes and a detailed understanding of how physical processes interact with the CMS detector are required to produce events in the same format as raw proton-proton collision data prior to undergoing the same reconstruction process. The simulation of a process involves the generation, simulation, digitisation and reconstruction of an event.

The generation stage involves the use of *event generators* to simulate all aspects of a physics event from the initial protons to the hadronised remnants of the collision and the remnants of the initial colliding protons [137, 138]. The initial stage models the hard interaction of the two incoming protons, where perturbative methods are used to calculate the Matrix Elements (ME) for the hard interaction, while the momentum fractions of the incoming partons are sampled from a PDF. The following *Parton Shower* (PS) stage models the hadronisation of the liberated partons through an iterative process until the factorisation scale for the shower is reached. The PS stage also includes simulating the radiation of gluons

or quarks from the initial state (ISR) and final state (FSR) partons. This stage also includes the *matching* of the separated particles produced by the ME stage that are above an energy threshold to the lower p_{T} particles in the PS stage in order to provide a coherent description of the event. Following the PS stage, the remaining particles undergo hadronisation using a non-perturbative modelling process, which is typically described by either the Lund String Model [35] or the Cluster Model [139]. As the hadronisation of the proton remnants that have not participated in the hard interaction, known as the underlying event (UE), cannot be derived from first principles, the parameters that control the modelling of the UE have to be experimentally determined [140]. A set of such parameters that have been simultaneously fitted in order to describe certain aspects of a dataset are known as a *tune*.

The various event generators used in the production of MC samples used in this thesis are discussed in Section 5.1.1.

Following the generation stage, the simulation and digitisation stages involves passing the generation output through a complete simulation of the CMS detector that has been with the GEANT4 program [141, 142]. This process models particle interactions and decays and the propagation of particles through the detector and the detector's electronics response. The output from this stage then undergoes the same reconstruction process that data does, as described in Section 5.2.

The simultaneous inelastic proton-proton collisions that occur known as pile-up are included in event simulation by sampling large statistics samples minimum bias events and overlapping them with the simulated events from the process being generated. As PU modelled in simulation does not adequately describe observed PU in data, it is reweighted as described in Section 7.2.6.

The MC events produced are weighted by a scale factor in order to correctly normalise them with respect to the data they are compared against. This normalisation scale factor is given by:

$$SF_{dataset} = \frac{\mathcal{L}\sigma}{N_{MC}^{Events}} \tag{5.1}$$

where $\mathcal{L}$ is the amount of total integrated luminosity considered in the data used, σ the cross section of the MC sample considered and N_{MC}^{Events} is number of simulated events considered for the process.

5.1.1 Event Generators

A number of event generators are used by CMS to produce the MC simulation samples used to describe the expected processes produced. While there are several general-purpose event generators that can describe an event from the initial hadron collision to final state particles, such generators can be interfaced with a specialist generator that that models a

specific physics aspect (i.e. ME calculations or PS simulation) or process (e.g. tau decays) in order to provide a complete event.

Perturbative calculations of the MEs of the QCD and electroweak processes are done, where possible, to Next-To-Leading Order (NLO) in order to both enable precision measurements to be made and to accurately model processes that include multiple high energy jets.

The MC event generators used to model the background and signal processes for the analysis presented in this thesis are as follows:

- **MADGRAPH5_aMC@NLO 2.2.2** [143] is the new version of MadGraph5 and the aMC@NLO generators. It is capable of evaluating tree-level and one-loop Feynman diagrams for a given phase space point for all the Feynman diagrams produced to produce matrix elements at NLO. As the leading and higher order terms can destructively interfere, the generator assigns negative weights to events arising such interference so that the cross section is simulated correctly. A scale factor, SF^{NLO}, is applied to correctly normalise simulated samples produced by this generator. This scale factor considers the ratio of the total number of events to the effective number of events (i.e. the difference in positively and negatively weighted events) in the sample and the sign of an individual event's weighting:

$$SF^{NLO} = \frac{N^{postiveevents} + N^{negativeevents}}{N^{postiveevents} - N^{negativeevents}} \times \frac{|eventweight|}{eventweight} \tag{5.2}$$

  The MLM- and FxFx-merging schemes are used by MADGRAPH5_aMC@NLO to match the ME calculations to PS for samples produced at LO and NLO, respectively.

- **POWHEG V2** (The Positive Weight Hardest Emission Generator) [144] is a framework that interfaces NLO ME calculations with PS generators. As its name suggests, POWHEG produces the hardest emission first by using the exact NLO ME and only produces positively weighted events. When it is interfaced with a specialist generator that orders emissions by p_{T} or allows the use of a p_{T}-veto, all emissions following the hardest emission are rejected. Therefore, the double counting of low-p_{T} emissions is avoided and thus the need for negatively weighted events. As POWHEG V2 was not capable of simulating the single top tW-channel process at the time the simulated samples were produced, the tW-channel samples listed in Section 7.1 were created using POWHEG V1.

- **PYTHIA 8:** [145] is a general-purpose generator that is capable of generating all aspects of a process to form a complete event. It can also be used to take the output of a ME event generator and perform the parton showering and hadronisation (using the Lund String model) required to produce the full event. For all of the MC samples considered in Section 7.1 for the analysis presented, PYTHIA 8 is used to develop the samples from their ME event generator output into a full event.

5.2 Object Reconstruction

Using the output of all the CMS sub-detectors, a full reconstruction of the triggered physics event is undertaken. This process involves the *Particle Flow* (PF) algorithm, which combines complementary information from each of the CMS sub-detectors, known as *elements*, to provide an optimal reconstruction and identification of all stable particles present in the event [146, 147, 148]. Using these reconstructed particles, additional objects such as b-jets and missing transverse energy can also be identified.

5.2.1 Charged Particle Tracks

As the charged particles produced in proton-proton collisions traverse the silicon tracker, they interact with it and leave energy deposits on the individual layers, known as *hits*. These hits are used to reconstruct the particles' trajectories using the Combinatorial Track Finder (CTF) algorithm, which is based on combinatorial Kalman Filtering [84, 132].

The CTF algorithm is iterative and consists of the following steps:

- **Seed generation:** Initial track candidates are formed from two or three hits in the inner part of the track in order to provide a first estimate of the tracks' helix parameters.
- **Track Finding:** A combinatorial Kalman Filter then builds a candidate by adding hits from successive layers that are compatible with the extrapolated trajectory. The candidate is updated with the addition of each subsequent hit, taking into account the hit's position, uncertainty and material traversed.
- **Track Fitting:** The initial estimate of a track's parameters is improved using two additional passes of the KF. The first pass minimises the bias from the seed generation step by working from the innermost layer outwards. The second minimises the bias from the track finding step by working from the outermost layer inwards. By performing these two passes any bias in the identification of incorrectly associated hits is minimised.
- **Track Selection:** Quantities, such as χ^2, the number of layers with hits and compatibility, are used to identify and reject tracks that have been incorrectly reconstructed.

Up to six iterations of the CTF are performed, with all hits associated to a track removed from consideration in subsequent iterations. The initial four iterations use seeds exclusively from the pixel tracker and the last two iterations use seeds from the strip tracker. This iterative approach ensures that a high track reconstruction efficiency and a minimal fake

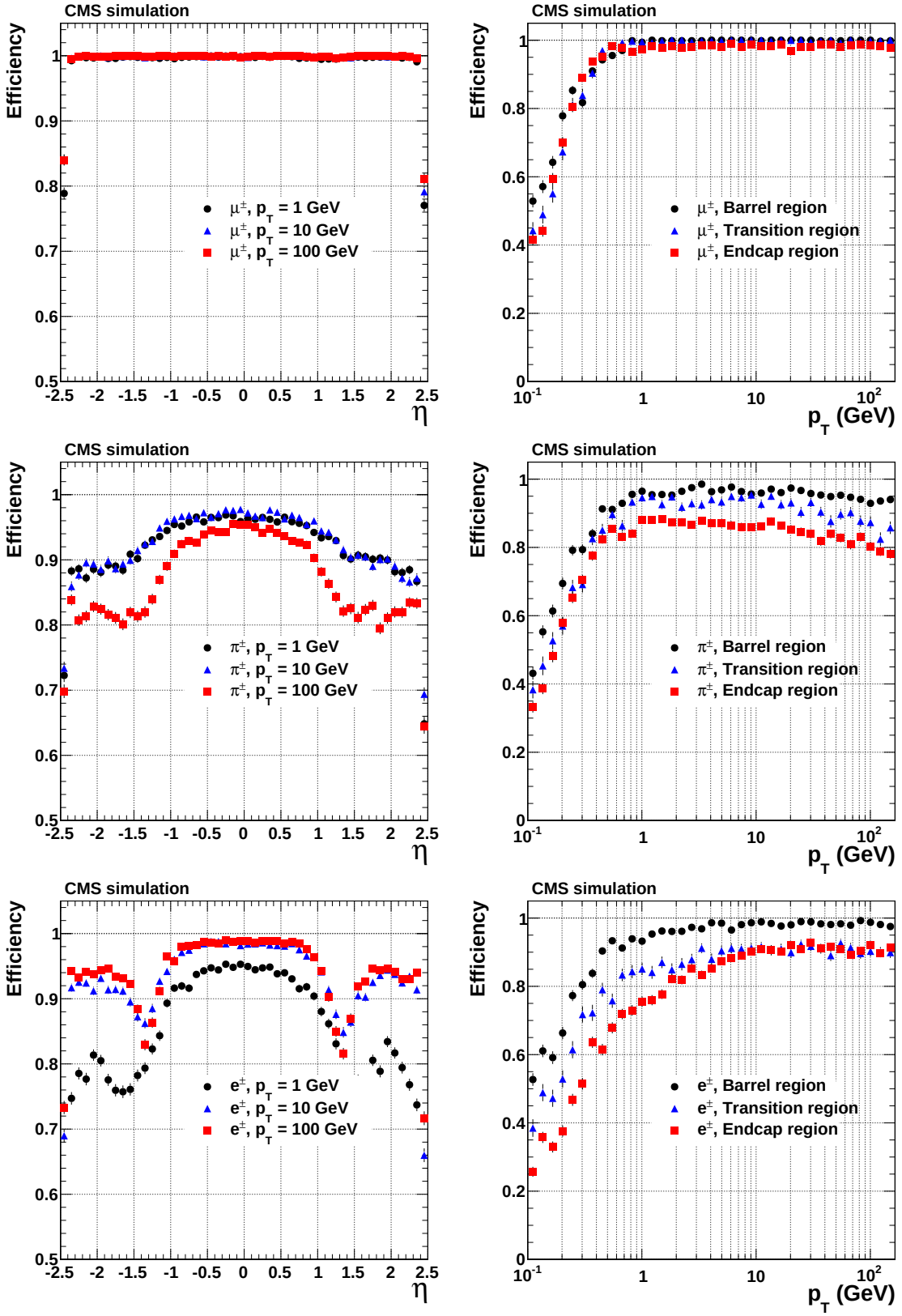

Figure 5.1: Track reconstruction efficiencies for single isolated muons (top), charged pions (middle) and electrons (bottom) as a function of p_{T} (left) and η (right). The barrel, transition and endcap regions are defined by the η intervals of $0-0.9$, $0.9-1.4$ and $1.4-2.5$, respectively. *High-purity* quality requirements are applied for all tracks [84].

rate is achieved, including for tracks originating from outside the pixel detector or those that did not leave any hits in the pixel tracker.

The track reconstruction efficiencies for single isolated muons, charged pions and electrons are shown in Figure 5.1 as a function of p_{T} and η [84]. Muon tracks are reconstructed at an efficiency greater than 99% for $1 < p_{\mathrm{T}} < 100\,\mathrm{GeV}$ across the entire volume of the tracking detector. Charged pions and electrons are not as efficiently reconstructed however, with both types of charged particles experiencing reconstruction inefficiencies of up to 20%. These loses occur as while muons predominantly interact with the detector medium through ionisation and produce negligible bremsstrahlung, pions experience elastic and inelastic nuclear interactions and electrons lose a large fraction of their energy through bremsstrahlung radiation.

5.2.2 Primary Vertices

The reconstructed tracks described above are used to reconstruct the positions where the proton-proton collisions occurred, known as *primary vertices* [84, 149]. Tracks are considered for primary vertex reconstruction if they are consistent with originating promptly from the interaction region, namely having a small d_0, a minimum number of hits in the pixel and strip trackers and a low $\frac{\chi^2}{ndf}$. Tracks meeting those requirements are then clustered along the z-axis at their point of closest approach to the beamspot using a deterministic annealing algorithm [150]. An adaptive vertex fitter is used to produce a 3D fit of the vertex track candidates and determine their uncertainties and variables such as the number of degrees of freom to discriminate against fake vertices [151].

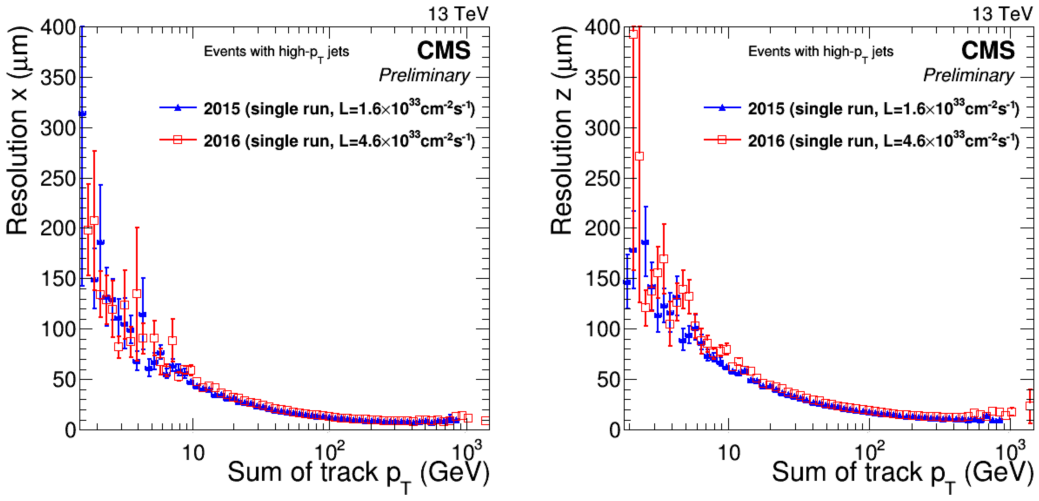

Figure 5.2: The x (left) and z (right) coordinate resolutions of the reconstructed primary vertices as a function of the scalar sum of the track p_{T}, measured in 13 TeV proton-proton collisions in 2015 (blue) and 2016 (red) [152].

Out of the resulting track candidates, the one with the greatest scalar transverse momentum is considered as the *primary vertex*, with the rest being assumed to represent PU vertices. Displaced vertices, such as those from the decay of heavy hadrons, are identified later in the reconstruction process.

Figure 5.2 shows the x and z coordinate resolutions of the reconstructed primary vertices measured in 13 TeV proton-proton collisions in 2015 and 2016 and their dependence on the scalar sum of the track p_{T}, which corresponds to the number of tracks present [152].

5.2.3 Calorimeter Energy Clusters

The energy deposited by particles in the calorimeters is independently clustered in each sub-detector, except for the HF where each large cell gives rise at most to just one cluster, to determine the energy and direction of the particles [146].

The clustering algorithm consists of three steps:

- **Cluster seeding:** Local cells with energies above a certain threshold are identified and considered as seeds.
- **Clustering:** Adjacent seed cells are summed together to form seed clusters.
- **Energy threshold:** A cluster is retained for further use if its energy is greater than two σ above the expected electronics noise in that part of the calorimeter (80 MeV in the EB, 300 MeV in the EE, and 800 MeV in the HCAL).

5.2.4 Particle Flow Algorithm

Through combining clusters in the calorimeters and charged particle tracks from the tracker and muon systems, the Particle Flow algorithm is able to use all the available information from an event to reconstruct and identify all the stable particles that it contains with far superior results than if each sub-detector were used individually [148].

The first stage of the algorithm involves associating or *linking* charged particle tracks with clusters in the calorimeters and between clusters in the different calorimeters. Following this, the linked elements are used by the PF algorithm to sequentially reconstruct and identify different PF particles types. As PF particles are identified, their associated tracks and clusters are removed from further consideration.

Charged particle tracks are linked to clusters by extrapolating a track's last measured hit in the tracker to the calorimeter systems. If a track's expected position in the calorimeters are within a cluster's boundaries, these elements are linked together. Similarly, tangents to the inner tracker tracks are extrapolated to the ECAL in order to identify and link

tracks to Bremsstrahlung photons. Calorimeter cluster links are formed if a cluster from the higher granularity detector (ECAL/ES) lies within the acceptance boundaries of the lower granularity detector considered (HCAL/ECAL).

The different particle types are then reconstructed in the following order:

- muons (see Section 5.2.6).
- electrons, associated Bremsstrahlung photons and isolated photons (see Section 5.2.5).
- HCAL clusters which are compatible with the remaining ECAL clusters and charged particle tracks are classified as charged hadrons.
- any remaining ECAL and HCAL clusters with no associated charged particle tracks are classified as photons and neutral hadrons, respectively.

After all these particle types are reconstructed, a post-processing stage is undertaken to mitigate against the small probability mis-identifying or reconstructing particles, usually high momentum muons. This avoids the appearance of an apparently large amount of missing transverse energy being present in an event.

5.2.5 Electrons

Electrons lose, on average, between 33% (minimal intervening material) and 86% (maximum intervening material) of their energy before reaching the ECAL through the production of Bremsstrahlung photons in the tracker layers [153], which often undergo electron pair production, potentially producing further Bremsstrahlung photons. It is essential that this radiated energy is collected in order to correctly determine the electron's initial energy.

As the magnetic field bends electrons trajectories in the ϕ direction, the ECAL crystals are clustered into strips in ϕ known as *superclusters* (SCs). Two clustering algorithms are used to form SCs of 5×1 and 5×5 ECAL crystals in η-ϕ for the EB and EE respectively due to their different geometrical arrangements [153]. In the EB, the so-called *hybrid* algorithm builds SCs. The algorithm initially identifies a seed crystal which contains at least $E_T > 1\,\text{GeV}$ and contains the largest energy deposit for a given region. Arrays of 5×1 crystals in $\eta \times \phi$, which contain at least $E_T > 0.1\,\text{GeV}$ and are within $\Delta\phi < 0.3$ of the seed crystal, are clustered together to form the SC. The so-called *multi* 5×5 algorithm builds SCs in a similar manner in the EE. Seed crystals are required to contain at least 0.18 GeV, and the arrays of 5×5 crystals added to the SC if the array has $E_T > 1\,\text{GeV}$ and is within $\Delta\phi < 0.3$ and $\Delta\eta < 0.07$ of the seed crystal.

The presence of Bremsstrahlung photons also necessitates the use of a Gaussian Sum Filter (GSF) [154] to fit electron tracks instead of a Kalman Filter as the process is non-Gaussian

and Kalman Filters assume only Gaussian noise contributions. The computationally heavy nature of the GSF algorithm, however, limits its use to refitting Kalman Filter track seeds and for the final fitting of the electron track parameters.

Electron track seeds, formed of the initial two or three hits in the tracker from which tracks are built, are constructed using two complimentary algorithms [153]:

- **ECAL-based approach** An electron's SC's energy and position is used to extrapolate the expected electron trajectory towards the primary vertex to determine where associated tracker hits would be expected for both electrons and positrons. Reconstructing electrons in jets however, suffers from large inefficiencies. This is due to the potential to incorrectly associate hits from other charged particles with the electron track and impact of jet energy deposits overlapping with the electron SC on the electron's assumed energy and position. Low p_{T} electrons are also poorly reconstructed as the increased bending of their trajectories results in the spread energy not being fully contained within a single SC.

- **Tracker-based approach** This approach is designed to compliment the ECAL-based approach by reconstructing non-isolated and low p_{T} electrons efficiently. A Kalman Filter (KF) is initially used for track finding as it is able to accurately reconstruct electrons that emit only a small amount of Bremsstrahlung in the tracker, with the KF track being matched to the closest ECAL SC. Tracks that are indicative of the emission of a significant amount of Bremsstrahlung are refitted with a GSF. Track parameters from both filters, such as the quality (χ^2) and how well matched the track is to the ECAL SC, are used by a Multivariate Analysis (MVA) technique to determine whether or not the tracker seed can be used as an electron seed.

The seeds collections produced by both algorithms are merged into a single set of seeds. From this combined set of seeds, electron tracks are iteratively built using a combinatorial Kalman Filter in which a series of cuts are applied in order to accommodate trajectory changes due to Bremsstrahlung and to maintain a high reconstruction efficiency. These electron tracks undergo a final fitting by the GSF to precisely determine the electron track parameters.

The electron reconstruction efficiency as a function of the SC η for electrons with $25 \leq p_{\mathrm{T}} \leq 500\,\mathrm{GeV}$ in 13 TeV proton-proton collisions in 2016 and simulation is shown in Figure 5.3. A reconstruction efficiency of at least 95% is observed across η, except for the transition region between the EB and EE and at high η due to the increased amount of material traversed and shorter effective lever arm available. The differences observed between data and MC at high η were due to a differing beam spot positions in data and MC.

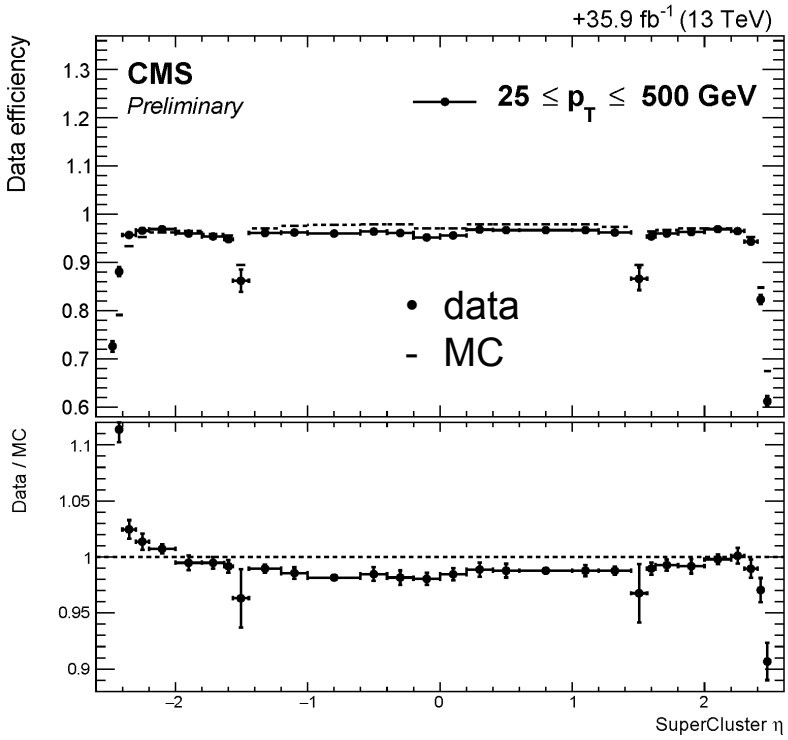

Figure 5.3: The reconstruction efficiency for electrons with $25 \leq p_{\mathrm{T}} \leq 500\,\mathrm{GeV}$ in 13 TeV proton-proton collisions in 2016 and simulation [155].

5.2.6 Muons

Muon tracks are independently reconstructed in both the inner tracker, as described in Section 5.2.1, and the muon chambers. Track reconstruction in the muon chambers is undertaken using a Kalman Filter to build tracks from the innermost track segments made up of clustered DT and CSC hits outwards using DT, CSC and RPC hits.

These two types of muon tracks are reconstructed using two methods [107]:

- **Global Muons** are reconstructed using an "*outside-in*" approach, where tracks in the muon chambers are extrapolated inwards towards the inner tracker where candidate tracks are then searched for. If a corresponding track is found, the hits from the best candidate in the inner tracker and the muon system are fitted using a Kalman Filter to form a Global Muon.

- **Tracker Muons** are conversely reconstructed with an "*inside-out*" approach, where inner tracker tracks with $p_{\mathrm{T}} > 0.5\,\mathrm{GeV}$ and $|p| > 2.5\,\mathrm{GeV}$ are extrapolated out to the muon system using a Kalman Filter that takes into account energy losses and multiple scattering. If at least one muon segment in the muon chambers is consistent with the extrapolated muon track, the track is classified as a Tracker Muon.

Given the high track reconstruction efficiencies of both the inner tracker and the muon chambers, approximately 99% of muons produced from the proton-proton collisions (prompt muons) are reconstructed as either a global or tracker muon, if not both. Global and tracker muons that share the same inner tracker track are merged into a single candidate muon to be considered by the PF algorithm.

5.2.7 Jets

Due to colour confinement, quarks and gluons produced in a proton-proton hard interaction rapidly hadronise, producing a collimated shower of hadrons that are clustered and reconstructed as *jets* [156]. Any jet reconstruction algorithm is required to be both *infrared safe* and *collinear safe*, i.e. so that the emission of soft gluons and the collinear splitting of gluons, respectively, do not change the jets that are actually constructed.

The main two types of jet algorithms are iterative cone and sequential recombination algorithms [156], and while both varieties are supported by CMS, the latter are typically used in the majority of analyses.

The general form of a sequential recombination algorithm is as follows:

- The distance, d_{ij}, for every pair of particles and the distance between each particle and the beamline, d_{iB}, is calculated.
- If the minimum value of d_{ij} is less than d_{iB}, the pair of particles are recombined into a single particle, and the process starts over.
- If the minimum value of d_{iB} is less than d_{ij}, the particle is classified as a jet and removed from the list of particles under consideration, and process begins again.

The process continues until no particles remain on the list.

These distance variables are defined as:

$$d_{ij} = min(p_{Ti}^{2k}, p_{Tj}^{2k}) \frac{\Delta R_{ij}^2}{R^2} \tag{5.3}$$

$$d_{iB} = \frac{1}{p_{Ti}^{2k}} \tag{5.4}$$

where $\Delta R_{ij}^2 = (y_i - y_j)^2 + (\phi_i - \phi_j)^2$; k is a parameter that governs the relative power of the energy scale against the geometric scale and R is the jet size parameter, which is typically set to 0.4 in CMS analyses to provide consistency with ATLAS and as it has been found to contain hadronic showers without being sensitive to PU. The *anti-*k_{T} algorithm [157], where

k = -1, which produces cone-shaped jets, is commonly used in CMS. The other values used for k, where k = 0, 1, correspond to the Cambridge/Aachen and k_{T} algorithms respectively.

PF jets are produced using the *anti-*k_{T} algorithm with R = 0.4 in conjunction with PF particles based on all the sub-detectors. Making use of PF jets allows a more accurate reconstruction to be undertaken than if only energy clusters from the calorimeters are used, given that jets are typically composed of 65% charged hadrons, 25% photons and 10% neutral hadrons, due to the precise charged hadron measurements from the tracker and ECAL, which are able to constrain the small neutral hadron contribution that relies on the relatively poor resolution of the HCAL.

The energy resolution of PF jets produced in 13 TeV proton-proton collisions in 2016 using the *anti-*k_{T} algorithm with R = 0.4, including the removal of charged hadrons that don't originate from the primary vertex, for central and forward detector regions is shown in Figure 5.4. In both the central and forward regions of the detector, the jet energy resolution was determined to be better than 10% for jets with $pT > 100/GeV$ and stable against the number of PU interactions. Further details regarding the jet energy scale and resolution and jet algorithm performance are discussed in [158, 159].

5.2.7.1 Jet Energy Corrections

Jet Energy Corrections (JECs) are used to take into account the effects of PU and the non-uniform response in p_{T} and η of the detector and any residual differences between simulation and data. Each of these effects is considered as a separate correction level; they are applied sequentially through the use of a scale factor applied to a jet's four-momentum in the following order:

- **L1 Pile-up.** Removes additional energy originating from PU interactions from the jet energy and is applied to both data and simulated events.
- **L2 Relative and L3 Absolute** Applied to data and simulation to account for the non-uniform detector response in η and p_{T}, respectively. The scale factor is derived by comparing generator level and reconstructed jets in the simulation.
- **L2L3 Residual** Applied to data only to account for any remaining small differences in the jet response between data and simulation, such as the absolute Jet Energy Scale (JES) following application of the previous corrections..

The uncertainties associated with these JECs are treated as systematic uncertainties, which are discussed in Chapter 7.5. Further details regarding the JECs can be found in [158].

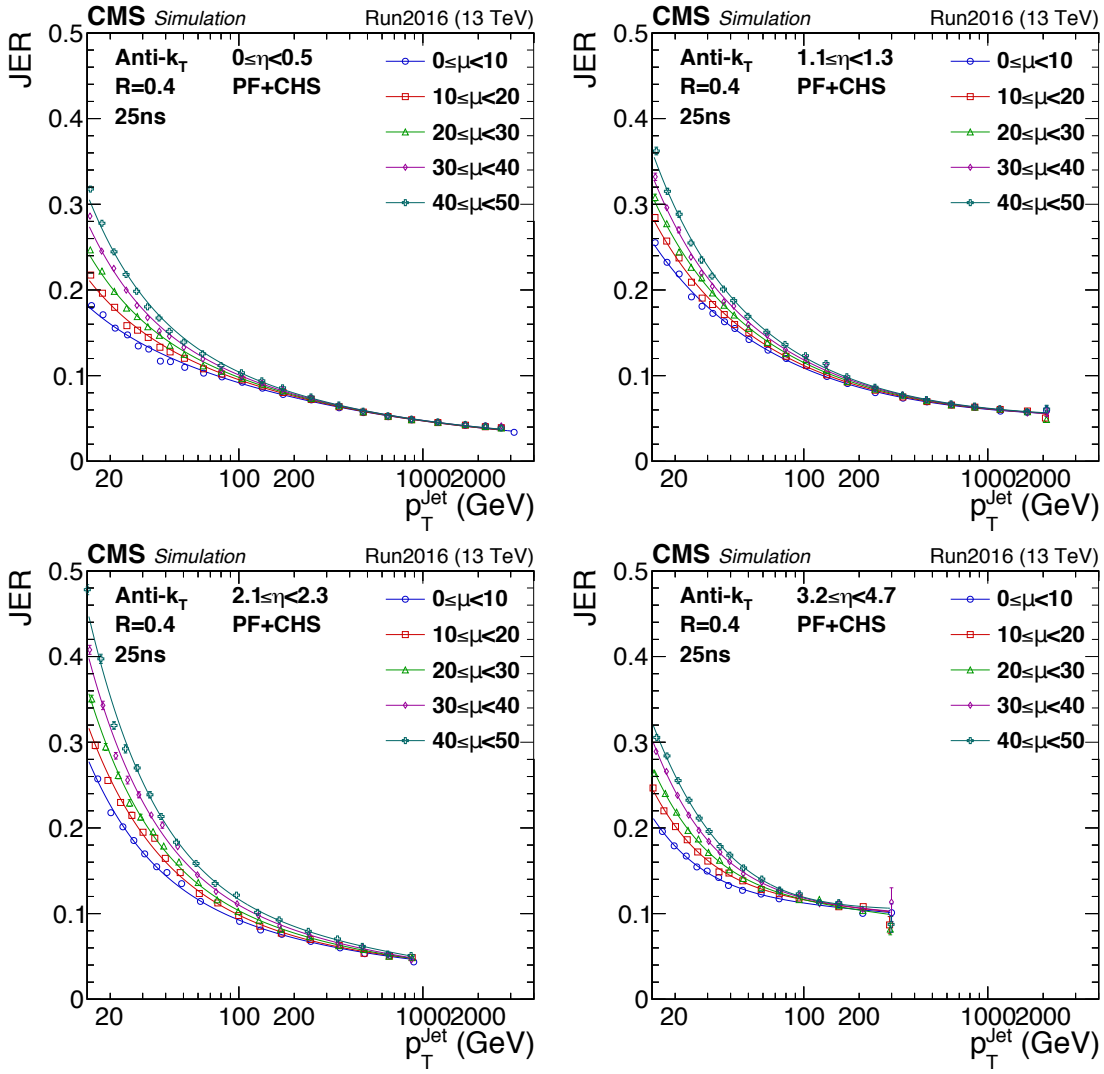

Figure 5.4: The energy resolution of PF jets with charged hadron subtraction (CHS) for central and forward regions for differing numbers of PU interactions (μ) in 13 TeV proton-proton collisions in 2016 [160].

5.2.8 b-tagging

Correctly determining whether or not a jet was the product of a b-quark hadronising is important for a variety of analyses, allowing them to better separate signal processes from topologically-similar background processes. b-jet identification is particularly pertinent for top physics searches due to the fact that the dominant decay mode for a top quark is to a W boson and a b-quark [9].

This process is known as *b-tagging* and exploits the fact that because b-hadrons have a relatively long lifetime of approximately 1.5 ps [161], they can travel a measurable distance away from the primary vertex before decaying. The resulting secondary vertices are exploited in b-tagging, which is performed in CMS by a number of algorithms supported by the CMS B-Tag and Vertexing (BTV) Physics Object Group (POG). The analysis presented uses the *Combined Secondary Vertex* version 2 (CSVv2) algorithm [162]. The CSVv2 algorithm uses information about displaced track and secondary vertices as input into a multilayer perceptron (MLP) (a class of neural network) to produce a discriminator value which characterises the likelihood that the likelihood a jet originated from a b-quark.

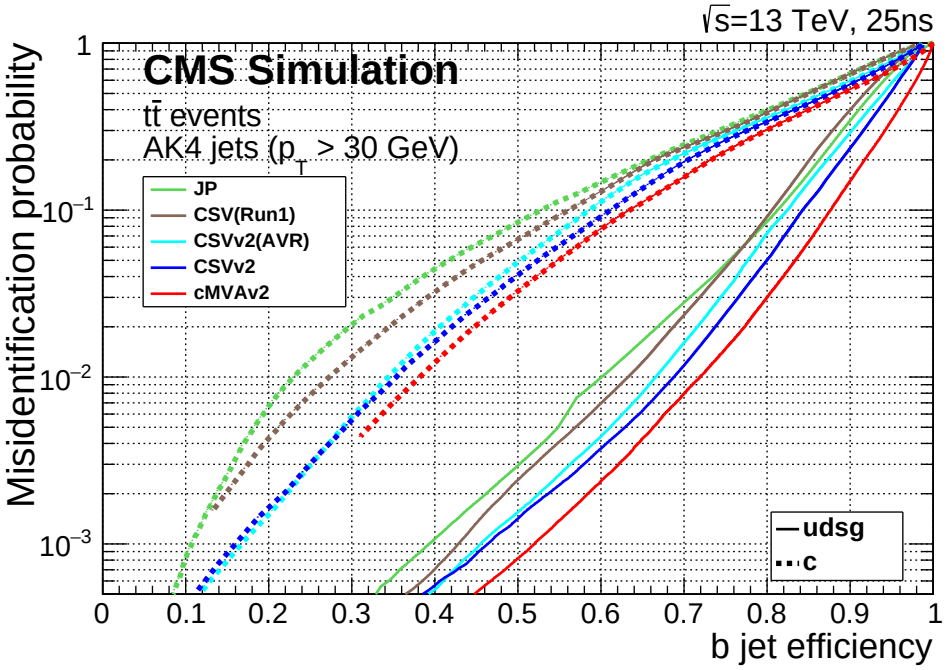

Figure 5.5: The light flavoured jets misidentification probability as a function of the efficiency of tagging genuine b-jets for the b-tagging algorithms supported within CMS [162].

Three different *working points* (loose, medium and tight) are defined by the BTV POG for b-tagging algorithms, such that the probability for incorrectly tagging light flavoured jets is 10%, 1% and 0.1% respectively. Figure 5.5 illustrates the negative impact that minimising the light jet misidentification probability has on the efficiency at selecting genuine b-jets for the b-tagging algorithms supported within CMS [162].

The selection efficiencies for b-jets, c-jets and light jets for each of the working points for the CSVv2 algorithm are given in Table 5.1.

Table 5.1: The CSVv2 algorithm's selection efficiencies and mis-identification rates for each of the three working points for b-(ϵ_b), c-(ϵ_c), and light jets (ϵ_{udsg}) with $p_{\mathrm{T}} > 20\,\mathrm{GeV}$ in simulated $t\bar{t}$ events [162].

CSVv2 WP Name (value)	ϵ_b (%)	ϵ_c (%)	ϵ_{udsg} (%)
Loose (0.5426)	84	39	8.3
Medium (0.8484)	66	13	0.8
Tight (0.9535)	46	2.6	0.1

5.2.9 Missing Transverse Energy

Particles that only weakly interact with matter, such as neutrinos and some hypothesised BSM particles, escape the detector without being directly observed. Their presence however, can be inferred by imposing conservation of transverse momentum to any given event. The missing energy in the plane transverse to the beam line, $\overrightarrow{E_{\mathrm{T}}^{\mathrm{miss}}}$, is defined as the negative vector sum of the transverse momentum in the event:

$$\overrightarrow{E_{\mathrm{T}}^{\mathrm{miss}}} = -\sum \overrightarrow{p_{\mathrm{T}}} \tag{5.5}$$

There are several different algorithms, using differing variables and techniques, that are used in CMS analyses to determine $E_{\mathrm{T}}^{\mathrm{miss}}$.

PF $E_{\mathrm{T}}^{\mathrm{miss}}$, produced using PF particles, is used in this analysis because of its high performance [163]. It must however, first be corrected before it can be used. The so-called *Type-I* $E_{\mathrm{T}}^{\mathrm{miss}}$ corrections replace the PF jets used to determine the $E_{\mathrm{T}}^{\mathrm{miss}}$ of an event with the PF jets with the JECs [164]).

Chapter 6

Analysis Strategy and Event Selection

The following three chapters of this thesis describe the search for the production of a single top quark in association with a Z boson using the dilepton final state with $35.9\,\text{fb}^{-1}$ of proton-proton collision data at $\sqrt{s} = 13\,\text{TeV}$ collected by the CMS experiment during 2016.

While the dilepton final state allows for the full reconstruction of all the particles involved, including the top quark, the presence of two leptons and multiple jets is identical to the final states of a large number of background processes. Consequently, as each of these backgrounds have cross sections many orders of magnitude larger than that for tZq, the signal region will inevitably be background dominated.

Therefore, the analysis was designed to ensure that the backgrounds are understood and constrained as far as possible and to have the highest possible acceptance of the signal in order to maximise the expected tZq yield. To further enhance the separation of the signal from the background processes, a multivariate analysis is performed and is described in Section 7.6.

This chapter describes the event selection criteria used for the signal and control regions used in this search, the blinding method used, and the background processes that were considered. The selection criteria for the physics objects described in Sections 6.1-6.2 are defined in detail in Section 6.6.

6.1 Signal Region

At leading order, the final state produced by the signal process consists of a top quark, a recoil quark and a Z boson, as illustrated in Figure 2.7. The top quark decays to a b-quark almost 100% of the time, with the W boson required to decay hadronically. As the Z boson

is required to decay leptonically, the final state objects of interest consist of two leptons (electrons or muons) that are compatible with a Z boson decay, four jets, one from the top quark decay (which must be b-tagged), two from the W boson, and the recoil jet.

Exactly two leptons are required to pass high purity (tight) identification and isolation criteria with no additional leptons which have passed the most efficient (veto/loose) identification and isolation criteria. These criteria ensure that there is a low lepton misidentification acceptance rate and a high rejection efficiency of events containing a differing number of leptons of either flavour or that were not produced from a W or Z boson decay.

The presence of a Z boson in the final state means that the two leptons selected must be consistent with being from a Z boson decay. Thus, the leptons must have the same flavour and opposite charge and an invariant mass that is within $\pm 20\,\text{GeV}$ of the measured Z boson mass of $91.2\,\text{GeV}$ [9]. This mass window was chosen as was sufficiently wide to account for detector resolution effects, leading to a high acceptance rate of leptons produced from Z boson decays.

As additional jets may be produced by gluon splitting from by initial or final state radiation the maximum number of jets considered is limited to six. Thus four to six jets are required to be present, each of which must satisfy $p_{\text{T}} > 30\,\text{GeV}$ and $|\eta| < 4.7$ and pass a highly efficient jet identification criteria.

Given the top quark has a near 100% probability of decaying into a b-quark and a W boson, the event selection requires at least one of the selected jets to be b-tagged and satisfy $|\eta| < 2.7$. The b-tagging algorithm and selection criteria are described in Section 6.6.2.2 As the W boson and the recoil quark may also be b-quarks, up to two of the selected jets are allowed to be b-jets. This limit was chosen as it was found that there was minimal signal ($< 1\%$) present for events with more than two b-tagged jets. Consequently, given the background dominated nature of this search, it would have been challenging to separate this small signal contribution from the background processes.

With all the jets identified, the W boson candidate constructed from the two jets with the closest invariant mass to the known W boson mass of $80.4\,\text{GeV}$ [9] is considered. To ensure the two selected jets are consistent with a W boson decay, their invariant mass is required to be within $\pm 20\,\text{GeV}$ of the known W boson mass. The leading b-jet however, is not considered to have been produced by the W boson decay as the hardest b-jet was found to be predominantly that from the decay of the top quark.

To summarise the complete event selection for the signal region was chosen to be:

- Exactly two same flavour and opposite sign electrons or muons which pass the tight identification and isolation cuts. The leading and sub-leading electrons must have a $p_{\text{T}} > 35\,\text{GeV}(15\,\text{GeV})$ and be within $|\eta| < 2.50$. The leading and sub-leading muons $p_{\text{T}} > 26\,\text{GeV}(20\,\text{GeV})$ respectively and be within $|\eta| < 2.4$.

- No additional electrons or muons that pass the same kinematic cuts and the veto or loose identification and isolation cuts respectively.
- The invariant mass of the two selected leptons must be within 20 GeV of the known Z boson mass.
- Four to six jets that pass the jet identification requirements and have a $p_{\mathrm{T}} > 30\,\mathrm{GeV}$ and are within $|\eta| < 4.7$.
- One or two of the selected jets are considered to be b-tagged and are within $|\eta| < 2.4$.
- The invariant mass of the two jets that are closest to the known W boson mass must be within 20 GeV. The leading b-jet is not considered to have originated from the W boson decay.

6.2 Control Regions

For any high energy particle physics analysis lacking a high signal to background ratio, the accurate modelling of its background processes is essential in order to extract the signal yield and make a precise measurement. As the main challenge in the search for the dilepton final state of the tZq process is the understanding and constraining of its irreducible backgrounds, it is especially important to ensure that the background processes are accurately modelled in simulation.

Therefore, background enriched control regions whose kinematic distributions are similar to the signal region's were constructed and used to check the modelling of the Z+jets and $t\bar{t}$ production process, as these were anticipated to be the most important background processes. Consequently, the control regions for both of these processes had the same trigger, event cleaning, and baseline event selection of two oppositely charged leptons, jet multiplicities and W and Z boson mass selections as the signal region. Where required, these control regions would be extrapolated to provide a data-driven estimation of the background in the signal region as discussed in Section 7.4.

6.2.1 Z+jets Background Control Regions

Despite the majority of the Z+jets contribution being rejected by the signal selection criteria, it still represents the largest background contribution due to this high cross section for this process. Given the size of this background it is essential to ensure that both the normalisation and modelling of his process are well described.

Initially, a high statistics Z+jets-enriched control region was defined by requiring that none of the jets present are b-tagged, in contrast to the one to two required for the signal region.

Given the large cross section and that the vast majority of the jets produced in the Z+jets process are light quark jets, and the decays of $t\bar{t}$ processes produce lots of b-jets, this produces a high purity region with large statistics.

Despite this, as the kinematics of b-jets differ from light quark jets, this control region may not provide a sufficiently similar kinematic phase space to the signal region. Thus an alternative Z+jets enriched control region was defined. This alternative control region required the same b-jet selection (one to two b-jets) as the signal region, but with an inverted W boson mass threshold and that the $E_{\mathrm{T}}^{\mathrm{miss}}$ present in the event was less than 50 GeV. The inverted W boson mass threshold rejects events containing a hadronically decaying W boson (such as the signal process) and the $E_{\mathrm{T}}^{\mathrm{miss}}$ threshold suppresses $t\bar{t}$ which contains significant quantities of $E_{\mathrm{T}}^{\mathrm{miss}}$ from the leptonically decaying W bosons.

The performance of both of these control regions is discussed in Section 7.4.2.

6.2.2 $t\bar{t}$ Background Control Region

$t\bar{t}$ events that decay dileptonically contribute to the background when the leptons are compatible with originating from a Z boson decay. Given the size of the $t\bar{t}$ production cross section, these events were found to form the second largest background contribution.

The selection criteria for the $t\bar{t}$ control region differs from the signal region definition defined in Section 6.1, by requiring that:

- the two oppositely-charged leptons to have different flavours (i.e. one is an electron and the other a muon).
- p_{T} cuts of 35 GeV and 26 GeV are used for the electron and muon respectively.

As the branching ratio for a W boson (produced in top and anti-top quark decays) to decay into either an electron or muon is, within uncertainty, equal [9], this produces a $t\bar{t}$-enriched background control region which is topologically similar to the $t\bar{t}$ contributions in the signal region.

The performance of this control region is discussed in Section 7.4.3.

6.3 Experimental Blinding

Despite even the best intentions, there is the potential for experimental procedure to be inadvertently biased by previous observations [165]. In order to prevent this from happening, experiments are "blinded" so that the result is not known until the analysis has been optimised using simulation and/or data outside of the signal region.

Before unblinding, a χ^2-like variable was used to define a side-band region outside the expected signal region where data and simulation distributions could be compared prior to the training and testing of the MVA described in Section 7.6. The MVA was blinded throughout its optimisation, training and testing as it only made use of simulated events. Prior to unblinding pseudo-data was used to evaluate the expected outcomes of the measurement, as described in Chapter 8.

Unblinding this analysis was achieved by completely removing the selection requirement applied to the χ^2-like variable. Once this had been done, all of the data and simulation comparisons were remade and the corresponding observed results are given in Chapter 6. This unblinding procedure was performed specifically for this thesis after receiving approval from the CMS collaboration to do so. These results will not appear in this form in any other public document.

The χ^2-like variable was inspired by the ones used by the CMS and ATLAS searches for the decay of a Higgs boson to two b-quark pairs [166, 167] as inspiration, and uses the reconstructed top quark mass and the W boson mass to define the blinded region in phase space where the signal is expected to be.

Tç is defined as follows:

$$\chi^2 = \left(\frac{m_{\mathrm{jj+b}} - m_{\mathrm{t}}}{\sigma_{\mathrm{t}}}\right)^2 + \left(\frac{m_{\mathrm{jj}} - m_{\mathrm{W}}}{\sigma_{\mathrm{W}}}\right)^2 \tag{6.1}$$

where m_{jj} is the W boson mass reconstructed from the two candidate jets, σ_{W} is the known W boson mass, $m_{\mathrm{jj+b}}$ is the top quark mass reconstructed from the leading b-jet thus the two two jets associated with the W boson decay, m_{t} is the known top mass, and σ_{t} and σ_{W} represent the mass resolution for the top quark and W boson respectively. Both σ_{t} and σ_{W} were determined by taking the standard deviation of a Gaussian fitted to their corresponding reconstructed peaks and were determined to be $\sigma_{\mathrm{t}} = 30\,\mathrm{GeV}$ and $\sigma_{\mathrm{W}} = 8\,\mathrm{GeV}$, respectively.

Using the simulated samples, a Signal Region (SR) and *Side Band* (SB) were defined as the regions enclosed by $\chi^2 < \chi^2_{SR}$ and $\chi^2_{SR} < \chi^2 < \chi^2_{SB}$, respectively.

The choice of value used for χ^2_{SR} and χ^2_{SB} had to balance the need for:

- the signal region to contain the majority of the signal process;
- the *side band* region to contain sufficient signal-like events to make the analysis possible.

Therefore, χ^2_{SB} was defined so that it contained all events where m_{jj} was within $5\sigma_{\mathrm{W}}$ and χ^2_{SB} defined to contain 68% of the simulated signal events. Using these definitions, for $\sigma_{\mathrm{t}} = 30\,\mathrm{GeV}$ and $\sigma_{\mathrm{W}} = 8\,\mathrm{GeV}$, χ^2_{SB} and χ^2_{SR} were defined as 5 and 30, respectively.

Figure 6.1 shows the side-band region bounded between the two contour lines in the reconstructed top quark mass and W boson mass distributions for the tZq simulation sample (left) and all the simulation samples that were considered (right) (see Section 7.1).

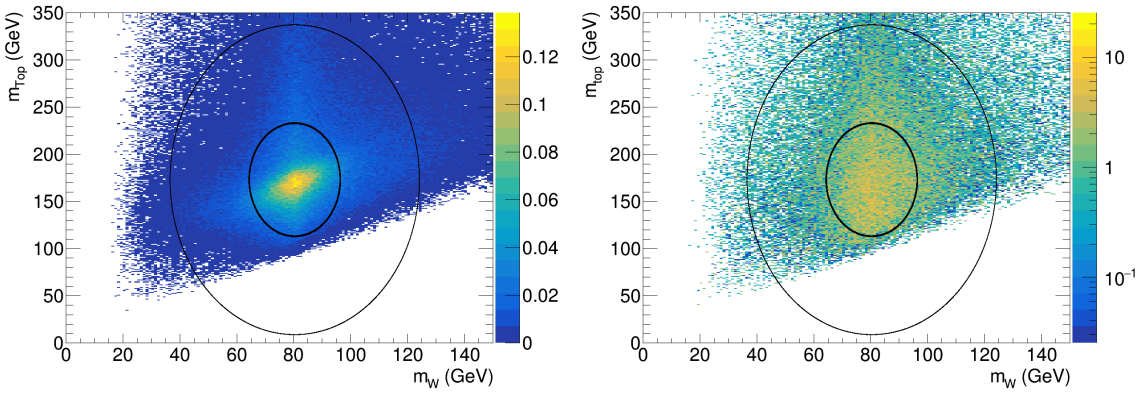

Figure 6.1: The reconstructed top quark mass and w boson mass distributions for the tZq simulation sample (left) and all simulation samples (right) for both the ee and $\mu\mu$ channels following the application of the signal region criteria described in Section 6.1. The signal region is defined as the area within the inner contour line and the side-band region is defined as the are bounded between the two contour lines.

6.4 Trigger Strategy

As the search for the tZq dilepton final state relies on the identification of the two leptons from the Z boson decay, the trigger strategy consists of selecting events from datasets identified by the triggering of an electron or muon trigger. Given that the signal process being searched for is dominated by background processes and will likely be limited by event yield, it is essential to reconstruct and select as many signal events as possible. To this end, in order to obtain the maximum event selection efficiency, events are required to have triggered a single lepton or a double lepton trigger for the ee and $\mu\mu$ final states.

In simulation an event is required to pass either the single or double lepton triggers for the relevant channel. In data however, there is the potential to double count events which are present in both the single lepton and double lepton datasets. In order to avoid double counting events, events that have been found in a double lepton dataset are not considered for the single lepton dataset. The trigger logic for each of the final states is illustrated in Table 6.1.

Ideally the, single and double lepton triggers with the lowest possible transverse momentum thresholds would be considered to ensure that the maximum possible event yield can be obtained over the largest possible phase space. The high instantaneous luminosity at the start of the most luminous data taking periods, however, required a number of the L-1

Table 6.1: The trigger logic used for each of the CMS datasets considered, where *EM* refers to the muon and electron triggers, *EE* to the double electron triggers, *E* to the single electron triggers, *MM* to the double muon triggers, *M* to the single muon triggers and *!* to a trigger not being passed.

Final State	**Dataset**	**Trigger logic**
$e\mu$	Muon and Electron	EM and !EE and !MM
	Single Muon	M and !E and !EE and !MM and !EM
	Single Electron	E and !M and !EE and !MM and !EM
$\mu\mu$	Double Muon	MM and !EM and !EE
	Single Muon	M and !E and !EE and !MM and !EM
ee	Double Electron	EE and !EM and !MM
	Single Electron	E and !M and !EE and !MM and !EM

triggers to be prescaled to prevent the trigger bandwidth constraints being exceeded. As only the triggers considered for the ee channel were impacted by this; these triggers were chosen on the basis of the amount of luminosity they were not prescaled for with the lowest possible transverse momenta thresholds.

Table 6.2 lists the triggers used to select data and simulation events for each channel, including the eμ final state which is considered for a $t\bar{t}$ enriched control region (see Section 6.2.2). In these trigger path names, *Ele* and *Mu*, refer to a reconstructed electron and muon, respectively. The number following the lepton flavour denotes the minimum p_{T} a lepton must have to fire the trigger. In order to avoid raising p_{T} thresholds to maintain the trigger data rate, additional criteria are used by the triggers. These include simple identification (*Id*) and isolation (*Iso*) criteria, which are extracted from the calorimeter (*Calo*) and tracker (*Trk*) systems, and filters to reject candidates that have not originated from the interaction point (*DZ*).

Table 6.2: Triggers and datasets used for each decay channel.

Final State	**Dataset**	**HLT Trigger Conditions**
ee	DoubleElectron	HLT_Ele23_Ele12_CaloIdL_TrackIdL_IsoVL_DZ
	SingleElectron	HLT_Ele32_eta2p1_WPTight_Gsf
$\mu\mu$	DoubleMuon	HLT_Mu17_TrkIsoVVL_(Tk)Mu8_TrkIsoVVL(_DZ)
	SingleMuon	HLT_Iso(Tk)Mu24
$e\mu$	MuonEG	HLT_Mu12_TrkIsoVVL_Ele23_CaloIdL_TrackIdL_IsoVL(_DZ)
		HLT_Mu23_TrkIsoVVL_Ele12_CaloIdL_TrackIdL_IsoVL(_DZ)

6.5 Event Cleaning

beam backgrounds/detector noises After selecting an event that meets the trigger requirements described in Section 6.4, a number of filters are applied to remove events containing beam backgrounds or detector noise from further consideration:

- **Primary Vertex Filter:** Ensures that the primary vertex is well reconstructed by requiring it to be within $|z| \leq 24\,\text{cm}$ of the interaction point and within $d_0 < 2\,\text{cm}$ of the beam line.
- **Beam Halo Filter:** Beam halos are machine-induced particles (i.e. produced from the beam interacting with the pipe and residual gas in the pipes) that circulate with the beam at radii of up to 5 cm. This filter removes events with calorimeter and muon chamber energy deposits consistent with those expected to be produced by either halo particles or particle showers. These effects are caused by beam halos interacting with the collimator blocks that are used to clean halos from the beam.
- **HBHE Noise and Isolation Filters:** Remove events where anomalous noise is observed in the HCAL's hybrid photodiodes or readout boxes, which registers as large isolated energy deposits which would infer the presence of large $E_{\text{T}}^{\text{miss}}$, by considering the channel multiplicities, pulse shape of the readout and the neighbouring activity in the calorimeters and tracker.
- **ECAL Trigger Primitive Filter:** The L-1 trigger primitive readout can be used to estimate the energy deposited in approximately 70% of the channels that lack regular data links and which ignored in the offline reconstruction. As trigger primitives have a narrower energy acceptance range than the read-out, when the energy is near their saturation energy the measured energy is likely to be underestimated, resulting in high anomalous $E_{\text{T}}^{\text{miss}}$.
- **Bad Charged Hadron Filter:** Removes events where a muon is not defined as a PF muon due to its low quality, but instead makes its way into the PF MET calculation as a mis-identified charged hadron candidate.

6.6 Physics Objects

In order select events consistent with the objects expected to be in the final states of the signal enriched region and background enriched control regions described in Sections 6.1-6.2, a number of event selection criteria are applied to the physics objects that have been reconstructed using the particle flow algorithm described in Chapter 5. The following section describes the selection criteria used in this analysis and how the final state products are used to reconstruct their mother particles.

6.6.1 Lepton Selection

All PF electrons and muons identified by the PF algorithm must pass a set of kinematic requirements and a set of quality criteria defined by CMS. The kinematic requirements are applied to ensure that the leptons lie fully within the detector's acceptance and that their transverse momentum lies in the region where the trigger is both fully efficient and well described in simulation. The identification criteria have been designed to be efficient at selecting isolated leptons produced from W and Z boson decays and rejecting leptons that have been from decays from within jets or taus or from incorrectly reconstructed tracks.

Different "working points" (WPs) are determined for the set of variables used by each of identification criteria supported by the CMS Physics Object Groups. The WPs are defined by their average selection efficiency in simulation, with the tighter WPs being less efficient, but having a lower misidentification rate. For both electrons and muons considered in the analysis, the "tightest" working point is used to select high purity collections of leptons, with the "loosest" working point used to veto events with any additional leptons.

6.6.1.1 Electrons

For any PF electron candidate to be considered in the final analysis it must meet the following kinematic requirements:

- the p_{T} of the leading and subleading electrons considered must be greater than the 35 GeV and 15 GeV, respectively;
- electrons must have $|\eta| \leq 2.50$ to ensure that the electrons are fully within the ECAL acceptance;
- electrons with $1.4442 \leq \eta \leq 1.566$ are not considered as accurate reconstruction cannot be undertaken in the transition region between the ECAL barrel and endcap;
- the longitudinal impact parameter, d_z, of the electron must be less than 0.10 cm in the barrel and 0.20 cm in the endcap disks;
- and the transverse impact parameter, d_{xy}, of the electron must be less than 0.05 cm in the barrel and 0.10 cm in the endcap disks.

The impact parameter cuts are applied to ensure that the electron originates from within the interaction point of the detector.

The *tight* and *veto* working points (WPs) of the CMS recommended electron identification criteria, which are approximately 70% and 95% efficient respectively, are used to select electrons and to veto any additional electrons. This set of identification criteria uses a

mixture of predetermined variables and multivariate analysis (MVA) tuned variables for both the barrel and endcap disks. The values of the latter were set by the MVA determining the optimum values for a given selection efficiency, using simulated Z+jets and $t\bar{t}$ +jets events as the signal and background processes respectively.

The predetermined variables are:

- $N_{innerhits}^{missing}$**:** As photons that subsequently convert into e^+e^- pairs do not leave hits in the innermost layers of the tracker, electrons are rejected if the expected number of missing hits is exceeded.
- **a conversion veto** - is applied for all working points. The photon to electron conversion veto tests if a pair of electron tracks originate from a common displaced vertex. Any electron which fails this criteria is rejected.

The MVA tuned variables include:

- **Full** $5 \times 5\sigma_{i\eta i\eta}$**:** Describes the lateral extension of the shower along the η direction, i.e. the RMS alongside the η direction inside the 5×5 iη tower.
- $\Delta\eta_{seed}$ **and** $\Delta\phi_{seed}$**:** The distances in η and ϕ between the ECAL supercluster and where the track has been extrapolated to from the primary vertex, respectively.
- $\frac{h}{E}$**:** The ratio of hadronic to electromagnetic energy deposited in the supercluster around the crystal with the largest energy deposit.
- I_{EA}^{rel}**:** The relative isolation of the electron with effective area pileup alleviation for a cone size of 0.3, which is described further in Section 6.6.1.3.
- $1/E - 1/p$**:** The difference between the inverse energy of the ECAL supercluster and the inverse of the track momentum, which is used to describe the energy loss of the electron due to material effects.

The selection requirements that define the tight and veto WPs for these variables are given in Table 6.3.

6.6.1.2 Muons

PF muons are also required to meet an equivalent set of kinematic requirements along with identification and isolation criteria.

PF muons candidates are required to meet the following kinematic requirements:

- the p_{T} of the leading and subleading electrons considered must be greater than 26 GeV and 20 GeV, respectively;

Table 6.3: The selection requirements used for the tight and veto working points of the cut based identification criteria for electrons for the barrel and endcap disks.

Variable	**Tight WP**		**Veto WP**	
	Barrel	Endcap	Barrel	Endcap
Full $5 \times 5\sigma_{i\eta i\eta}$	< 0.00998	< 0.0292	< 0.0115	< 0.037
$\Delta\eta_{seed}$	< 0.00308	< 0.00605	< 0.00749	< 0.00895
$\Delta\phi_{seed}$	< 0.0816	< 0.0394	< 0.228	< 0.213
$\frac{h}{E}$	< 0.0414	< 0.0641	< 0.356	< 0.211
I_{EA}^{rel}	< 0.0588	< 0.0571	< 0.175	< 0.159
$1/E - 1/p$	< 0.0129	< 0.0129	< 0.299	< 0.15
$N_{innerhits}^{missing}$	≤ 1	≤ 1	≤ 2	≤ 3
pass conversion veto	✓	✓	✓	✓

- muons must have $|\eta| \leq 2.40$ to ensure that a muon is fully within the acceptance of the muon systems.

The *tight* and *loose* identification and isolation criteria [107] are used to select muons and veto any additional muons.

The tight muon criteria suppress hadronic punch-through into the muon system and selection of non-prompt muons, creating a high purity collection of particle flow muons.

These criteria are:

- As well as being identified as a PF Muon, it is also identified as both a tracker muon and global muon;
- χ^2/ndf of the global muon track fit is less than ten;
- at least one muon chamber is included in the global track fit;
- that associated muon segments are found in at least two muon stations;
- $d_0 < 0.2\,\text{cm}$ and $d_z < 0.5\,\text{cm}$;
- the muon must have at least one hit in the pixel detector.
- the muon must have hits that are present in at least six tracker layers in order to achieve a good p_{T} measurement.

The tight muon isolation criteria applied to the resultant tight collection of muons is 95% efficient and rejects muons that have a relative isolation greater than 0.15 for a cone size of 0.4. By definition all PF muons considered pass the loose identification cut. The loose

isolation cut is 98% efficient and rejects muons with a relative isolation that is greater than 0.25. The $\Delta\beta$ pileup corrections used for relative isolation with muons is described below in Section 6.6.1.3.

6.6.1.3 Lepton Isolation

A relative isolation variable I^{rel} is used in order to:

- differentiate between leptons produced promptly at the primary vertex from those resulting from heavy flavour jet or tau decays;
- to ensure that leptons are sufficiently separated from hadrons and photons to enable a precise momentum measurement of the lepton .

I^{rel} is defined as the summed energy of all PF particles within a cone of fixed radius ΔR around the PF lepton (with the estimated neutral charged pileup contamination, ρ, removed), divided by the lepton p_{T}.

As only charged hadrons (CH) have associated tracks that can be used to determine if they are consistent with the primary vertex, the pileup contamination contribution from neutral hadrons (NH) and photons is typically estimated using one of two methods.

In the analysis presented here, the ρ * effective area ($rho*A_{\mathrm{eff}}$) technique with a ΔR of 0.3 is used for the electron. This method estimates the neutral pileup contributions by estimating and subtracting the median energy density per area of pileup contamination, ρ, which has been multiplied by the effective area of the electron, A_{eff}. This effective area is characterised as a function of the supercluster's η:

$$I^{rel}_{rho*A_{eff}} = \sum p_T(CH) + max(0.0, \sum E_{\mathrm{T}}(NH) + \sum E_{\mathrm{T}}(Photon) - \rho * A_{\mathrm{eff}})/p_T \quad (6.2)$$

where the $max()$ function ensures that the corrected hadronic energy never negative.

The alternative $\Delta\beta$ pileup mitigation method is used for muons with a ΔR of 0.4 in the analysis presented here. Using the fact that the ratio of neutral to charged hadron production in the hadronisation of pileup interactions is approximately 0.5, half of the transverse energy of charged hadrons from pileup is subtracted from the neutral hadron and photon transverse energies [168]:

$$I^{rel}_{\Delta\beta} = \sum p_T(CH) + max(0.0, \sum E_{\mathrm{T}}(NH) + \sum E_{\mathrm{T}}(Photon) - 0.5 * \sum E_{\mathrm{T}}(PU))/p_T \quad (6.3)$$

6.6.2 Jet, b-tagging, W Boson and Top Quark Candidate Requirements

6.6.2.1 Jet Requirements

Jets belonging to the PF jet collection are considered, which are reconstructed using the *anti-*k_{T} algorithm [157] with R = 0.4 with charged hadrons originating from PU vertices excluded from clustering.

Jets are considered in this analysis if they have a $p_{\mathrm{T}} > 30\,\mathrm{GeV}$, are within $|\eta| < 4.7$ and meet the *loose* working point jet identification criteria developed by CMS. The loose WP was chosen not only because it had a high selection efficiency and rejected the majority of the fake tracks, but also because the tight working point didn't increase the sensitivity of the search. In addition, selected leptons (electron or muon) that lie within a cone of $\Delta R = 0.4$ of a selected jet are not considered to be a prompt leptons but are instead considered to be part of the jet in question.

The loose jet working point was designed to reject the majority of fake tracks produced within the detector and/or electronics noise. This working point maintains a high selection efficiency for real jets by requiring all jets to have part of their energy deposited in both the ECAL and HCAL and be composed of more than one particle.

For jets with $|\eta| \leq 2.70$, the loose working point criteria are:

- the fraction of the jet energy from both neutral electromagnetic particles in the ECAL and neutral hadronic particles in the HCAL is less than 0.99.
- the jet must consist of at least two particles.

The following criteria are additionally applied for jets for $|\eta| \leq 2.40$:

- the fraction of the jet energy from charged electromagnetic particles in the ECAL is less than 0.99 and greater than 0.0 for charged hadronic particles in the HCAL.
- at least one charged particle is present within the jet.

For jets with $2.70 \leq |\eta| \leq 3.0$ the loose working point criteria are:

- the fraction of the jet energy from neutral electromagnetic particles in the ECAL is greater than than 0.01 and less than 0.98 for neutral hadronic particles in the HCAL.
- at least three neutral particles are present within the jet.

For jets with $|\eta| > 3.0$ the loose working point criteria are:

- the fraction of the jet energy in the ECAL that is from neutral electromagnetic particles is less than 0.90.
- at least eleven neutral particles are present within the jet.

6.6.2.2 b-tagging Requirements

The CSVv2 tagging algorithm described in Section 5.2.8 is used to select jets that are deemed to have been initiated by a b-quark. If the value of a jet's discriminator exceeds that of the Medium WP threshold and has $|\eta| < 2.40$, the jet is considered to be a b-jet. Out of the *Loose*, *Medium* and *Tight* WPs thresholds [162] defined in Table 5.1 in Section 5.2.8, the medium WP was selected. This was because it provided the optimum performance in terms of providing as large a sample as possible for the signal process without too great a compromise on the purity of the selection.

6.7 Background Processes

This next section discusses the background processes considered which can have the same final state as the signal process, their anticipated contributions to the background, and how they have been constrained.

The additional contributions from processes not considered here, where events that involve at least one jet that has been incorrectly reconstructed as a lepton or a lepton from the decay of a heavy quark, are discussed in Section 7.4.1.

6.7.1 Vector Boson in association with multijet backgrounds

Multijet events in association with a vector boson have the largest cross sections of any process which produces prompt leptons at the LHC, as illustrated in Figure 3.3. As only one promptly produced lepton from the W boson decay is expected for W+jets, the presence of any additional leptons would have to be the result of a real heavy quark decay or fake reconstructed jet. Requiring any selected lepton to be sufficiently isolated from hadronic activity in the event will suppress the contribution from these events.

In contrast, while the Z+jets cross section is an order of magnitude smaller than the W+jets cross section, the two prompt leptons from the Z boson decay makes it much more difficult to distinguish between this background and the signal. Despite requirement at least four jets, with at least one being a b-jet, in the signal region will reject the majority of the Z+jets events, the size of the Z+jets cross section ensures that the contribution from this process is still significant after all the selection criteria have been applied.

6.7.2 Top physics backgrounds

$t\bar{t}$ has the next largest production cross section after W+jets and Z+jets. While lepton isolation and jet cleaning criteria will significantly suppress the hadronic and lepton+jets

final states, the dilepton final state provides the second largest background contribution when the two leptons that have been produced meet the Z boson selection criteria.

Similarly, the only single top production process anticipated to produce a significant background is the tW-channel when, due to gluon splitting and the two W bosons decaying leptonically, the final state that passes the event selection is indistinguishable from the $t\bar{t}$ dilepton final state. In contrast, negligible contributions are expected from the t- and s-channel processes where no prompt leptons are produced in their respective final states after the event selection is applied.

While the processes where $t\bar{t}$ is produced in association with a vector boson have cross sections many orders of magnitude smaller than $t\bar{t}$ and single top production, only $t\bar{t}Z$ where the Z boson decays leptonically is expected to be a significant background due to its indistinguishable topology from the signal process. As the leading order final state has little to no expected $E_{\mathrm{T}}^{\mathrm{miss}}$, jets from W boson decays, and six jets, some of which may not be reconstructed due to merged or falling outside the detector acceptance, the vast majority of these events will pass the signal region criteria. The lack of a real Z boson decay in $t\bar{t}W$, $t\bar{t}H$ and tHq however, will result in the vast majority of events from these processes being rejected from consideration.

The rarest background considered is production of a single top quark in association with both a W and Z boson, tWZ. While the dilepton final state of tWZ will be indistinguishable from the signal process, the tWZ cross section is an order of magnitude smaller than the tZq cross section. Thus, this process, which also probes the top-W/Z couplings, will only contribute a very small number of events.

6.7.3 Multi-boson backgrounds

Multiple vector bosons produced through electroweak production form the remainder of the background processes considered.

Diboson processes involving the presence of a leptonically decaying Z boson and either a W or Z boson decaying hadronically with additional jets from gluon splitting were found to be the predominant source of background from these processes. Smaller contributions from the other diboson final states are expected when multiple W bosons decay hadronically and/or jets are misreconstructed as leptons. The tribosonic backgrounds form small contributions to the background due to their small production cross sections.

Chapter 7

Background Estimation

7.1 Data and Simulation Samples

Out of the $37.8\,\text{fb}^{-1}$ of proton-proton collision data at $\sqrt{s} = 13\,\text{TeV}$ collected by the CMS experiment during 2016, $35.9\,\text{fb}^{-1}$ was certified by the collaboration as being of sufficient quality to be used for physics analysis. The difference between the certified value and the total data recorded is the result of various factors such as the unavailability of a detector due to power failures. Events were considered from the dataset certified to be good for physics if they pass one of the triggers in accordance with the trigger strategy described in Section 6.4. Due to the prescaling of all of the electron triggers considered during the start of the most luminous data taking runs (as discussed in Section 6.4) the ee channel uses a reduced dataset corresponding to $35.6\,\text{fb}^{-1}$ where none of the triggers considered were prescaled.

The MC samples used to model both the model signal and background processes considered here are listed in Table 7.1. For each of the processes considered, the table includes information on the number of events generated, the cross section used in their generation and the order in perturbative accuracy in QCD to which the generators calculated the processes. The PS and hadronisation stages for all of the samples was performed using PYTHIA 8. The CUETP8M2T4 underlying event tune was used by PYTHIA 8 for the $t\bar{t}$ process simulation samples and the CUETP8M1 underlying event tune for all other simulation samples [169]. The NNPDF3.0 family of PDF sets [170] was used in the generation of all of the samples considered.

To determine the impact of a variety of different theoretical uncertainties for several of the processes defined in Table 7.1, dedicated MC samples were used, which are listed in Table 7.2. The entries labelled "scale", "matching", "ISR" and "FSR" correspond to the variations of the theoretical uncertainties considered in this analysis. These theoretical uncertainties are discussed further in Section 7.5.2.

Table 7.1: The MC processes and their associated sample sizes, cross sections and generators used. Two generators were considered for the simulation of the Z+jets process; both samples are included in the table.

MC process	**Events**	**Cross section (pb)**	**Generator (Order)**
tZq	14.5M	0.0758	MADGRAPH5_aMC@NLO 2.2.2 (NLO)
tHq	3.5M	0.07462	MADGRAPH5_aMC@NLO 2.2.2 (LO)
tWZ/tWll	50K	0.01104	MADGRAPH5_aMC@NLO 2.2.2 (LO)
single top tW production (t)	7M	35.85	POWHEG V1 (NLO)
single top tW production ($\bar{t}$)	6.9M	35.85	POWHEG V1 (NLO)
single top s-channel	2.9M	10.32	MADGRAPH5_aMC@NLO 2.2.2 (NLO)
single top t-channel (t)	67.2M	136.02	POWHEG V2 (NLO)
single top t-channel ($\bar{t}$)	38.8M	80.95	POWHEG V2 (NLO)
$t\bar{t}$	77.1M	831.76	POWHEG V2 (NLO)
$t\bar{t}Z \rightarrow ll\nu\nu$	13.9M	0.2529	MADGRAPH5_aMC@NLO 2.2.2 (NLO)
$t\bar{t}Z \rightarrow qq$	749K	0.5297	MADGRAPH5_aMC@NLO 2.2.2 (NLO)
$t\bar{t}W \rightarrow l\nu$	5.3M	0.2001	MADGRAPH5_aMC@NLO 2.2.2 (NLO)
$t\bar{t}W \rightarrow qq$	833K	0.405	MADGRAPH5_aMC@NLO 2.2.2 (NLO)
$t\bar{t}H \rightarrow bb$	3.8M	0.2942	POWHEG V2 (NLO)
$\rightarrow$ non bb	4.0M	0.2123	POWHEG V2 (NLO)
W+jets	24.1M	61526.7	aMC@NLO (NLO)
Z+jets ($m_Z \geq 50\,\text{GeV}$)	146M	5765.4	MADGRAPH5_aMC@NLO 2.2.2 (LO)
Z+jets ($10\,\text{GeV} \leq m_Z < 50\,\text{GeV}$)	35.3M	18610.0	MADGRAPH5_aMC@NLO 2.2.2 (LO)
Z+jets ($m_Z \geq 50\,\text{GeV}$)	151M	5765.4	MADGRAPH5_aMC@NLO 2.2.2 (NLO)
Z+jets ($10\,\text{GeV} \leq m_Z < 50\,\text{GeV}$)	106M	18610.0	MADGRAPH5_aMC@NLO 2.2.2 (NLO)
WW $\rightarrow l\nu qq$	9.0M	49.997	POWHEG V2 (NLO)
$\rightarrow ll nu\nu$	2.0M	12.178	POWHEG V2 (NLO)
WZ $\rightarrow l\nu qq$	24.2M	10.73	MADGRAPH5_aMC@NLO 2.2.2 (NLO)
$\rightarrow llqq$	26.5M	5.606	MADGRAPH5_aMC@NLO 2.2.2 (NLO)
$\rightarrow lll\nu$	1.9M	5.26	MADGRAPH5_aMC@NLO 2.2.2 (NLO)
ZZ $\rightarrow ll\nu\nu$	8.8M	0.5644	POWHEG V2 (NLO)
$\rightarrow llqq$	15.3M	3.222	MADGRAPH5_aMC@NLO 2.2.2 (NLO)
$\rightarrow llll$	10.7M	1.204	MADGRAPH5_aMC@NLO 2.2.2 (NLO)
WWW	240K	0.2086	MADGRAPH5_aMC@NLO 2.2.2 (NLO)
WWZ	250K	0.1651	MADGRAPH5_aMC@NLO 2.2.2 (NLO)
WZZ	247K	0.05565	MADGRAPH5_aMC@NLO 2.2.2 (NLO)
ZZZ	249K	0.01398	MADGRAPH5_aMC@NLO 2.2.2 (NLO)

Table 7.2: The dedicated MC samples used to estimate some theoretical uncertainties. The table includes the associated size of the samples, cross sections and generators used.

MC process	**Events**	**Cross section (pb)**	**Generator (Order)**
tZq scale up	6.9M	0.0758	aMC@NLO (NLO)
tZq scale down	7.0M	0.0758	aMC@NLO (NLO)
single top tW production (t) scale up	998K	35.85	POWHEG V2(NLO)
single top tW production (t) scale down	994K	35.85	POWHEG V2 (NLO)
single top tW production ($\bar{t}$) scale down	1.0M	35.85	POWHEG V2 (NLO)
single top tW production ($\bar{t}$) scale down	999K	35.85	POWHEG V2 (NLO)
single top t-channel (t) scale up	5.7M	136.02	POWHEG V2 (NLO)
single top t-channel (t) scale down	5.9M	136.02	POWHEG V2 (NLO)
single top t-channel (t) matching up	6.0M	136.02	POWHEG V2 (NLO)
single top t-channel (t) matching down	6.0M	136.02	POWHEG V2 (NLO)
single top t-channel ($\bar{t}$) scale up	4.0M	80.95	POWHEG V2 (NLO)
single top t-channel ($\bar{t}$) scale down	3.9M	80.95	POWHEG V2 (NLO)
single top t-channel ($\bar{t}$) matching up	4.0M	80.95	POWHEG V2 (NLO)
single top t-channel ($\bar{t}$) matching down	4.0M	80.95	POWHEG V2 (NLO)
$t\bar{t}$ ISR up	156.5M	831.76	POWHEG V2 (NLO)
$t\bar{t}$ ISR down	149.8M	831.76	POWHEG V2 (NLO)
$t\bar{t}$ FSR up	152.6M	831.76	POWHEG V2 (NLO)
$t\bar{t}$ FSR down	156.0M	831.76	POWHEG V2 (NLO)
$t\bar{t}$ matching up	58.9M	831.76	POWHEG V2 (NLO)
$t\bar{t}$ matching down	58.2M	831.76	POWHEG V2 (NLO)

7.2 Simulation Corrections

As simulation is unable to fully recreate all the effects observed in data, corrective scale factors are used to reweight MC samples on a per event basis to account for mismodelled variables.

These scale factors were used to correct simulation for any modelling discrepancies in the lepton identification, isolation and reconstruction efficiencies, lepton and jet energy scales and resolutions, b-tagging efficiencies, the poor modelling of pileup in simulation, and the resolutions of the detectors.

7.2.1 Miscalibrated Tracker APV Chips

During the first half of data taking in 2016 the silicon strip detector suffered from an instantaneous-luminosity-dependent hit finding inefficiency. This particularly affected high occupancy regions, due to saturation in the pre-amplifier in the front-end electronics [171], and was resolved by changing the configuration of the electronics. The 55% of the total 2016 dataset that was affected by this issue has since been reprocessed by CMS in order to mitigate the impact on the quality of the data taken.

Despite this mitigation however, there was still a negative impact on the reconstructing tracks efficiency for physics objects that rely upon tracking data. This reduced detector efficiency was accounted for by using the weighted average of the scale factors that have been derived separately for both the affected and unaffected portions of the dataset.

7.2.2 Lepton Efficiency

The identification, isolation and reconstruction efficiency scale factors for leptons were produced centrally by CMS and were determined by using a large sample of of $Z \to l^+l^-$ events and the so-called *tag-and-probe* method [172]. From a high-purity sub-sample of these events, where the dilepton invariant mass lies within the window $60 < m_{ll} < 120\,\text{GeV}$, the lepton that passes a tight selection criteria is "tagged" and other lepton is "probed" against a loose selection criteria. For each type and lepton flavour, the efficiency is the fraction of events where the probe leptons passed the selection criteria under study. The corrective scale factors determined from these efficiencies were used to reweight events as functions of their leptons' p_T, η, and flavour.

As shown in Figure 7.1, the efficiency of the electron cut-based identification's tight working point for 13 TeV proton-proton collisions in 2016 varies between $24-90\%$, with the identification efficiency being greatest in the EB and decreasing as p_T decreases. Data and simulation were found to agree within 5.5% for $\eta < 1.444$ and within 20% for $1.566 < \eta < 2.500$.

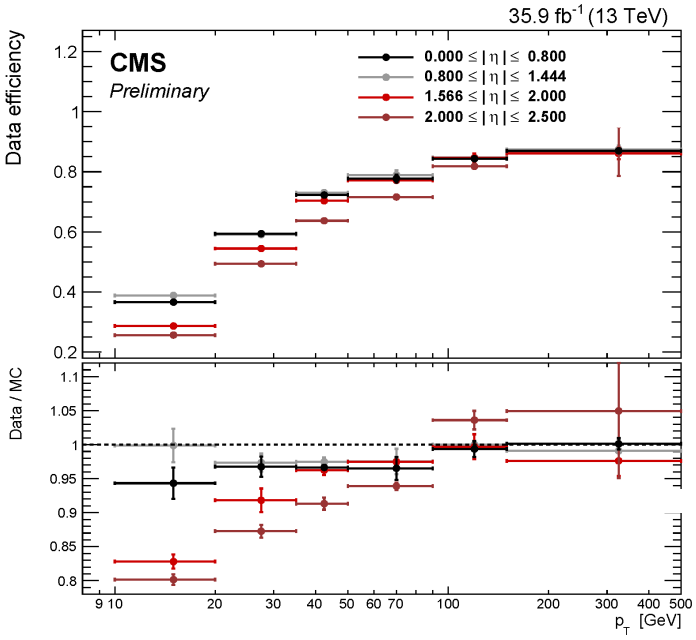

Figure 7.1: The electron cut-based identification's tight working point's efficiency for 13 TeV proton-proton collisions in 2016 (top) and data to simulation efficiency ratios (bottom). The efficiency measured is shown in five η ranges as a function of p_{T} [155].

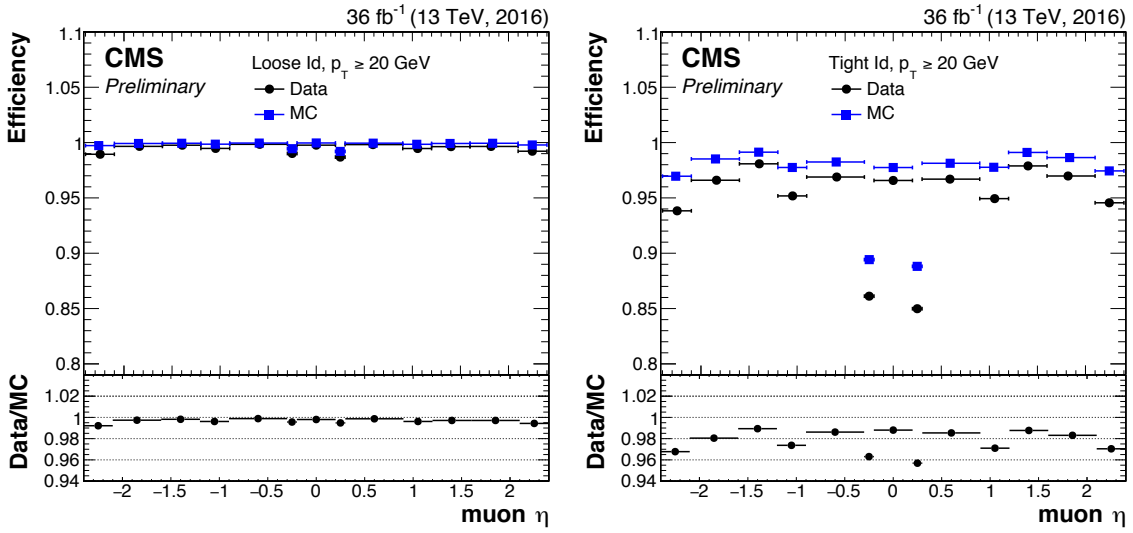

Figure 7.2: The muon loose (left) and tight (right) identification working points' efficiencies for 13 TeV proton-proton collisions in 2016 and simulation (top) and data to simulation efficiency ratios (bottom) measured as a function of η [173].

The efficiency of the loose and tight identification working points for muons are shown Figure 7.2 [173]. The loose identification working point's efficiency in 2016 data was measured to be greater than 98% across all η and data and simulation agree to within 1%. The tight

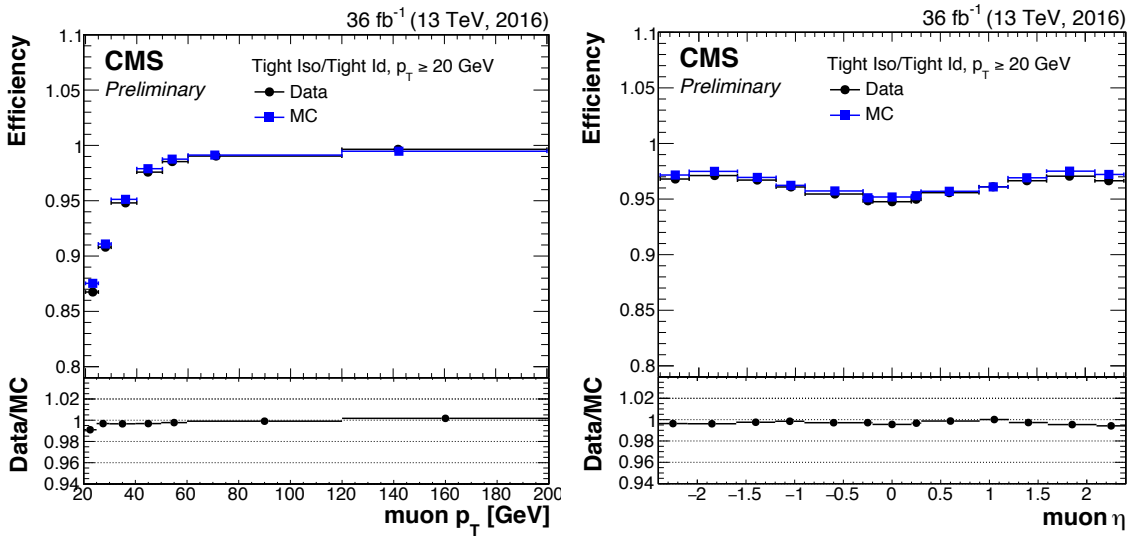

Figure 7.3: The muon tight isolation efficiency for the tight identification working point for 13 TeV proton-proton collisions in 2016 and simulation (top) and data to simulation efficiency ratios (bottom) measured as a function of p_{T} (left) and η (right) [173].

identification working point's efficiency varies between $94-98\%$, except for two drops to 85% due to the space between the wheels of the DT system, and data and simulation were found to agree to within $1-5\%$.

Figure 7.3 shows the tight isolation efficiency for muons with $p_{\mathrm{T}} > 20\,\mathrm{GeV}$ that have passed the tight identification criteria [173]. While a decline in tight isolation efficiency was observed for low p_{T} muons, the overall efficiency for all muons with $p_{\mathrm{T}} > 20\,\mathrm{GeV}$ across all η was measured to be greater than 95% and the agreement between data and simulation was found to be better than 1%.

The efficiencies of the triggers used in the analysis were determined using the *cross-trigger* method that were used in the measurement of the $t\bar{t}$ production cross section using the $e\mu$ final state by the CMS collaboration [174]. The implementation of this methodology was validated by reproducing the $t\bar{t}$ analysis's trigger efficiencies, their statistical uncertainties and the correlation between the $E_{\mathrm{T}}^{\mathrm{miss}}$ and lepton trigger selection requirements.

The cross-trigger methodology determines the trigger efficiencies by using events that pass other trigger combinations that are weakly correlated with those used in the analysis, known as *cross-triggers* (X triggers). The trigger efficiency is estimated as follows:

$$\epsilon_{trigger} = \frac{N_{Xtriggers+leptontriggers}}{N_{Xtriggers}} \tag{7.1}$$

where $N_{Xtriggers}$ is the number of events that have passed the analysis' lepton selection criteria and the cross-triggers, and $N_{Xtriggers+leptontriggers}$ is $N_{Xtrigger}$ and the number of

events that additionally passed at least one of the lepton triggers for the relevant lepton flavour.

As the trigger requirements were applied to both simulated and data events, scale factors of the ratio of the trigger efficiency in data and in simulation were calculated and used to weight the simulation to account for any modelling discrepancies.

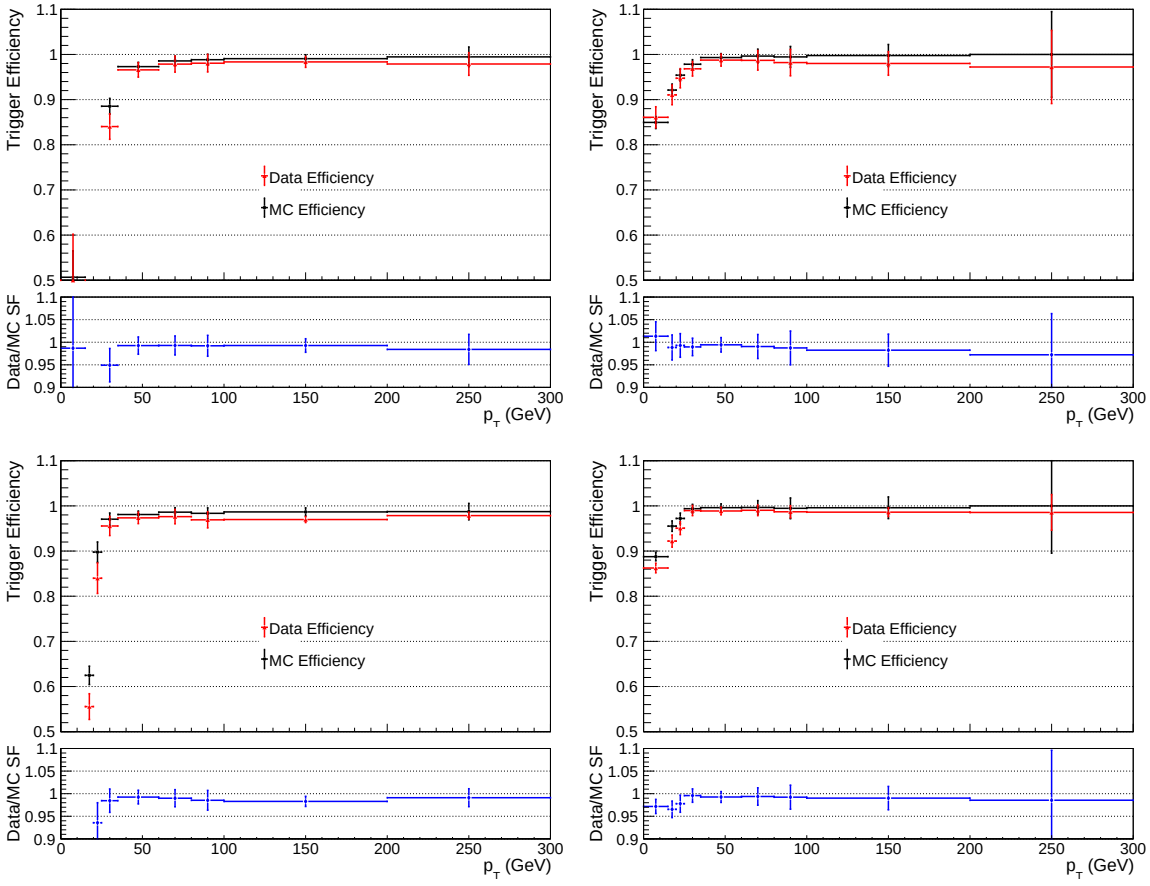

Figure 7.4: The data and $t\bar{t}$ simulation efficiencies and scale factors for the ee (top) and $\mu\mu$ final states as determined for the OR of the respective dilepton and single lepton triggers considered as a function of the leading and sub-leading leptons' p_{T}. Above the minimum lepton selection p_{T} requirements, the trigger efficiencies are highly efficient and good agreement is observed between data and simulation.

Using data and simulated $t\bar{t}$ events, the trigger efficiencies were initially determined as functions of each of the selected leptons' p_{T} and η. It was found that the triggers were highly efficient for leptons exceeding their respective minimum lepton p_{T} selection requirements and that simulation well described the trigger efficiencies observed in data across all η and above the minimum lepton selection p_{T}, with their differences covered by their statistical uncertainties. These high trigger efficiencies and the good description of them by simulation, as a function of the leptons' p_{T}, is illustrated in Figure 7.4 for the ee and $\mu\mu$ final states.

The trigger efficiencies in simulation and data as a function of the leptons' p_{T} and η for the ee, $\mu\mu$ and $e\mu$ final states are provided in Appendix C.1.

Given that simulation well described the trigger efficiencies observed in data across all η and for the lepton p_{T} selection requirements, a constant scale factor for each final state was determined to be sufficient to account for the differences in the trigger efficiency between data and simulation. The resultant trigger efficiency scale factors for each final state are given in Table 7.3 with their associated statistical uncertainties. The systematic uncertainties associated with these trigger scale factors are discussed in Section 7.5.

Table 7.3: The trigger efficiencies for the lepton selection criteria for data and simulation and the resultant corrective scale factors applied to simulation. The uncertainties given only include the statistical uncertainty associated with each value. The determination of the systematic uncertainties is given in Section 7.5.

Channel	ϵ_{data}	ϵ_{MC}	**Scale Factor**
ee	0.976 ± 0.001	0.988 ± 0.001	0.987 ± 0.001
$\mu\mu$	0.985 ± 0.001	0.992 ± 0.001	0.993 ± 0.000
$e\mu$	0.964 ± 0.011	0.977 ± 0.005	0.987 ± 0.007

7.2.3 Lepton Energy Corrections

7.2.3.1 Electron Regression and Energy Scale and Smearing Corrections

Energy regression and energy scale and smearing corrections that have been produced by the CMS Electron Gamma (EGM) Physics Object Group were applied to the reconstructed electrons. The energy regression uses detector information to correct the electron energy recorded in order to obtain the best possible resolution of the reconstructed particle. The energy scale and smearing corrections were used to correct the energy scale and resolution in simulation.

7.2.3.2 Rochester Corrections

The muon momentum scale and resolution correction methods developed by the University of Rochester [175], known as *Rochester Corrections*, were used to remove any muon momentum bias arising from any possible detector misalignment and any error in the measurement of the magnetic field for both MC and data. These corrections were derived using a sample of high $p_{\mathrm{T}} > 20\,\mathrm{GeV}$ muons from $\mathrm{Z} \to \mu^{+}\mu^{-}$ decays using a two-step method. The first of the two steps determines a correction factor that is defined as the difference in the mean inverse transverse momenta of the muons from a perfectly aligned simulation and reconstructed data or simulation. These corrections were tuned in the second step using the $M_{\mu}M_{\mu\prime}$ peak

for a perfectly aligned detector to calibrate the corrections. This removes any dependence on detector efficiency or physics modelling.

The Rochester Corrections were applied to each muon as an event weight that is a function of the muon's charge, p_{T}, η and ϕ.

7.2.4 Jet Energy Corrections

As described in Section 5.2.7.1, the Jet Energy Corrections were applied to account for the non-uniform response in p_{T} and η of the detector by comparing the differences between the generator level and detector level responses in simulation and any residual differences between simulation and data.

In addition to these corrections, as the Jet Energy Resolution (JER) observed in data is approximately 10% poorer than that observed in simulation, the 4-vectors of simulated jets were smeared as functions of generator level and reconstructed p_{T} and η to account for this [158].

7.2.5 b-tagging Efficiency

The CMS B-Tag and Vertexing (BTV) Physics Object Group measures the b-tagging efficiency and misidentification rates for b- and light-flavoured jets in data and MC simulation considering both multijet and $t\bar{t}$ processes for the algorithms that they support [162]. From these measurements b-tagging efficiency scale factors were produced and provided for analysts to apply to simulated events to correct for differences observed between data and simulation. These scale factors, as functions of the jet flavour, p_{T} and η, were used to alter the weight of the MC events. This methodology was chosen as it involves only changing the weight of the selected MC events which, unlike other methods, avoids events migrating into different b-tag multiplicity bins and having events with potentially undefined variables such as the top mass (i.e. the top mass cannot be defined in an event with zero b-tagged jets).

7.2.6 PU Modelling

It is challenging to model variations in the number of PU interactions that result from the changing LHC conditions. To achieve this, MC events were reweighted as a function of the number of primary vertices so that the simulated PU distributions resemble those observed in data.

The PU SF is determined as a function of the number of primary vertices, n_{PV}, by comparing the n_{PV} distribution in minimum bias data over the running period considered to the corresponding n_{PV} distribution in simulated events.

7.2.7 Top quark p_{T}

A scale factor is used to reweight all simulated $t\bar{t}$ events to account for the differences in the top quark p_{T} distribution observed between data and both LO and NLO simulation [176].

7.3 Signal Region Background Estimation

Good agreement between simulation and data is observed in the signal region at each stage of applying selection criteria and simulation corrections, as shown in Figure 7.5. The final event yields for each process considered for the ee and $\mu\mu$ channels and their combination is given in Table 7.4.

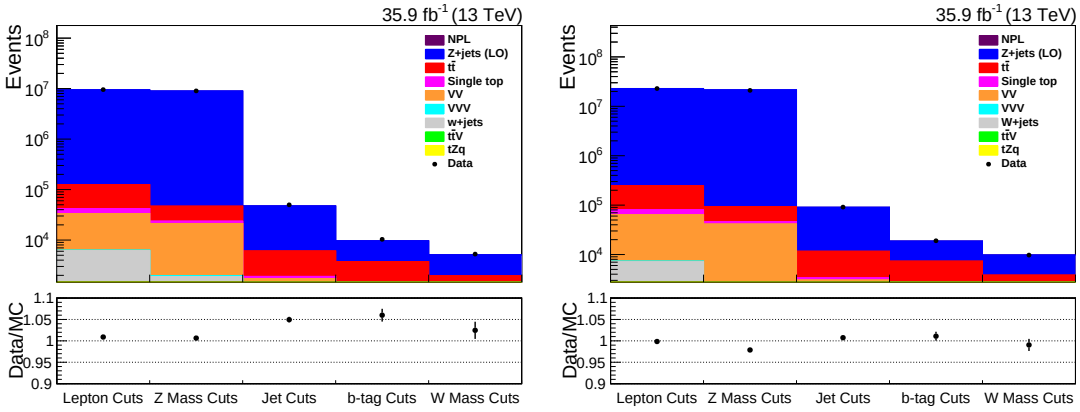

Figure 7.5: The overall event yield for data and simulation at each stage of applying the signal region selection criteria and simulation corrections for the ee channel (left) and the $\mu\mu$ channel (right).

In Figure 7.5 it can be seen that the jet cleaning and tight isolation criteria for leptons has significantly reduced the contributions from processes lacking a leptonic Z boson decay, completely removing the W+jets process. The remaining backgrounds in the signal region consist of processes that involve the decay of a real Z boson into two leptons or the leptonic decay of two W bosons where the resultant two leptons are consistent with a Z boson decay. The two dominant background processes are Z+jets and $t\bar{t}$, with the single top tW-channel, t$\bar{\mathrm{t}}$Z, WZ and ZZ processes contributing a similar order of events as tZq processes. The remaining single top (tHq, tWZ, s-channel, t-channel), t$\bar{\mathrm{t}}$W, t$\bar{\mathrm{t}}$H, WW and triboson backgrounds produce contributions smaller than the signal process.

Good agreement between simulation and data is also observed for the reconstructed variables. Examples of such good agreement include the distributions of the reconstructed Z boson mass following the lepton selection cuts in Figure 7.6; the invariant p_{T} of all the jets in an event following the jet selection criteria in Figure 7.7; and the reconstructed W boson

Table 7.4: The number of observed events in data, expected events in simulation and data and the data-driven estimate of the non-prompt leptons (NPLs) in the signal region following the full event selection. The number of observed events is given for each of the separate channels and their combination. The statistical uncertainties for each simulated process is given and the LO Z+jets sample is used for the Z+jets contribution.

Process	ee	$\mu\mu$	**Combined**
tZq	30.38 ± 0.07	55.49 ± 0.10	85.87 ± 0.12
tWZ	6.44 ± 0.21	10.96 ± 0.29	17.40 ± 0.36
tHq	0.17 ± 0.01	0.37 ± 0.02	0.54 ± 0.02
ttW	7.38 ± 0.14	10.83 ± 0.15	18.21 ± 0.21
ttZ	62.23 ± 0.21	111.98 ± 0.29	174.21 ± 0.36
ttH	4.94 ± 0.10	9.73 ± 0.14	14.67 ± 0.17
$t\bar{t}$	1658.73 ± 23.77	3277.48 ± 34.22	4936.21 ± 41.67
tW	55.98 ± 3.02	109.59 ± 4.33	165.57 ± 5.28
s-channel	0.0 ± 0.0	0.19 ± 0.19	0.19 ± 0.19
t-channel	0.61 ± 0.19	1.12 ± 0.25	1.73 ± 0.31
WW	1.34 ± 0.47	2.29 ± 0.69	3.63 ± 0.83
WZ	72.88 ± 0.67	127.32 ± 0.89	200.20 ± 1.11
ZZ	51.80 ± 0.50	94.64 ± 0.68	146.44 ± 0.84
WWW	0.11 ± 0.06	0.27 ± 0.10	0.38 ± 0.12
WWZ	1.32 ± 0.17	2.20 ± 0.22	3.32 ± 0.28
WZZ	1.53 ± 0.11	2.62 ± 0.14	4.15 ± 0.18
ZZZ	0.65 ± 0.04	1.12 ± 0.05	1.77 ± 0.06
W+jets	0.0 ± 0.0	0.0 ± 0.0	0.0 ± 0.0
Z+jets	3280.20 ± 62.63	5877.51 ± 87.79	9157.71 ± 107.84
NPLs	69.47 ± 0.76	114.01 ± 1.25	183.48 ± 2.01
Total MC	5236.69 ± 67.07	9695.71 ± 94.33	14 932.40 ± 115.74
Total MC + NPLs	5306.16 ± 67.07	9754.23 ± 94.34	15 060.39 ± 115.75
Data	5274.0	9750.0	15024.0

following application of the b-tagging criteria in Figure 7.8. A larger selection of data and simulation comparison plots for both the ee and $\mu\mu$ channels is provided in Appendix B.1.

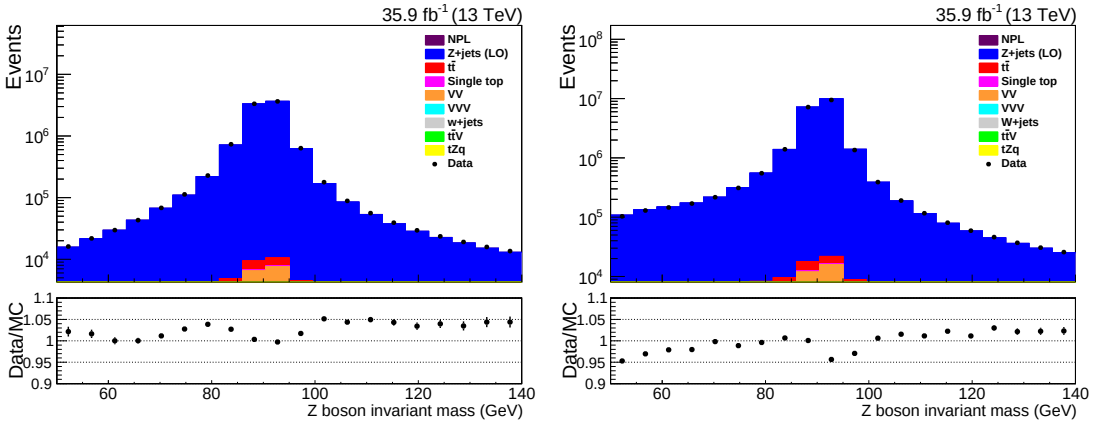

Figure 7.6: The distributions of the reconstructed Z boson mass for the ee and $\mu\mu$ channels, left and right respectively, following the application of only the lepton selection criteria and corrections.

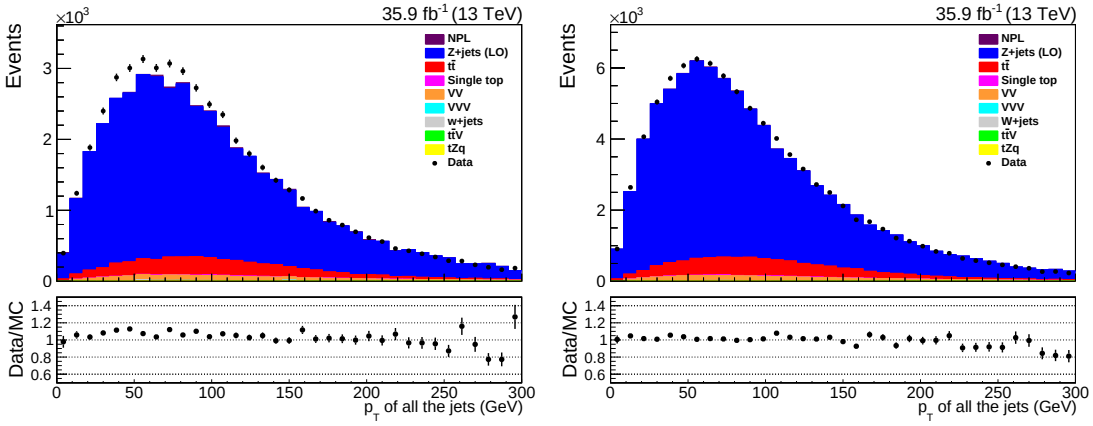

Figure 7.7: The distributions of the invariant p_{T} of all the jets in an event for the ee and $\mu\mu$ channels, left and right respectively, following the application of the jet selection criteria and corrections.

7.4 Data-driven Background Estimation

7.4.1 Non-Prompt Leptons

Leptons that are produced from events where at least one jet is incorrectly reconstructed as a lepton (predominately electrons) or a lepton from the decay of heavy quarks (predominately muons) are known as *non-prompt leptons* (NPLs). The majority of these events are produced by semi-leptonic $t\bar{t}$ decays, and W+jets production, with smaller contributions from QCD

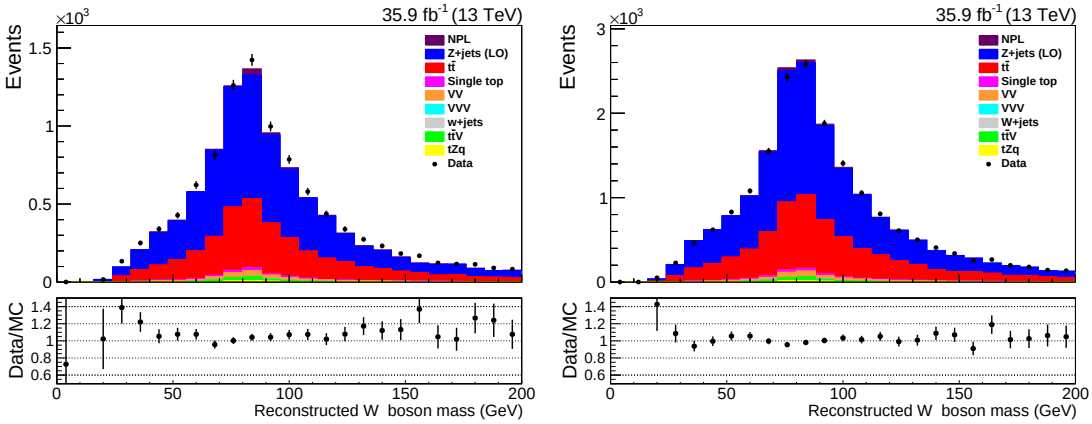

Figure 7.8: The distributions of the reconstructed W boson mass for the ee and $\mu\mu$ channels, left and right respectively, following the application of all the event selection criteria and selections except the W boson mass cut.

and single top production. As it is difficult to accurately model QCD processes the NPL contribution is estimated with data.

This data-driven estimate is based on the methodology used in top quark pair production [177] and same sign SUSY searches [178]. This approach takes advantage of the fact that the vast majority of events containing same sign lepton pairs result from non-prompt and charge misidentified leptons, with some contributions from prompt leptons (such as $t\bar{t}V$). As these backgrounds are independent of the charge of the lepton pairs, it is expected that the nominal opposite sign event selection would have a contribution with a similar magnitude.

Thus, by inverting the signal region's opposite sign lepton pair requirement (i.e. by requiring the leptons to have the same, not opposite, sign), a same sign control region can be defined that is dominated by NPL events while containing a small admixture of from prompt lepton events, charge misidentification and real same sign lepton pairs.

Using this control region, a data-driven estimate of the contribution of opposite sign NPLs can be derived as follows:

$$N_{data}^{OSnon-prompt} = (N_{data}^{SS} - N_{real+mis-ID}^{SS}) \cdot \frac{N_{MC}^{OSnon-prompt}}{N_{MC}^{SSnon-prompt}} \tag{7.2}$$

where N_{data}^{SS} is the total number of same sign events observed in data and $N_{real+mis-ID}^{SS}$ is the expected number of real same sign events and events with charge misidentification.

The ratio of opposite sign and same sign NPLs in simulation, $N_{MC}^{OSnon-prompt}$ and $N_{MC}^{SSnon-prompt}$, respectively, is used to appropriately normalise this estimate and uses the generator level information in simulation to correctly identify how the leptons were produced. The $t\bar{t}Z$, $t\bar{t}W$, and single top simulated samples that have sufficient statistics in the same sign control

region were used to calculate this ratio as these simulation indicates that these processes are the predominant source of non-prompt leptons for this analysis.

The event yields of the simulated samples and data following the full event selection in the same lepton sign control region, the same sign background contributions not accounted for by simulation, ratio of same sign to opposite sign event yields and the data-driven NPL contribution estimate are given in Table 7.5.

Table 7.5: The event yields following the full event selection ratio of same to opposite sign lepton events, the same sign background contributions not accounted for by simulation, ratio of same sign to opposite sign event yields and the estimated non-prompt lepton contribution following all selection cuts.

Source	ee	$\mu\mu$
$N_{t\bar{t}}^{SS}$	5.85 ± 0.30	8.93 ± 1.47
$N_{t\bar{t}V}^{SS}$	4.81 ± 0.11	11.81 ± 0.10
$N_{\text{single top}}^{SS}$	0.90 ± 0.18	0.97 ± 0.11
N_{Z+jets}^{SS}	37.53 ± 6.85	0.0 ± 0.0
N_{VV}^{SS}	1.89 ± 0.22	0.35 ± 0.13
N_{VVV}^{SS}	0.0 ± 0.0	0.23 ± 0.09
N_{MC}^{SS} background	50.98 ± 6.98	22.29 ± 2.21
N_{data}^{SS}	126.0 ± 11.22	125.0 ± 1.18
$N_{\text{data}}^{SS} - N_{MC}^{SS}$	30.64 ± 13.21	102.71 ± 6.27
$N_{MC}^{OS\text{ non-prompt}}$	1.58 ± 0.03	2.38 ± 0.04
$N_{MC}^{SS\text{ non-prompt}}$	1.71 ± 0.03	2.14 ± 0.04
$N_{MC}^{OS\text{ non-prompt}}/N_{MC}^{SS\text{ non-prompt}}$	0.93 ± 0.02	1.11 ± 0.03
$N_{\text{data}}^{OS\text{ non-prompt}}$	69.47 ± 12.95	114.01 ± 7.61

7.4.2 Z+jets Background

In Section 6.2.1 two Z+jets enriched control regions were defined to produce orthogonal regions that were topologically similar to the signal region to validate the modelling of the simulated Z+jets samples. These control regions differed from the signal region by either requiring zero b-tagged jets in the event (0-bjet) or an inverted W boson mass threshold and less than 50 GeV of $E_{\text{T}}^{\text{miss}}$ is present in an event (m_W^{inv}).

Two different simulated samples were considered for modelling the Z+jets processes: one generated at LO and the other at NLO. Given that the final state of the signal process contains multiple jets, it would be preferable to use the NLO description of this large multi-jet background. Both of these samples are listed in Table 7.1.

The final event yields for the 0-bjet region are given in Table 7.6 and the corresponding

yields for the m_W^{inv} region are given in Table 7.7. It was observed that 94% of the simulated events in the 0-bjet region were produced by Z+jets processes compared to 82% in the m_W^{inv} region. Consequently, it was decided to use the 0-bjet region to validate the modelling of the Z+jets processes.

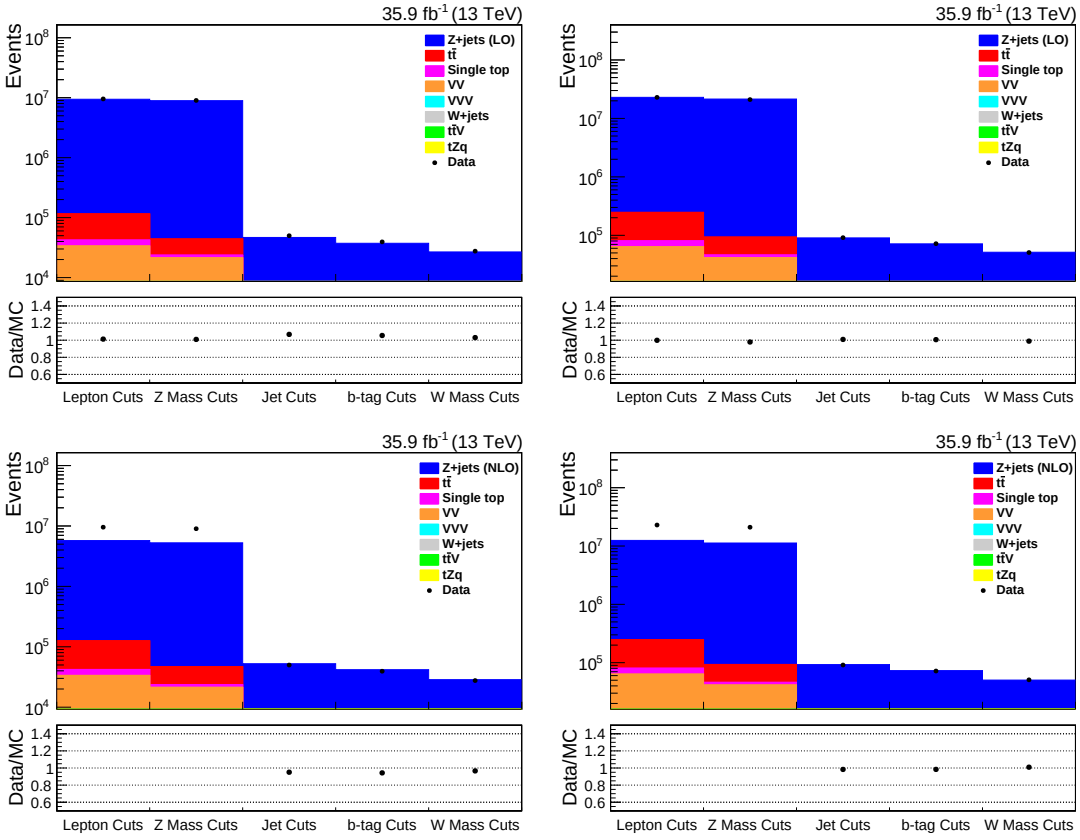

Figure 7.9: The overall event yield for data and simulation at each stage of applying the 0-bjet region selection criteria and simulation corrections for when the LO (top) and NLO (bottom) simulation samples are used to model the Z+jets processes. The event yields for the ee channel and the $\mu\mu$ channel are shown on the left and right, respectively.

Based on the final event yields in both control regions, as given in Tables 7.6-7.7, it was observed that the NLO Z+jets sample did not correctly describe the normalisation of the Z+jets process. Further studies into the NLO Z+jets sample were done using a simple scale factor based on the final event yields to correctly normalise this Z+jets sample.

During these studies it was found that the NLO Z+jets normalisation scale factor only resolves the incorrect normalisation of this process following the application of the jet selection criteria, as shown in Figure 7.9. In contrast consistently good agreement is observed at all stages of applying the 0-bjet region selection criteria when the LO Z+jets sample is used.

As illustrated in Figure 7.10, the disagreement that is observed between simulation and data when using the NLO Z+jets sample is the result of the NLO sample incorrectly describing

low jet multiplicities. The LO Z+jets sample however, correctly describes jet multiplicities throughout the application of the 0-bjet region selection criteria selection criteria. Data and simulation comparison plots for other distributions in the 0+bjet Z+jets enriched control region are provided in Appendix B.3.

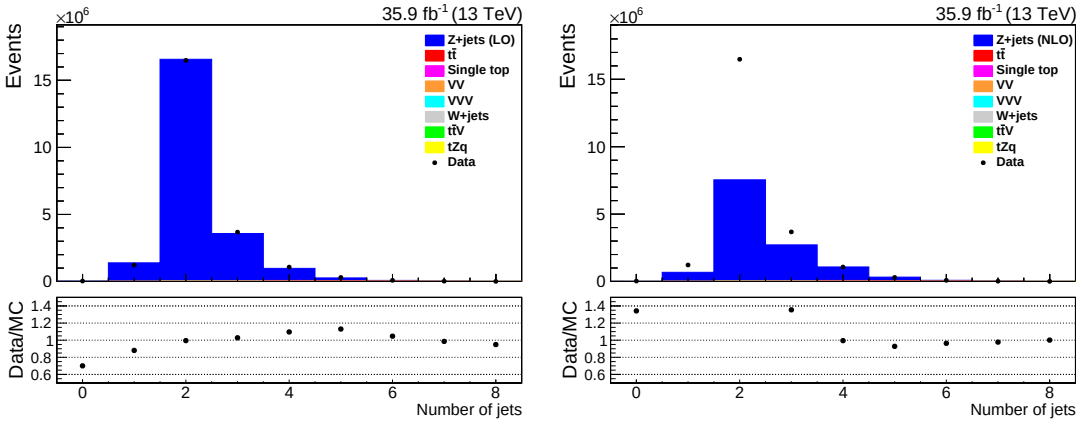

Figure 7.10: The distributions of the number of jets in the 0-bjet region following the lepton selection criteria and associated simulation corrections for the LO (left) and NLO (right) Z+jets samples in the $\mu\mu$ channel.

Consequently, it was decided to use the LO Z+jets sample to model Z+jets processes despite the NLO sample providing a better description of the p_{T} of the higher order jets (as shown in Figure 7.11). The reasons why the NLO Z+jets sample does not correctly normalise and poorly describes events with low jet multiplicities will need to be understood before it can be considered in the future.

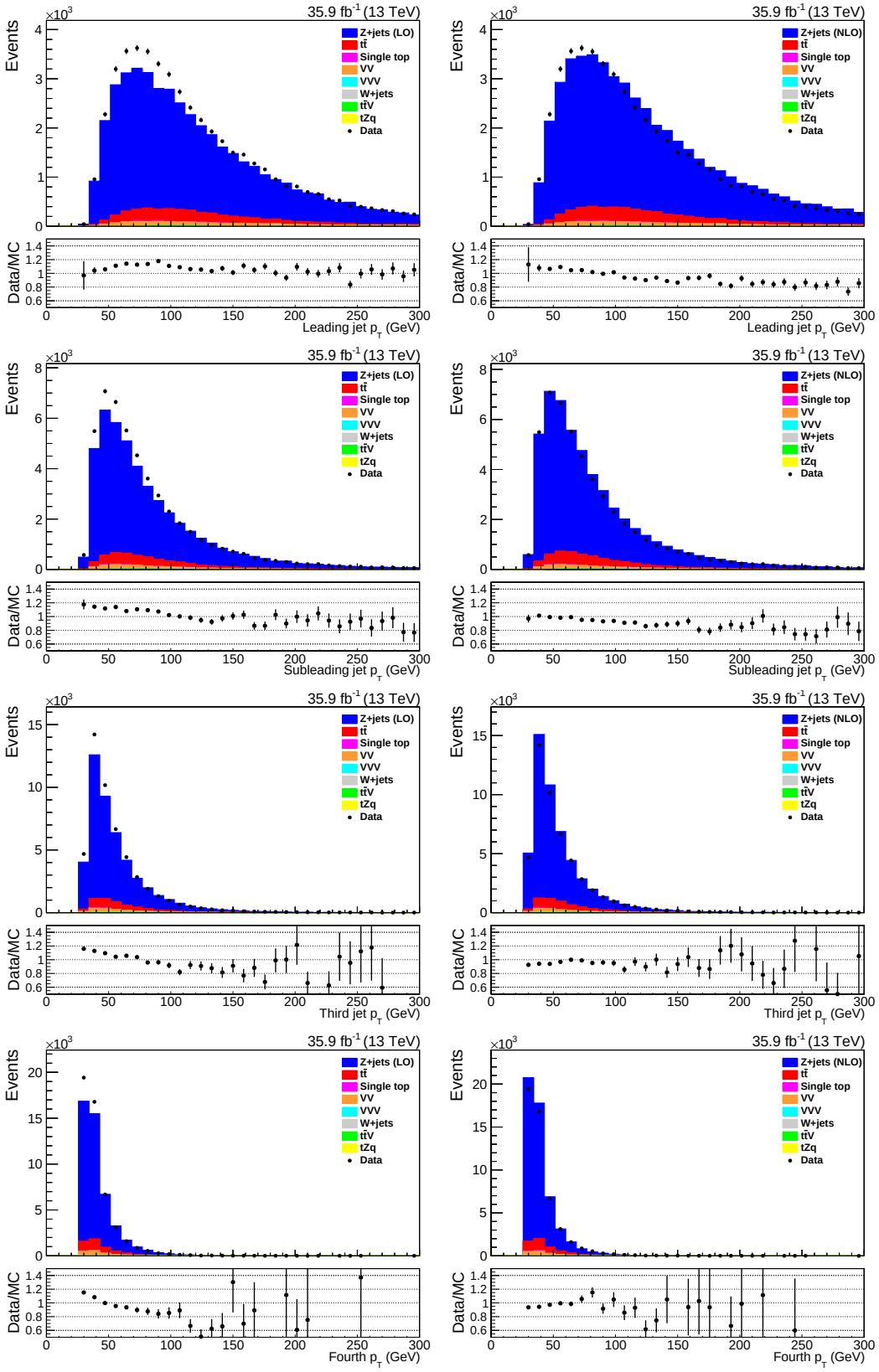

Figure 7.11: The distributions of the leading four jets p_{T} in the 0-bjet region following the application of the jet selection criteria and simulation corrections for the LO (left) and NLO (right) Z+jets samples in the *ee* channel.

Table 7.6: The number of observed events in data and the number of expected events from simulation (and their statistical uncertainties) for the 0-bjet Z+jets control region following the application of the full event selection and simulation corrections. The number of observed events is given for each of the separate channels and their combination.

Process	***ee***	***μμ***	**Combined**
tZq	20.96 ± 0.06	38.47 ± 0.08	59.43 ± 0.10
tWZ	4.38 ± 0.18	7.17 ± 0.24	11.55 ± 0.30
tHq	0.10 ± 0.01	0.17 ± 0.01	0.27 ± 0.01
ttW	2.26 ± 0.07	4.90 ± 0.12	7.16 ± 0.14
ttZ	26.05 ± 0.14	43.92 ± 0.18	69.97 ± 0.23
ttH	1.29 ± 0.05	2.36 ± 0.07	3.65 ± 0.09
$t\bar{t}$	568.32 ± 14.67	1182.74 ± 21.78	1751.06 ± 26.26
tW	30.09 ± 2.31	56.88 ± 3.22	86.97 ± 3.96
s-channel	0.0 ± 0.0	0.0 ± 0.0	0.0 ± 0.0
t-channel	0.21 ± 0.12	1.48 ± 0.32	1.69 ± 0.34
WW	14.92 ± 1.69	29.21 ± 2.43	44.13 ± 2.96
WZ	733.13 ± 2.12	1282.83 ± 2.85	2015.96 ± 3.55
ZZ	246.36 ± 1.07	444.69 ± 1.48	691.05 ± 1.83
WWW	0.69 ± 0.15	1.65 ± 0.23	2.34 ± 0.27
WWZ	10.08 ± 0.47	17.17 ± 0.63	27.25 ± 0.79
WZZ	6.19 ± 0.22	9.96 ± 0.28	16.15 ± 0.36
ZZZ	1.65 ± 0.05	2.84 ± 0.07	4.49 ± 0.09
W+jets	0.0 ± 0.0	0.0 ± 0.0	0.0 ± 0.0
Z+jets (LO)	25 102.15 ± 180.24	48 148.21 ± 253.62	73 250.36 ± 311.14
Z+jets (NLO)	66 092.62 ± 331.51	125 392.21 ± 464.40	191 484.83 ± 570.58
Total MC (LO)	26 768.85 ± 180.84	51 274.61 ± 254.62	78 043.46 ± 312.31
Total MC (NLO)	67 759.32 ± 331.91	128 518.61 ± 464.90	196 277.93 ± 571.22
Data	27598.0	50814.0	78412.0

Table 7.7: The number of observed events in data and the number of expected events from simulation (and their statistical uncertainties) for the m_W^{inv} Z+jets control region following the application of the full event selection and simulation corrections. The number of observed events is given for each of the separate channels and their combination.

Process	***ee***	***μμ***	**Combined**
tZq	13.16 ± 0.05	24.32 ± 0.07	37.48 ± 0.09
tWZ	1.01 ± 0.08	1.99 ± 0.12	3.00 ± 0.14
tHq	0.05 ± 0.01	0.10 ± 0.01	0.15 ± 0.01
ttW	0.66 ± 0.04	1.33 ± 0.06	1.99 ± 0.07
ttZ	9.86 ± 0.08	17.87 ± 0.11	27.73 ± 0.14
ttH	0.52 ± 0.03	1.24 ± 0.05	1.76 ± 0.06
$t\bar{t}$	403.56 ± 11.78	827.84 ± 17.31	1234.40 ± 20.94
tW	10.83 ± 1.31	25.79 ± 2.11	36.62 ± 2.48
s-channel	0.0 ± 0.0	0.0 ± 0.0	0.0 ± 0.0
t-channel	0.22 ± 0.10	0.68 ± 0.21	0.90 ± 0.23
WW	0.18 ± 0.10	0.0 ± 0.0	0.18 ± 0.10
WZ	39.43 ± 0.50	68.57 ± 0.67	108.0 ± 0.84
ZZ	33.43 ± 0.42	59.54 ± 0.57	92.97 ± 0.71
WWW	0.0 ± 0.0	0.04 ± 0.04	0.04 ± 0.04
WWZ	0.25 ± 0.06	0.78 ± 0.13	1.03 ± 0.14
WZZ	0.48 ± 0.06	0.71 ± 0.07	1.19 ± 0.09
ZZZ	0.20 ± 0.02	0.25 ± 0.02	0.45 ± 0.03
W+jets	0.0 ± 0.0	0.0 ± 0.0	0.0 ± 0.0
Z+jets (LO)	2259.54 ± 54.52	4363.72 ± 77.24	6623.2 ± 94.54
Z+jets (NLO)	6922.41 ± 107.88	13 147.40 ± 151.84	20 069.81 ± 186.26
Total MC (LO)	2773.34 ± 55.80	5394.72 ± 79.19	8168.06 ± 96.87
Total MC (NLO)	7436.21 ± 108.53	14 178.40 ± 152.84	21 614.61 ± 187.45
Data	2940.0	5718.0	8658.0

7.4.3 $t\bar{t}$ Background

In Section 6.2.2 a $t\bar{t}$ enriched control regions was defined to produce an orthogonal region that was topologically similar to the signal region to validate the modelling of the simulated $t\bar{t}$ sample used. This control region differed from the signal region by requiring that the event contained an electron and muon, rather than a pair of electrons or muons.

Good agreement is observed between the normalisation of simulation and data at every stage of applying the simulation corrections and control region selection criteria, as illustrated in Figure 7.12.

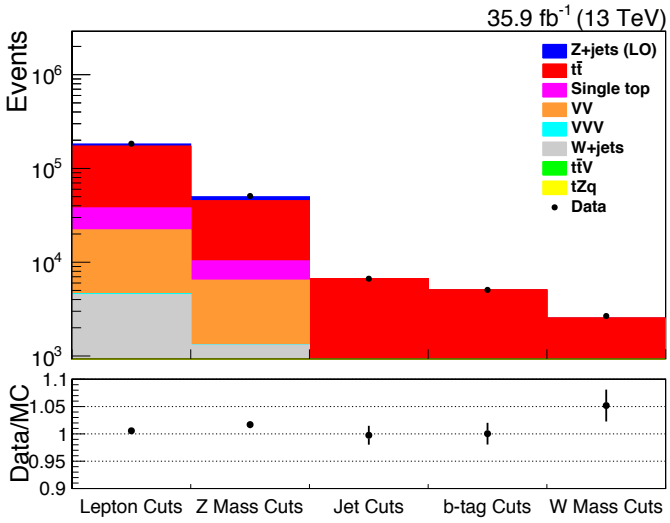

Figure 7.12: The overall event yield for data and simulation at each stage of applying the $t\bar{t}$ control region selection criteria and simulation corrections. The statistical uncertainties for each simulated process is given and the LO Z+jets sample is used for the Z+jets contribution.

From Table 7.8, it can be seen that the full application of the control region's criteria selection produces an enriched region where 97.5% of the expected events are from $t\bar{t}$ production. Of the remaining events, 70% are expected to be from tW single top production.

Good agreement is also observed for the reconstructed variables, as illustrated by the distributions of the number of jets and b-jets in Figure 7.13; the p_{T} of the four leading jets in Figure 7.14; and the invariant mass and p_{T} of the two leptons in Figure 7.15. A larger selection of data and simulation comparison plots for this $t\bar{t}$ enriched control region is provided in Appendix B.3.

Given the good agreement observed between data and simulation, it was determined that the $t\bar{t}$ MC sample accurately modelled data. Consequently, a data-driven estimate of the $t\bar{t}$ contribution was deemed unnecessary.

Table 7.8: The event yields, and the statistical uncertainties associated with them, following the full event selection and simulation corrections for the $t\bar{t}$ control region.

Process	$e\mu$		
tZq	0.34	±	0.01
tWZ	0.13	±	0.03
tHq	0.29	±	0.01
ttW	10.53	±	0.13
ttZ	9.64	±	0.11
ttH	7.71	±	0.11
$t\bar{t}$	2400.77	±	21.61
tW	103.67	±	5.31
s-channel	0.0	±	0.0
t-channel	0.64	±	0.24
WW	1.76	±	0.55
WZ	0.60	±	0.16
ZZ	0.09	±	0.02
WWW	0.15	±	0.05
WWZ	0.07	±	0.04
WZZ	0.0	±	0.0
ZZZ	0.0	±	0.0
W+jets	0.0	±	0.0
Z+jets	0.0	±	0.0
Total MC	2536.39	±	22.26
Data	2668.0		

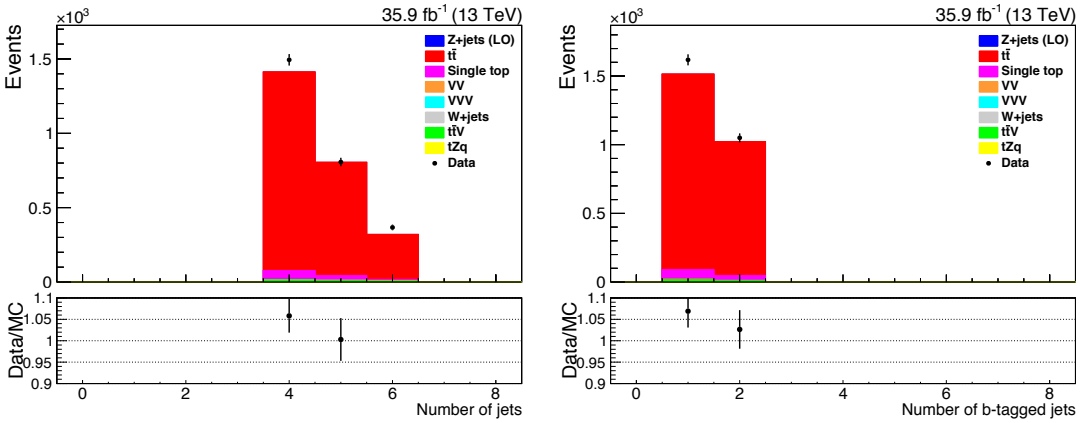

Figure 7.13: The distributions of the number of jets (left) and the number b-tagged jets for the $t\bar{t}$ control region following the application of the full control region selection criteria and simulation corrections.

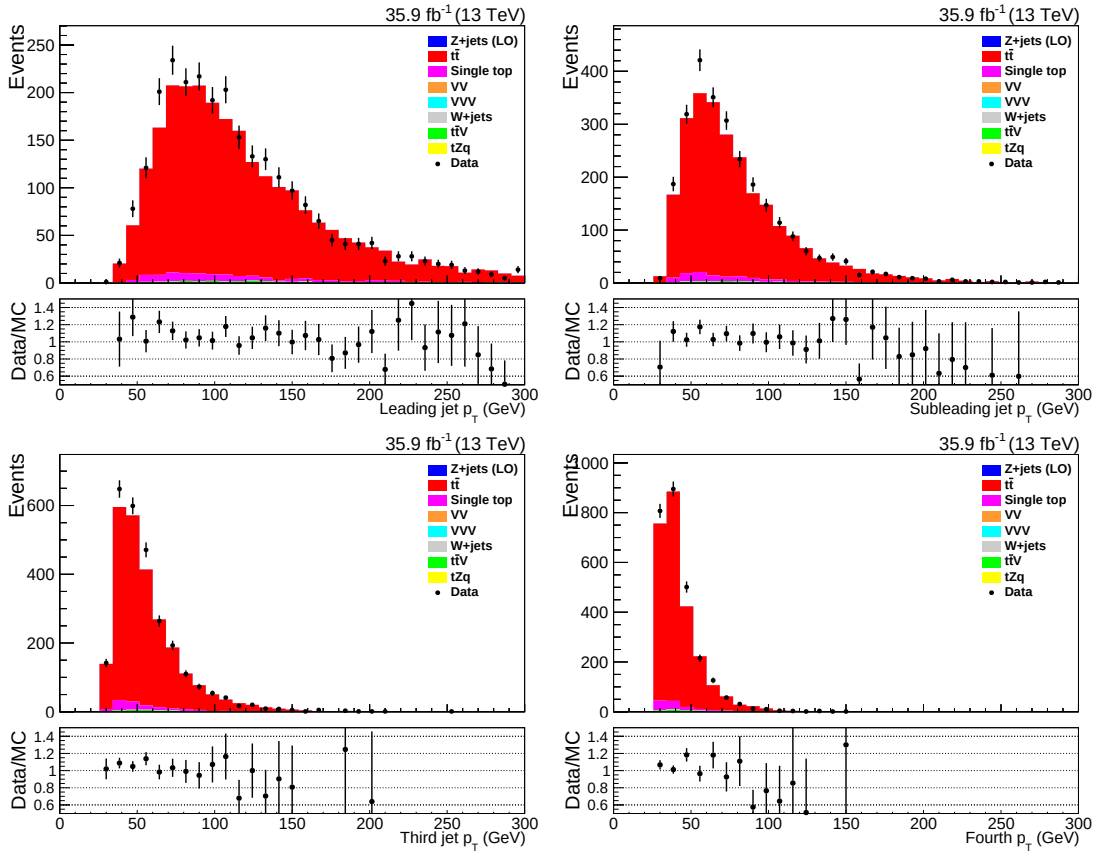

Figure 7.14: The distribution of the p_{T} of the four leading jets for the $t\bar{t}$ control region following the application of the full control region selection criteria and simulation corrections.

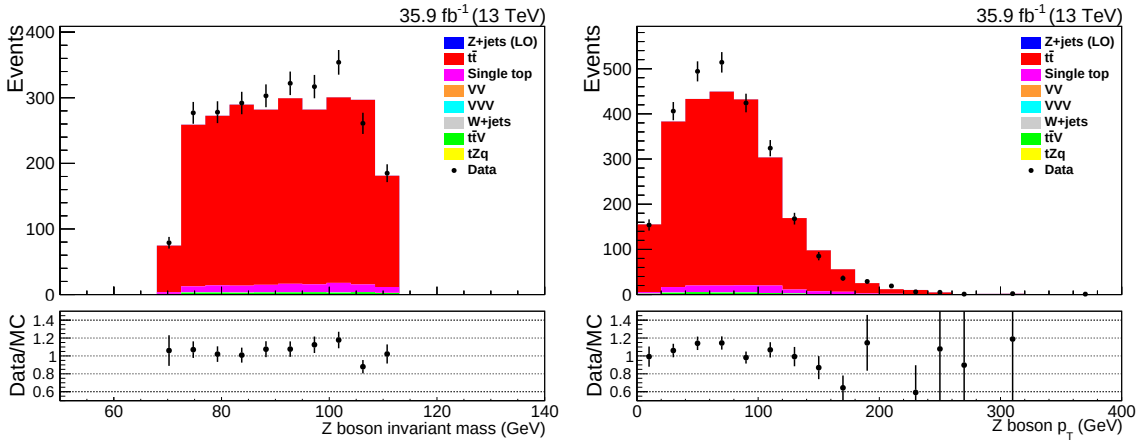

Figure 7.15: The distribution of the selected electron's and muon's combined invariant mass and p_{T} for the $t\bar{t}$ control region following the application of the full control region selection criteria and simulation corrections.

7.5 Systematic Uncertainties

For any meaningful and robust measurement to be made in any physics analysis, it is vital that the sources of systematic uncertainties associated with it are both understood and controlled. This is particularly important for this analysis as the low signal process production cross section compared to those of the backgrounds result in the scale of the statistical uncertainties being comparable to that of the systematic uncertainties of the measurement.

These sources of uncertainty originate from either experimental or theoretical uncertainties and influence the normalisation of the distributions considered and/or the shape of the distributions. The statistical uncertainties arising from the size of the simulated samples available were also considered.

These uncertainties were treated as nuisance parameters in the signal extraction, which is described, along with the impact of the uncertainties on the result, in Section 8.1.

7.5.1 Experimental Uncertainties

Jet Energy Corrections

The CMS Jet Energy Corrections group provides the uncertainties associated with the JES and JER values they determine (discussed in Sections 5.2.7.1 and 7.2.4) [158].

The impact of the JES is evaluated by varying the JES values applied to all jets up and down by a standard deviation. The uncertainty associated with the JER smearing is accounted for by varying the smearing factor up and down by the associated statistical uncertainty.

Missing Transverse Energy Uncertainties

As missing transverse energy is calculated from the sum of the p_{T} of all PF objects in a given event along with the remaining unclustered energy deposits, the uncertainties associated with both have to be considered.

The impact of the uncertainties associated with both the JES and JER on the PF $E_{\mathrm{T}}^{\mathrm{miss}}$ were accounted for by propagating the JEC uncertainties through to the $E_{\mathrm{T}}^{\mathrm{miss}}$ and evaluating the impact they have. As the unclustered energy remains uncorrected, the impact on the $E_{\mathrm{T}}^{\mathrm{miss}}$ uncertainty is evaluated by varying the contributions to the unclustered energy from each particle by their respective resolution.

Pileup Reweighting

The uncertainty associated with the PU reweighting (see Section 7.2.6) is determined by varying the expected minimum bias cross section in simulation by $\pm 4.6\%$.

Parton Density Functions

As PDFs are derived from data measured by different experiments, the uncertainties associated with each measurement must be propagated to the momentum fractions and energies that have been assigned to partons of the incoming protons.

The impact of the PDF uncertainties, along with the uncertainty associated with the value used for α_S, were evaluated according to PDF4LHC recommendations [179], namely as the standard deviation of the weights of the nominal and the variations of the PDF set . For almost all of the MC samples considered, this is achieved by considering the nominal event weight and one hundred alternative PDF weights and the $\pm\sigma$ variations of α_S .

The single top tW-channel samples were the exception to this as at the time of their generation it was not possible to generate the required per-event weights. In this case, the LHAPDF (Les Houches Accord Parton Distribution Function) library was used to access 100 eigenvalues from the NNPDF3.0 PDF set [36] in order to produce 200 alternative weights for each event.

b-tagging Uncertainties

The uncertainties associated with the b-tagging scale factors described in Section 7.2.5 were obtained by varying their value by $\pm 1\sigma$.

Non-prompt Lepton Contributions

Based on the experience of other analyses which determine similar background contributions, a 30% normalisation uncertainty is applied to conservatively cover the uncertainties related to the variation of the ratio of opposite-sign over same-sign events as a function of the lepton flavour and the cut level [177, 178].

Luminosity Uncertainties

The overall uncertainty in the integrated luminosity collected by CMS in 2016 was estimated to be 2.5% [115].

Lepton Efficiencies

The uncertainties associated with the lepton identification, isolation and reconstruction efficiency scale factors discussed in Section 7.2.2 were varied by $\pm 1\sigma$.

Several systematic studies were performed to estimate the systematic uncertainty associated with the trigger scale factors. These studies were the comparison of the trigger efficiencies

$t\bar{t}$ and Z+jets processes in simulation and the strength of the correlation of the $E_{\mathrm{T}}^{\mathrm{miss}}$ trigger selection to the lepton triggers used in the analysis.

When comparing the trigger efficiencies in simulation between the $t\bar{t}$ and Z+jets samples, it was found that the differences between the trigger efficiencies for the ee and $\mu\mu$ final states was covered by their statistical uncertainties for both when the trigger efficiency was and was not a function of the leptons' p_{T} and η.

The trigger efficiencies determined for all in events the $t\bar{t}$ and Z+jets simulation samples for the ee and $\mu\mu$ final states are shown in Table 7.9 and the distributions of the trigger efficiencies for the $t\bar{t}$ and Z+jets simulation samples as functions of p_{T} are illustrated in Figure 7.16. Plots comparing the trigger efficiencies for the $t\bar{t}$ and Z+jets simulation samples as functions of η are provided in Appendix C.2.

Table 7.9: The trigger efficiencies for the lepton selection criteria for $t\bar{t}$ and Z+jets in simulation. The uncertainties given only include the statistical uncertainty associated with each value.

Channel	**MC Sample**	ϵ_{MC}
ee	$t\bar{t}$	0.98823 ± 0.00086
	Z+jets	0.98849 ± 0.00309
$\mu\mu$	$t\bar{t}$	0.99192 ± 0.00074
	Z+jets	0.99258 ± 0.00083

In order to evaluate the independence of the $E_{\mathrm{T}}^{\mathrm{miss}}$ and lepton triggers used, the efficiency of each set of triggers is first considered individually. If both sets triggers are independent, then the efficiency of fulfilling both trigger selections can be expressed as:

$$\frac{\epsilon_{X+leptontriggers}}{\epsilon_{Xtriggers} \times \epsilon_{leptontriggers}} = \alpha \tag{7.3}$$

If the $E_{\mathrm{T}}^{\mathrm{miss}}$ and lepton trigger selection requirements are uncorrelated, then the ratio (α) expressed in Equation 7.3 will be 1. Table 7.10 shows that for the all channels, α only exhibits small differences from unity, indicating negligible correlation between the triggers used.

Table 7.10: The values of α, expressing the strength of correlation between the lepton and cross triggers used to determine the trigger scale factors, for each channel.

Channel	α
ee	0.99890 ± 0.01379
$\mu\mu$	1.00151 ± 0.01291
$e\mu$	0.98775 ± 0.09182

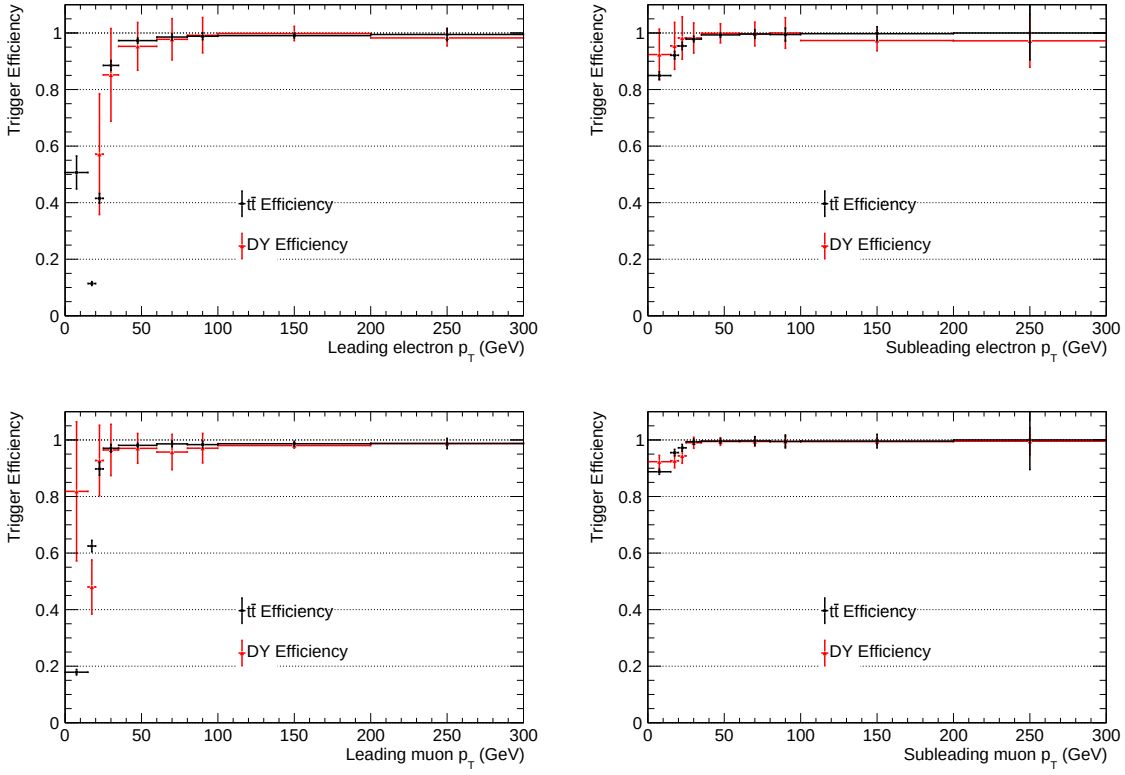

Figure 7.16: The data and $t\bar{t}$ simulation efficiencies and scale factors for the ee (top) and $\mu\mu$ final states as determined for the OR of the respective dilepton and single lepton triggers considered as a function of the leading and sub-leading leptons' p_{T}.

Both the statistical uncertainties of the trigger efficiencies and the results of the above studies were consistent with those determined for other top physics analyses. As such, it was determined that systematic uncertainties of 1.0%, 1.0% and 2.0% for the ee, $\mu\mu$, and $e\mu$ channels, respectively, would be sufficient to account for the residual differences in trigger efficiency between data and simulation.

7.5.2 Theoretical Uncertainties

7.5.2.1 Cross section normalisation

The uncertainty associated with the cross sections of the simulated samples was taken into account by associating a normalisation uncertainty with each of the simulated samples considered. The CMS Collaboration's search for tZq production using the trilepton channel at $\sqrt{s} = 13\,\text{TeV}$ had assumed a value of 30% for this source of systematic uncertainty, which reflected the theoretical uncertainties in the corresponding cross sections and a scaling up of a factor of two or more to account for possible modelling limitations [62]. Following the publication of the above search and discussions with CMS Top Physics colleagues, it was decided to assume a value of 10% for the cross section normalisation uncertainties. This smaller value was decided upon as it reflected the scaling of the theoretical uncertainties in the cross sections of the dominant backgrounds by a factor or two or greater in order to account for potential modelling limitations. Furthermore, the value also reflected an increased confidence in the theoretical modelling of all of the backgrounds considered, given the improved precision cross section measurements that have been made since the search for tZq production using the trilepton final state [180, 181].

7.5.2.2 Factorisation and renormalisation scales

The impact of the uncertainty associated with the choice of factorisation (μ_F) and renormalisation scales (μ_R) used in perturbative QCD is evaluated by varying each scale up and down by a factor or 2 from their nominal value.

Events weights were produced for the variation of μ_F and μ_R at the ME level, where both scales are varied individually and simultaneously in order to evaluate the impact of the uncertainties for these scales. The impact of varying μ_F and μ_R for the PS level however, was evaluated through the use of dedicated samples for certain processes. These centrally produced samples are listed in Table 7.2 as the "scale up" and "scale down" samples.

The scale variations for initial-state radiation and final-state radiation were considered separately for the $t\bar{t}$ simulation samples. The dedicated $t\bar{t}$ samples used to evaluation the impact of independently varying the scale for ISR and FSR are listed in Table 7.2 as the "isr/fsr up" and "isr/fsr down" samples.

As mentioned above in Section 7.5.1, it was not possible for the single top tW production simulation samples to be produced with per-event weights to account for the matrix element factorisation and renormalisation scales. To account for this, the "scale up" and "scale down" samples listed in Table 7.2 for tW production also include the impact of varying μ_F and μ_R for both the ME and PS levels.

7.5.2.3 Matrix Element - Parton Shower Matching Thresholds

The POWHEG V2 matching threshold energy is defined as $\frac{h_{damp}^2}{h_{damp}^2+p_T^2}$, where h_{damp} has been tuned to be $1.58 \times m_{top}$. The uncertainty associated with this matching threshold was evaluated using dedicated samples for the $t\bar{t}$ and single top t-channel processes where h_{damp} is varied up and down by one standard deviation [182]. These dedicated simulated samples are listed in Table 7.2 as "matching up " and "matching down" for the respective variations of h_{damp}.

7.5.3 Pre-Fit Impact of the Systematic Uncertainties

The impact of the each of the systematics on the event yield (in percentage) of the simulated processes following the application of the signal region selection criteria is shown in Table 7.11 for both of the final states considered. These rates, whilst giving an overview of which systematics were the most important, do not show how the shape of the fitted variable, the BDT discriminant, is influenced by each uncertainty when performing .

Prior to performing the likelihood fit described in Chapter 8, the theoretical sources of uncertainty were observed to have the greatest impact on the observed yields of all the simulated samples. While the majority of the experimental uncertainties have a smaller impact on the event yields than the theoretical uncertainties, the JER and PDF uncertainties were observed to have a greatest impact on the yields of the Z+jets and tZq processes, respectively.

Table 7.11: Impact of systematic uncertainties on MC event yields following the application of the full event selection criteria.

Systematic	tZq	Z+jets	$t\bar{t}$	t$\bar{t}$V	VV	Other
(ee / $\mu\mu$)	(%)	(%)	(%)	(%)	(%)	(%)
Statistical	$\pm 0.23\%$ / ± 0.18	$\pm 2.03\%$ / $\pm 1.49\%$	$\pm 1.43\%$ / $\pm 1.04\%$	$\pm 0.32\%$ / $\pm 0.25\%$	$0.66 \pm \%$ / $0.50 \pm \%$	$\pm\%$ / $1.64 \pm \%$
Lepton Eff.	$^{+5.42\%}_{-5.41\%}$ / $^{+4.87\%}_{+0.77\%}$	$^{+5.45\%}_{-4.88\%}$ / $^{+4.77\%}_{+0.69\%}$	$^{+5.14\%}_{-5.35\%}$ / $^{+5.19\%}_{+1.19\%}$	$^{+5.48\%}_{-5.63\%}$ / $^{+5.24\%}_{+1.21\%}$	$^{+6.48\%}_{-5.13\%}$ / $^{+4.85\%}_{+0.61\%}$	$^{+5.01\%}_{-4.34\%}$ / $^{+4.10\%}_{+0.48\%}$
JER	$^{+3.85\%}_{-4.12\%}$ / $^{+4.01\%}_{-4.48\%}$	$^{+13.87\%}_{-11.53\%}$ / $^{+14.42\%}_{-12.09\%}$	$^{+7.71\%}_{-7.02\%}$ / $^{+8.93\%}_{-8.08\%}$	$^{-1.22\%}_{-0.08\%}$ / $^{+0.20\%}_{+0.08\%}$	$^{+8.41\%}_{-8.34\%}$ / $^{+8.99\%}_{-8.42\%}$	$^{+8.48\%}_{-6.67\%}$ / $^{+9.67\%}_{-10.53\%}$
JES	$^{+0.08\%}_{-0.17\%}$ / $^{-0.14\%}_{-0.14\%}$	$^{-0.65\%}_{-0.69\%}$ / $^{-0.16\%}_{+0.12\%}$	$^{-0.01\%}_{-0.68\%}$ / $^{-0.34\%}_{-0.11\%}$	$^{-0.03\%}_{-0.14\%}$ / $^{+0.18\%}_{-0.16\%}$	$^{+0.50\%}_{+0.46\%}$ / $^{+0.36\%}_{+0.01\%}$	$^{-1.25\%}_{+1.57\%}$ / $^{-0.67\%}_{-0.16\%}$
Pileup	$^{-0.59\%}_{+0.59\%}$ / $^{-0.32\%}_{+0.01\%}$	$^{+0.34\%}_{-1.54\%}$ / $^{+2.08\%}_{-2.15\%}$	$^{-0.92\%}_{-0.41\%}$ / $^{+0.28\%}_{-0.97\%}$	$^{-0.81\%}_{+0.57\%}$ / $^{-0.15\%}_{+0.11\%}$	$^{+0.99\%}_{-0.55\%}$ / $^{+1.68\%}_{-1.39\%}$	$^{+0.44\%}_{+0.13\%}$ / $^{-1.34\%}_{-1.40\%}$
bTag	$^{+3.11\%}_{-2.97\%}$ / $^{+2.86\%}_{-3.4\%}$	$^{+5.42\%}_{-6.07\%}$ / $^{+4.83\%}_{-5.65\%}$	$^{+3.29\%}_{-3.01\%}$ / $^{+3.49\%}_{-3.75\%}$	$^{+3.19\%}_{-3.21\%}$ / $^{+3.14\%}_{-3.13\%}$	$^{+6.65\%}_{-5.86\%}$ / $^{+5.67\%}_{-5.98\%}$	$^{2.98+\%}_{-2.56\%}$ / $^{+3.34\%}_{-3.00\%}$
PDF	$^{+15.92\%}_{-16.13\%}$ / $^{+15.88\%}_{-16.39\%}$	$^{+7.28\%}_{-8.36\%}$ / $^{+7.95\%}_{-8.57\%}$	$^{+2.17\%}_{-2.70\%}$ / $^{+2.34\%}_{-2.30\%}$	$^{+6.74\%}_{-7.03\%}$ / $^{+7.23\%}_{-6.80\%}$	$^{+8.09\%}_{-7.14\%}$ / $^{+8.39\%}_{-5.45\%}$	$^{+8.07\%}_{-7.58\%}$ / $^{+6.70\%}_{-8.85\%}$
ME μ_R and μ_F scales	$^{-7.14\%}_{+7.33\%}$ / $^{-6.96\%}_{+6.26\%}$	$^{-8.05\%}_{+9.94\%}$ / $^{-8.98\%}_{+9.59\%}$	$^{-13.464\%}_{+15.84\%}$ / $^{-13.46\%}_{+15.04\%}$	$^{-18.82\%}_{+11.61\%}$ / $^{-11.38\%}_{+11.07\%}$	$^{-7.14\%}_{+10.86\%}$ / $^{-8.38\%}_{+10.14\%}$	$^{-8.08\%}_{+8.29\%}$ / $^{-9.57\%}_{+9.41\%}$
PS μ_R and μ_F scales	$^{+6.74\%}_{-10.33\%}$ / $^{+4.47\%}_{-6.51\%}$	–	–	–	–	$^{-9.90\%}_{-13.34\%}$ / $^{-5.01\%}_{-7.55\%}$
ISR	–	–	$^{+4.35}_{-6.57}$ / $^{+3.16}_{-6.44}$	–	–	–
FSR	–	–	$^{-3.87}_{+15.31}$ / $^{-5.78}_{+12.63}$	–	–	–
ME-PS matching scale	–	–	$^{-2.15}_{-9.01}$ / $^{+1.02}_{-5.89}$	–	–	–
Cross section normalisation	$^{+10.0\%}_{-10.0\%}$ / $^{+10.0\%}_{-10.0\%}$	$^{+10.0\%}_{-10.0\%}$ / $^{+10.0\%}_{-10.0\%}$	$^{+10.0\%}_{-10.0\%}$ / $^{+10.0\%}_{-10.0\%}$	$^{+8.43\%}_{-8.34\%}$ / $^{+7.82\%}_{-7.82\%}$	$^{+6.74\%}_{-6.74\%}$ / $^{+6.71\%}_{-6.71\%}$	$^{+6.03\%}_{-6.03\%}$ / $^{+6.10\%}_{-6.10\%}$
Luminosity	$^{+2.5\%}_{-2.5\%}$ / $^{+2.5\%}_{-2.5\%}$	$^{+2.5\%}_{-2.5\%}$ / $^{+2.5\%}_{-2.5\%}$	$^{+2.5\%}_{-2.5\%}$ / $^{+2.5\%}_{-2.5\%}$	$^{+2.5\%}_{-2.5\%}$ / $^{+2.5\%}_{-2.5\%}$	$^{+2.5\%}_{-2.5\%}$ / $^{+2.5\%}_{-2.5\%}$	$^{+2.5\%}_{-2.5\%}$ / $^{+2.5\%}_{-2.5\%}$

7.6 Multivariate Analysis Techniques

Multivariate Analysis (MVA) techniques are used to enhance the separation between signal and background processes which are difficult to discriminate between by applying individual selection criteria.

Therefore, a MVA technique was used to enhance the separation between the signal process from the background processes present following the application of the selection requirements described in Chapter 6. *Boosted Decision Trees* (BDTs) were chosen for this analysis as they were found to give superior performance compared to other MVA techniques and they are a widely used and supported technique with CMS existing expertise.

7.6.1 Boosted Decision Trees

As illustrated in Figure 7.17, a decision tree is a series of sequential binary decisions (nodes) used to classify an event. At each node in the decision tree, a single input variable is compared against a threshold to determine which of the next two nodes it will be sent to. When the last node is reached, the object is classified as either signal (S) or background (B).

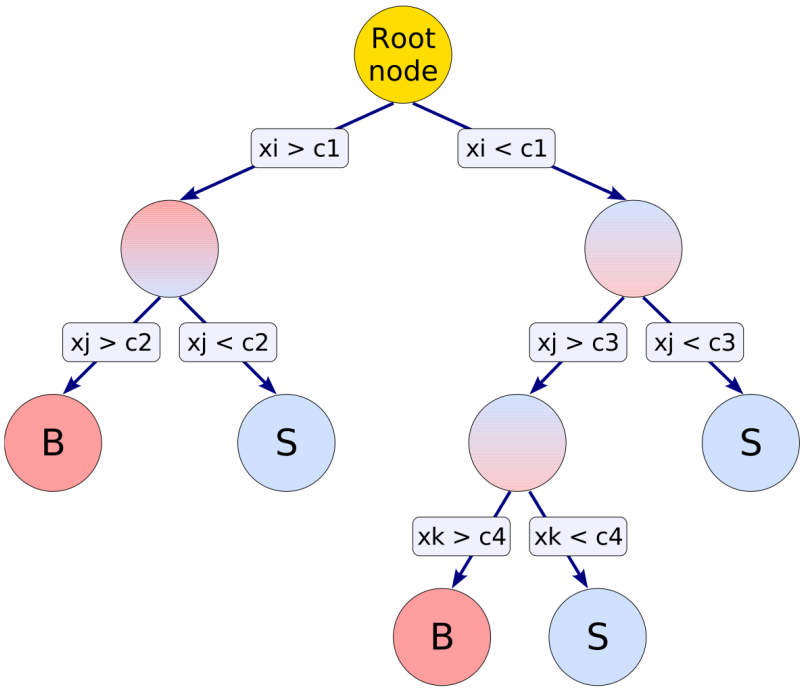

Figure 7.17: A simple decision tree where repeated cuts a member of the set of variables **x** are performed until a leaf node is reached and the object is classified as either signal (S) or background (B) [183].

As the decision criterion for each node is dependent on the decisions of the preceding nodes, decision trees have the potential to obtain better separation between signal and background processes through individual cuts on isolated variables. Without any prior knowledge of the system however, a single isolated tree is not expected to be an efficient classifier. Despite this however, such a weak learner will still contain some knowledge about the underlying structure of the classification problem.

Boosting aims to exploit this knowledge by using an ensemble of repeatedly trained weak learners to produce a more effective classifier. Following each training iteration the dataset is reweighted based on the success of the previous classifiers in order to force the weak learners to attempt to classify objects that are harder to identify. At the end of this process a weighted average of all the weak learners are combined to produce a single strong learner.

Therefore by extending boosting to decision trees, the resultant forest of Boosted Decision Trees produces a classifier that is both much more effective and resilient to fluctuations in the training sample than one created by a single tree. Typically the classifier produced by a BDT takes the form of a single discriminator whose response ranges between -1 to $+1$, denoting completely background-like and signal-like objects, respectively.

BDTs are however, particularly sensitive to the effects of *overtraining*. This phenomena occurs when a BDT is overly optimised on correctly classifying events from the training dataset and results in the poor classification of unseen data. In order to minimise the potential of overtraining occurring, the signal and background process samples are typically split into training and testing samples. The testing samples are not trained on in order to check the effectiveness of the BDT trained using the training sample.

Two of the most common boosting algorithms used with decision trees are the Adaptive Boosting (*AdaBoost*) [184] and *Gradient Boosting* [185, 186] algorithms. Adaboost adjusts the weighting assigned to both misclassified objects and the best performing weak learners after each iteration so that the best learners are trained to correctly identify the most difficult objects. In contrast, gradient boosting uses gradient descent following each iteration to determine the residuals of the objects in order to focus on correctly classifying the objects with the largest residuals.

A number of studies were performed to determine the optimal settings for this analysis. These included the evaluation of:

- a number of different boosting algorithms;
- which simulated background processes should be included in the training processes;
- whether or not multiple BDTs trained on separate backgrounds would be more effective than a single BDT;

- how to determine which input variables possessed the greatest discriminating power (i.e. the fraction of times they were used to split the decision tree);
- and which *hyperparameters*, the set of options used to control BDT behaviour, and associated values gave the optimal classification performance.

It was determined that the *eXtreme Gradient Boosting* (XGBoost) implementation of the Gradiant Boost algorithm for a single BDT trained on all the MC simulation samples gave the optimal performance for this search [187].

7.6.2 BDT Optimisation and Evaluation

The methods used for determining the optimal input variables and model hyperparameters for this BDT are described in the following subsection. Both the input variables and model hyperparameters were chosen separately for ee and $\mu\mu$ channels and all the simulated MC samples were considered.

Once the optimisation is complete, the BDT is trained. The BDT produces the output discriminant for each of the data and simulation samples considered. These output discriminant distributions were used to extract the signal strength and its statistical significance, as described in Chapter 8.

BDT Input Variable Optimisation

From the selected reconstructed physics objects, a large number of possible input variables were constructed and considered as inputs for the BDT. Training a BDT with all of the possible input variables increases its vulnerability to overtraining, as correlated input variables are considered multiple times and statistical fluctuations in poorly discriminating input variables may give the illusion of discriminative power.

In order to determine the optimal set of input variables, recursive feature elimination was used to those that had the greatest discriminating power between signal and background [188]. This process iteratively removes the least important input variable and retrains the BDT until every input variable has been ranked in order of their removal. From this process, the highest ranked input variables are identified for use in the BDT.

The input variables chosen by this method for the ee and $\mu\mu$ channels and their discriminating powers are given in Table 7.12. As can be seen in Figures 7.18-7.19, the majority of these variables were weakly correlated, as indicated by pale squares, signifying that they provide unique and useful information to the BDT. Table D.1 in Appendix D provides a list of all the input variables that were considered.

Table 7.12: The name and descriptions of the variables chosen by recursive feature elimination to be used as input to the BDT to discriminate between potential tZq signal events and the dominant backgrounds.

Input variable	**Description**	**Discriminating Power**	
		ee	$\mu\mu$
topMass	Reconstructed top quark mass	1.449×10^{-1}	1.794×10^{-1}
zMass	Reconstructed Z boson mass	1.202×10^{-1}	1.372×10^{-1}
jetMass	Total mass of every jet in an event	1.079×10^{-1}	9.304×10^{-2}
met	Missing transverse energy	9.100×10^{-2}	9.382×10^{-2}
bTagDisc	Leading b-tagged jet CSVv2 discriminant	6.773×10^{-2}	6.372×10^{-2}
leadJetPt	Leading jet p_{T}	6.093×10^{-2}	4.926×10^{-2}
jjDelR	ΔR between the leading jets	5.300×10^{-2}	3.987×10^{-2}
wPairMass	Reconstructed W boson mass	5.093×10^{-2}	4.808×10^{-2}
lepHt	H_{T} of the Z boson's leptons	4.620×10^{-2}	5.395×10^{-2}
totHtOverPt	Total H_{T} divided by total p_{T}	4.487×10^{-2}	3.284×10^{-2}
leadJetEta	Leading jet η	4.467×10^{-2}	6.138×10^{-2}
jetHt	H_{T} of all the jets in an event	-	5.629×10^{-2}
secJetPt	Second jet p_{T}	4.453×10^{-2}	-
zlQuark2DelR	ΔR between the leading lepton and W boson's subleading jet	4.093×10^{-2}	-
thirdJetPt	Third jet p_{T}	3.720×10^{-2}	3.753×10^{-2}
zlb1DelR	ΔR between the leading lepton and leading b-tagged jet	-	3.245×10^{-2}
zEta	Reconstructed Z boson η	-	2.111×10^{-2}
zlb2DelR	ΔR between subleading lepton and leading b-tagged jet	2.627×10^{-2}	-
fourthJetPt	Fourth jet p_{T}	1.873×10^{-2}	-

Figures 7.20, 7.21, 7.22, 7.23 and 7.24 show that good agreement was observed between simulation and data for the selected input variables. Given the number of input variables used, when an input variable is used by both the ee and $\mu\mu$ channels, only the distributions for the one of the two channels are given in this chapter. The complete set of distributions for both channels is given in Appendix D.

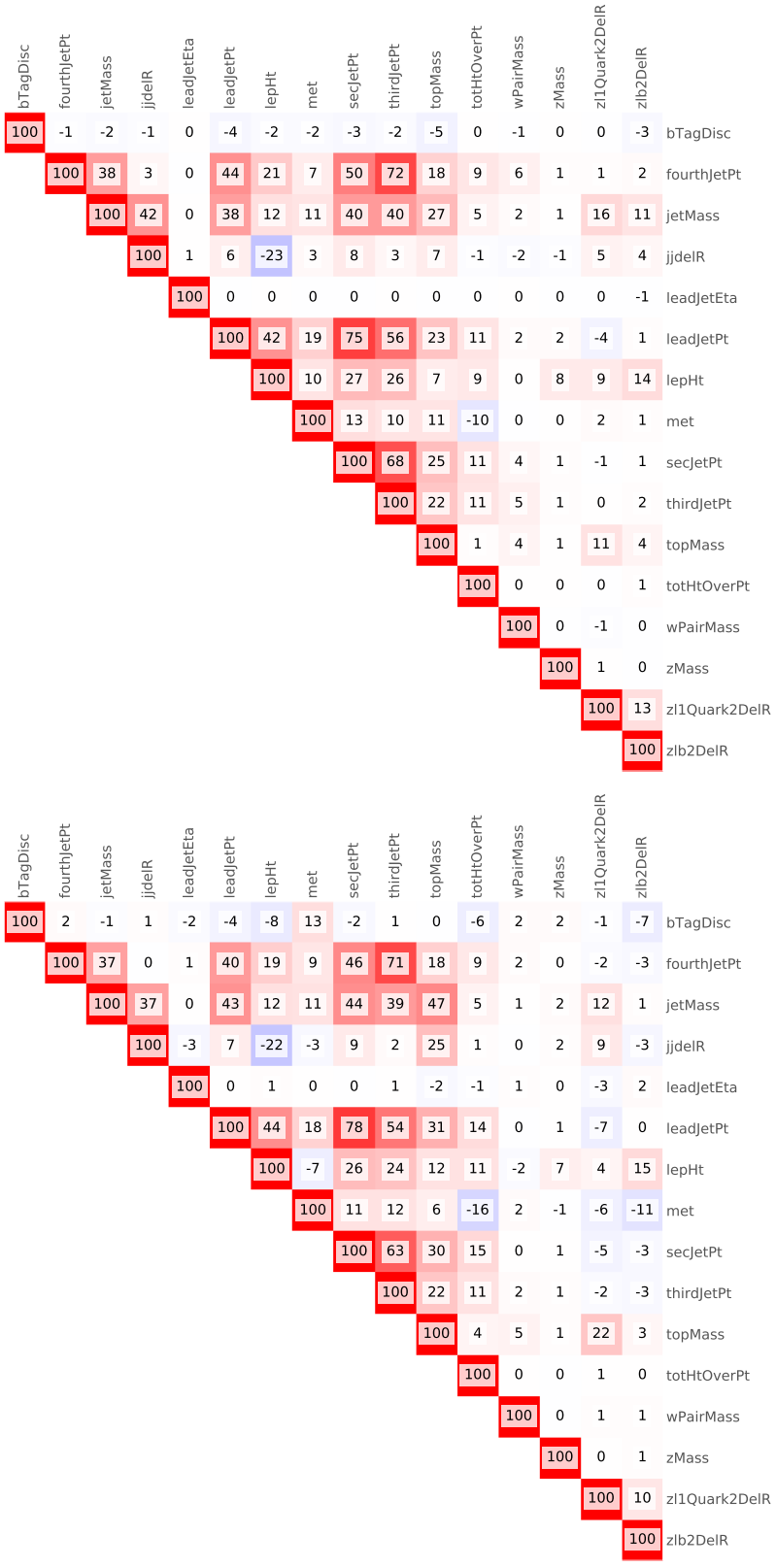

Figure 7.18: The correlations between the input variables chosen for use with the BDT for the signal (top) and background (bottom) samples for the *ee* channel.

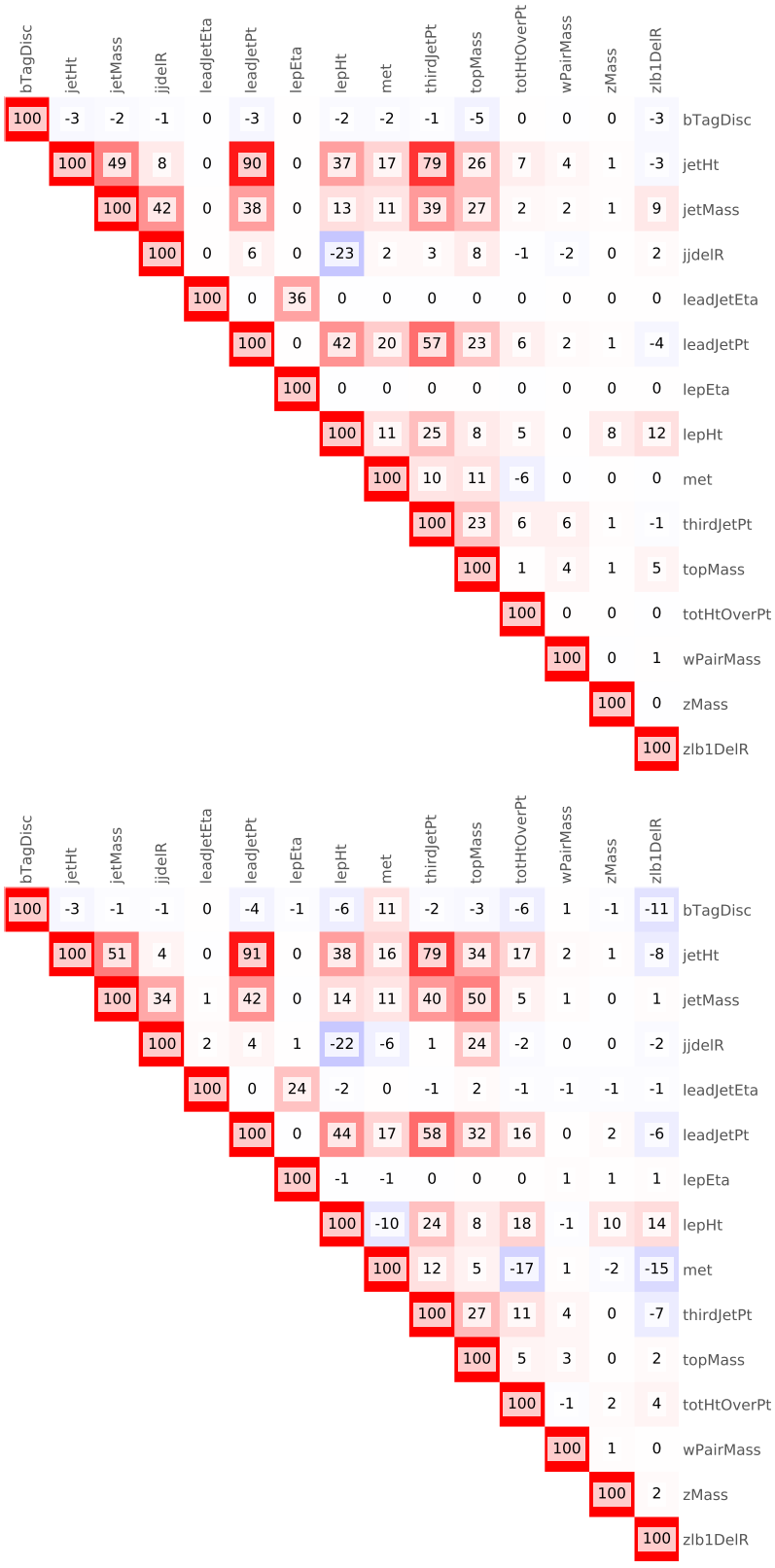

Figure 7.19: The correlations between the input variables chosen for use with the BDT for the signal (top) and background (bottom) samples for the $\mu\mu$ channel.

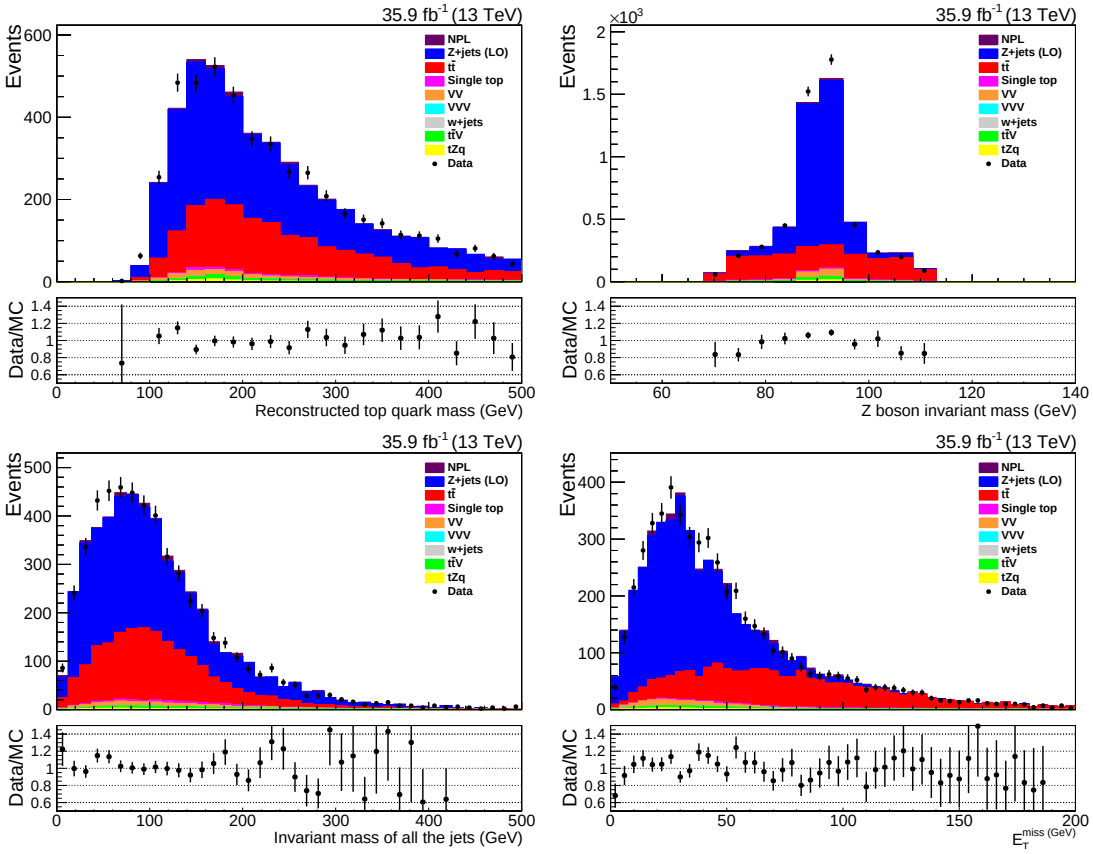

Figure 7.20: Reconstructed top mass, Z boson mass, total jet mass, and $E_{\mathrm{T}}^{\mathrm{miss}}$ distributions for the *ee* channel comparing the agreement between data and simulation for the variables used as input variables in the BDT training.

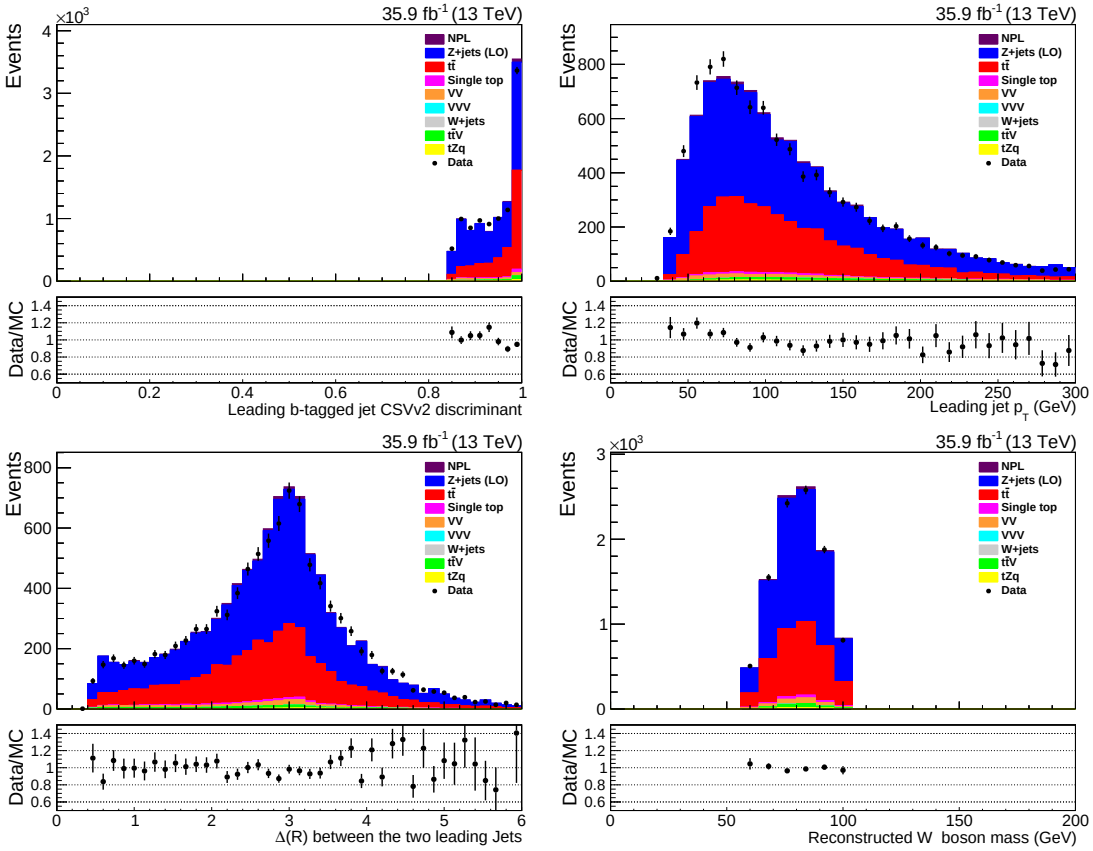

Figure 7.21: Leading b-tagged jet CSVv2 discriminant, leading jet p_{T}, ΔR between the leading jets, and reconstructed W boson mass distributions for the $\mu\mu$ channel comparing the agreement between data and simulation for the variables used as input variables in the BDT training.

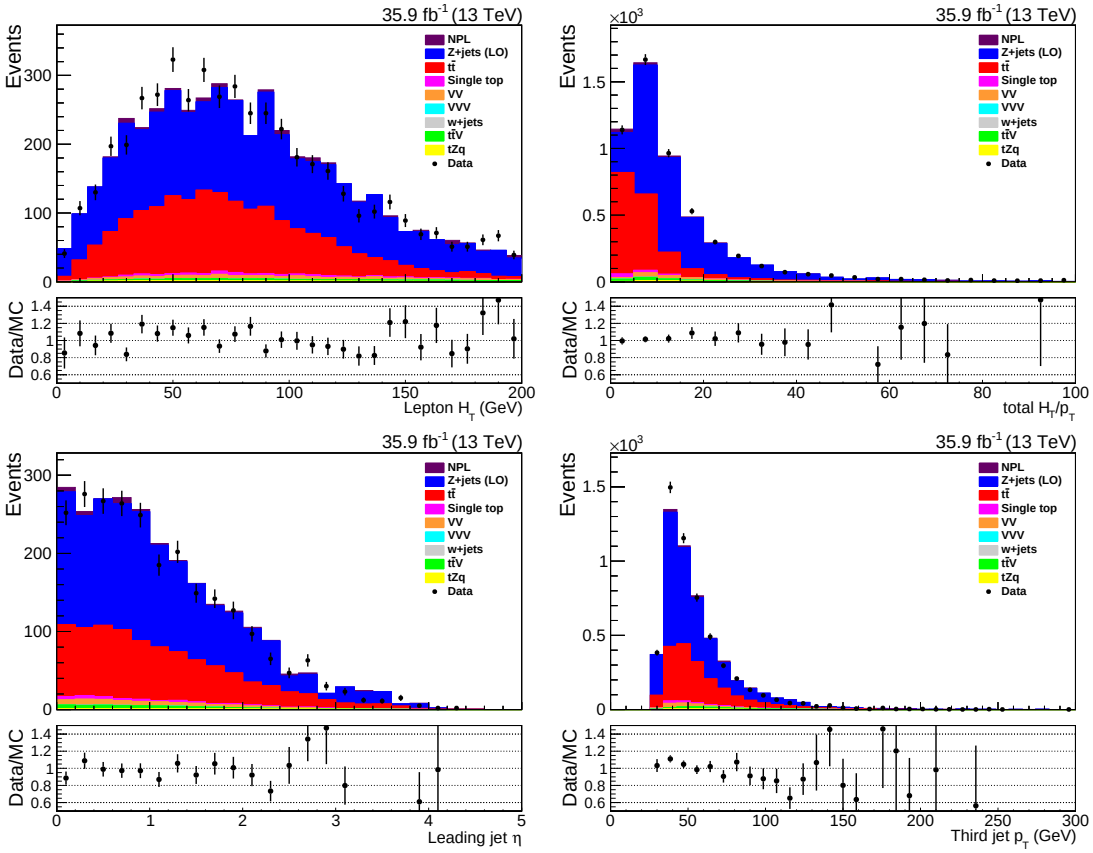

Figure 7.22: Lepton H_{T}, total H_{T} divided by total p_{T}, leading jet η and third jet p_{T} distributions for the ee channel comparing the agreement between data and simulation for the variables used as input variables in the BDT training.

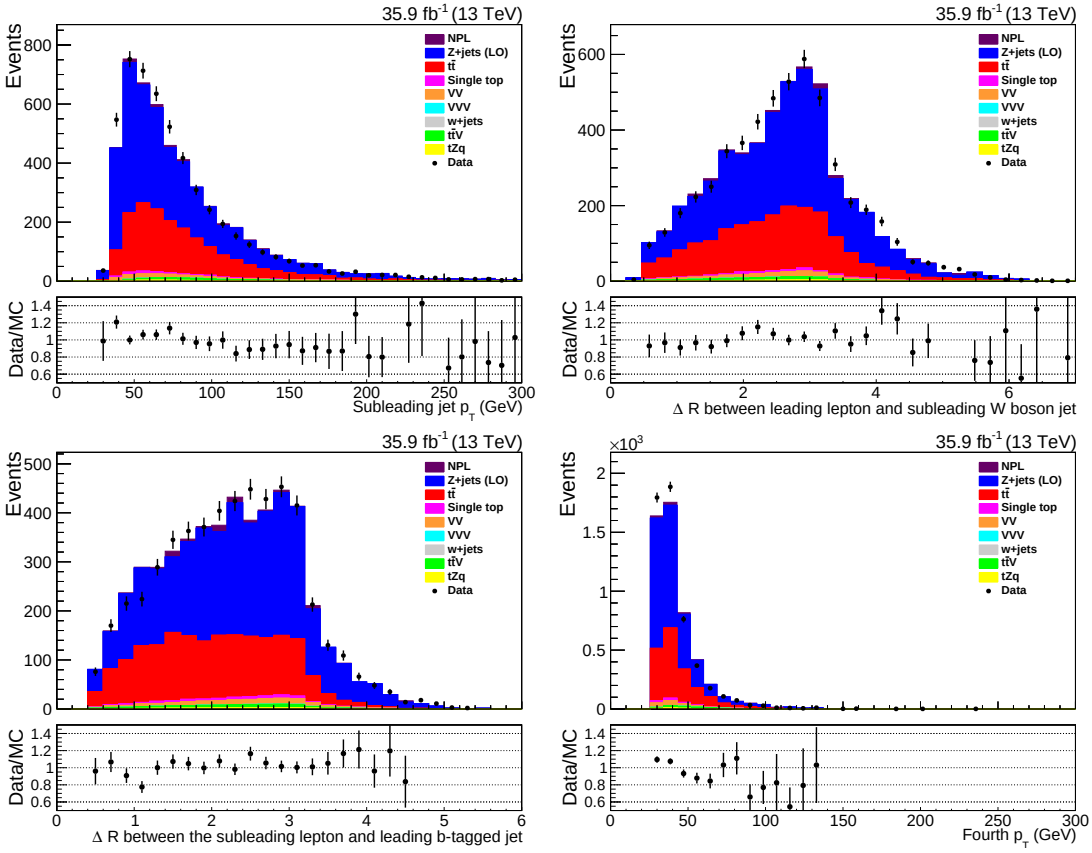

Figure 7.23: Second jet p_{T}, ΔR between subleading lepton and leading b-tagged jet, ΔR between subleading lepton and leading b-tagged jet and fourth jet p_{T} distributions for the *ee* channel comparing the agreement between data and simulation for the variables used as input variables in the BDT training.

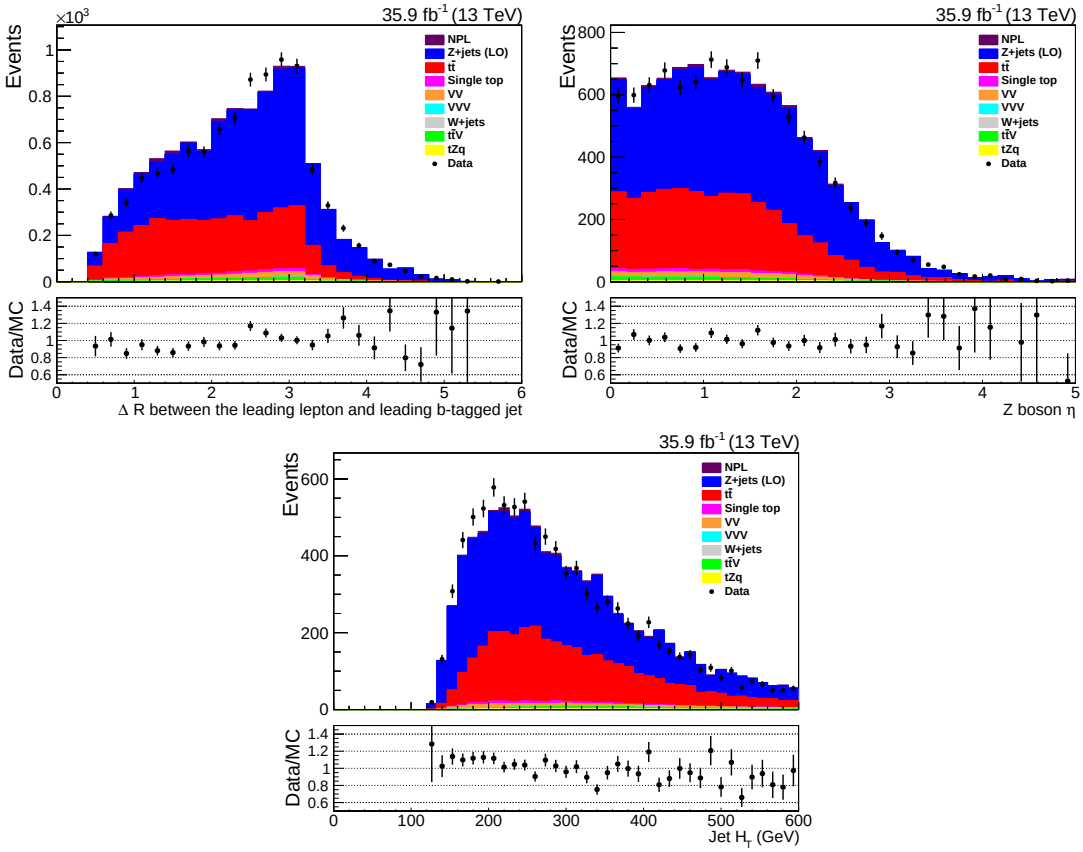

Figure 7.24: ΔR between leading lepton and leading b-tagged jet, reconstructed Z boson η, and jet H_{T} distributions for the $\mu\mu$ channel comparing the agreement between data and simulation for the variables used as input variables in the BDT training.

BDT Hyperparameter Optimisation

Instead of tuning the of choice hyperparameters for optimal classification performance either by hand or using a time and computationally expensive grid search, a regression model was constructed and evaluated using the *Scikit-Optimize* library [189]. This regression model identifies the set of optimal hyperparameters as the minima of a metric used to rank the hyperparameters considered.

Table 7.13 lists the set of hyperparameters and their values for the ee and $\mu\mu$ channels whose optimal values differ from their default values. Further descriptions of all of the hyperparameters available are given in [187].

Table 7.13: The optimal hyperparameters for the ee and $\mu\mu$ channels for XGBoost that were found by the regression model and the maximum and minimum values that they can take.

Option	ee	$\mu\mu$
Number of estimators	5000	3282
Subsample	0.5	1.0
Learning rate	2.82×10^{-3}	19.56×10^{-3}
Maximum tree depth	2	2
Minimum child weight	1.496	1×10^{-5}
γ	56.2×10^{-3}	5.404
α	1.63×10^{-3}	2.89
λ	0.606	1.473

Figure 7.25 shows the BDT responses for the ee and $\mu\mu$ channels for both the training and testing samples. As the response of the BDT classifier for both the training and testing samples were consistent with each other, this implies that negligible overtraining had occurred.

The distributions of the chosen input variables for the ee and $\mu\mu$ channels, shown in Figures 7.26 and 7.27 respectively, illustrate how the small differences present between signal and background distributions can lead to the larger separation between them by the BDT classifiers shown in Figure 7.25).

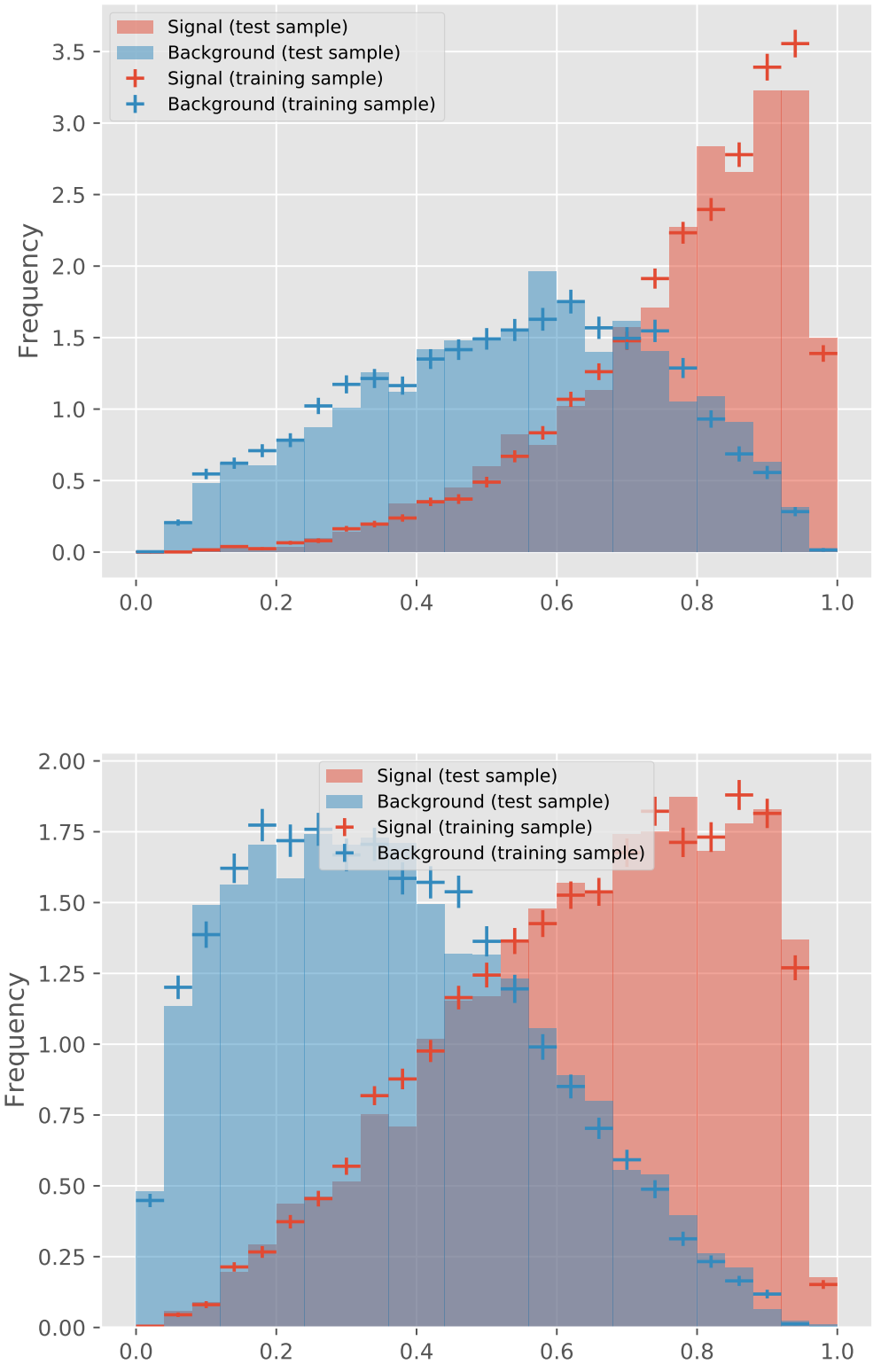

Figure 7.25: The BDT classifier's response for both training and testing samples for the signal and background processes for the ee (top) and $\mu\mu$ (bottom) channels .

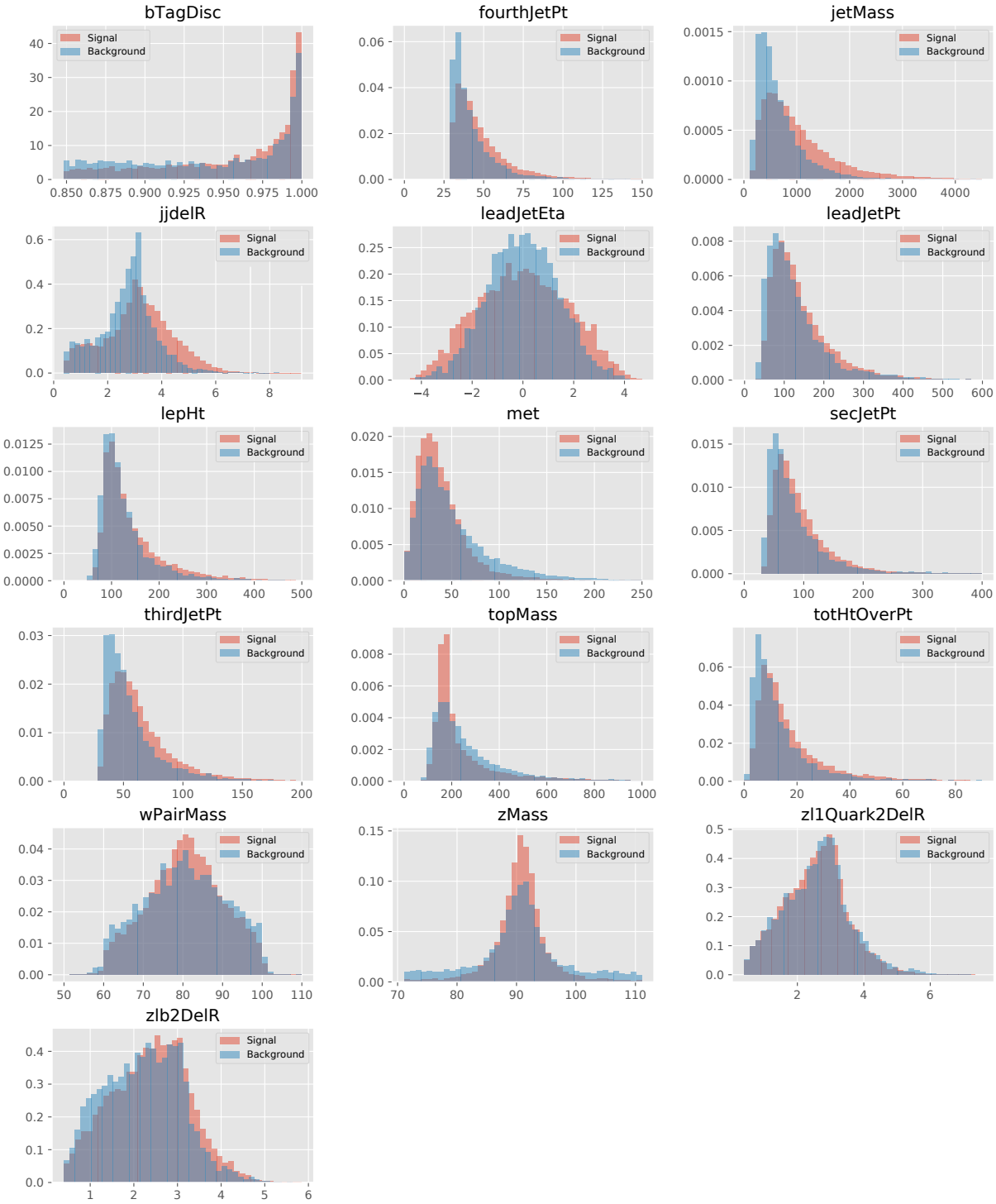

Figure 7.26: Distributions of the chosen input variables for the signal (red) and background (blue) samples for the *ee* channel.

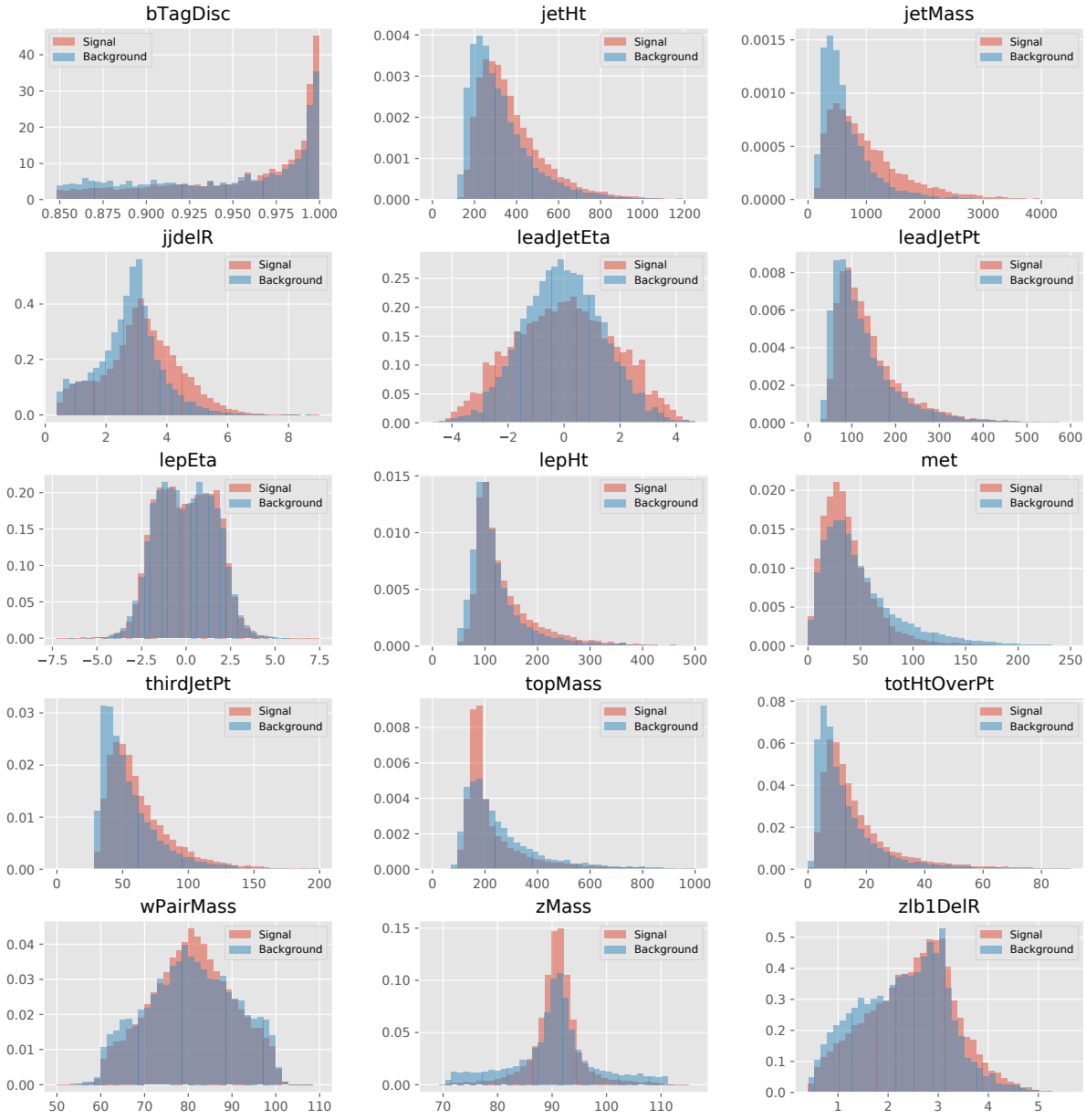

Figure 7.27: Distributions of the input variables chosen for use with the BDT for the signal (red) and background (blue) samples for the $\mu\mu$ channel.

BDT Evaluation

Following the optimisation of the BDT input variables and hyperparameters, the BDT was trained. The resultant output discriminant distributions shown in Figure 7.28, illustrate that there is both good agreement between simulation and data and that the BDT is effective at separating the majority of the backgrounds from the signal.

The output distributions were binned using a recursive binning strategy that ensured that each bin contained at least one background event and that the statistical error did not exceed 10% for either signal or background simulation. These conditions were applied to ensure that when performing the maximum likelihood fit described in the following chapter, each of the distributions' bins contained sufficient statistics to avoid causing [180, 190]:

- statistical fluctuations that would result in an artificial enhancement or suppression of the sensitivity in a given bin;
- excessively large fluctuations in shape-based systematic uncertainties, with respect to the nominal, that would influence the measurement's sensitivity;
- ill-defined probability density functions, due to bins populated by zero background or signal events, resulting in zero trust of the significance of a data event as it is impossible to determine if the significance is the result of a negligible background or lack of statistics.

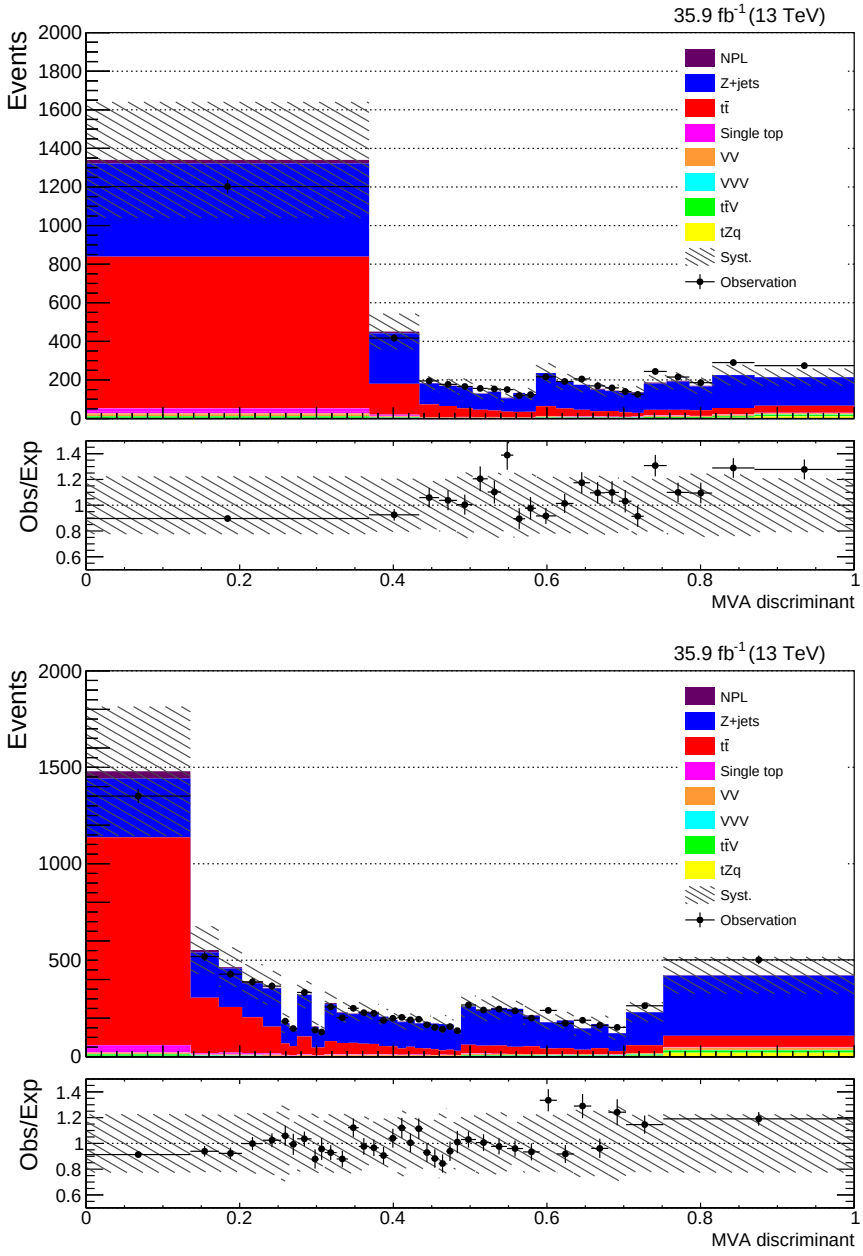

Figure 7.28: Pre-fit distributions of the BDT discriminant for the ee channel (top) and $\mu\mu$ channel (bottom) for simulation and data.

Chapter 8

Results

Following providing the multivariate analysis technique described in Section 7.6 with the simulated samples, and their systematic variations, and data, the resultant set of BDT discriminator distributions can be used to perform a measurement.

The following chapter describes the statistical methodology used to analyse these distributions and produce the first measurement of the signal process' cross section along with its expected significance. Following a discussion of the impact that the systematic uncertainties have on the fitted results, the result presented is compared with those from the already published searches for tZq production made using the trilepton final state.

8.1 Statistical Methodology

The Higgs Analysis Combined Limit (`combine`) tool [191], a framework based on the RooStats package [192, 193], was used to perform a binned Maximum Likelihood Fit (MLF) to determine the cross section of the signal process using the profile likelihood method [194].

8.1.1 Likelihood Model

For the signal and background processes considered in the search, the expected event yield λ in bin i of the distribution considered (i.e. the BDT discriminator) is given by Equation (8.1):

$$\lambda_i = \mu s_i + \sum_{j}^{n_{bkgs}} b_j \tag{8.1}$$

where s and b are the expected number of signal and background events, respectively, the index j runs over the number of background sources, n_{bkgs}, and μ is the signal strength modifier. The signal strength modifier is typically used instead of directly determining the

expected (and observed) cross section of a process as it makes the comparison of different results (particularly from different experiments) more straightforward. The relationship between μ and the observed and expected cross sections, σ_{obs} and σ_s, is given by Equation (8.2):

$$\mu = \frac{\sigma_{obs}}{\sigma_s} \tag{8.2}$$

The uncertainties associated with the simulated predictions for the signal and background processes are accounted for by the inclusion of a set of nuisance parameters θ. Therefore, as s_i and b_i are dependent on θ, they become $s_i = s_i(\theta)$ and $b_i = b_i(\theta)$.

Assuming that the number of observed events, n_i, in any given bin of the distribution considered will be distributed according to Poisson statistics, the probability of observing n_i is given by Equation (8.3):

$$\mathcal{P}(n_i|\lambda_i) = \frac{\lambda_i}{n_i!}e^{-\lambda_i} = \frac{\big(\mu s_i(\theta) + b_i(\theta)\big)^{n_i}}{n_i!}e^{-\mu s_i(\theta) - b_i(\theta)} \tag{8.3}$$

A probability density function, $\rho(\theta|\tilde{\theta})$, is used to describe all the sources of uncertainty for the nuisance parameters, where $\tilde{\theta}$ is the set of nominal values for the the best estimate of the nuisances. For the search presented in this thesis, it is assumed that each source of systematic uncertainty is either 100% correlated or uncorrelated. This allows each systematic uncertainty to be incorporated into the likelihood function in a clean factorised form. Shape uncertainties are modelled by vertically morphing the nominal shape template up and down by one σ. The normalisation/rate uncertainties are treated as log-normal distributed nuisance parameters [194, 195].

Thus, the likelihood for the entire dataset can be expressed as the product of the Poisson probabilities, $\mathcal{P}$, for all bins and the nuisance parameters' probability density function, as given by Equation (8.4).

$$\mathcal{L}(n_i|\mu,\theta) = \prod_{i=1}^{N} \mathcal{P}\big(n_i|\mu s_i(\theta) + b_i(\theta)\big)\rho(\theta|\tilde{\theta}) \tag{8.4}$$

A test statistic, q_μ, can be constructed to evaluate the compatibility of data with the *signal plus background* (s+b) ($\mu = 1$) and *background only* (b-only) ($\mu = 0$) hypotheses or between the different hypotheses. The test statistic used by the ATLAS and CMS is defined as the log-likelihood ratio in Equation (8.5):

$$q_\mu = -2\ln\frac{\mathcal{L}(data|\mu,\hat{\theta}_\mu)}{\mathcal{L}(data|\hat{\mu},\hat{\theta})} \text{ , where } 0 \leq \hat{\mu} \leq \mu \tag{8.5}$$

where $\hat{\theta}_\mu$ refers to the maximum likelihood estimators of θ for a given μ, $\hat{\mu}$ and $\hat{\theta}$ correspond to the global maximum of the likelihood and can refer to either real observed data or *pseudo-data*. By definition $\hat{\mu}$ cannot take negative values as physics defines the signal rate as positive. The constraint $\hat{\mu} < \mu$ is applied to ensure a one-sided confidence interval.

8.1.2 Signal Strength Modifier Calculation and Significance

The signal strength modifier for the signal process was calculated using the profile likelihood method, which maximises the likelihood function in Equation (8.4) by allowing μ and θ to float. Using the global likelihood maximum values of μ and θ, $\hat{\mu}$ and $\hat{\theta}$, the test statistic was used to determine the 68% confidence limits for the measured signal strength modifier by allowing $\hat{\theta}_\mu$ to float in order to maximise the likelihood and varying μ until a value that represents 68% agreement is obtained.

Both the expected and observed significances for the signal strength modifier were calculated by evaluating the s+b hypothesis and data, respectively, against the b-only hypothesis using the the test statistic in Equation (8.5). Therefore the significances are the fractions of the events for the b-only hypothesis likelihood function whose likelihood values exceed that of the observed value for data or the median value for the s+b hypothesis.

As producing pseudo-data using an ensemble of toy MC samples to obtain the values for s+b and b hypotheses' likelihood functions can be computationally intensive, the *asymptotic* method is used when the number of expected events is sufficiently large. The asymptotic method produces one representative dataset, known as the *Asimov dataset*, that which is defined as being constructed such that all observable quantities are equal to their expectation values. This method was used for the analysis presented as it removed the need to generate toy MC datasets. A full description of the asymptotic approximation is given in [194].

8.2 Statistical Analysis Results

The observed signal strength for tZq production was determined to be $6.213^{+2.339}_{-2.695}$ and $4.725^{+1.916}_{-2.015}$ for the ee and $\mu\mu$ channels, respectively, corresponding to a significances of 2.722σ and 2.501σ, respectively. Using the reference NLO cross section of $\sigma(tZq, Z \to l^+l^-)$ = 94.2 fb [58], these signal strengths corresponds to cross section of $194.8^{+73.4}_{-84.7}$ fb and $148.5^{+60.3}_{-63.4}$ fb for the ee and $\mu\mu$ final states, respectively. These results are consistent within two σ of the SM predictions and the measured combined signal strengths of 0.75 ± 0.28 and $1.45^{0.48}_{-0.42}$ made using the trilepton final state at $\sqrt{s} = 13\,\text{TeV}$ by the ATLAS and CMS collaborations, respectively [61, 62].

The results presented here are the initial results obtained following the unblinding of the analysis for this thesis. Whilst CMS has given permission for this unblinding, the results have not been fully reviewed by the collaboration and therefore these results should not be considered to have been endorsed by CMS. It is expected that further work will need to be done in order to achieve the required standard for journal publication on behalf of the CMS collaboration. At their request, no combined result for the two final states has been presented in this thesis.

The observed signal strengths, cross sections, and expected and observed significances for the ee and $\mu\mu$ channels are shown in Table 8.1.

Table 8.1: The expected signal strengths and corresponding cross sections for the ee and $\mu\mu$ channels.

Channel	ee	$\mu\mu$	Combined
Signal Strength	$6.21^{+2.34}_{-2.70}$	$4.73^{+1.92}_{-2.02}$	-
Cross section (fb)	$194.8^{+73.4}_{-84.7}$	$148.5^{+60.3}_{-63.4}$	-
Significance (expected) (σ)	0.46	0.54	0.70
Significance (observed) (σ)	2.72	2.50	-

8.2.1 Post-fit BDT Discriminant Distributions

The BDT discriminant distributions following the MLF for data and simulation are shown in Figure 8.1. When compared to the pre-fit distributions in Figure 8.1, it can be seen that the MLF has constrained the impact of the systematic uncertainties and increased the tZq yield to obtain the best possible answer. While the tZq contribution is more evident in the BDT discriminant distributions following the MLF, it is clear from the $\hat{\mu}$ that the tZq yield is still consistent with the SM predictions.

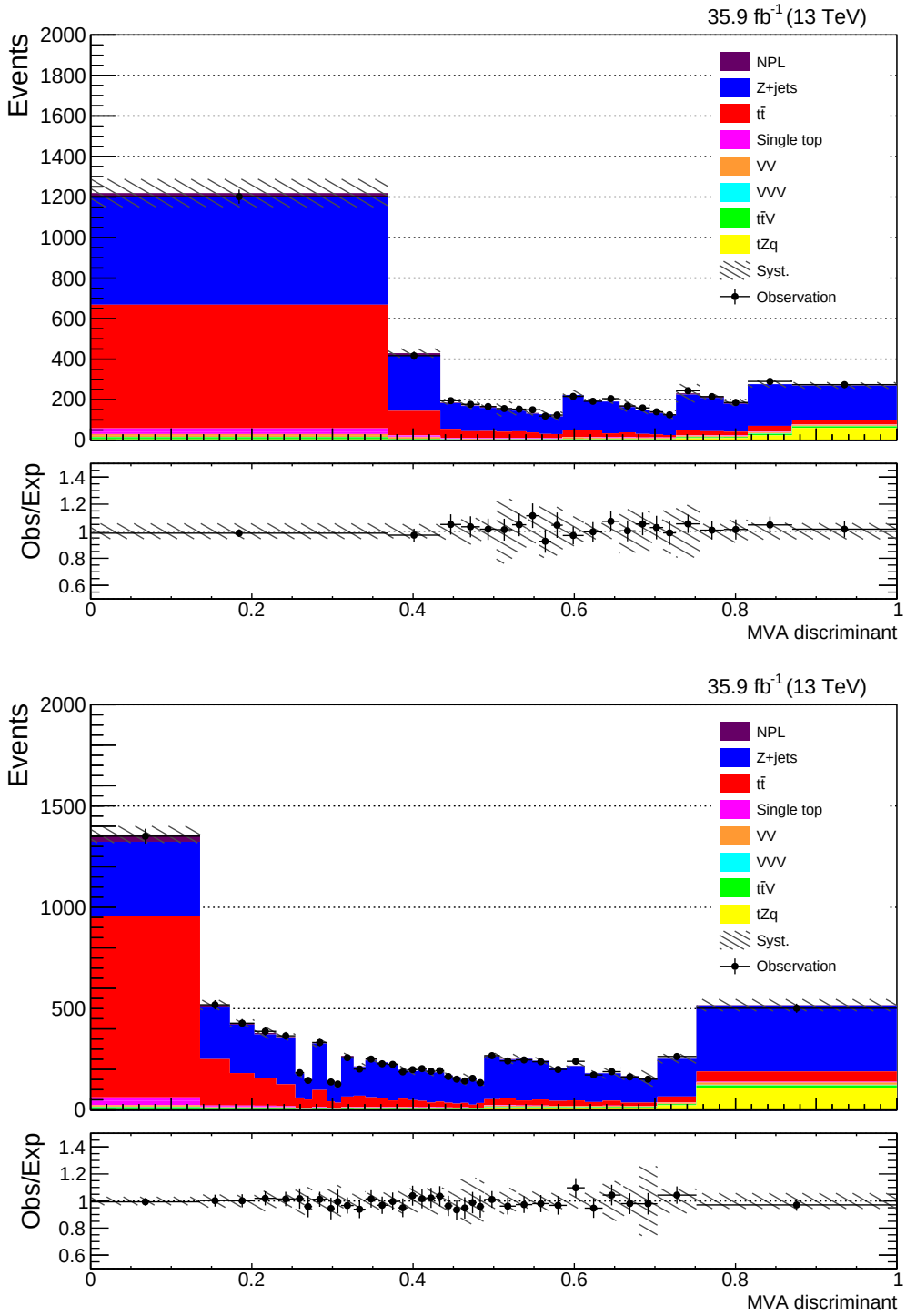

Figure 8.1: Post-fit distributions of the BDT discriminant for the ee channel (top) and $\mu\mu$ channel (bottom) for simulation describing the s+b hypothesis and data.

8.2.2 Post-fit Impact of the Systematic Uncertainties

Figure 8.2 illustrates the impact of each of the sources of systematic uncertainty on the signal strength modifier $\hat{\mu}$ for the ee and $\mu\mu$ channels. The left-hand side of this plot shows best fit value of the nuisance parameters where the asymmetric error bars are the pre-fit uncertainty divided by the post-fit uncertainty. The right-hand side illustrates the impact of varying a nuisance parameter to its $\pm\sigma$ post-fit values on the $\hat{\mu}$.

All of the experimental and theoretical scale uncertainties were constrained by the MLF, with the ME and PS scale and PDF uncertainties having the greatest, and comparable, impact on the $\hat{\mu}$ for both of the signal process' final states. In addition, it was found that the impact of the ME - PS matching energy threshold nuisances parameters were comparable to that of the most significant non-PDF experimental uncertainties. Consequently, the measurement's precision would be best improved by an improved theoretical understanding of tZq production and the dominant background processes and by a reduction in the uncertainty on the parton distributions used for generating MC samples. Reducing the jet energy corrections' and the luminosity measurement's uncertainties would further improve the result's precision given that their effect on the $\hat{\mu}$ was similar to the most impactful non-PDF experimental uncertainties for both of the final states.

Whilst the cross section normalisation uncertainties associated with the NPLs and minor background contributions were not constrained by the MLF, they have a negligible impact on the $\hat{\mu}$. In contrast, despite being constrained in the fit, both the $t\bar{t}$ and Z+jets normalisation uncertainties had a significant impact on the $\hat{\mu}$, with the $t\bar{t}$ cross section uncertainty having an impact on the $\hat{\mu}$ comparable to the theoretical scale for the $\mu\mu$ final state. In addition, it was found that both the $t\bar{t}$ and Z+jets cross section normalisation nuisance parameters were offset from their pre-fit values. Given that the cause for these offsets was not understood at the time of the unblinding of this analysis, it is imperative for future measurements that their cause is established in order to ensure that the two most important background processes for this search are properly understood.

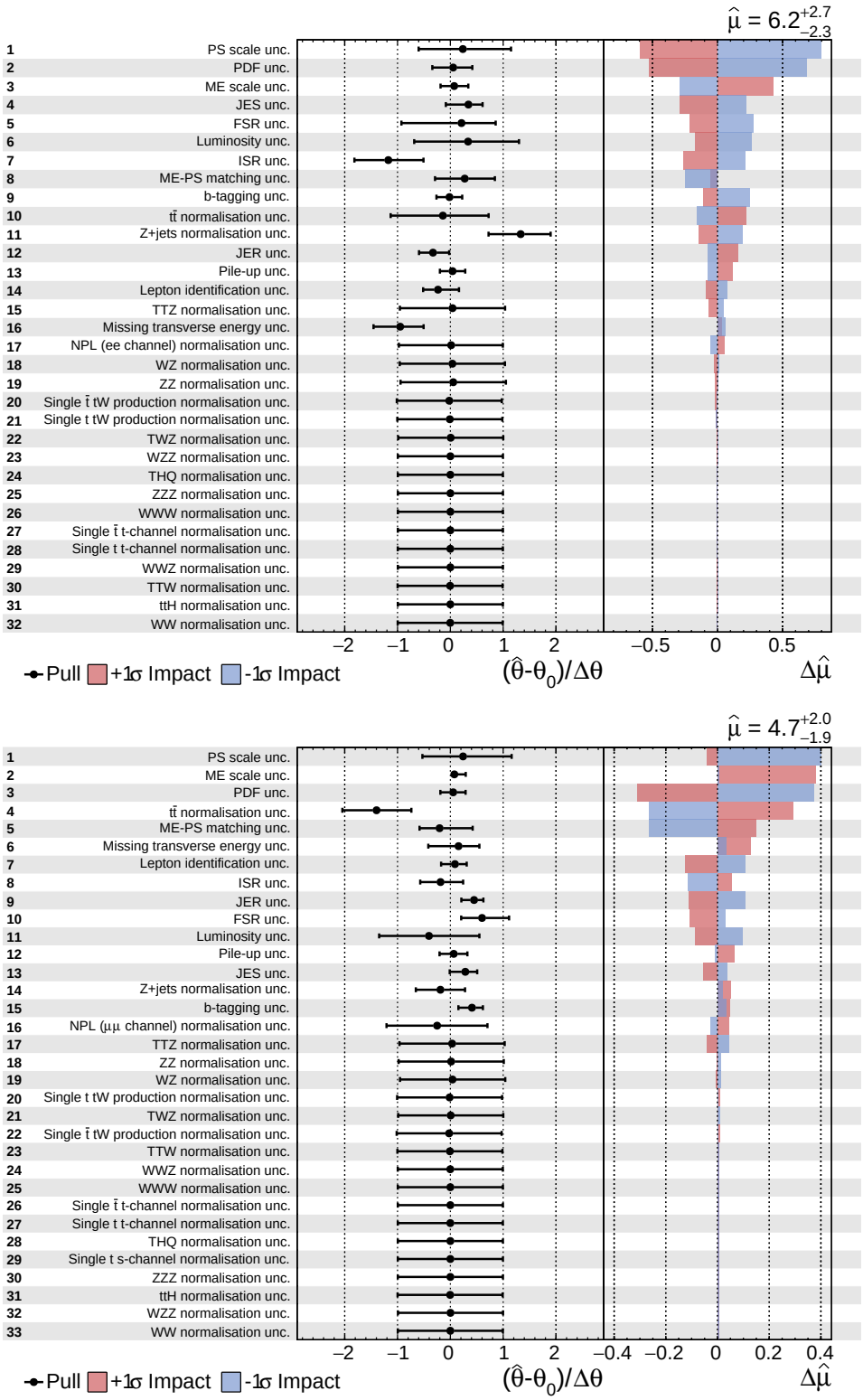

Figure 8.2: The best fit value and uncertainties of the nuisance parameters are shown on the left-hand side of the plot, where $\widehat{\theta}$ and θ_0 are the post-fit and pre-fit values for a nuisance parameter and $\Delta\theta$ is the pre-fit uncertainty. The right-hand side of the plot shows the impact that each systematic uncertainty has on the signal strength parameter $\hat{\mu}$ when varied by $\pm 1\sigma$. The top and bottom plots refer to the ee and $\mu\mu$ channels, respectively.

8.3 Discussion of other searches for tZq at the Large Hadron Collider

The search for the decay of a single top quark produced in association with a Z boson presented in this thesis is the first one that has been made using the dilepton final state at the LHC.

Previously the production of a single top quark in association with a Z boson has been searched for using the trilepton final state at the LHC by the ATLAS and CMS collaborations. The CMS Collaboration has performed analyses at both $\sqrt{s} = 8\,\text{TeV}$ and $\sqrt{s} = 13\,\text{TeV}$. The search at $\sqrt{s} = 8\,\text{TeV}$ used the 2012 dataset of $19.7\,\text{fb}^{-1}$ and measured a signal strength of $1.22^{+0.98}_{-0.85}$, corresponding to an observed (expected) significance of 2.4σ (1.8σ) [60]. The subsequent search by CMS observed tZq production at $\sqrt{s} = 13\,\text{TeV}$, using the 2016 dataset of $35.9\,\text{fb}^{-1}$. This search measured a signal strength of $1.31^{+0.35}_{-0.33}(\text{stat})^{+0.31}_{-0.25}(\text{syst})$ with an observed (expected) significance of 3.7σ (3.1σ) [62]. The first evidence for tZq production was found by the ATLAS collaboration at $\sqrt{s} = 13\,\text{TeV}$ using $36.1\,\text{fb}^{-1}$ of data collected during 2015-2016, measuring a signal strength of 0.75 ± 0.28 at an observed (expected) significance of 4.2σ (5.4σ) [61].

The signal strength measured using the dilepton final state is consistent within two standard deviations of both the SM prediction and the measurements of tZq that have been made using the trilepton final state. The difference between the expected and observed significances of the trilepton final state measurements and the expected significance of the dilepton final state measurement presented is due to the differing backgrounds of these two final states. As searches for the trilepton final state require the presence of three leptons, backgrounds with only two leptons are suppressed. Therefore, the largest background processes for this final state are WZ+jets, $\text{t}\bar{\text{t}}\text{Z}$ and those with large production cross sections that contribute to the NPL background, such as Z+jets and $t\bar{t}$. In contrast, the dilepton final state's requirement of two leptons that are compatible with a Z boson decay suppresses processes that do not produce leptons from a Z boson decaying and those that contribute to the NPL background. The final state of two leptons and multiple jets however, is identical to those of a large number of background processes that have cross sections many orders of magnitude larger than those for the trilepton final state, such as Z+jets and $t\bar{t}$. Consequently, searches for tZq production using the dilepton final state are statistically limited to a greater degree than those using the trilepton final state.

Chapter 9

Conclusion

9.1 Summary of the tZq analysis

Following the restart of the LHC in 2015, the LHC's increased centre-of-mass collision energies and instantaneous luminosities have made it possible to undertake measurements of rare processes involving top quark and electroweak interactions. In this thesis a search was presented for the production of a top quark in association with a Z boson using the dilepton final state using a shape based analysis. This analysis focussed on understanding and constraining processes that involve the production of two promptly produced leptons that are consistent with a Z boson decay and those that involve at least one non-promptly produced lepton. A Boosted Decision Tree was used to further enhance the separation between the signal from tZq production and background, using a set of variables that were identified as having the greatest discriminating power. Using a Maximum Likelihood Fit, signal strengths of $6.213^{+2.339}_{-2.695}$ and $4.725^{+1.916}_{-2.015}$ were measured for the signal process in the ee and $\mu\mu$ channels, respectively. These measurements correspond to an observed excess over the background-only hypothesis of 2.72σ and 2.50σ for the ee and $\mu\mu$ channels, respectively. Using simulation, the expected significances for the ee and $\mu\mu$ channels and their combination were determined to be 0.46σ, 0.54σ and 0.70σ, respectively.

These results constitute the first measurement of tZq that has been made using the dilepton final state and are consistent within two standard deviations of the SM prediction and measurements made using the trilepton final state. Given that these results have not been fully reviewed by the CMS collaboration, further work is required in order to interpret this measurement and to achieve the standard required for journal publication on behalf of the CMS collaboration.

9.2 Future measurements

As the observation of tZq is primarily limited by statistics of the dataset used, the single greatest improvement to the sensitivity of this analysis would be the incorporation of additional data collected by the CMS experiment. It is anticipated that including the $41.5\,\text{fb}^{-1}$ of proton-proton collision data at $\sqrt{s} = 13\,\text{TeV}$ collected by the CMS experiment during 2017 will improve the expected significance of the result to approximately 1.1σ.

Further to including addition data for future measurements, it will be imperative to understand why the observed significance of the measurement presented is considerably larger than the expected significance. Part of this work will involve ensuring that the Z+jets and $t\bar{t}$ processes are accurately modelled, including investigating the use of data-driven estimates for these processes and determining why the Z+jets sample simulated at NLO does not describe data well. Understanding the largest backgrounds for the analysis is especially pertinent given that it is not currently understood why the nuisance parameters associated with the uncertainty of their cross sections are offset from their pre-fit values to varying degrees in both channels.

The precision of the cross section measurement made would also benefit from improved modelling of the theoretical uncertainties of the signal and dominant backgrounds and by a reduction in the parton distributions' uncertainties as these sources of systematic uncertainties were found to have the greatest impact on the post-fit signal strength.

The result presented was based on the February 2017 reprocessing of the 2016 data and September 2016 reprocessing of the corresponding simulation samples. These datasets have subsequently been reprocessed to incorporate updated jet energy corrections and improved alignments and calibrations of the CMS detector. As such, future measurements will benefit from the improved accuracy of the jet energy scale and resolution corrections of these reprocessed datasets.

Future measurements may potentially benefit from using alternative physics object selection algorithms that have been shown to improve the performance of other CMS analyses. b-tagging algorithms that use deep neural networks to produce a discriminator have been demonstrated to have higher b-tagging efficiencies, lower misidentification rates and smaller uncertainties than the CSVv2 algorithm used in the analysis presented. Other analyses have found that MVA-based lepton identification algorithms have lower NPL misidentification rates than the cut-based identification algorithm used in the analysis presented. While the modelling of the NPL background is not a major limiting factor of the analysis presented, it is not currently known if a MVA-based lepton identification algorithm would be significantly more efficient than the current lepton identification algorithms.

The robustness of the blinding methodology would be improved by parametrising the χ^2-like variable so that it better describes the structure present in the σ_t and σ_W distributions

observed in the signal sample and by optimising the values of χ^2 used to define the signal and side band regions on the basis of the expected significance of the result in each.

Once an accurate measurement of the tZq cross section can be made, it should be possible to probe the strength of the tZ and WWZ couplings. Given that tZq production is expected to be as sensitive to the strength of the WWZ coupling as WZ production, this process will provide valuable complimentary measurements of this coupling [58].

9.3 Summary of the TMTT track finding processor system studies

The *TMTT* collaboration has proposed a track finder system for the CMS tracker at the HL-LHC that is capable of contributing information to the CMS Level-1 trigger. The *TMTT* track finding system identifies track candidates using time-multiplexed Hough Transforms in the r-φ plane, a Kalman Filter to filter these candidates and precisely fit track parameters to them and a duplicate removal process. In this thesis a number of studies were presented that were undertaken as part of the development of the this track finding system.

Prior to the hardware demonstrator review in 2016 of the three proposed track finding systems, a linearised χ^2 track fitting algorithm was explored as an alternative to the Kalman Filter. The linearised χ^2 track fitting algorithm was shown to be capable of both fitting precise helix parameters to the tracks found by the Hough Transform and filtering out hits incorrectly assigned to tracks and incorrectly reconstructed tracks. Following the evaluation and comparison of both the χ^2 track fit algorithm and the Kalman Filter, it was decided not to continue development of the former algorithm. This decision was made as it was determined that the Kalman Filter filtering and fitting performance was superior than that of the χ^2 track fit, particularly in the forward regions.

The flexibility for the upgraded tracker to be able to reconstruct tracks down to a lower p_{T} threshold of 2 GeV is potentially desirable and was initially studied as part of the 2016 demonstrator review. The ability of the proposed track finding system to reconstruct such low transverse momenta tracks ($2\,\mathrm{GeV} < p_{\mathrm{T}} < 3\,\mathrm{GeV}$) was shown to be considerably improved by accounting for the effects of multiple scattering. For the Hough Transform, this involved using decreased precision Hough Transform cells to mitigate against scattering causing stubs to be found in adjacent cells. The Kalman Filter's covariance matrix was modified to incorporate the uncertainty in the hit position caused by the effects of multiple scattering by including a term that described the average scattering angle as a function of p_{T}.

9.4 Future track finding processor system development

If the the linearised χ^2 track fitting algorithm is to be considered a viable alternative to the other track fitters developed for the *TMTT* project. While only a small number of track derivatives are required for the calculations in the barrel region, it is uncertain whether there are sufficient resources to tabulate the endcap derivatives required on current hardware. If it can be demonstrated that current FPGAs can implement this algorithm, it will need to be demonstrated that the χ^2 track fitter's performance is competitive with the Kalman Filter and Linear Regression. While it may not be possible to make the χ^2 track fitter filter tracks as effectively as the Kalman Filter or Linear Regression, other improvements, such including the fitting of the transverse impact parameter, may improve its competitiveness.

Despite the improving the proposed system's ability to reconstruct tracks with low p_{T}, there are still a number of key areas that require investigating in order to understand the current limitations of the work done so far and how it may be improved upon. Currently it is not understood why the duplicate rate increases near the boundary between normal and reduced precision Hough Transform cells. This effect needs to be understood before an optimal value for the cell merging threshold can be determined. The Kalman Filter's performance is likely to be further improved by using a scattering constant term that accurately takes the volume of material a track has passed through into account. Implementing separate Kalman Filter χ^2 cuts for the r-φ and r-z planes is another potential improvement given that the dominant uncertainty contribution for the former varies depending on p_{T}.

The *TMTT* collaboration demonstrated in the 2016 review that a complete track finding system for the upgraded CMS tracker that met the baseline system requirements could be built using currently available technology. Since 2016 the development and optimisation of *TMTT* track finding system has continued using the so-called tilted barrel geometry for anticipated hardware for the final track finding system. By the end of 2018 it is anticipated that the proposed systems of the *TMTT* and *tracklet* projects will begin to converge to produce an all-FPGA hybrid track finding system. The final prototype for this all-FPGA track finding system system is anticipated to tested and validated by 2022 in order to ensure a successful installation, integration and commissioning of the upgraded tracker in 2025 prior to the start of HL-LHC operations.

Appendix A

Maths Notations

This appendix gives the definitions of the Pauli matrices and Dirac matrics [17] used in Chapter 2.

Pauli Matrices

$$\sigma = (\sigma_1, \sigma_2, \sigma_3) \tag{A.1}$$

$$\sigma_1 = \begin{matrix} 0 & 1 \\ 1 & 0 \end{matrix}, \sigma_2 = \begin{matrix} 0 & -i \\ i & 0 \end{matrix}, \sigma_3 = \begin{matrix} 1 & 0 \\ 0 & -1 \end{matrix} \tag{A.2}$$

Dirac Matrices

$$\gamma^\mu, \gamma^\nu = 2g^{\mu\nu} \tag{A.3}$$

where $g^{\mu\nu}$ is the Minkowski metric:

$$g^{\mu\nu} = \pm \begin{matrix} -1 & 0 & 0 & 0 \\ 0 & 1 & 0 & 0 \\ 0 & 0 & 1 & 0 \\ 0 & 0 & 0 & 1 \end{matrix} \tag{A.4}$$

Appendix B

Data and Simulation Comparison Plots

This appendix contains a selection of comparison plots between data and simulation for the signal region and the $t\bar{t}$ and Z+jets 0-bjet control regions. Unless otherwise stated, for the signal region and Z+jets 0-bjet control region plots, those on the left-hand side correspond to the ee channel and those on the right-hand side correspond to the $\mu\mu$ channel.

B.1 Signal Region

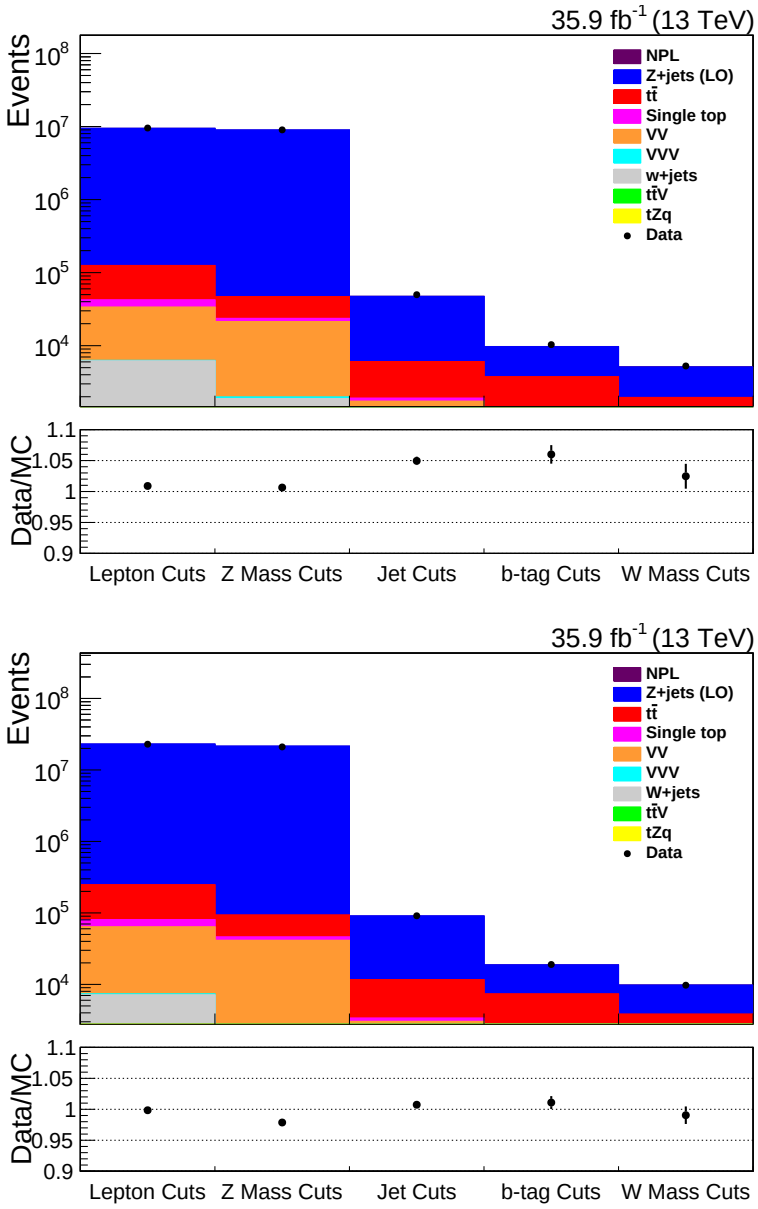

Figure B.1: The overall event yield for data and simulation at each stage of applying the signal region selection criteria and simulation corrections for the ee channel (top) and the $\mu\mu$ channel (bottom).

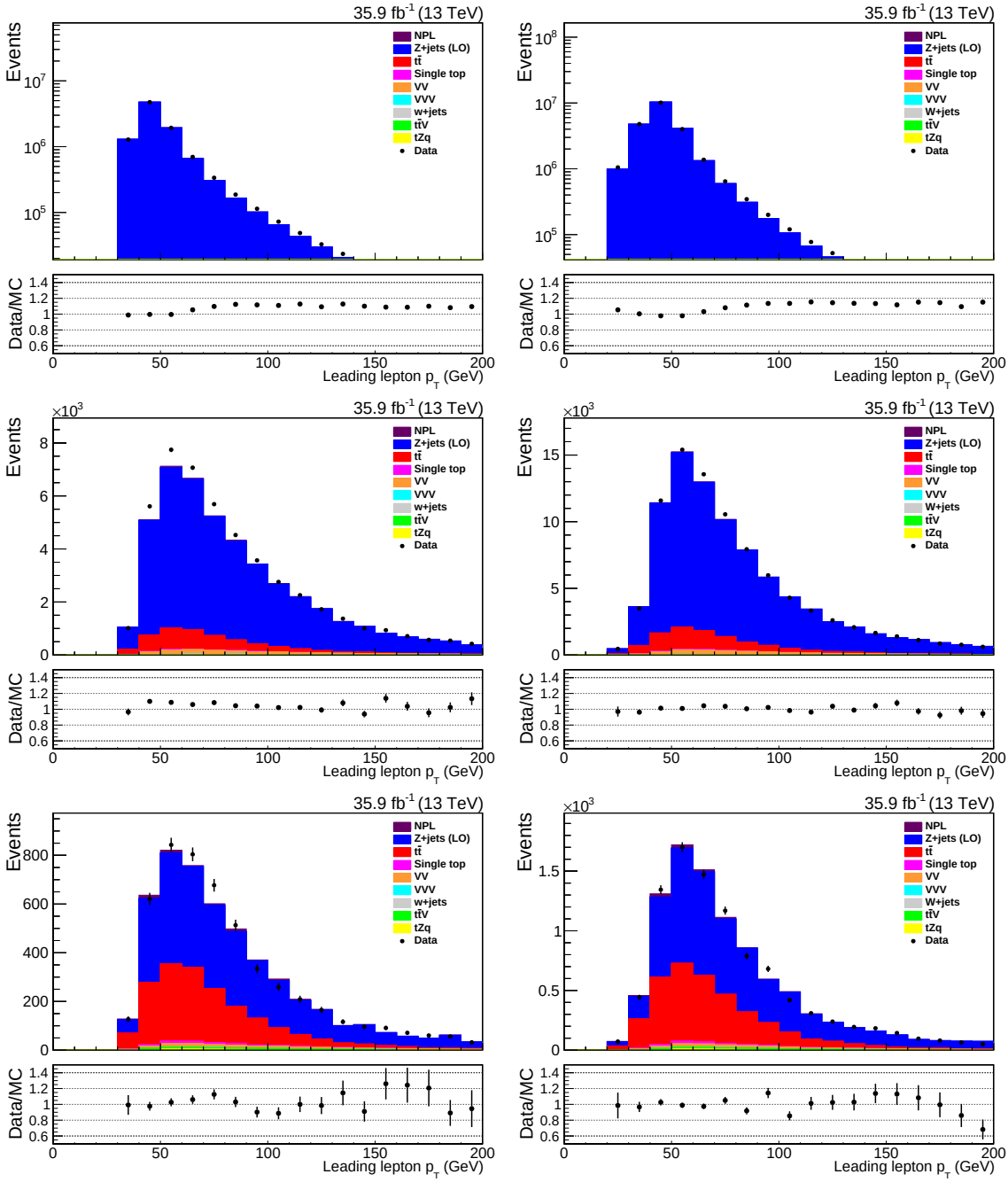

Figure B.2: The leading lepton p_{T} following only the lepton selection criteria (top), the jet selection criteria (middle) and all of the signal region selection criteria (bottom).

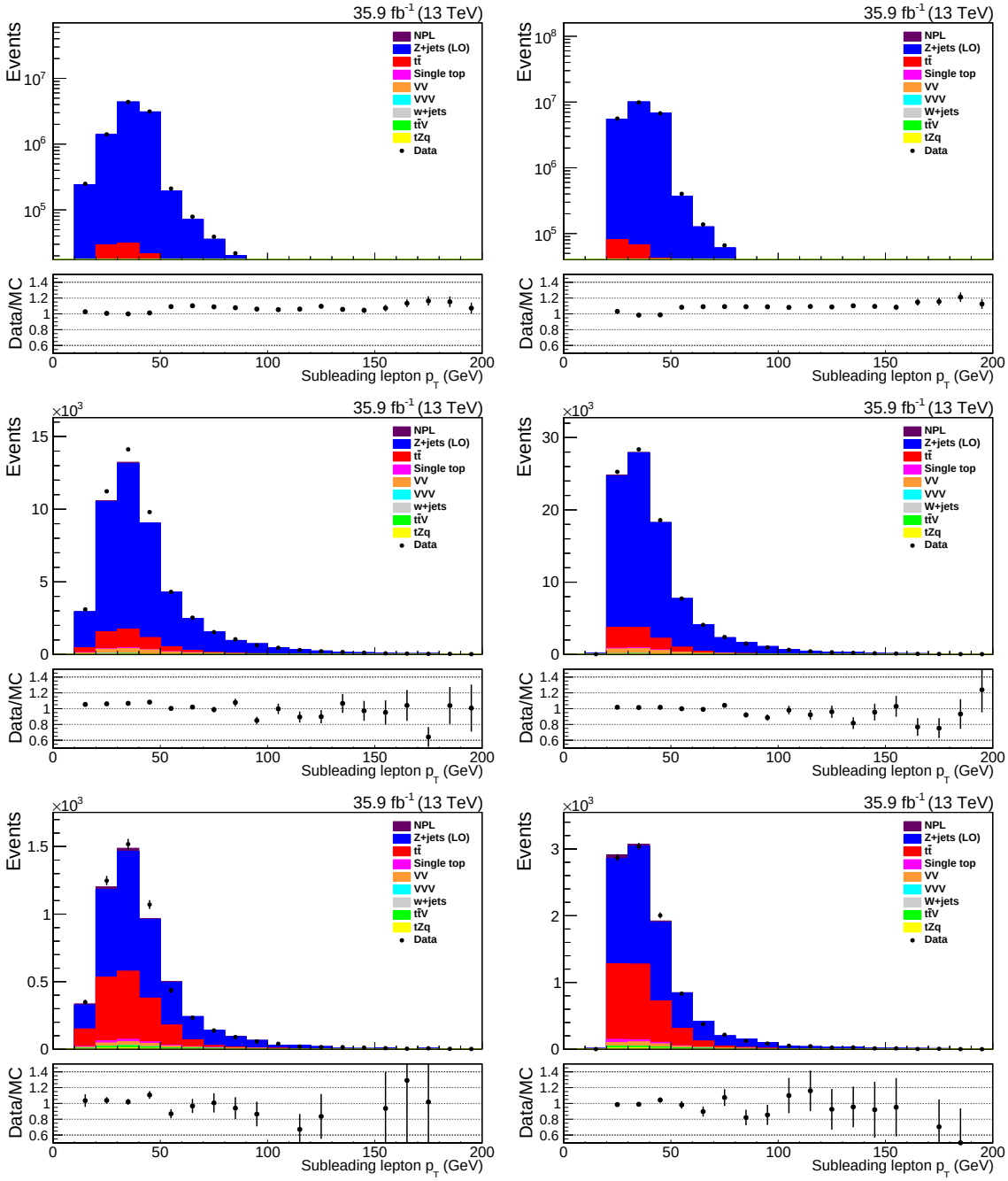

Figure B.3: The subleading lepton p_{T} following only the lepton selection criteria (top), the jet selection criteria (middle) and all of the signal region selection criteria (bottom).

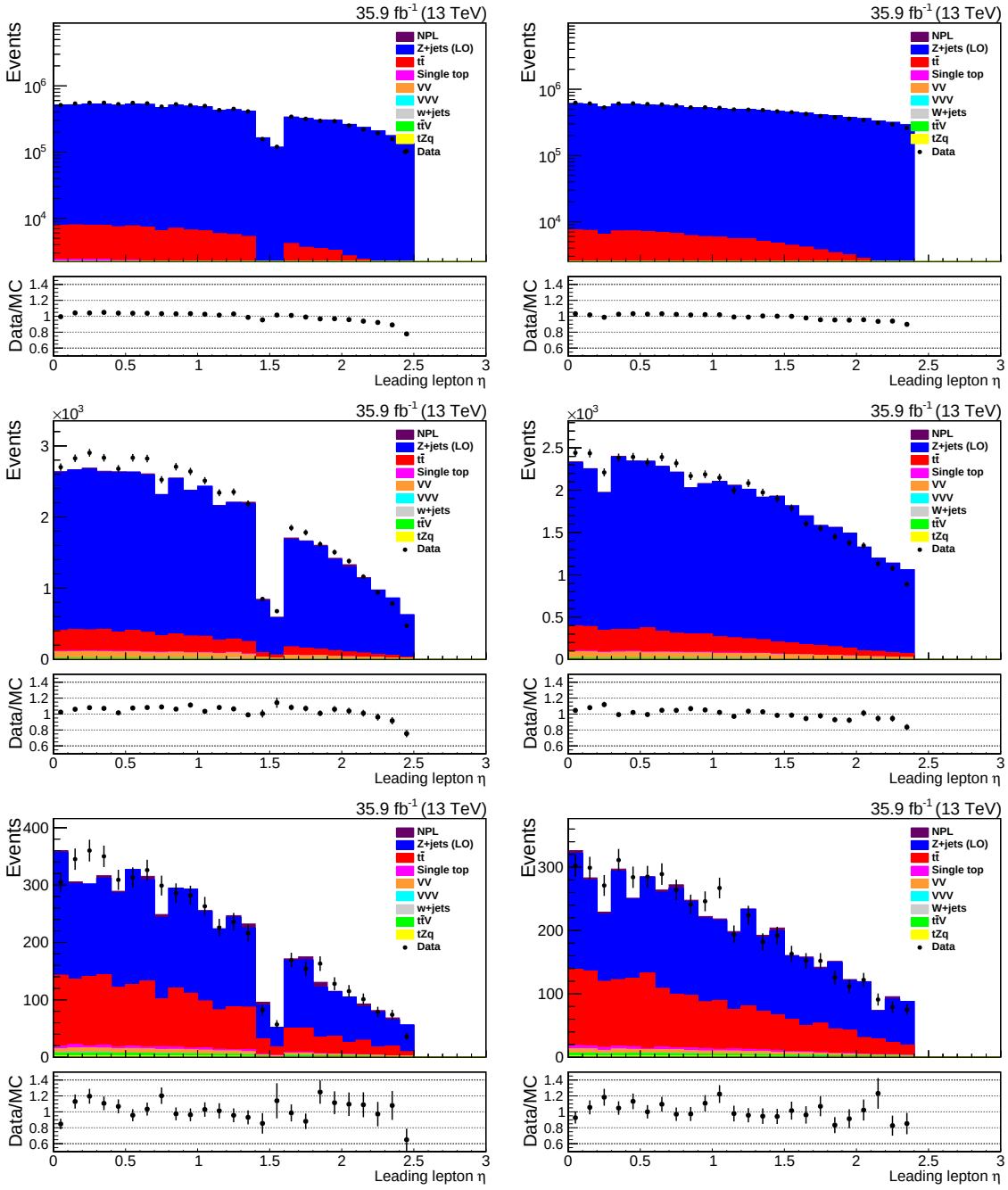

Figure B.4: The leading lepton η following only the lepton selection criteria (top), the jet selection criteria (middle) and all of the signal region selection criteria (bottom).

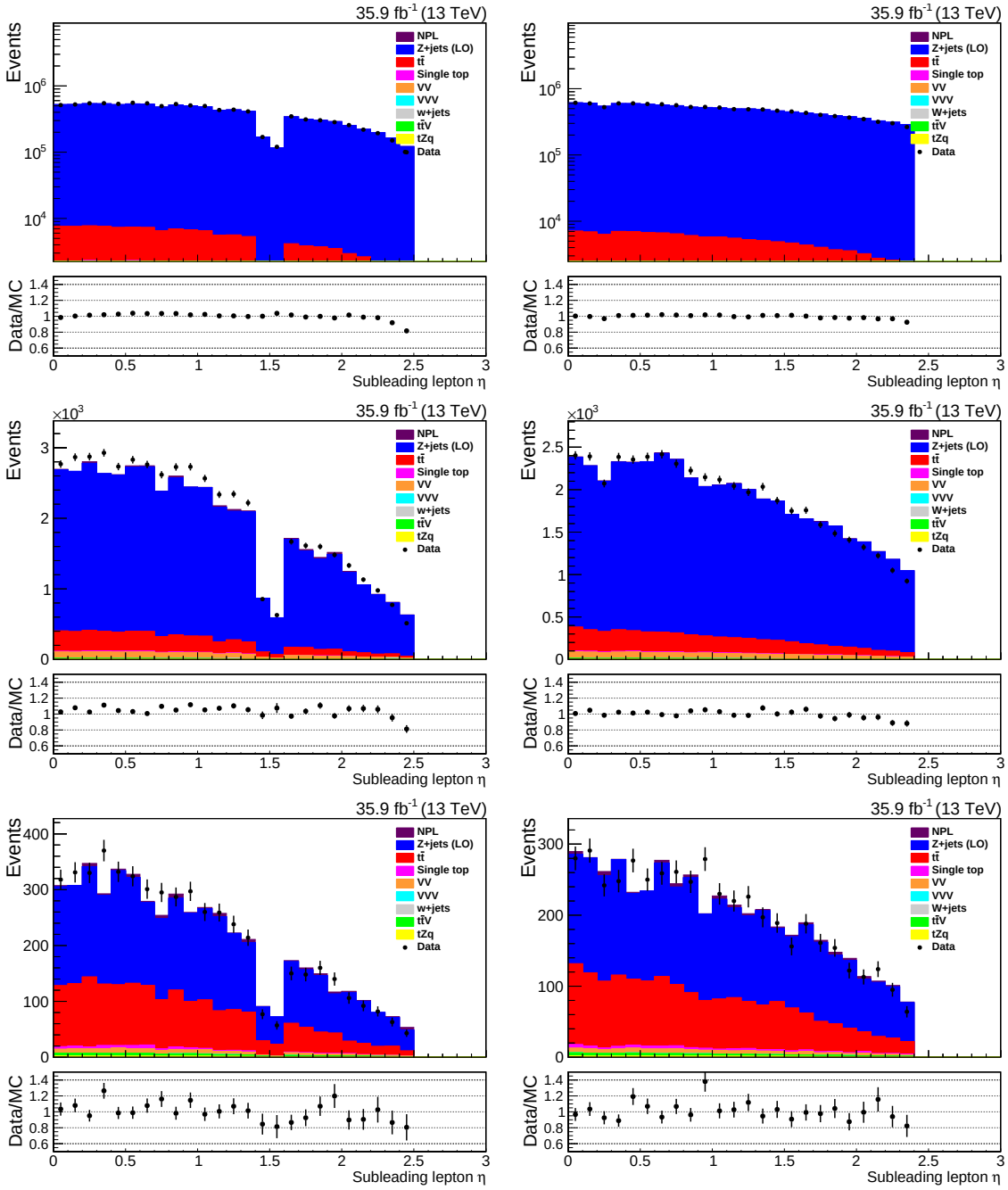

Figure B.5: The subleading lepton η following only the lepton selection criteria (top), the jet selection criteria (middle) and all of the signal region selection criteria (bottom).

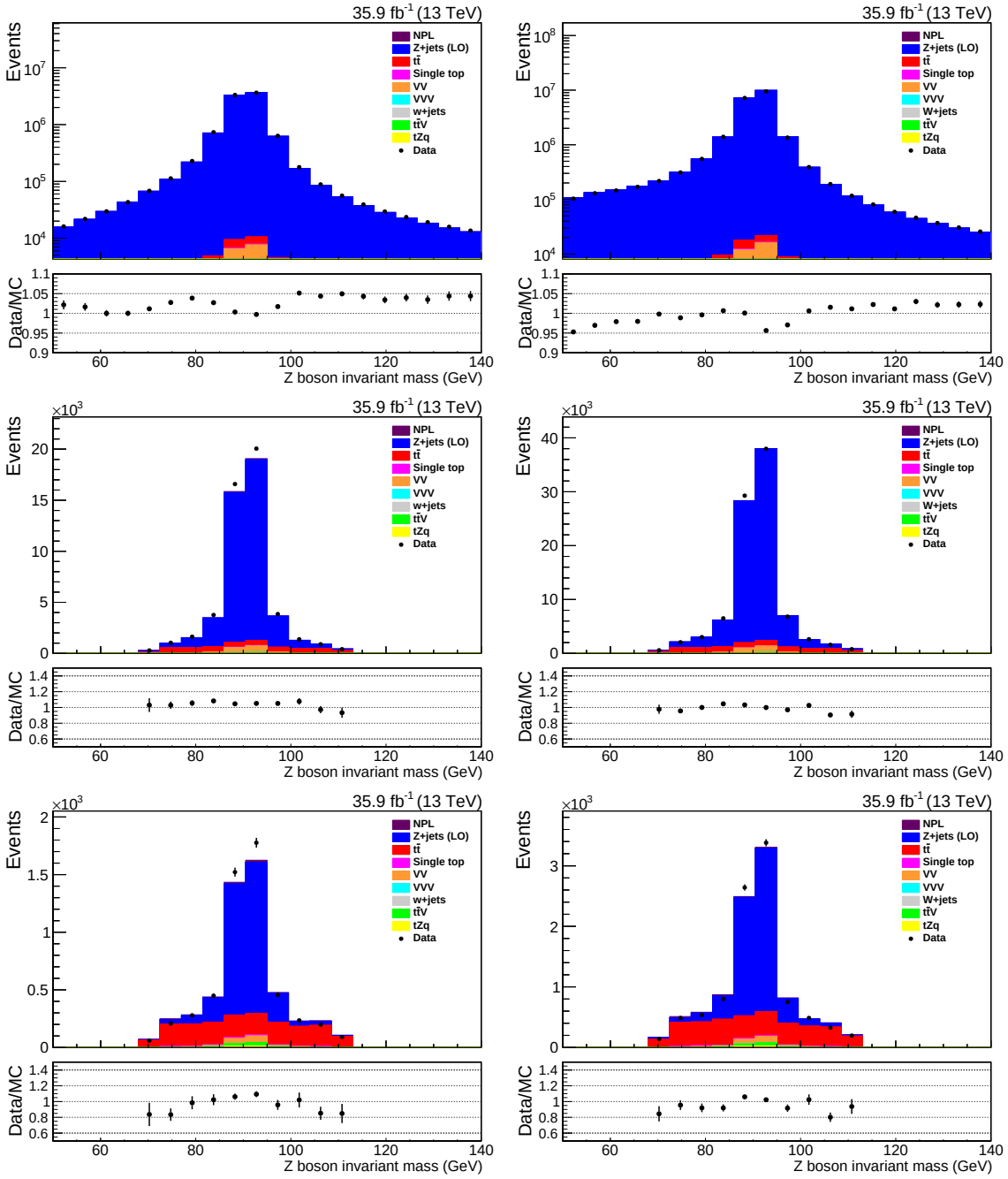

Figure B.6: The reconstructed Z boson mass following only the lepton selection criteria (top), the jet selection criteria (middle) and all of the signal region selection criteria (bottom).

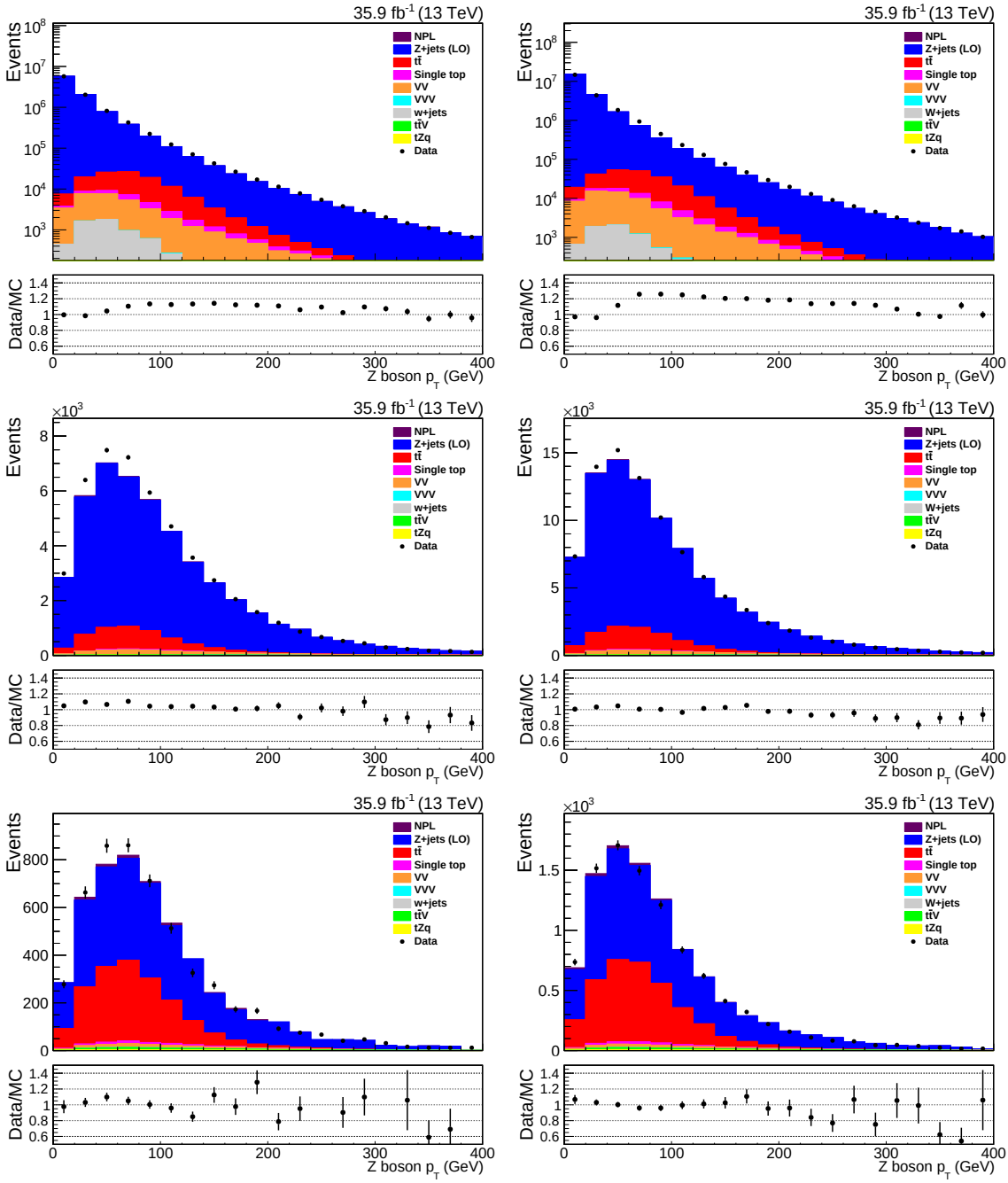

Figure B.7: The reconstructed Z boson mass p_{T} following only the lepton selection criteria (top), the jet selection criteria (middle) and all of the signal region selection criteria (bottom).

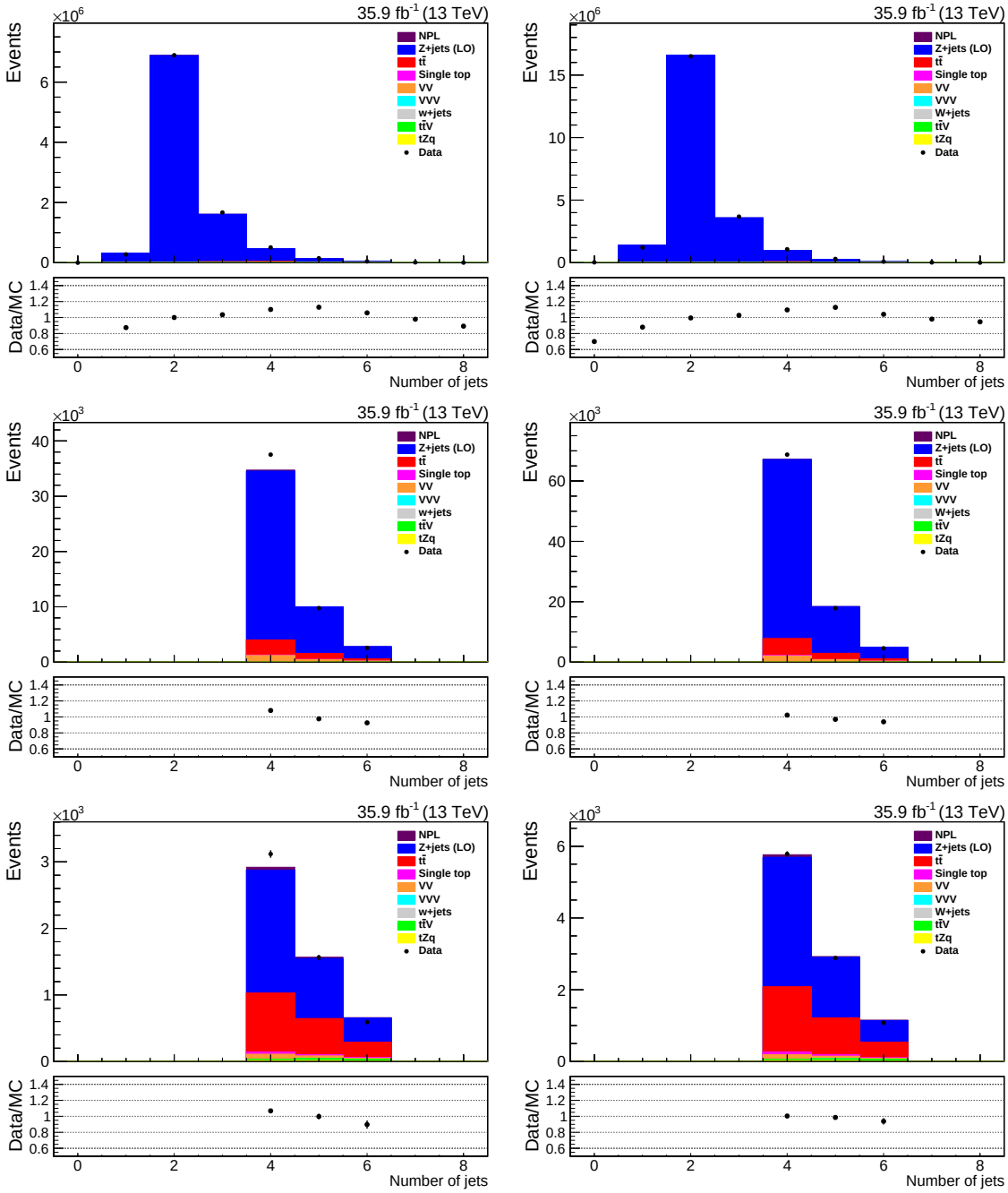

Figure B.8: The number of jets following only the lepton selection criteria (top), the jet selection criteria (middle) and all of the signal region selection criteria (bottom).

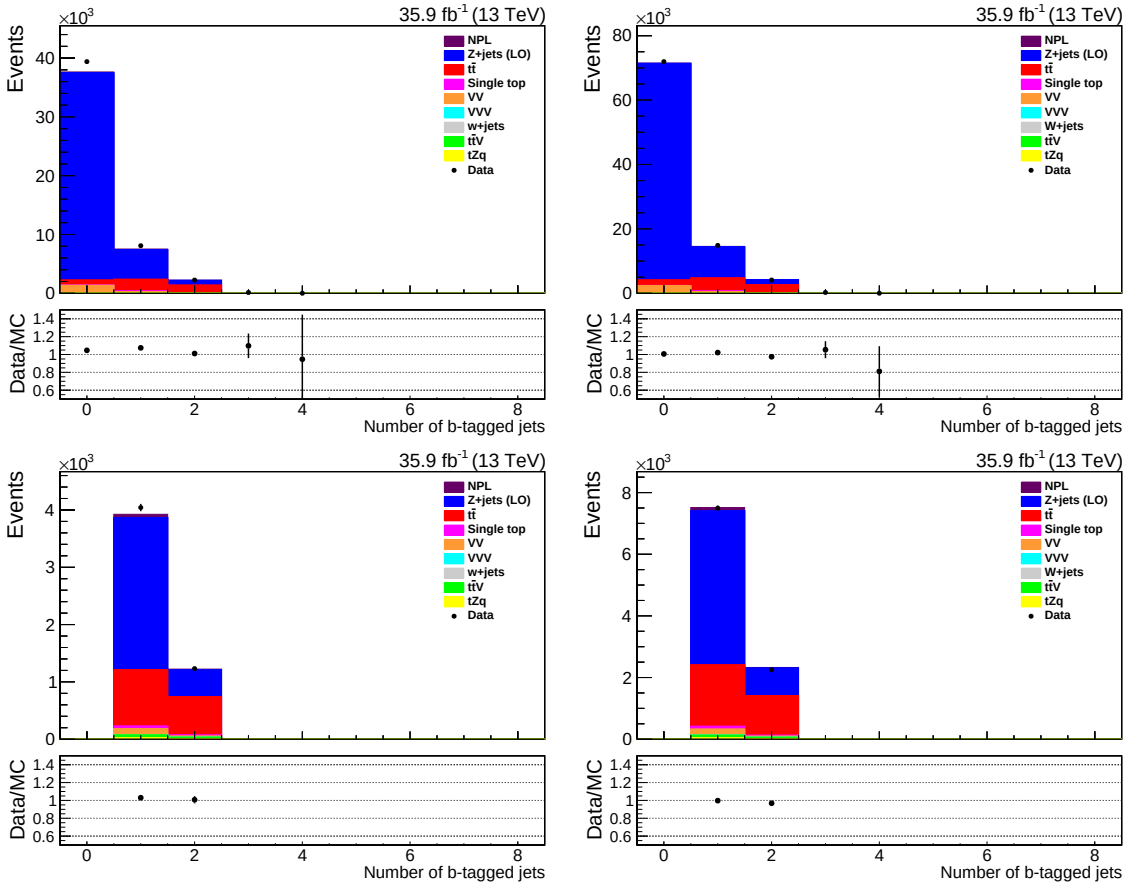

Figure B.9: The number of b-tagged jets following only the jet selection criteria (top) and all of the signal region selection criteria (bottom).

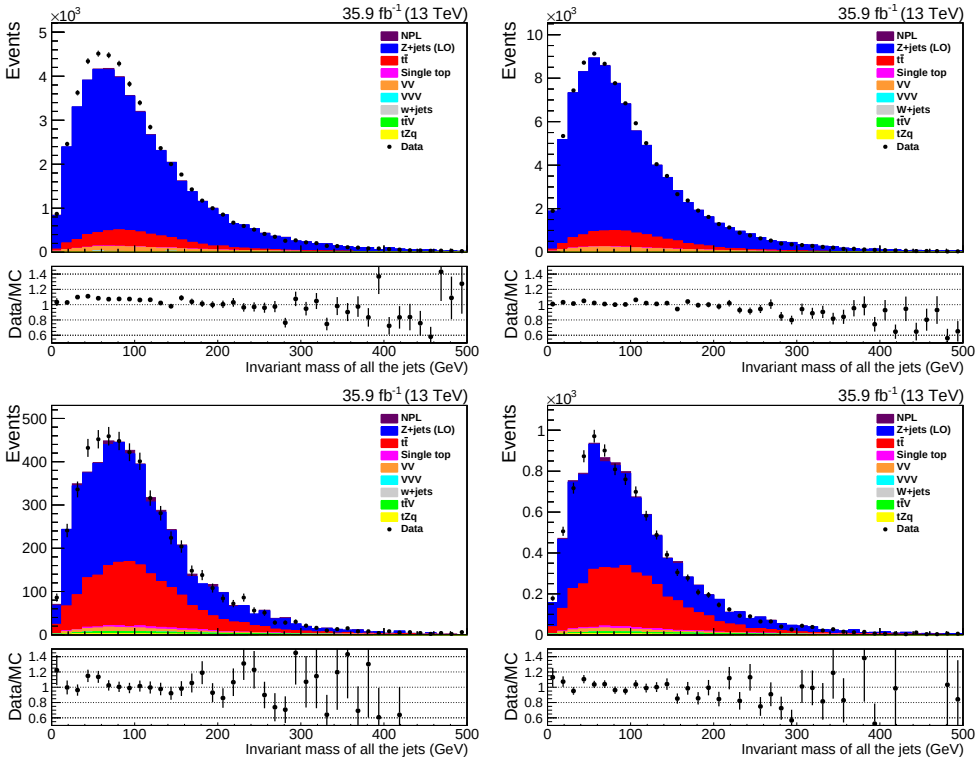

Figure B.10: The invariant mass of all of the jets in an event following only the jet selection criteria (top) and all of the signal region selection criteria (bottom).

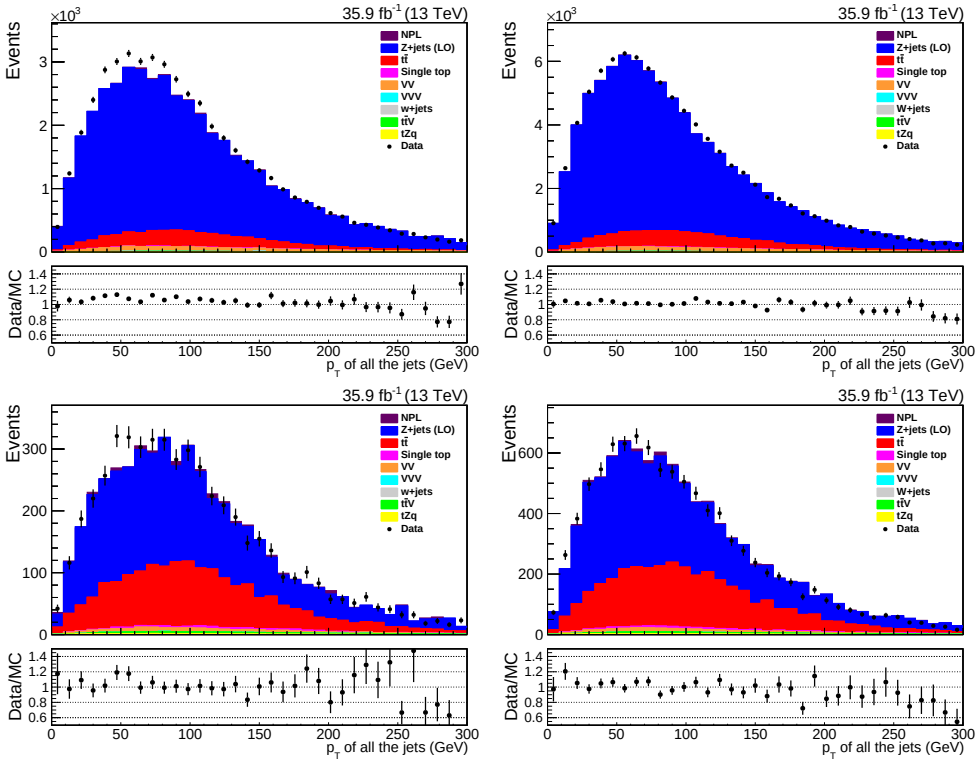

Figure B.11: The total p_{T} of all of the jets in an event following only the jet selection criteria (top) and all of the signal region selection criteria (bottom).

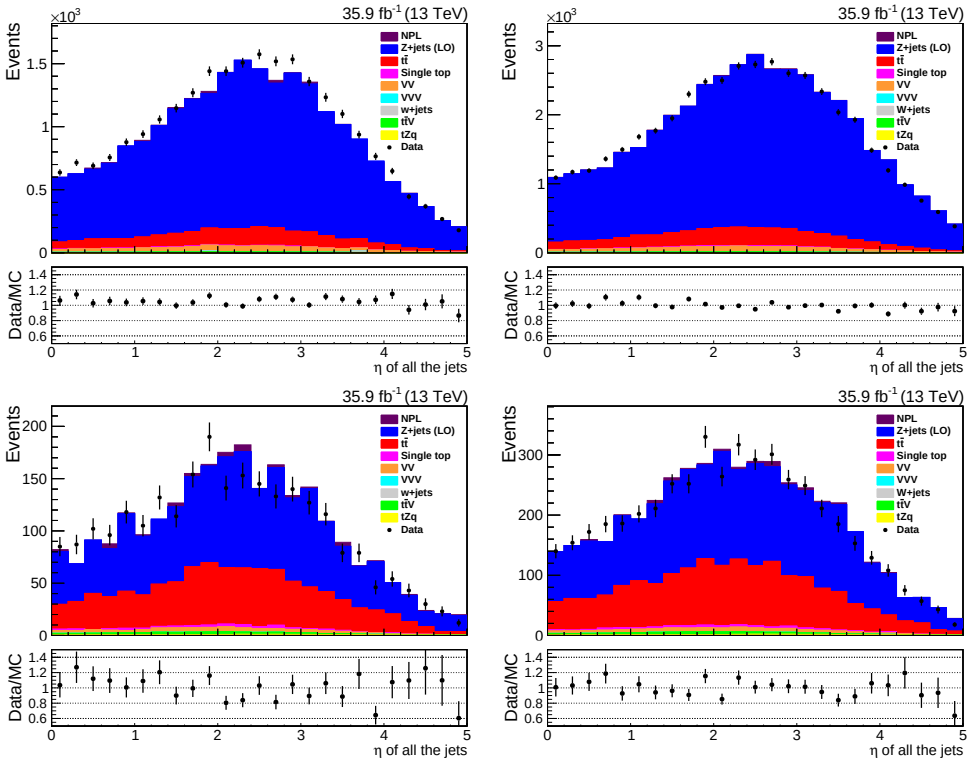

Figure B.12: The total η of all of the jets in an event following only the jet selection criteria (top) and all of the signal region selection criteria (bottom).

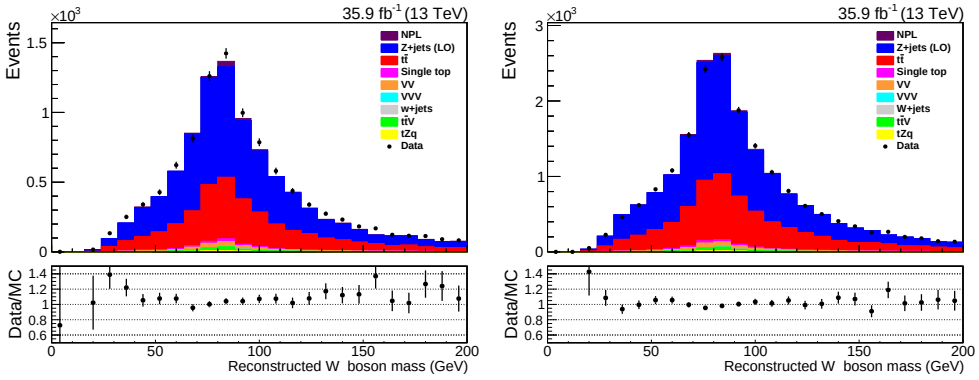

Figure B.13: The reconstructed W boson's mass following all of the signal region selection criteria except the W boson mass cut.

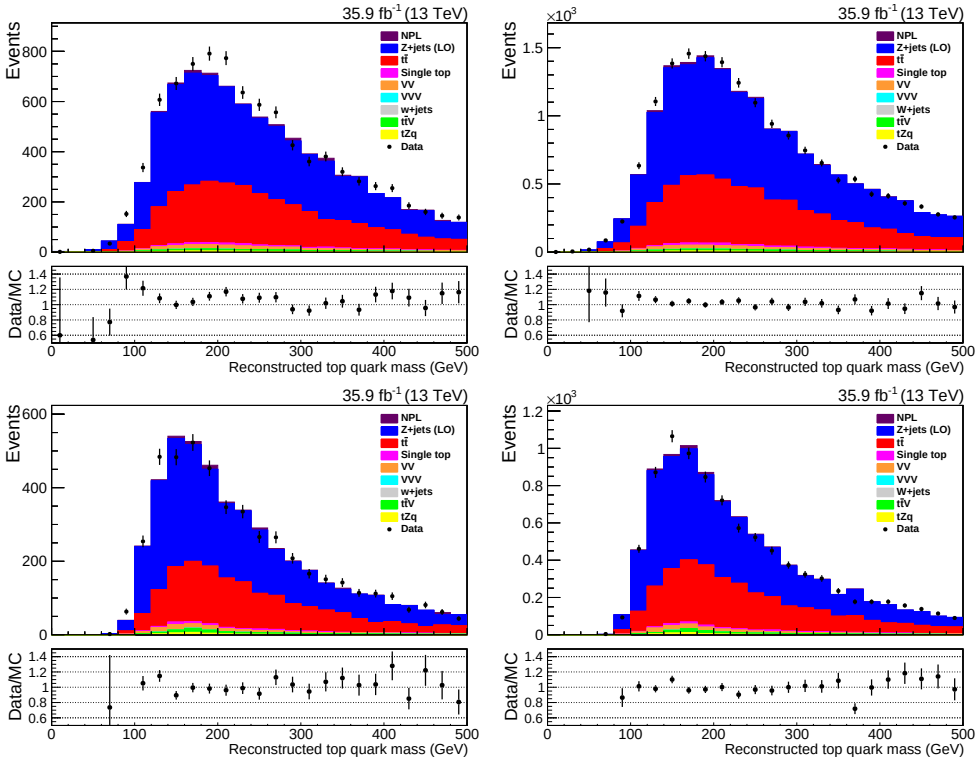

Figure B.14: The reconstructed top quark's mass following the b-jet selection criteria (top) and all of the signal region selection criteria (bottom).

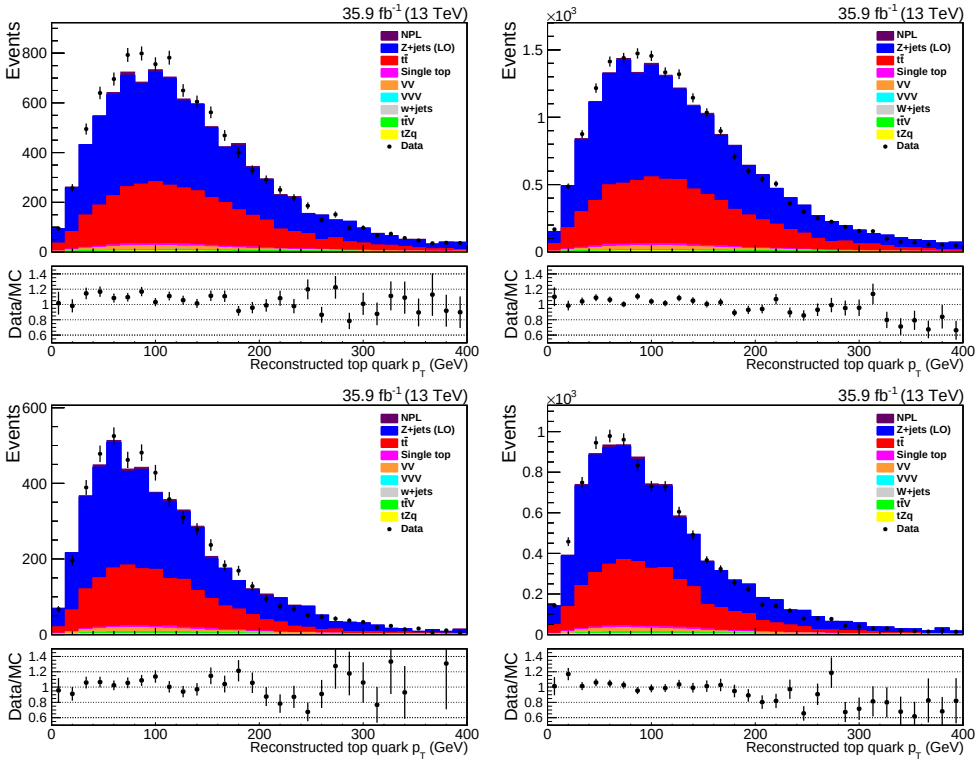

Figure B.15: The reconstructed top quark's p_{T} following the b-jet selection criteria (top) and all of the signal region selection criteria (bottom).

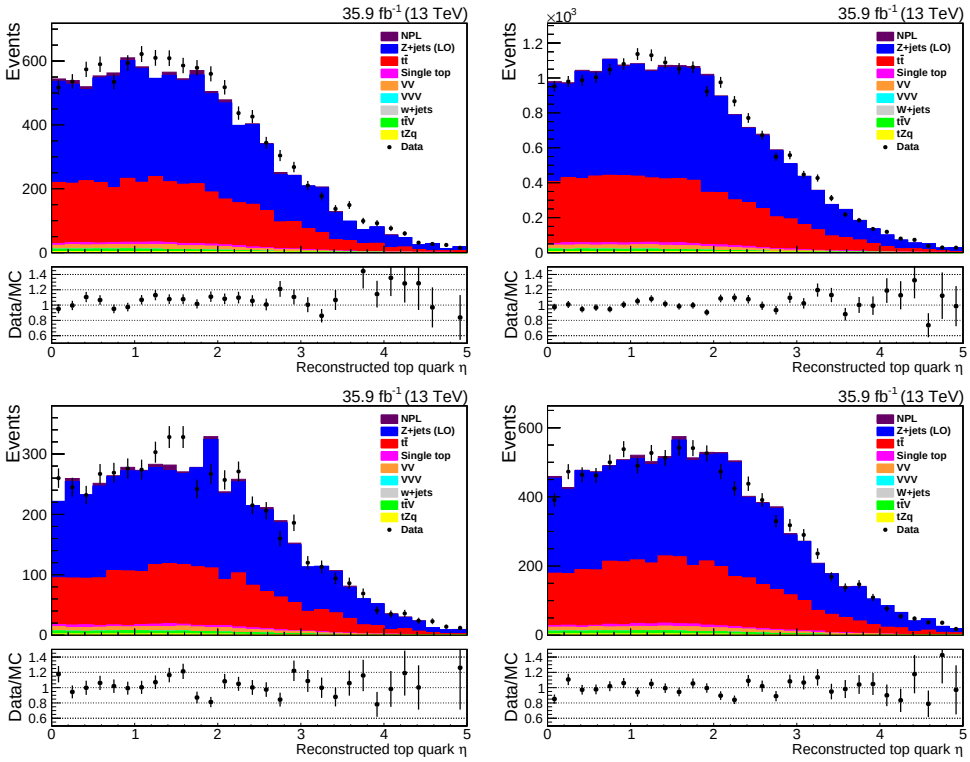

Figure B.16: The reconstructed top quark's η following the b-jet selection criteria (top) and all of the signal region selection criteria (bottom).

B.2 Z+jets Control Region

B.2.1 LO Z+jets Sample

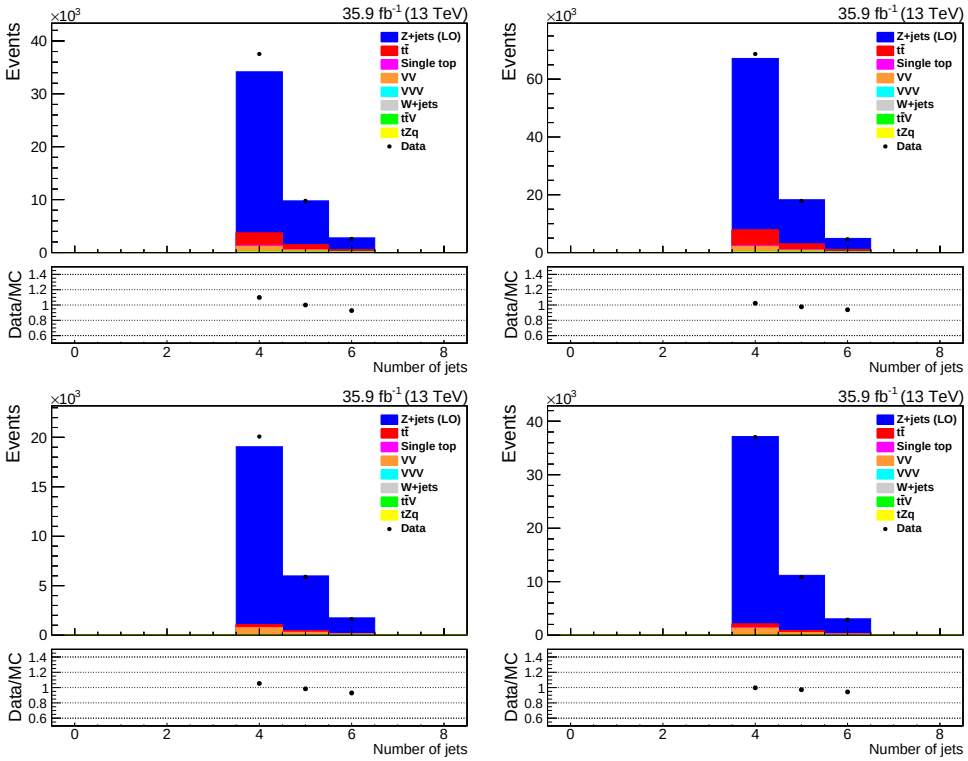

Figure B.17: The number of jets following only the lepton selection criteria (top) and all of the Z+jets 0-bjet control region selection criteria (bottom).

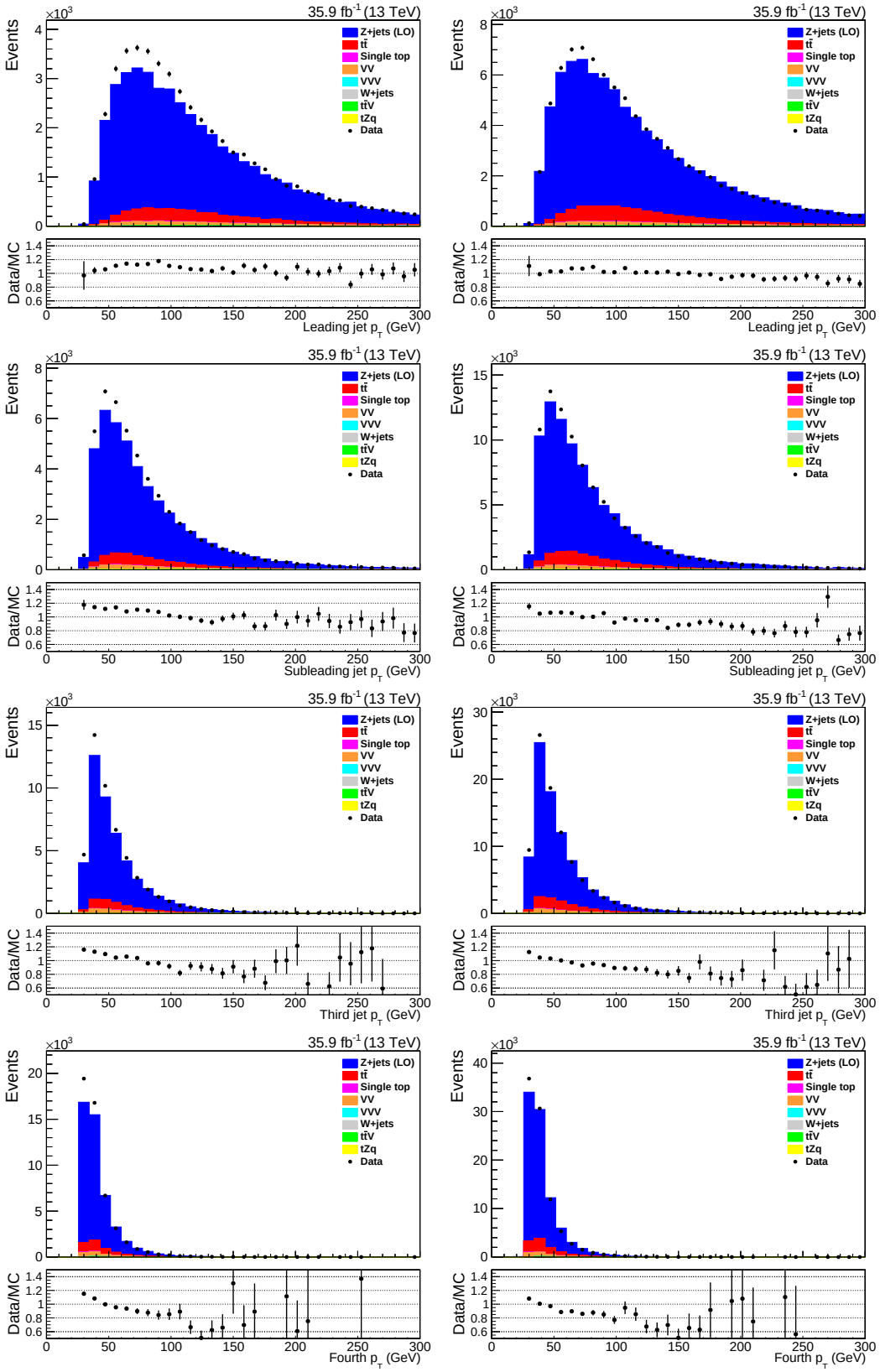

Figure B.18: The distributions of the leading four jets p_{T} in the 0-bjet region following the application of the Z+jets 0-bjet control region selection criteria.

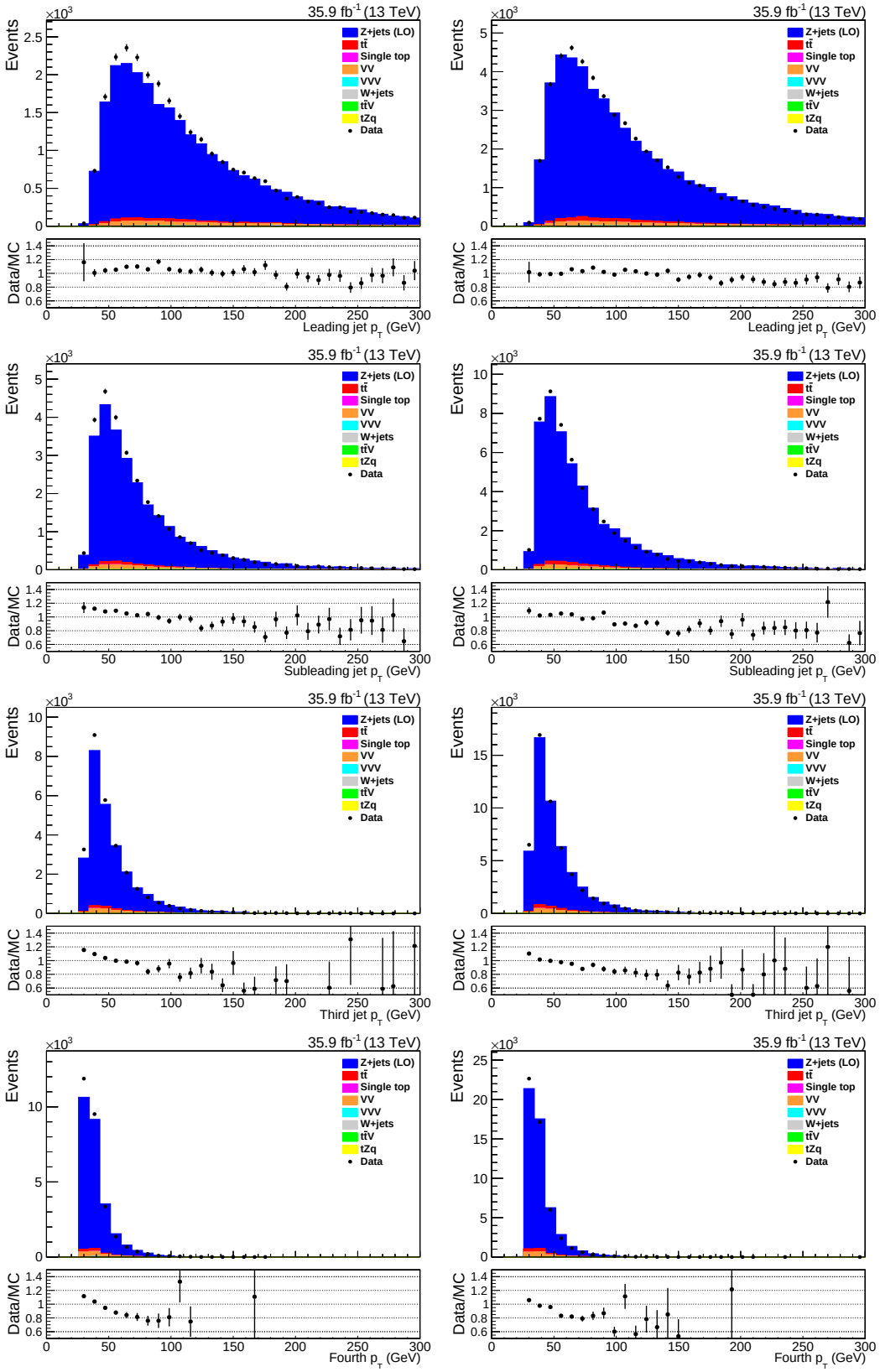

Figure B.19: The distributions of the leading four jets p_{T} in the 0-bjet region following the application of the all of the Z+jets 0-bjet control region selection criteria.

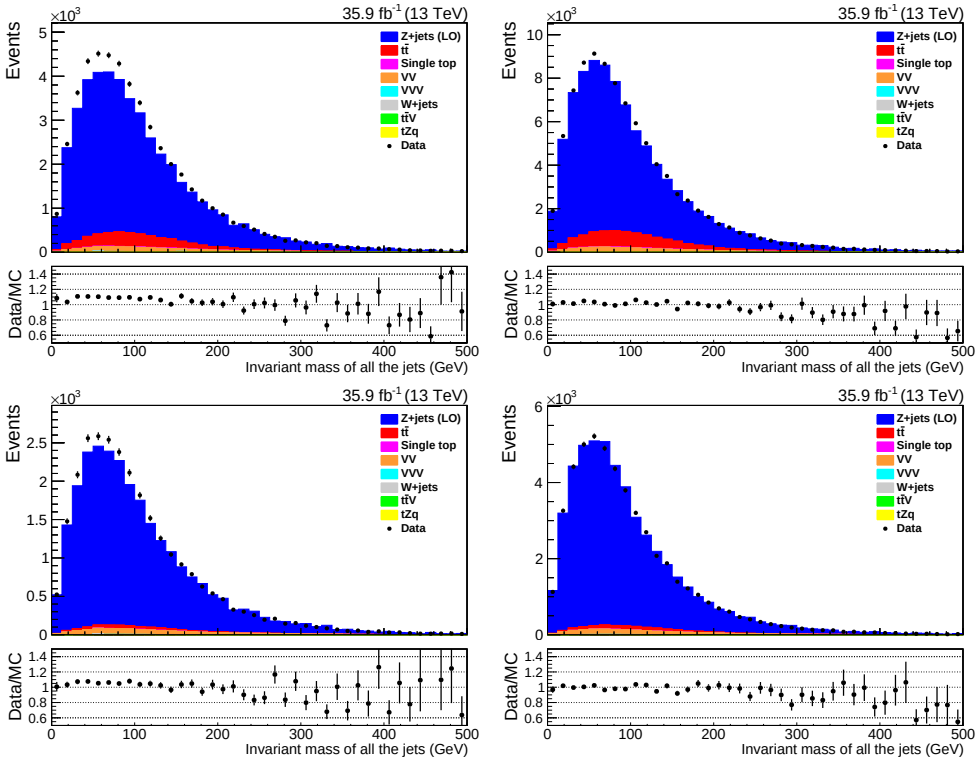

Figure B.20: The invariant mass of all of the jets in an event following only the jet selection criteria (top) and all of the Z+jets 0-bjet control region selection criteria (bottom).

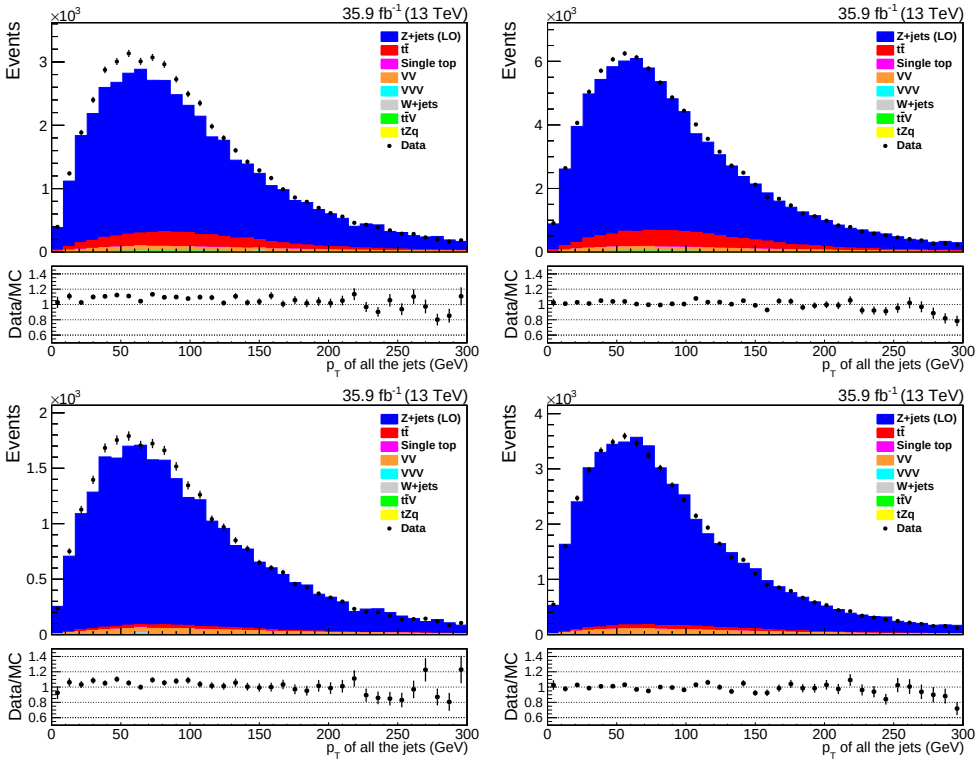

Figure B.21: The total p_{T} of all of the jets in an event following only the jet selection criteria (top) and all of the Z+jets 0-bjet control region selection criteria (bottom).

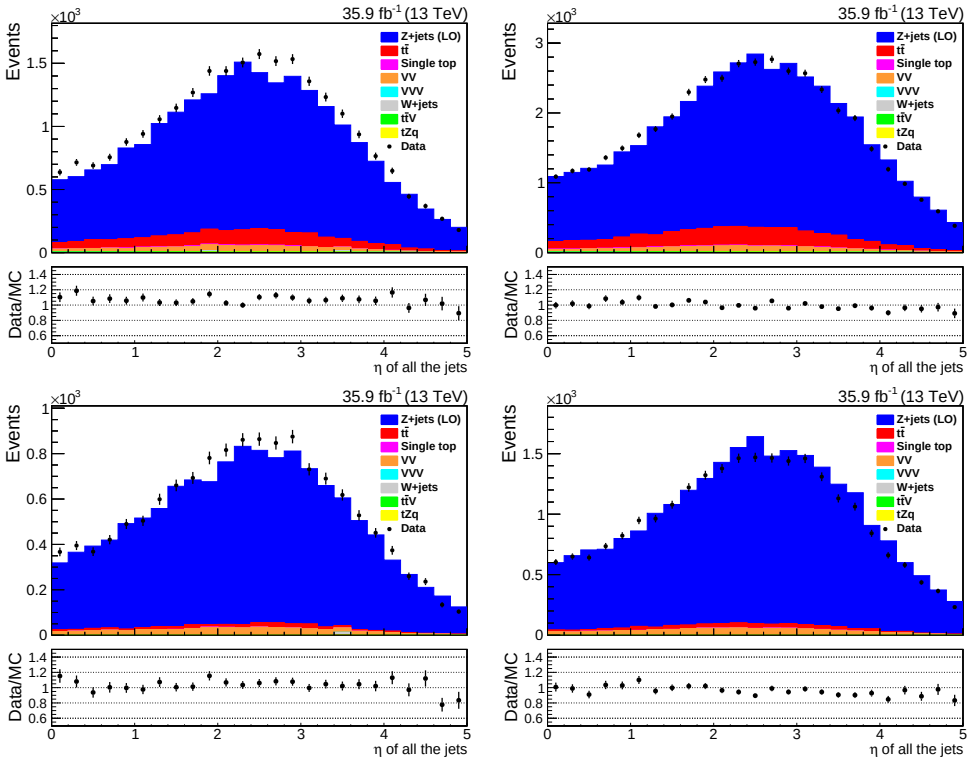

Figure B.22: The total η of all of the jets in an event following only the jet selection criteria (top) and all of the Z+jets 0-bjet control region selection criteria (bottom).

B.2.2 NLO Z+jets Sample

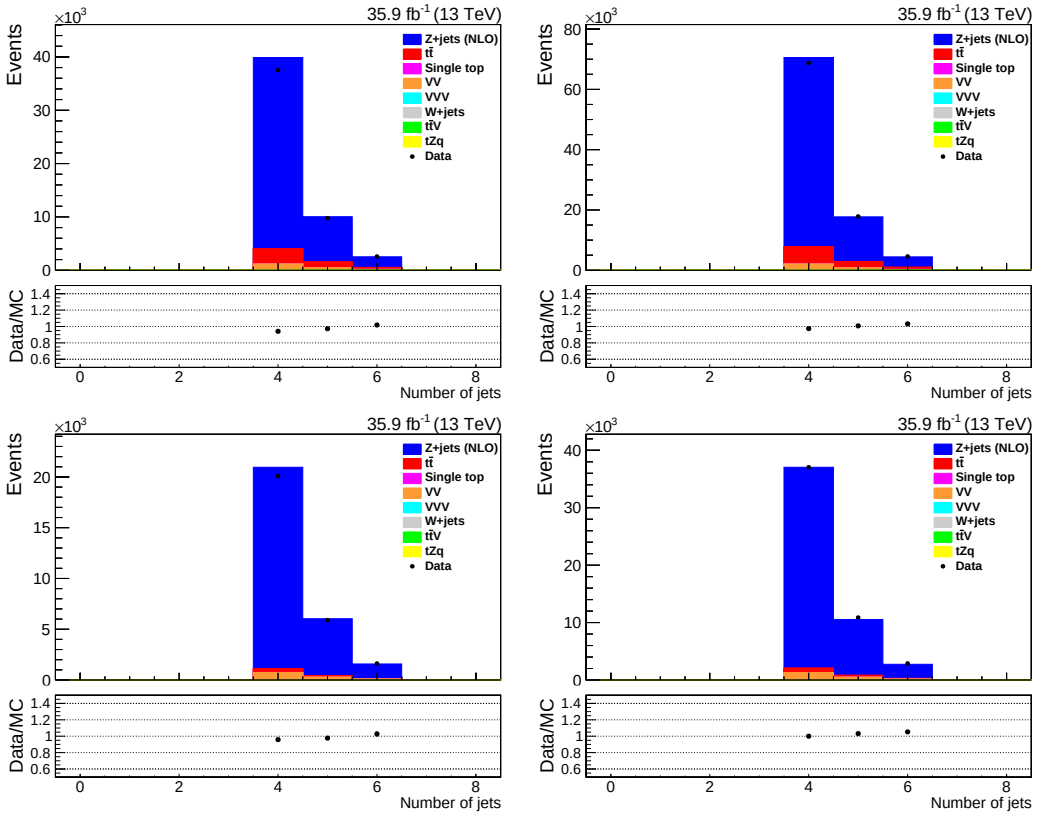

Figure B.23: The number of jets following only the lepton selection criteria (top) and all of the Z+jets 0-bjet control region selection criteria (bottom).

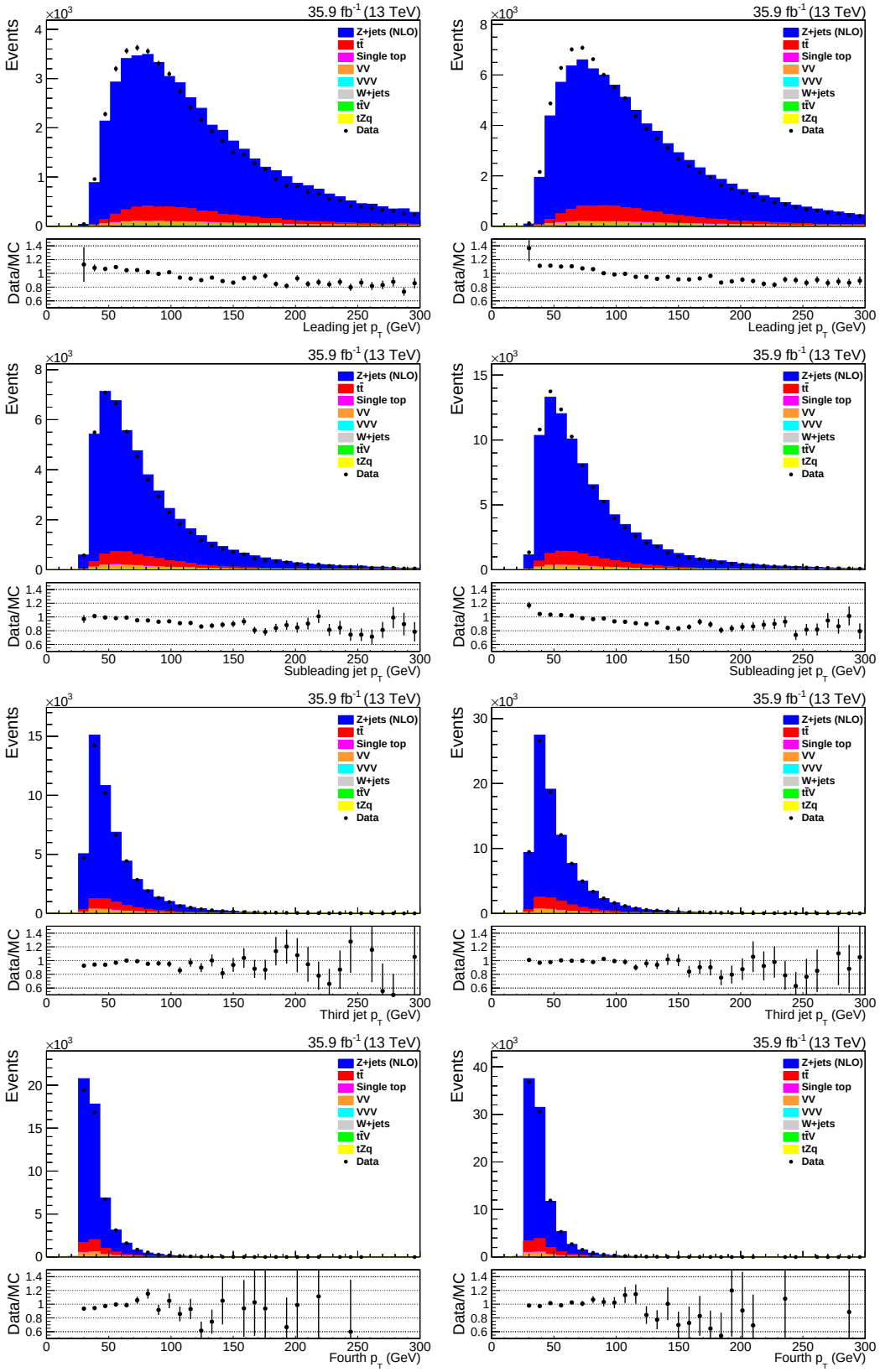

Figure B.24: The distributions of the leading four jets p_{T} in the 0-bjet region following the application of the Z+jets 0-bjet control region selection criteria.

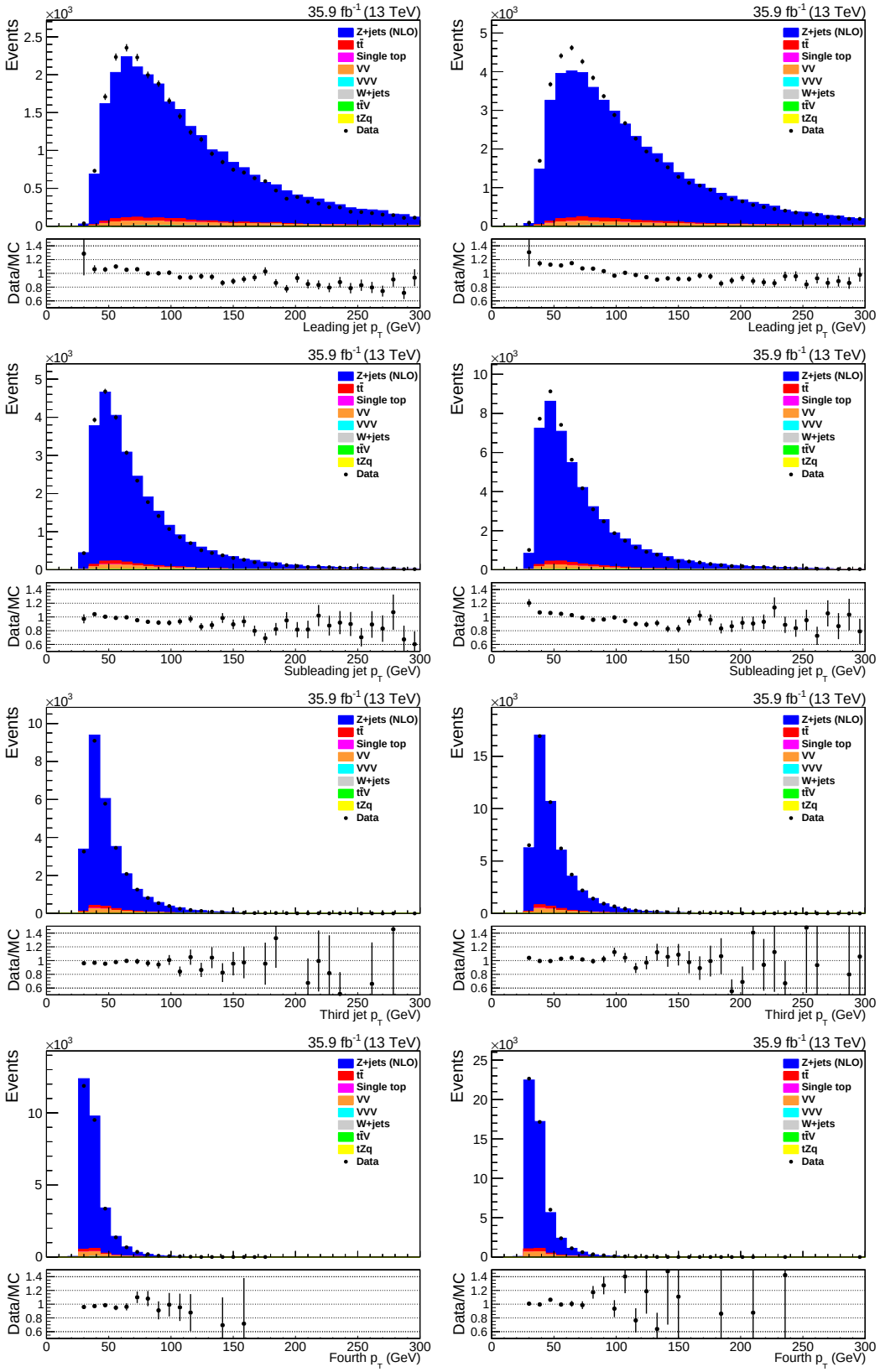

Figure B.25: The distributions of the leading four jets p_{T} in the 0-bjet region following the application of the all of the Z+jets 0-bjet control region selection criteria.

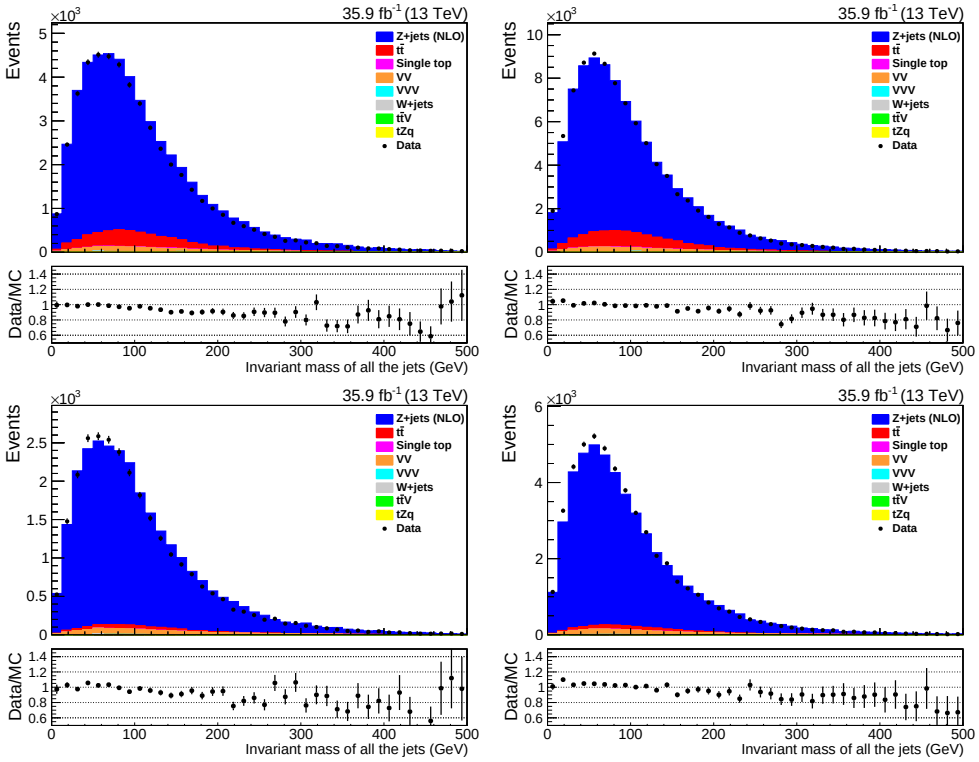

Figure B.26: The invariant mass of all of the jets in an event following only the jet selection criteria (top) and all of the Z+jets 0-bjet control region selection criteria (bottom).

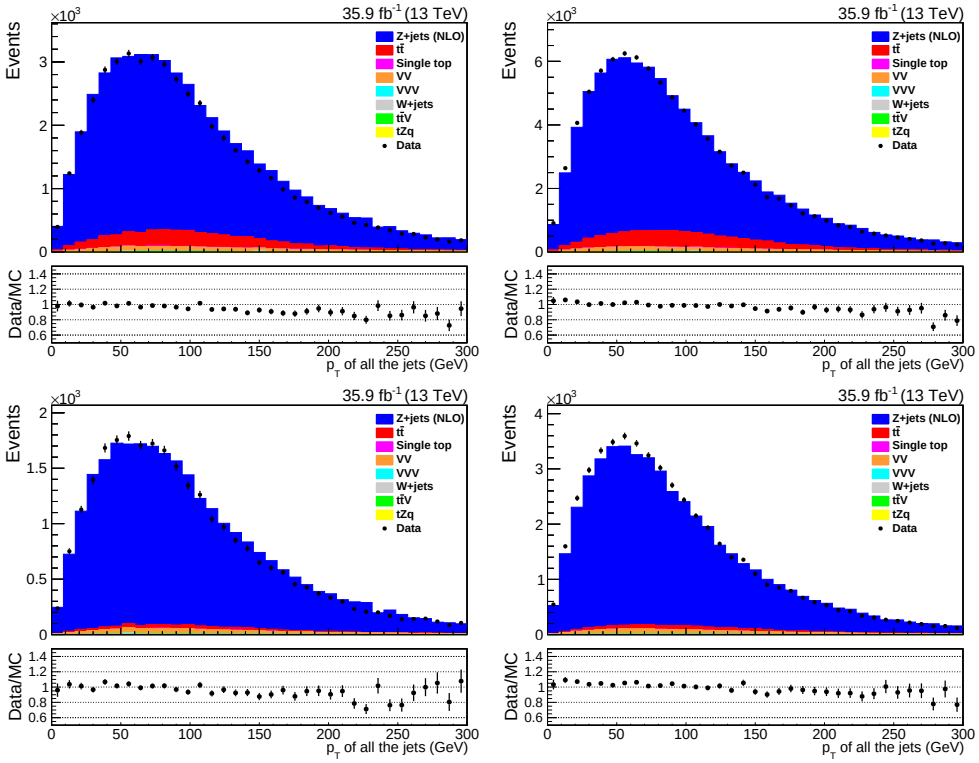

Figure B.27: The total p_{T} of all of the jets in an event following only the jet selection criteria (top) and all of the Z+jets 0-bjet control region selection criteria (bottom).

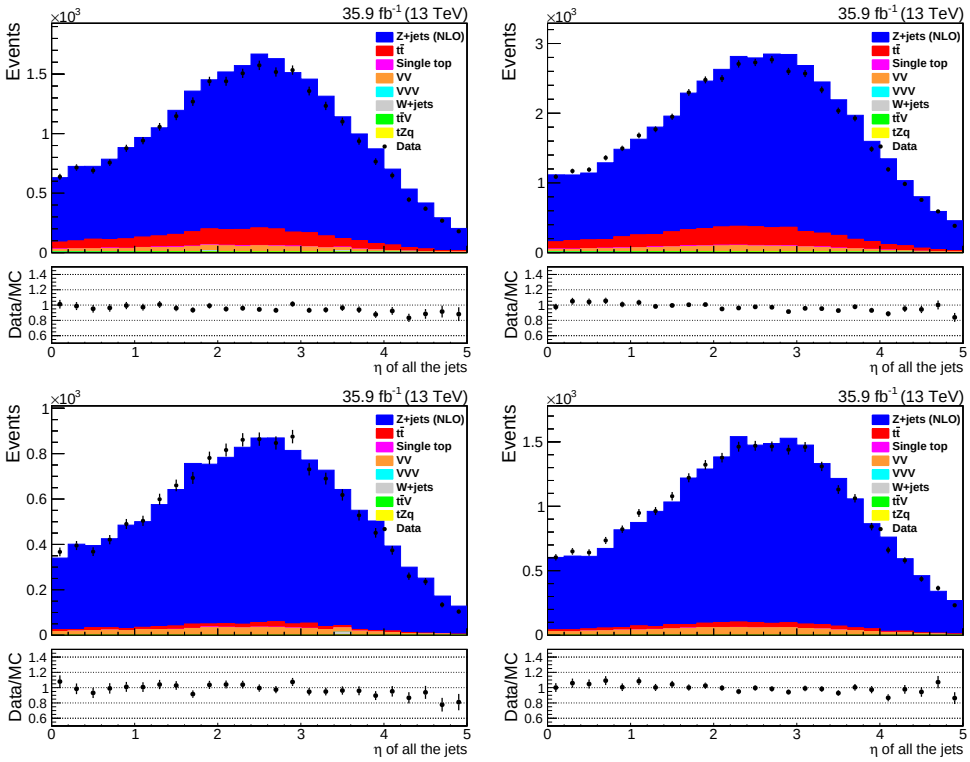

Figure B.28: The total η of all of the jets in an event following only the jet selection criteria (top) and all of the Z+jets 0-bjet control region selection criteria (bottom).

B.3 $t\bar{t}$ Control Region

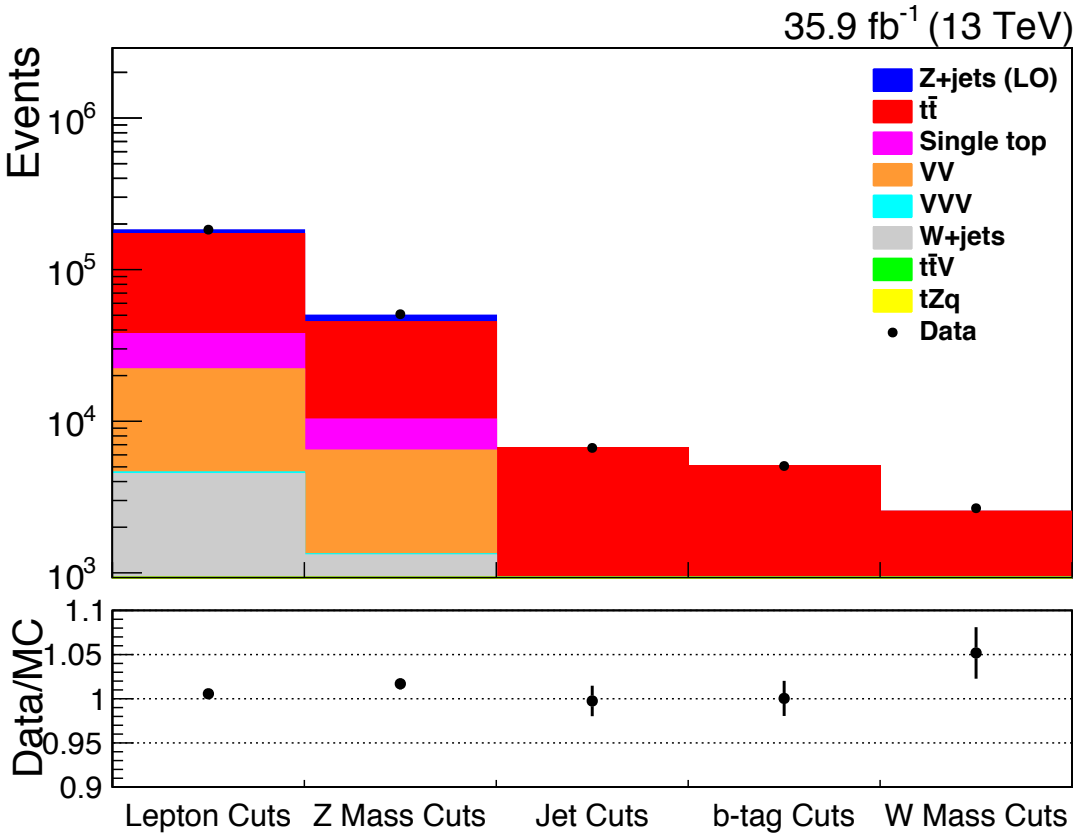

Figure B.29: The overall event yield for data and simulation at each stage of applying the $t\bar{t}$ control region selection criteria and simulation corrections.

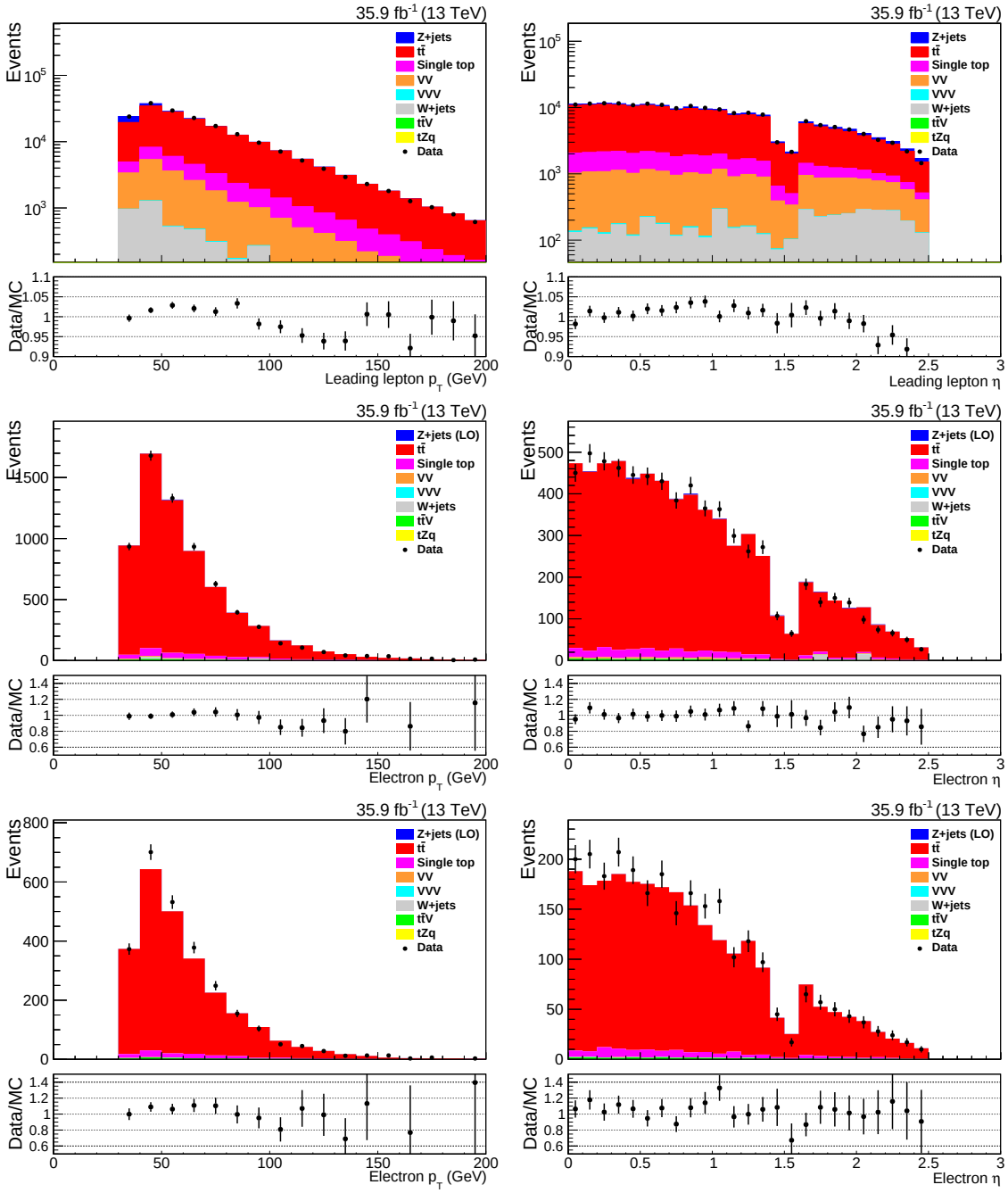

Figure B.30: The electron p_{T} (left) and η (right) following applying the lepton selection criteria (top), the jet selection criteria (middle) and all of the $t\bar{t}$ control region selection criteria (bottom).

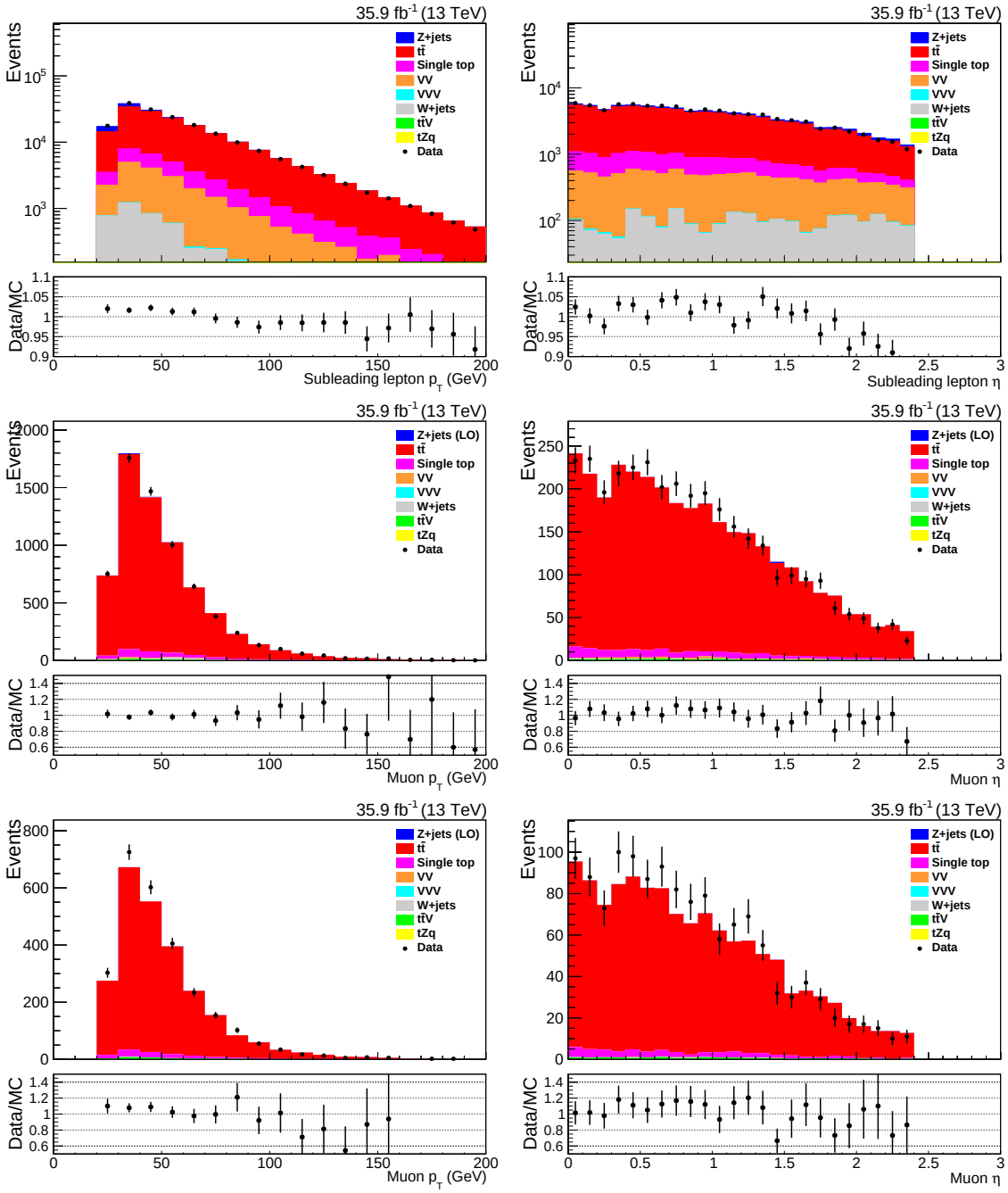

Figure B.31: The muon p_{T} (left) and η (right) following applying the lepton selection criteria (top), the jet selection criteria (middle) and all of the $t\bar{t}$ control region selection criteria (bottom).

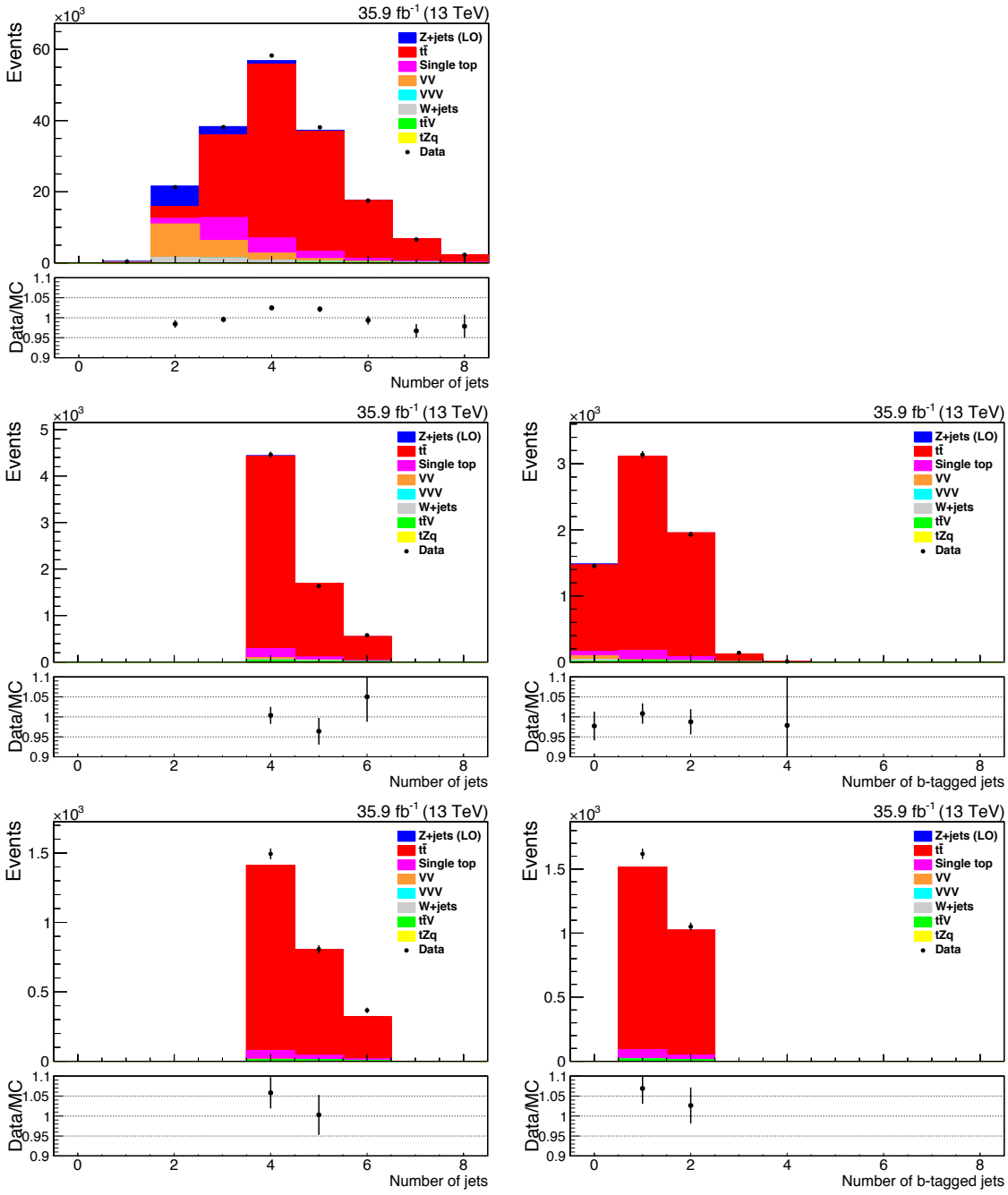

Figure B.32: The number of jets (left) and b-tagged jets (right) following applying the lepton selection criteria (top), the jet selection criteria (middle) and all of the $t\bar{t}$ control region selection criteria (bottom).

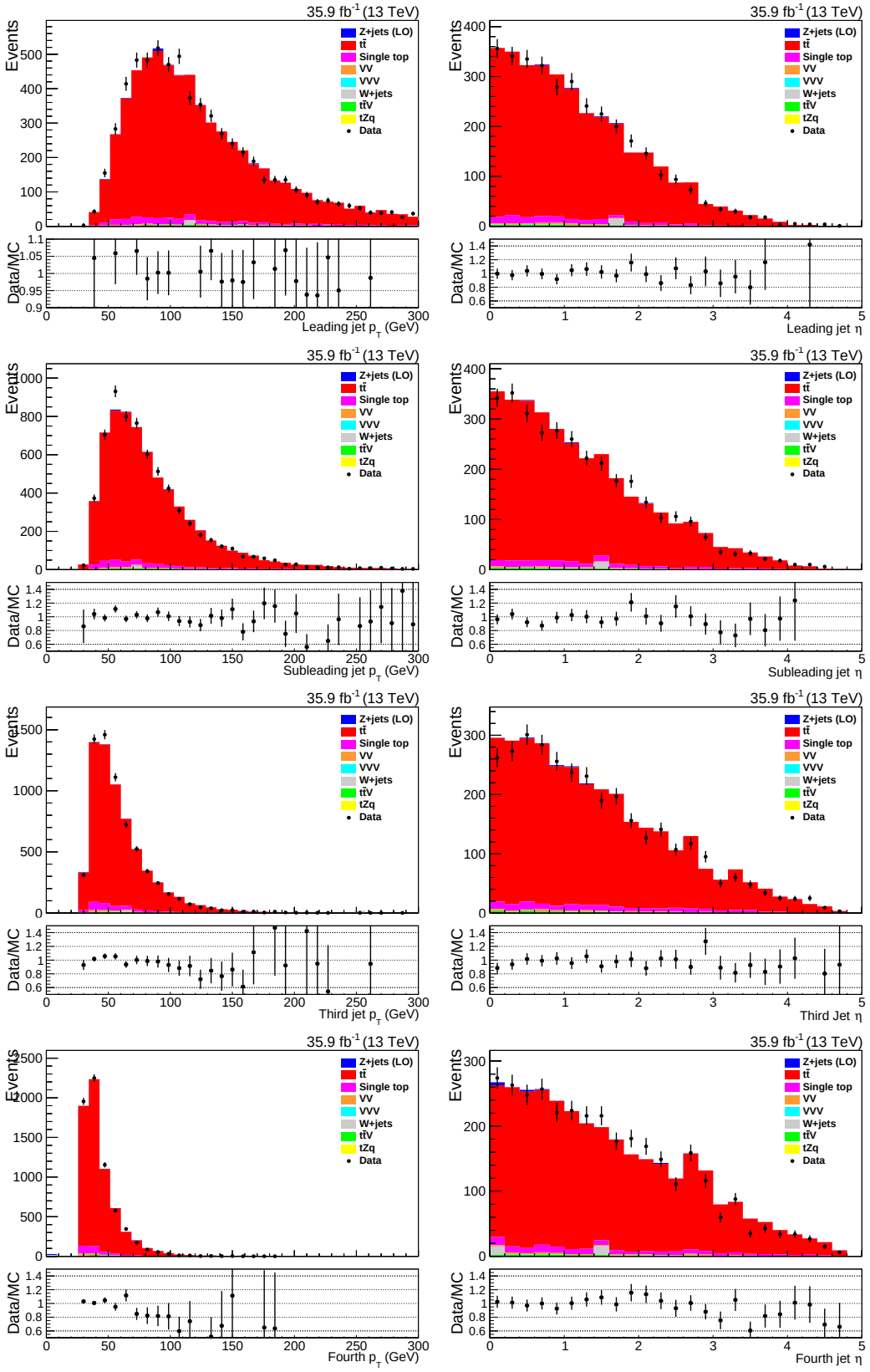

Figure B.33: The p_{T} (left) and η (right) of the leading (top), sub-leading (upper middle), third (lower middle) and fourth (bottom) jets following the application of the jet selection criteria.

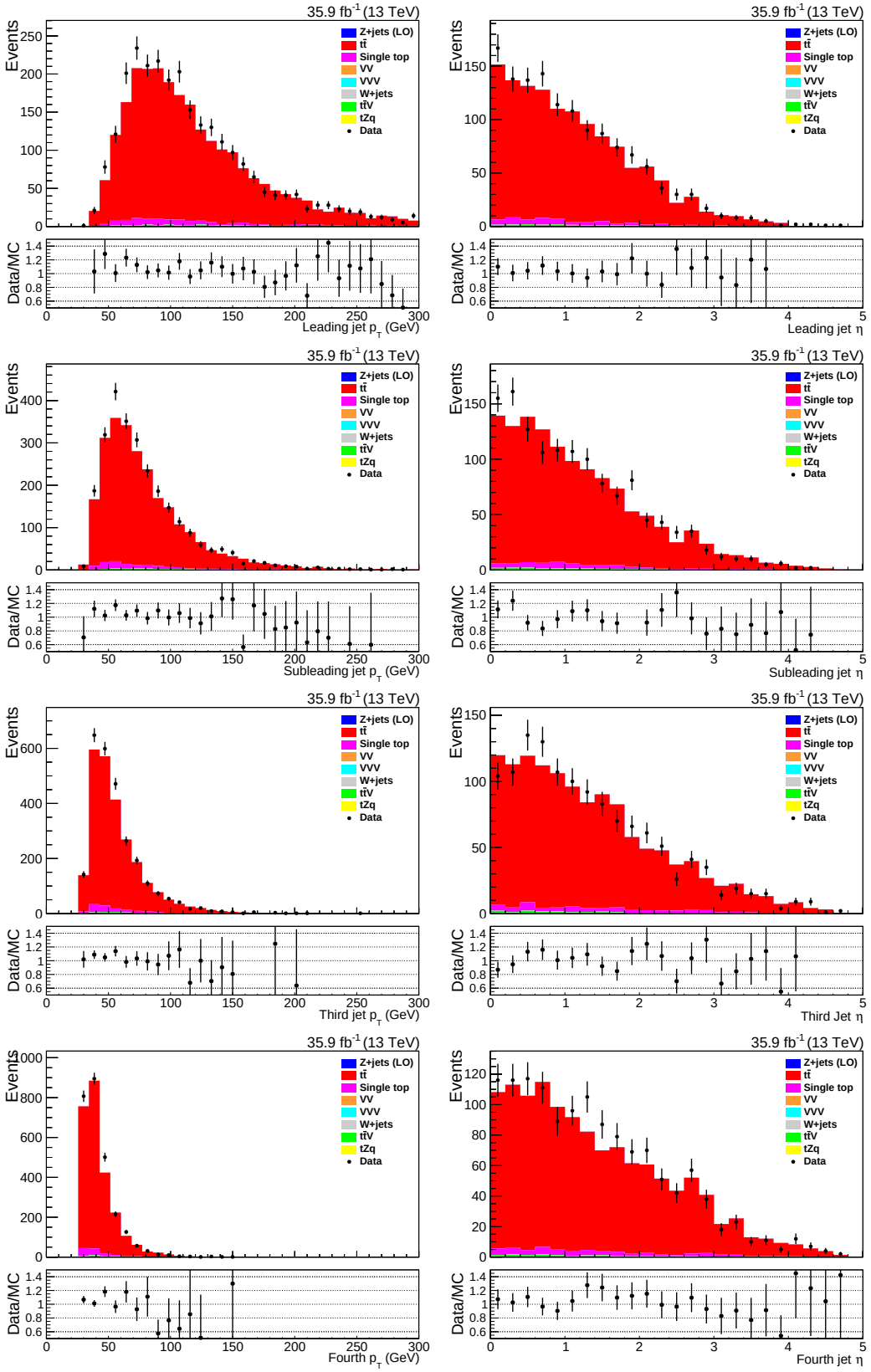

Figure B.34: The p_{T} (left) and η (right) of the leading (top), sub-leading (upper middle), third (lower middle) and fourth (bottom) jets following the application of all of the $t\bar{t}$ control region selection criteria.

Appendix C

Trigger Efficiency Studies Plots

This appendix contains the trigger efficiency measured in data and simulation and the resultant data/MC scale factors that would be required to account for the trigger modelling discrepancies in simulation as functions of the leptons' p_{T} and η.

Section C.1 shows the distributions for the trigger efficiencies in MC for $t\bar{t}$ and the MET datasets for 2016 and their resultant scale factors for each of the final states considered in the analysis presented in this thesis.

The distributions for the efficiencies in MC for $t\bar{t}$ and DY are shown in Section C.2. These comparisons were undertaken as part of the systematics studies undertaken to estimate the systematic uncertainty on the trigger scale factors that were determined. As shown in the distributions below in Section C.2, the differences in the trigger efficiency measured across η and for p_{T} above the lepton trigger thresholds are minimal and are covered by their respective statistical uncertainties.

C.1 Dilepton OR single lepton trigger efficiencies for data and $t\bar{t}$ simulation

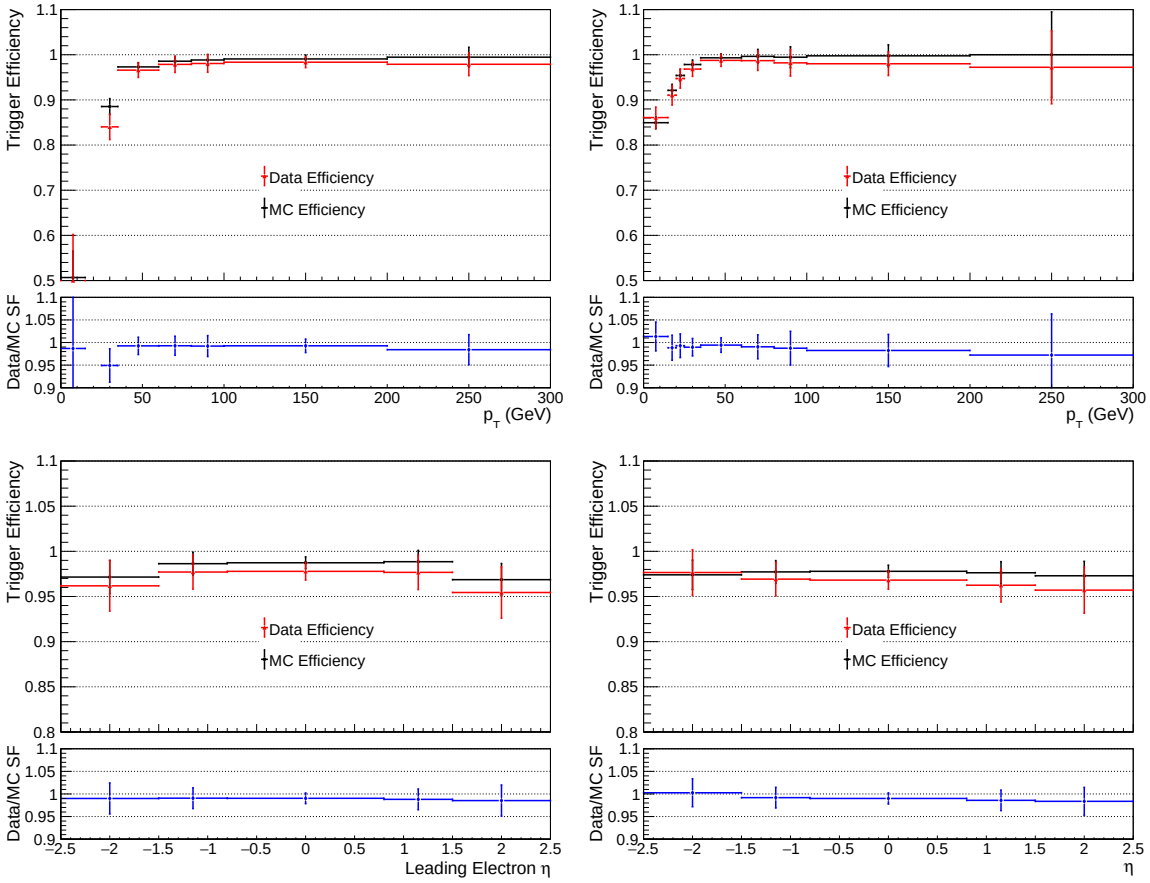

Figure C.1: The data and $t\bar{t}$ simulation efficiencies and scale factors for the ee channel as determined for the OR of dilepton and single lepton triggers as a function of the leading and sub-leading electrons' p_{T} and η.

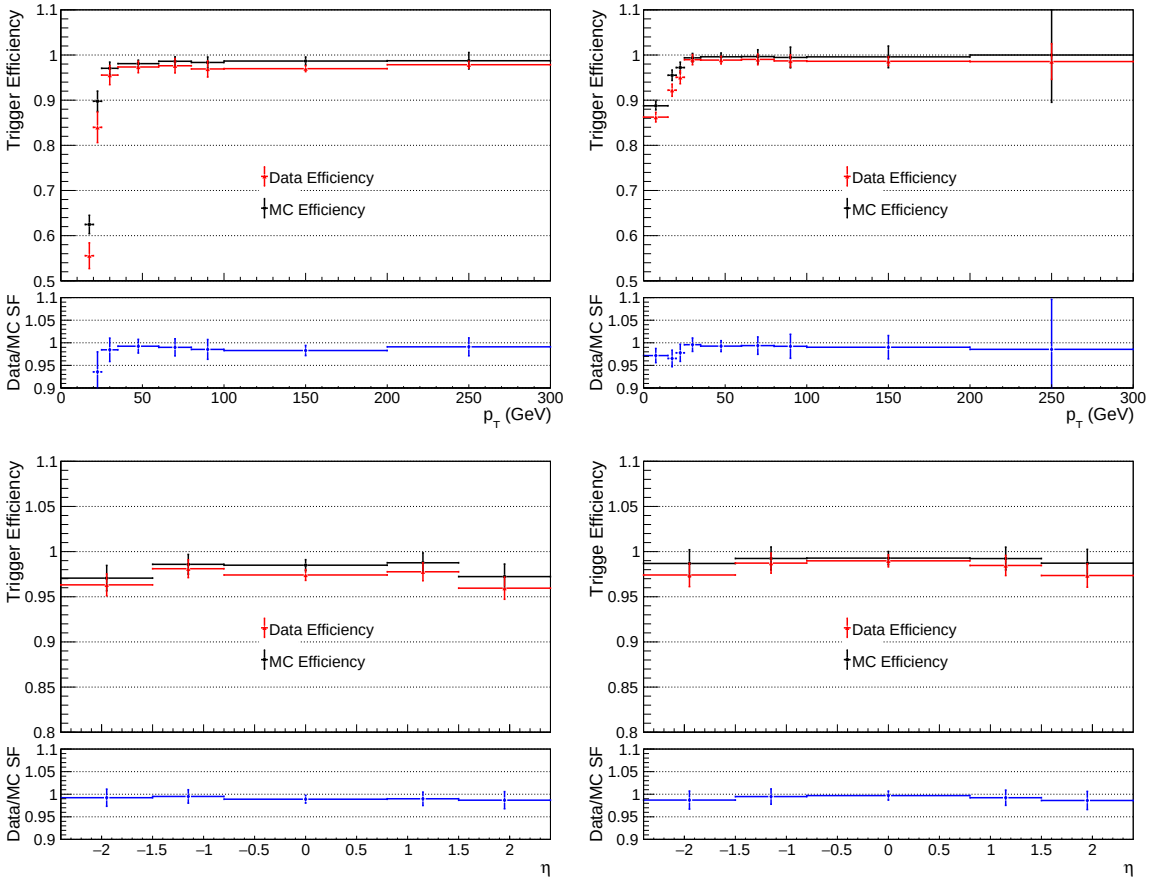

Figure C.2: The efficiencies and scale factors for the $\mu\mu$ channel as determined for the OR of dilepton and single lepton triggers as a function of the leading and sub-leading muon' p_{T} and η.

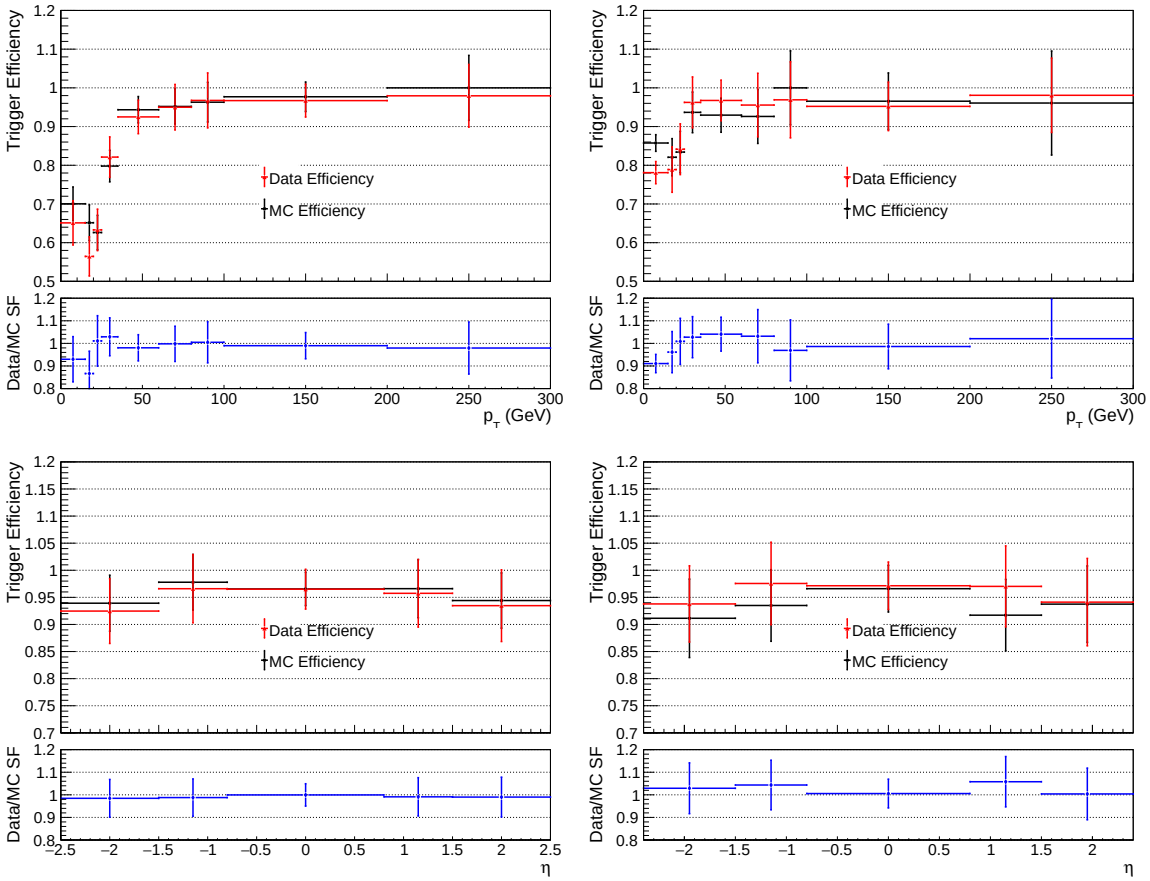

Figure C.3: The efficiencies and scale factors for the $e\mu$ channel as determined for the OR of dilepton and single lepton triggers as a function of the electron's and muon's p_{T} and η.

C.2 Dilepton OR single lepton trigger efficiencies in MC for $t\bar{t}$ and DY

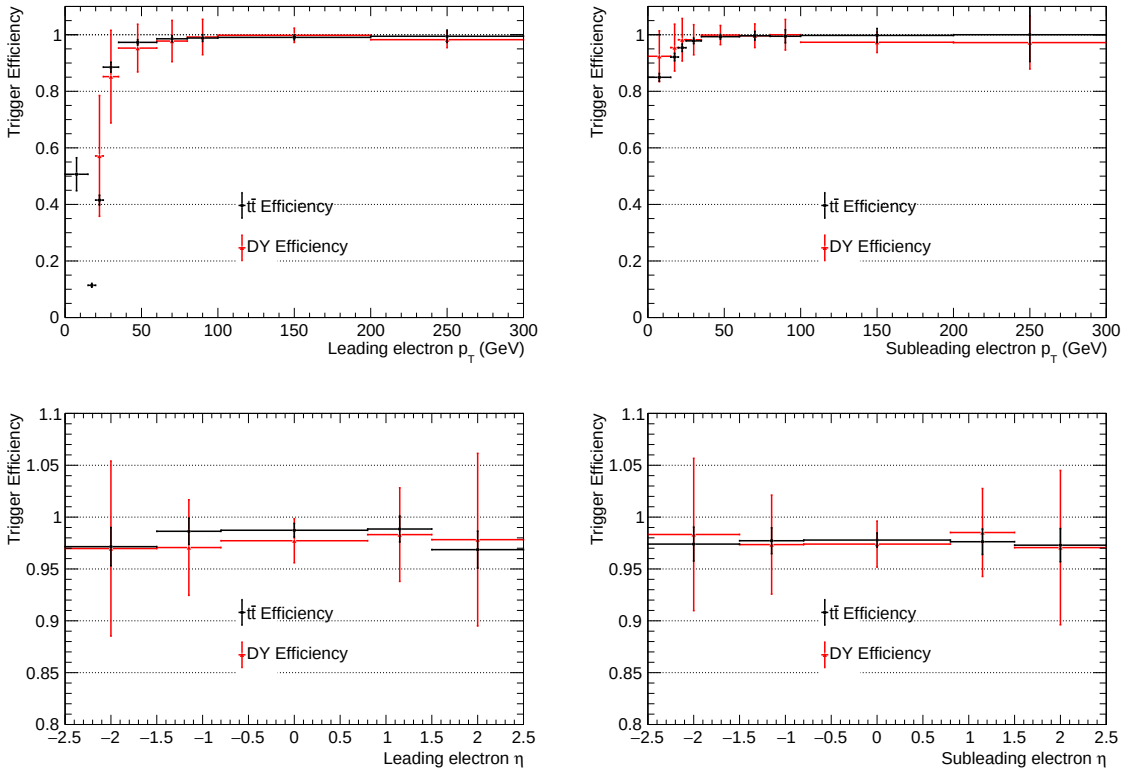

Figure C.4: The efficiencies in MC for the *ee* channel for $t\bar{t}$ and DY as determined for the OR of dilepton and single lepton triggers as a function of the leading and sub-leaiding electron's p_{T} and η.

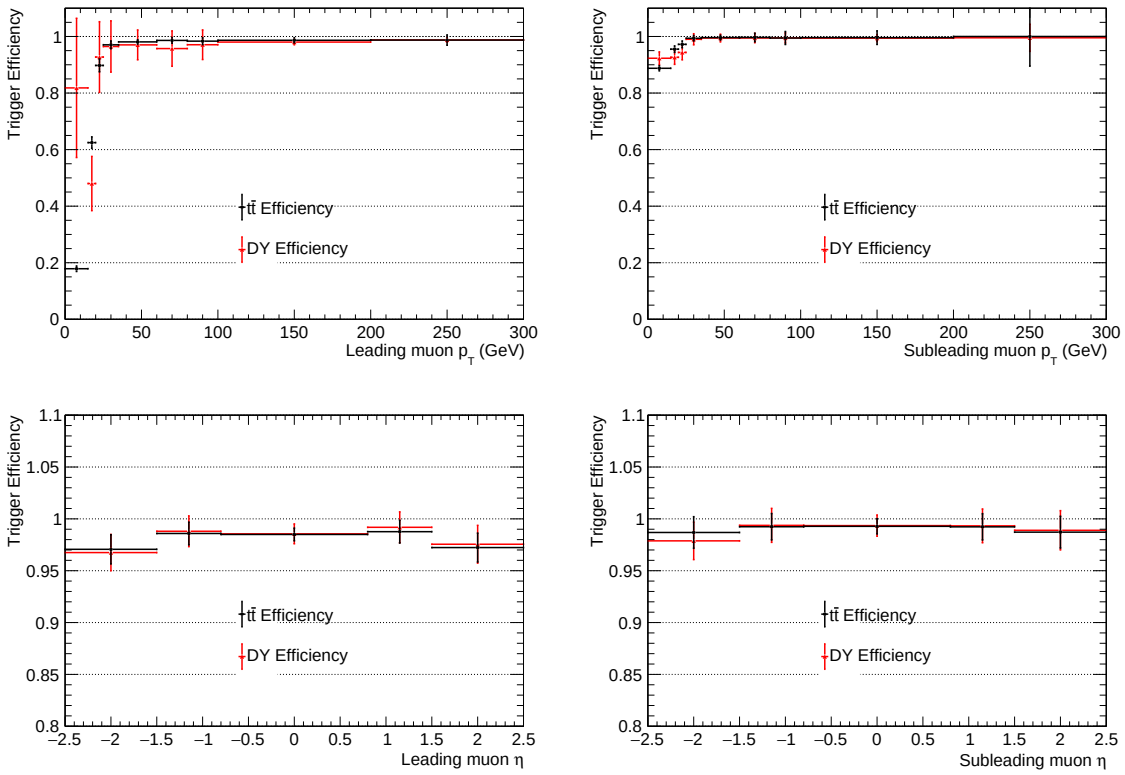

Figure C.5: The efficiencies in MC for the $\mu\mu$ channel for $t\bar{t}$ and DY as determined for the OR of dilepton and single lepton triggers as a function of the leading and sub-leaiding muon's p_{T} and η.

Appendix D

BDT Input Variables

D.1 List of all potential Input Features

Following the application of the event selection criteria, as described in Chapter 6, a large number of input variables which were considered for use in the boosted decision trees used were constructed from the selected reconstructed physics objects.

The complete list of variables and their descriptions are listed in Table D.1.

Table D.1: The list of the names and descriptions of all of variables considered by recursive feature elimination to be used as input to the BDT to discriminate between potential tZq signal events and the dominant backgrounds.

Variable	**Description**
wQuark1Pt	Leading W boson candidate jet p_{T}
wQuark1Eta	Leading W boson candidate jet η
wQuark1Phi	Leading W boson candidate jet ϕ
wQuark2Pt	Subleading W boson candidate jet p_{T}
wQuark2Eta	Subleading W boson candidate jet η
wQuark2Phi	Subleading W boson candidate jet ϕ
wPairMass	Reconstructed W boson mass
wPairPt	Reconstructed W boson p_{T}
wPairEta	Reconstructed W boson η
wPairPhi	Reconstructed W boson ϕ
mTW	W boson transverse mass
met	Missing transverse energy
nJets	Number of jets
j1j2delR	ΔR between the leading and subleading jets
j1j2delPhi	$\Delta\phi$ between the leading and subleading jets
leadJetPt	Leading jet p_{T}
leadJetPhi	Leading jet ϕ
leadJetEta	Leading jet η
leadJetbTag	Leading jet b-tag output discriminant
secJetPt	Subleading jet p_{T}
secJetPhi	Subleading jet ϕ
secJetEta	Subleading jet η
secJetbTag	Subleading jet b-tag output discriminant
thirdJetPt	Third jet p_{T}
thirdJetPhi	Third jet ϕ
thirdJetEta	Third jet η
thirdJetbTag	Third jet b-tag output discriminant

Variable	Description
fourthJetPt	Fourth jet p_{T}
fourthJetPhi	Fourth jet ϕ
fourthJetEta	Fourth jet η
fourthJetbTag	Fourth jet b-tag output discriminant
nBjets	Number of b-tagged jets
bTagDisc	Leading b-tagged jet b-tag output discriminant
lep1Pt	Leading lepton p_{T}
lep1Eta	Leading lepton η
lep1Phi	Leading lepton ϕ
lep1RelIso	Leading lepton I^{rel}
lep1D0	Leading lepton d_0
lep2Pt	Subleading lepton p_{T}
lep2Eta	Subleading lepton η
lep2Phi	Subleading lepton ϕ
lep2RelIso	Subleading lepton I^{rel}
lep2D0	Subleading lepton d_0
zMass	Z boson mass
zPt	Reconstructed Z boson p_{T}
zEta	Reconstructed Z boson η
zPhi	Reconstructed Z boson ϕ
topMass	Reconstructed top quark mass
topPt	Reconstructed top quark p_{T}
topEta	Reconstructed top quark η
topPhi	Reconstructed top quark ϕ
w1w2delR	ΔR between the W boson candidate's jets
w1w2delPhi	$\Delta\phi$ between the W boson candidate's jets
zLepdelR	ΔR between the Z boson candidate leptons
zLepdelPhi	$\Delta\phi$ between the Z boson candidates leptons
zl1Quark1DelR	ΔR between the leading lepton and W boson candidate's leading jet
zl1Quark1DelPhi	$\Delta\phi$ between the leading lepton and W boson candidate's leading jet
zl1Quark2DelR	ΔR between the leading lepton and W boson candidate's subleading jet
zl1Quark2DelPhi	$\Delta\phi$ between the leading lepton and W boson candidate's subleading jet
zl2Quark1DelR	ΔR between the subleading lepton and W boson candidate's leading jet
zl2Quark1DelPhi	$\Delta\phi$ between the subleading lepton and W boson candidate's leading jet
zl2Quark2DelR	ΔR between the subleading lepton and W boson candidate's subleading jet
zl2Quark2DelPhi	$\Delta\phi$ between the subleading lepton and W boson candidate's subleading jet
zlb1DelR	ΔR between the leading lepton and leading b-tagged jet
zlb1DelPhi	$\Delta\phi$ between the leading lepton and leading b-tagged jet
zlb2DelR	ΔR between the subleading lepton and leading b-tagged jet
zlb2DelPhi	$\Delta\phi$ between the subleading lepton and leading b-tagged jet

Variable	Description
lepHt	H_{T} of the Z boson candidate's leptons
wQuarkHt	H_{T} of the W boson candidate's jets
totPtVec	p_{T} of the system
totEta	η of the system
totPhi	ϕ of the system
totVecM	Invariant mass of the system
totPt2Jet	Square of the sum of the two leading jets' p_{T}
totJetPt	Sum of all the jets' p_{T}
wZdelR	ΔR between the W and Z boson candidates
wZdelPhi	$\Delta\phi$ between the W and Z bosons candidates
zQuark1DelR	ΔR between the Z boson candidate and W boson candidate's leading jet
zQuark1DelPhi	$\Delta\phi$ between the Z boson candidate and W boson candidate's leading jet
zQuark2DelR	ΔR between the Z boson candidate and W boson candidate's subleading jet
zQuark2DelPhi	$\Delta\phi$ between the Z boson candidate and W boson candidate's subleading jet
zTopDelR	ΔR between the Z boson and top quark candidates
zTopDelPhi	$\Delta\phi$ between the Z boson and top quark candidates
zl1TopDelR	ΔR between the leading lepton and top quark candidates
zl1TopDelPhi	$\Delta\phi$ between the leading lepton and top quark candidates
zl2TopDelR	ΔR between the subleading lepton and top quark candidate
zl2TopDelPhi	$\Delta\phi$ between the subleading lepton and top quark candidate
wTopDelR	ΔR between the W boson and top quark candidates
wTopDelPhi	$\Delta\phi$ between the W boson and top quark candidates
w1TopDelR	ΔR between the W boson candidates's leading jet and the top quark candidate
w1TopDelPhi	$\Delta\phi$ between the W boson candidates's leading jet and the top quark candidate
w2TopDelR	ΔR between the W boson candidates's subleading jet and the top quark candidate
w2TopDelPhi	$\Delta\phi$ between the W boson candidates's subleading jet and the top quark candidate
zjminR	Minimum ΔR between the Z boson candidate and any jet
minZJetPhi	Minimum ϕR between the Z boson candidate and any jet
totHt	Total H_{T} of the system
jetHt	H_{T} of all the jets in an event
jetMass	Invariant mass of all the jets in an event
jetPt	p_{T} of all the jets in an event
jetEta	η of all the jets in an event
jetPhi	ϕ of all the jets in an event
jetMass3	Invariant mass of the leading three jets in an event
totHtOverPt	Total H_{T} divided by the system's p_{T}

D.2 List of all potential Input Features

The following section contains the full set of comparison plots between data and simulation for the chosen BDT input variables listed in Table 7.12 in Section 7.6.2.

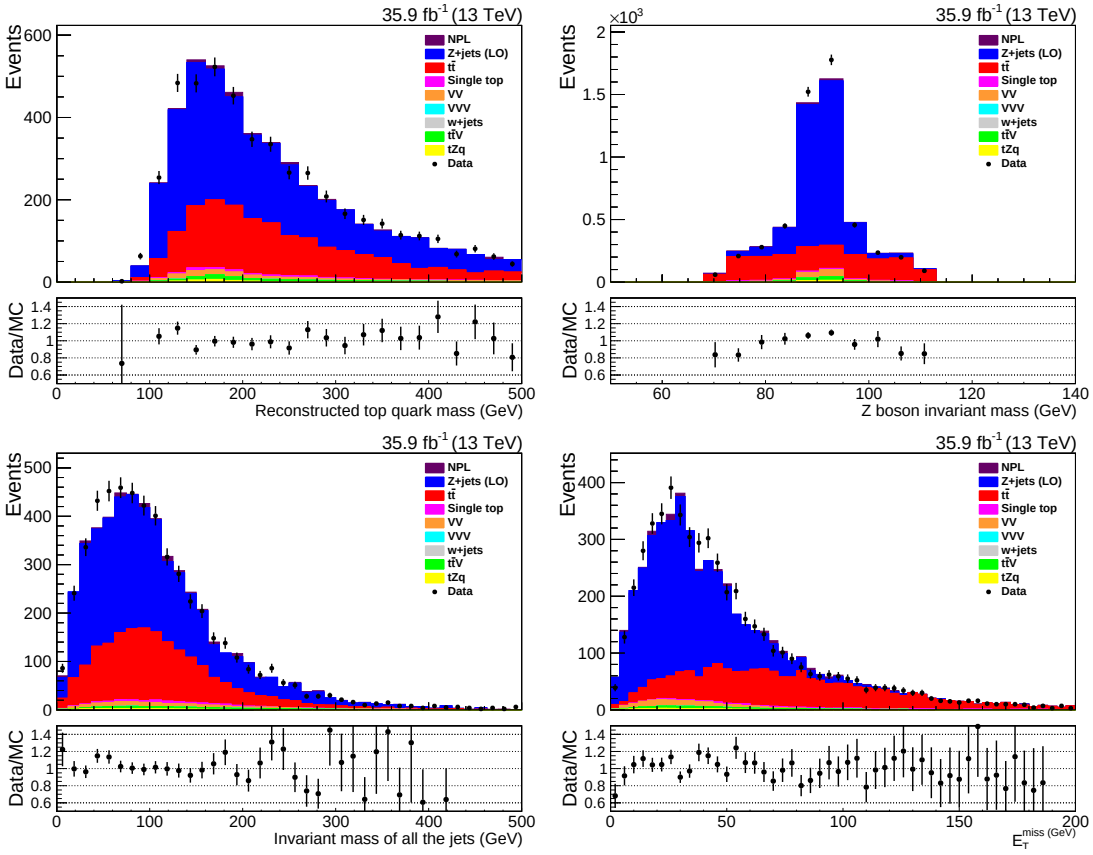

Figure D.1: Reconstructed top mass, Z boson mass, total jet mass, and $E_{\mathrm{T}}^{\mathrm{miss}}$ distributions for the *ee* channel comparing the agreement between data and simulation for the variables used as input variables in the BDT training.

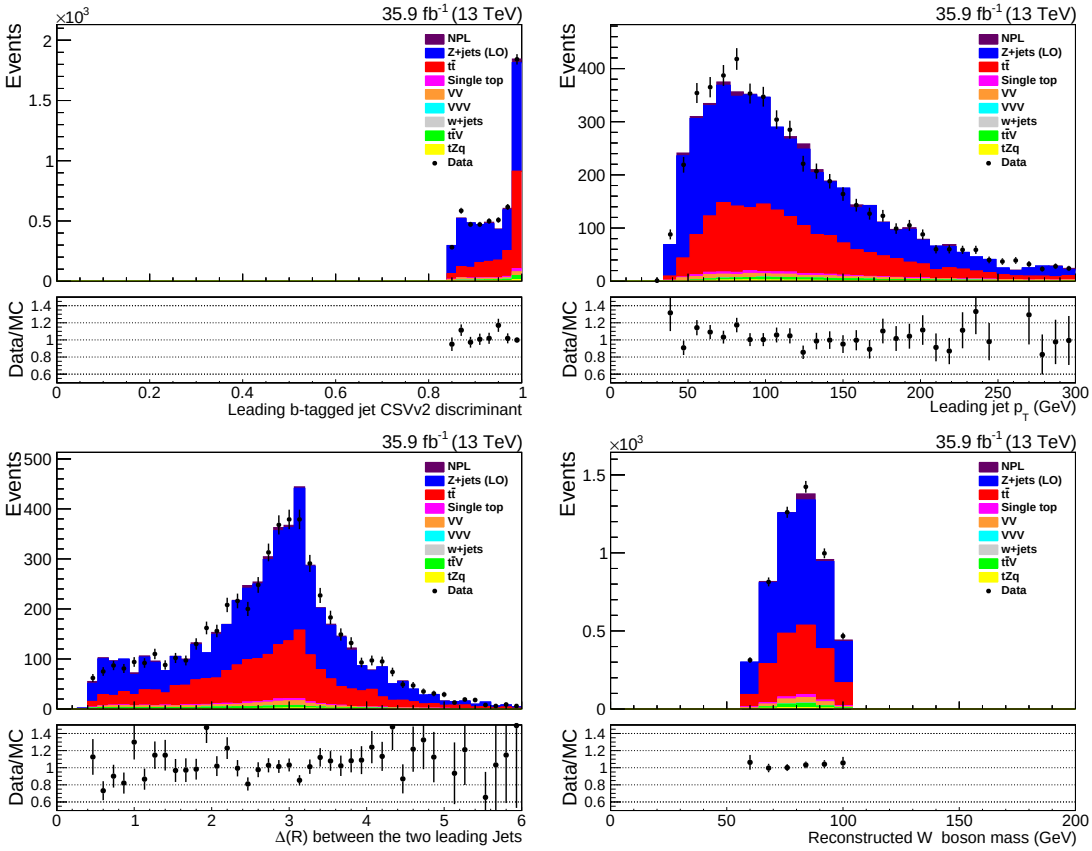

Figure D.2: Leading b-tagged jet CSVv2 discriminant, leading jet p_{T}, ΔR between the leading jets, and reconstructed W boson mass distributions for the *ee* channel comparing the agreement between data and simulation for the variables used as input variables in the BDT training.

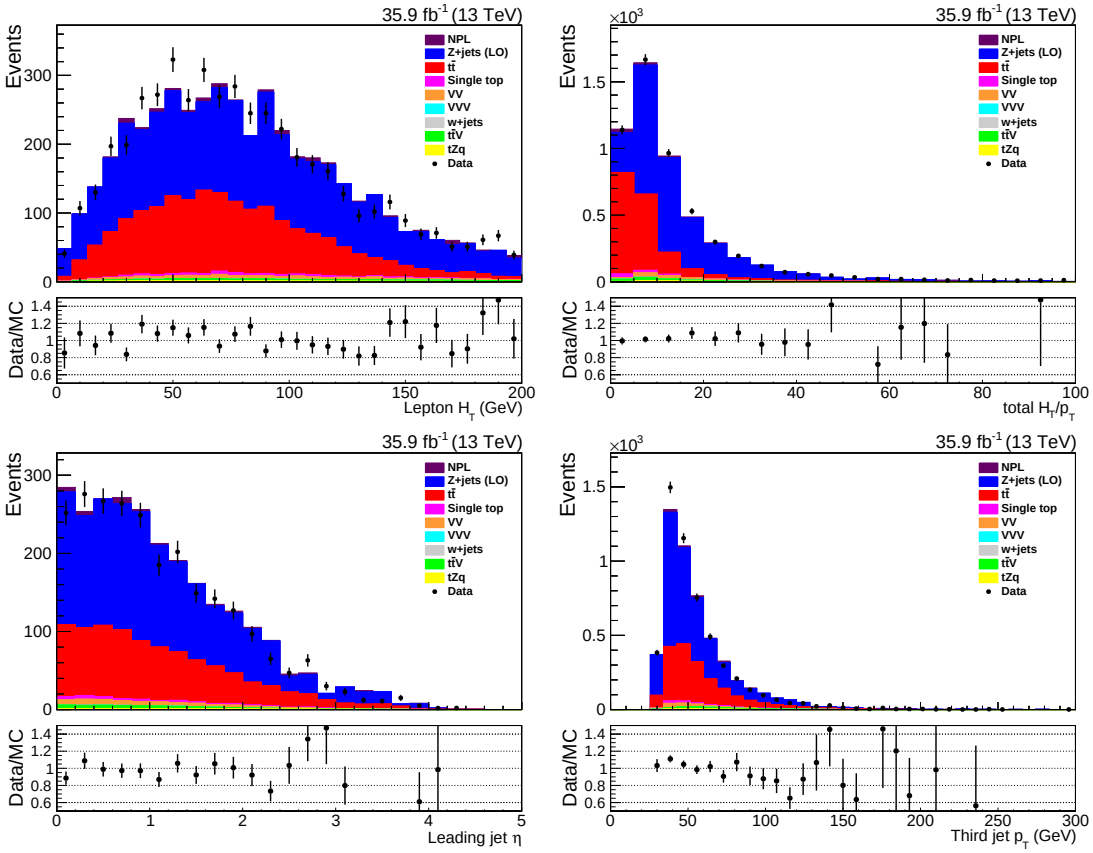

Figure D.3: Lepton H_{T}, total H_{T} divided by total p_{T}, leading jet η and third jet p_{T} distributions for the *ee* channel comparing the agreement between data and simulation for the variables used as input variables in the BDT training.

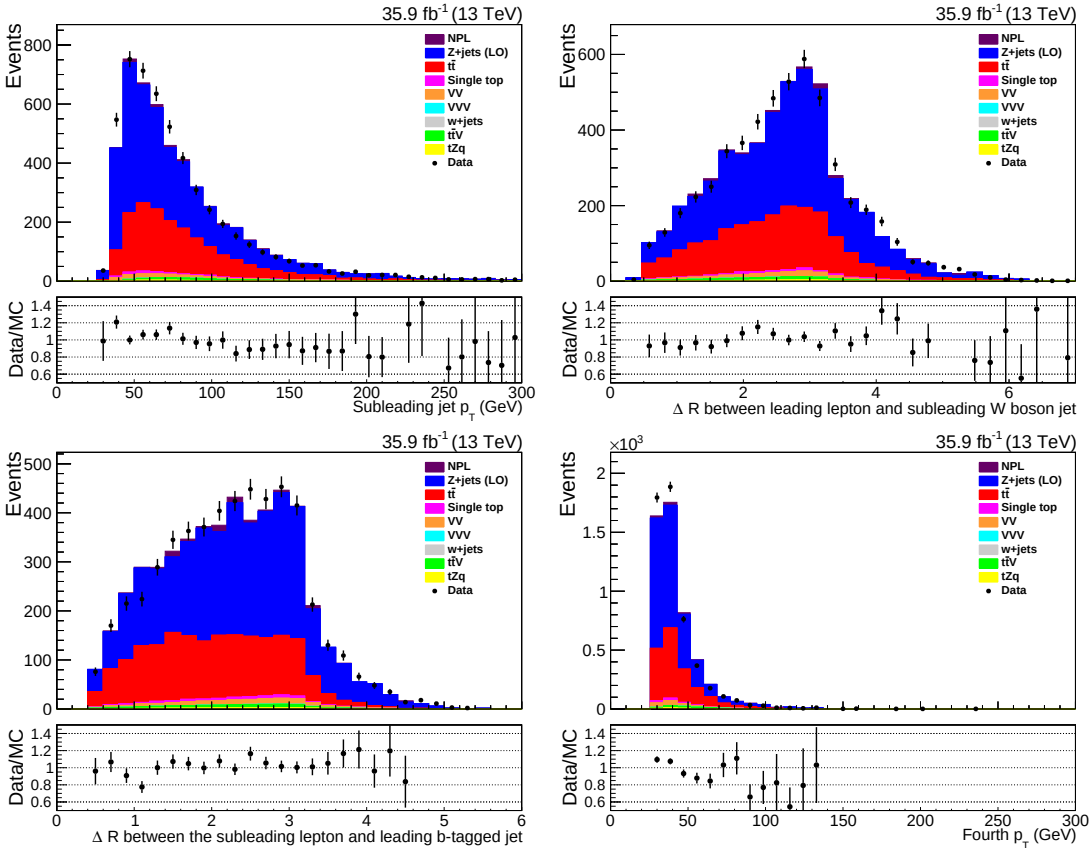

Figure D.4: Second jet p_{T}, ΔR between subleading lepton and leading b-tagged jet, ΔR between subleading lepton and leading b-tagged jet and fourth jet p_{T} distributions for the *ee* channel comparing the agreement between data and simulation for the variables used as input variables in the BDT training.

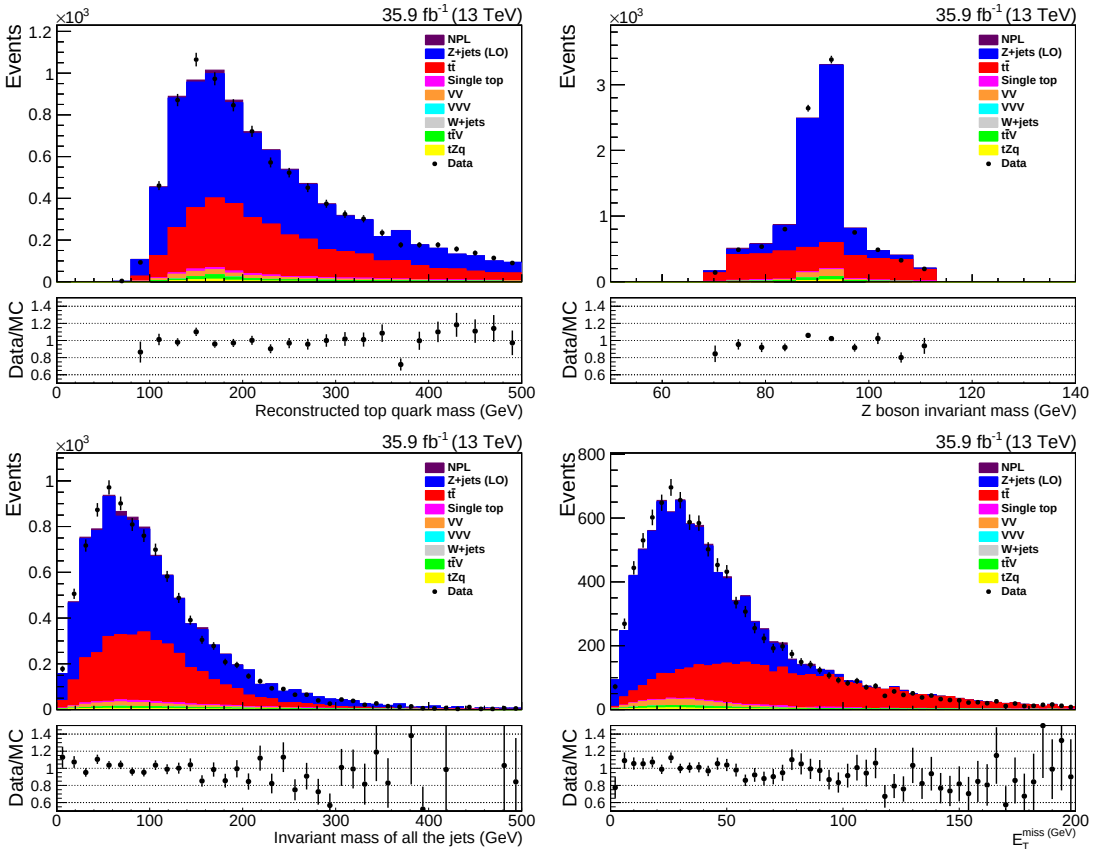

Figure D.5: Reconstructed top mass, Z boson mass, total jet mass, and $E_{\mathrm{T}}^{\mathrm{miss}}$ distributions for the $\mu\mu$ channel comparing the agreement between data and simulation for the variables used as input variables in the BDT training.

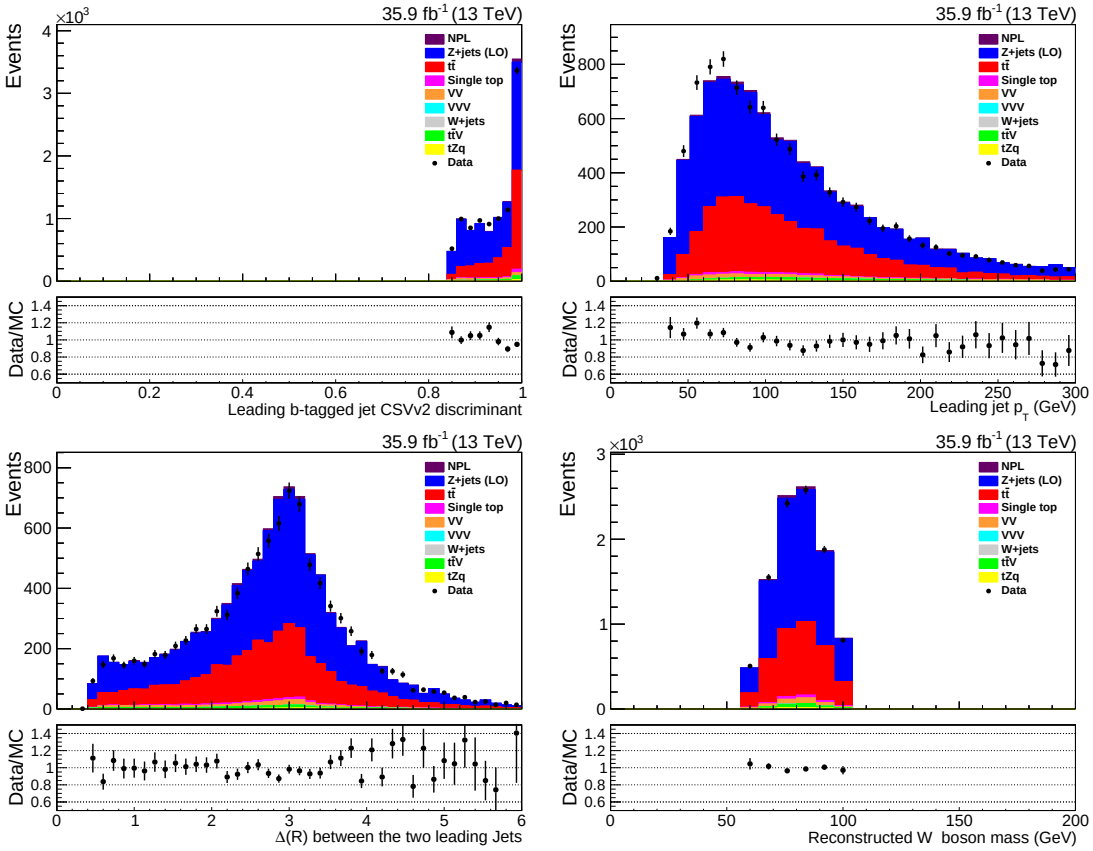

Figure D.6: Leading b-tagged jet CSVv2 discriminant, leading jet p_{T}, ΔR between the leading jets, and reconstructed W boson mass distributions for the $\mu\mu$ channel comparing the agreement between data and simulation for the variables used as input variables in the BDT training.

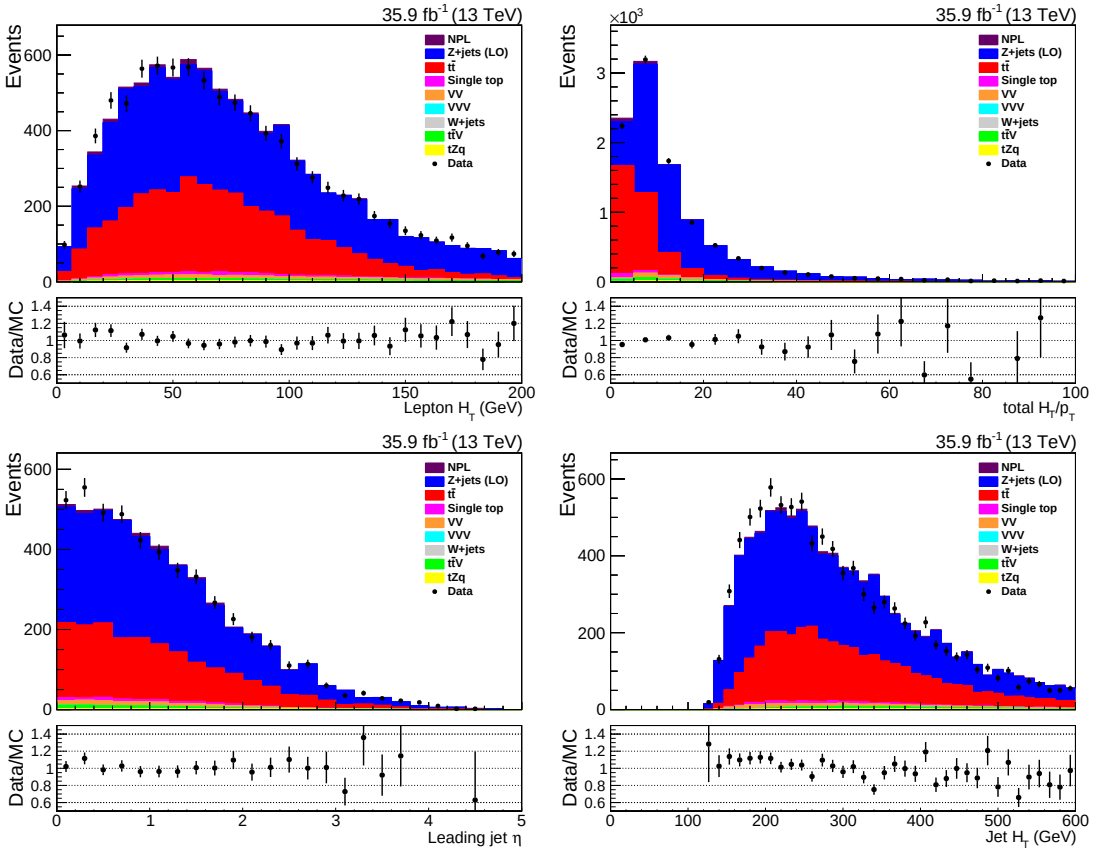

Figure D.7: Lepton H_{T}, total H_{T} divided by total p_{T}, leading jet η and jet H_{T} distributions for the $\mu\mu$ channel comparing the agreement between data and simulation for the variables used as input variables in the BDT training.

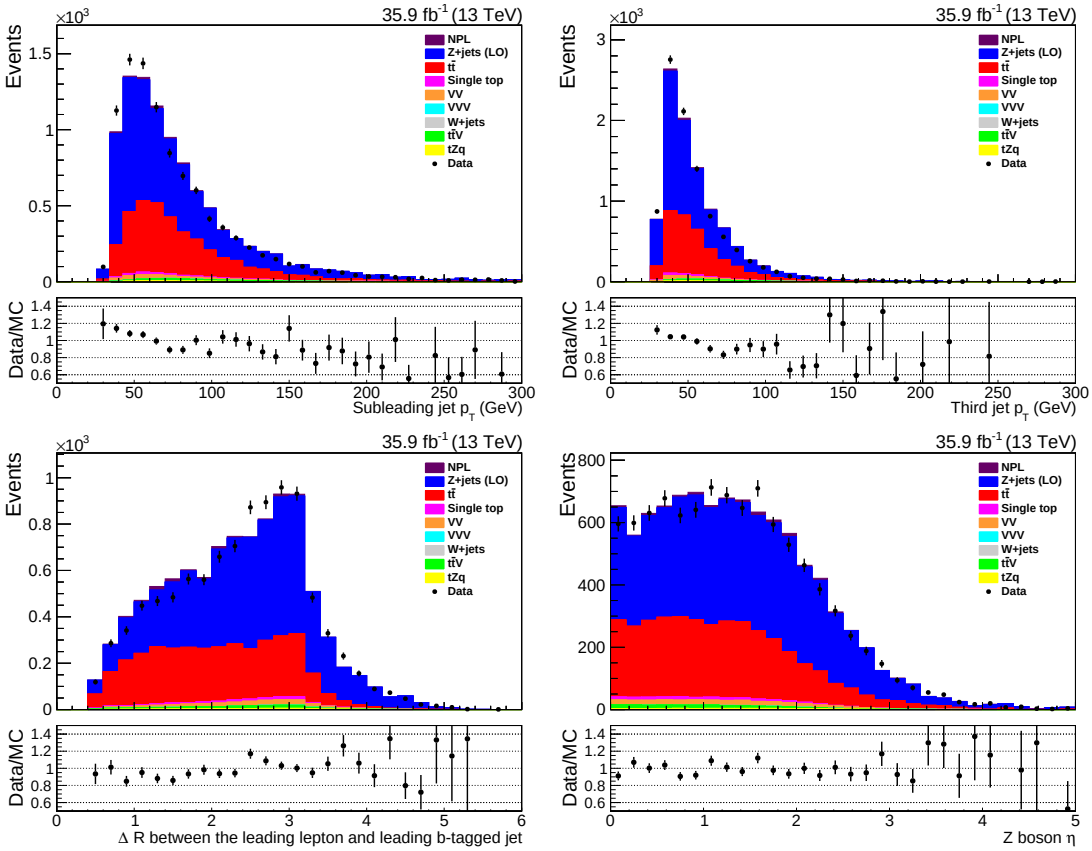

Figure D.8: Second jet p_{T}, third jet p_{T}, ΔR between leading lepton and leading b-tagged jet and reconstructed Z boson η distributions for the $\mu\mu$ channel comparing the agreement between data and simulation for the variables used as input variables in the BDT training.

Bibliography

[1] CMS Collaboration, S. Chatrchyan et al., *Observation of a new boson at a mass of 125 GeV with the CMS experiment at the LHC*, *Phys. Lett.* **B716** (2012) 30–61, [arXiv:1207.7235], doi:10.1016/j.physletb.2012.08.021.

[2] ATLAS Collaboration, G. Aad et al., *Observation of a new particle in the search for the Standard Model Higgs boson with the ATLAS detector at the LHC*, *Phys. Lett.* **B716** (2012) 1–29, [arXiv:1207.7214], doi:10.1016/j.physletb.2012.08.020.

[3] J. Sola, *Cosmological constant and vacuum energy: old and new ideas*, *J. Phys. Conf. Ser.* **453** (2013) 012015, [arXiv:1306.1527], doi:10.1088/1742-6596/453/1/012015.

[4] G. Bertone, D. Hooper and J. Silk, *Particle dark matter: Evidence, candidates and constraints*, *Phys. Rept.* **405** (2005) 279–390, [arXiv:hep-ph/0404175], doi:10.1016/j.physrep.2004.08.031.

[5] P. J. E. Peebles and B. Ratra, *The Cosmological constant and dark energy*, *Rev. Mod. Phys.* **75** (2003) 559–606, [arXiv:astro-ph/0207347], doi:10.1103/RevModPhys.75.559.

[6] Super-Kamiokande Collaboration, Y. Fukuda et al., *Evidence for oscillation of atmospheric neutrinos*, *Phys. Rev. Lett.* **81** (1998) 1562–1567, [arXiv:hep-ex/9807003], doi:10.1103/PhysRevLett.81.1562.

[7] SNO Collaboration, Q. R. Ahmad et al., *Measurement of the rate of $\nu_e + d \to p + p + e^-$ interactions produced by ^8B solar neutrinos at the Sudbury Neutrino Observatory*, *Phys. Rev. Lett.* **87** (2001) 071301, [arXiv:nucl-ex/0106015], doi:10.1103/PhysRevLett.87.071301.

[8] G. Burdman, *New solutions to the hierarchy problem*, *Braz. J. Phys.* **37** (2007) 506–513, [arXiv:hep-ph/0703194], doi:10.1590/S0103-97332007000400006.

[9] ParticleDataGroup Collaboration, M. Tanabashi et al., *Review of Particle Physics*, *Phys. Rev.* **D98** (2018) 030001, doi:10.1103/PhysRevD.98.030001.

[10] A. Dobado, A. Gómez-Nicola, A. L. Maroto and J. R. Peláex, *Effective Lagrangians for the Standard Model*. Springer, 1997.

[11] F. Scheck, *Electroweak and Strong Interactions*. Springer, 2012.

[12] LHCb Collaboration, R. Aaij et al., *Observation of the resonant character of the $Z(4430)^-$ state*, *Phys. Rev. Lett.* **112** (2014) 222002, [arXiv:1404.1903], doi:10.1103/PhysRevLett.112.222002.

[13] LHCb Collaboration, R. Aaij et al., *Observation of $J/\psi p$ Resonances Consistent with Pentaquark States in $\Lambda_b^0 \to J/\psi K^- p$ Decays*, *Phys. Rev. Lett.* **115** (2015) 072001, [arXiv:1507.03414], doi:10.1103/PhysRevLett.115.072001.

[14] P. Nath, *High Energy Physics and Cosmology at the Unification Frontier: Opportunities and Challenges in the coming years*, *Int. J. Mod. Phys.* **A33** (2018) 1830017, [arXiv:1807.05302], doi:10.1142/S0217751X1830017X.

[15] S. Haywood, *Symmetries and Conservation Laws in Particle Physics*. Imperial College Press, December, 2010.

[16] E. Noether, *Invariant Variation Problems*, *Gott. Nachr.* **1918** (1918) 235–257, [arXiv:physics/0503066], doi:10.1080/00411457108231446.

[17] T. P. Cheng and L. F. Li, *Gauge Theory Of Elementary Particle Physics*. 1984.

[18] F. Mandl and G. Shaw, *Quantum Field Theory Revised Edition*. John Wiley & Sons, August, 1993.

[19] G. Coughlan, J. Dodd and B. Gripaios, *The Ideas of Particle Physics: An Introduction for Scientists*. Cambridge University Press, 2006.

[20] T. D. Lee and C.-N. Yang, *Question of Parity Conservation in Weak Interactions*, *Phys. Rev.* **104** (1956) 254–258, doi:10.1103/PhysRev.104.254.

[21] C. S. Wu, E. Ambler, R. W. Hayward, D. D. Hoppes and R. P. Hudson, *Experimental Test of Parity Conservation in Beta Decay*, *Phys. Rev.* **105** (1957) 1413–1414, doi:10.1103/PhysRev.105.1413.

[22] J. H. Christenson, J. W. Cronin, V. L. Fitch and R. Turlay, *Evidence for the 2π Decay of the K_2^0 Meson*, *Phys. Rev. Lett.* **13** (1964) 138–140, doi:10.1103/PhysRevLett.13.138.

[23] S. L. Glashow, *Partial Symmetries of Weak Interactions*, *Nucl. Phys.* **22** (1961) 579–588, doi:10.1016/0029-5582(61)90469-2.

[24] A. Salam and J. C. Ward, *Electromagnetic and weak interactions*, *Phys. Lett.* **13** (1964) 168–171, doi:10.1016/0031-9163(64)90711-5.

[25] S. Weinberg, *A Model of Leptons*, *Phys. Rev. Lett.* **19** (1967) 1264–1266, doi:10.1103/PhysRevLett.19.1264.

[26] D. Griffiths, *Introduction to Elementary Particles*. John Wiley & Sons, 1987.

[27] F. Englert and R. Brout, *Broken Symmetry and the Mass of Gauge Vector Mesons*, *Phys. Rev. Lett.* **13** (1964) 321–323, doi:10.1103/PhysRevLett.13.321. [,157(1964)].

[28] P. W. Higgs, *Broken Symmetries and the Masses of Gauge Bosons*, *Phys. Rev. Lett.* **13** (1964) 508–509, doi:10.1103/PhysRevLett.13.508. [,160(1964)].

[29] G. S. Guralnik, C. R. Hagen and T. W. B. Kibble, *Global Conservation Laws and Massless Particles*, *Phys. Rev. Lett.* **13** (1964) 585–587, doi:10.1103/PhysRevLett.13.585. [,162(1964)].

[30] J. Ellis, *Higgs Physics*, in *Proceedings, 2013 European School of High-Energy Physics (ESHEP 2013): Paradfurdo, Hungary, June 5-18, 2013*, KCL-PH-TH-2013-49, LCTS-2013-36, CERN-PH-TH-2013-315, pp. 117–168, 2015, arXiv:1312.5672, doi:10.5170/CERN-2015-004.117.

[31] CMS Collaboration, A. M. Sirunyan et al., *Observation of* $\mathrm{t\bar{t}}H$ *production*, *Phys. Rev. Lett.* **120** (2018) 231801, [arXiv:1804.02610], doi:10.1103/PhysRevLett.120.231801, 10.1130/PhysRevLett.120.231801.

[32] CMS Collaboration, *Search for the associated production of the Higgs boson and a vector boson in proton-proton collisions at* $\sqrt{s} = 13$ *TeV via Higgs boson decays to* τ *leptons*, CERN-EP-2018-221. CMS-HIG-18-007-003, CERN, Geneva, Sep, 2018.

[33] CMS Collaboration, A. M. Sirunyan et al., *Search for resonant and nonresonant Higgs boson pair production in the* $\mathrm{b\bar{b}}\ell\nu\ell\nu$ *final state in proton-proton collisions at* $\sqrt{s} = 13$ *TeV*, *JHEP* **01** (2018) 054, [arXiv:1708.04188], doi:10.1007/JHEP01(2018)054.

[34] R. Devenish, E. Devenish, A. Cooper-Sarkar and O. U. Press, *Deep Inelastic Scattering*. Oxford University Press, 2004.

[35] B. Andersson, G. Gustafson, G. Ingelman and T. Sjostrand, *Parton Fragmentation and String Dynamics*, *Phys. Rept.* **97** (1983) 31–145. 10.1016/0370-1573(83)90080-7.

[36] NNPDF Collaboration, R. D. Ball et al., *Parton distributions for the LHC Run II*, *JHEP* **04** (2015) 040, [arXiv:1410.8849], doi:10.1007/JHEP04(2015)040.

[37] M. Kobayashi and T. Maskawa, *CP Violation in the Renormalizable Theory of Weak Interaction*, *Prog. Theor. Phys.* **49** (1973) 652–657, doi:10.1143/PTP.49.652.

[38] S. W. Herb et al., *Observation of a Dimuon Resonance at 9.5-GeV in 400-GeV Proton-Nucleus Collisions*, *Phys. Rev. Lett.* **39** (1977) 252–255, doi:10.1103/PhysRevLett.39.252.

[39] CDF Collaboration, F. Abe et al., *Observation of top quark production in $\bar{p}p$ collisions*, *Phys. Rev. Lett.* **74** (1995) 2626–2631, [arXiv:hep-ex/9503002], doi:10.1103/PhysRevLett.74.2626.

[40] DØ Collaboration, S. Abachi et al., *Observation of the top quark*, *Phys. Rev. Lett.* **74** (1995) 2632–2637, [arXiv:hep-ex/9503003], doi:10.1103/PhysRevLett.74.2632.

[41] Quadt, A., *Top quark physics at hadron colliders*, *Eur. Phys. J. C* **48** (2006) 835–1000, doi:10.1140/epjc/s2006-02631-6.

[42] CMS Collaboration, V. Khachatryan et al., *Measurement of top quark polarisation in t-channel single top quark production*, *JHEP* **04** (2016) 073, [arXiv:1511.02138], doi:10.1007/JHEP04(2016)073.

[43] A. Shibata, *Top Quark Physics at the LHC*, in *Hadron collider physics. Proceedings, 19th Symposium, HCP2008, Galena, USA, May 27-31, 2008*, ATL-PHYS-PROC-2008-056, ATL-COM-PHYS-2008-103, 2008, arXiv:0808.0031, http://weblib.cern.ch/abstract?ATL-PHYS-PROC-2008-056.

[44] CMS Collaboration, V. Khachatryan et al., *Measurement of the ratio $\mathcal{B}(t \to Wb)/\mathcal{B}(t \to Wq)$ in pp collisions at $\sqrt{s} = 8$ TeV*, *Phys. Lett.* **B736** (2014) 33–57, [arXiv:1404.2292], doi:10.1016/j.physletb.2014.06.076.

[45] DØ Collaboration, "Feynman diagrams for top physics talks and notes." https://www-d0.fnal.gov/Run2Physics/top/top_public_web_pages/top_feynman_diagrams.html.

[46] A. Giammanco and R. Schwienhorst, *Single top-quark production at the Tevatron and the LHC*, *Rev. Mod. Phys.* **90** (2018) 035001, [arXiv:1710.10699], doi:10.1103/RevModPhys.90.035001.

[47] F. Deliot, *Top Quark Physics At Hadron Colliders*, *PoS* **EPS-HEP2011** (2011) 007, [arXiv:1111.6274].

[48] CMS Collaboration, V. Khachatryan et al., *Search for s channel single top quark production in pp collisions at $\sqrt{s} = 7$ and 8 TeV*, *JHEP* **09** (2016) 027, [arXiv:1603.02555], doi:10.1007/JHEP09(2016)027.

[49] CDF Collaboration, T. Aaltonen et al., *First Observation of Electroweak Single Top Quark Production*, *Phys. Rev. Lett.* **103** (2009) 092002, [arXiv:0903.0885], doi:10.1103/PhysRevLett.103.092002.

[50] DØ Collaboration, V. M. Abazov et al., *Observation of Single Top Quark Production*, *Phys. Rev. Lett.* **103** (2009) 092001, [arXiv:0903.0850], doi:10.1103/PhysRevLett.103.092001.

[51] ATLAS Collaboration, P. Berta, *Highlights of top quark cross-section measurements at ATLAS*, *EPJ Web Conf.* **158** (2017) 04001, doi:10.1051/epjconf/201715804001.

[52] CMS Collaboration, A. D. Morton, *Single top quark production with the CMS experiment at the LHC*, *Nuclear and Particle Physics Proceedings* **294-296** (2018) 48–53, doi:10.1016/j.nuclphysbps.2018.03.013.

[53] CMS Collaboration, S. Chatrchyan et al., *Observation of the associated production of a single top quark and a W boson in pp collisions at* $\sqrt{s}$ *=8 TeV*, *Phys. Rev. Lett.* **112** (2014) 231802, [arXiv:1401.2942], doi:10.1103/PhysRevLett.112.231802.

[54] A. Guffanti and J. Rojo, *Top production at the LHC: The Impact of PDF uncertainties and correlations*, *Nuovo Cim.* **C033** (2010) 65–72, [arXiv:1008.4671], doi:10.1393/ncc/i2010-10668-y.

[55] CMS Collaboration, A. M. Sirunyan et al., *Measurement of the cross section for top quark pair production in association with a W or Z boson in proton-proton collisions at* $\sqrt{s} = 13$ *TeV*, *JHEP* **08** (2018) 011, [arXiv:1711.02547].

[56] CMS Collaboration, *Search for the associated production of a Higgs boson and a single top quark in pp collisions at* $\sqrt{s} = 13$ TeV, CMS-PAS-HIG-18-009, CERN, Geneva, 2018.

[57] F. Maltoni, K. Paul, T. Stelzer and S. Willenbrock, *Associated production of Higgs and single top at hadron colliders*, *Phys. Rev.* **D64** (2001) 094023, [arXiv:hep-ph/0106293], doi:10.1103/PhysRevD.64.094023.

[58] J. Campbell, R. K. Ellis and R. Röntsch, *Single top production in association with a Z boson at the LHC*, *Phys. Rev.* **D87** (2013) 114006, [arXiv:1302.3856], doi:10.1103/PhysRevD.87.114006.

[59] J. A. Aguilar-Saavedra, *Top flavor-changing neutral interactions: Theoretical expectations and experimental detection*, *Acta Phys. Polon.* **B35** (2004) 2695–2710, [arXiv:hep-ph/0409342].

[60] CMS Collaboration, A. M. Sirunyan et al., *Search for associated production of a Z boson with a single top quark and for tZ flavour-changing interactions in pp collisions at* $\sqrt{s} = 8$ *TeV*, *JHEP* **07** (2017) 003, [arXiv:1702.01404], doi:10.1007/JHEP07(2017)003.

[61] ATLAS Collaboration, M. Aaboud et al., *Measurement of the production cross-section of a single top quark in association with a Z boson in proton–proton collisions at 13 TeV with the ATLAS detector*, *Phys. Lett.* **B780** (2018) 557–577, [arXiv:1710.03659], doi:10.1016/j.physletb.2018.03.023.

[62] CMS Collaboration, A. M. Sirunyan et al., *Measurement of the associated production of a single top quark and a Z boson in pp collisions at* $\sqrt{s} = 13$ *TeV*, *Phys. Lett.* **B779** (2018) 358–384, [arXiv:1712.02825], doi:10.1016/j.physletb.2018.02.025.

[63] R. J. Adler, B. Casey and O. C. Jacob, *Vacuum catastrophe: An Elementary exposition of the cosmological constant problem*, *Am. J. Phys.* **63** (1995) 620–626, doi:10.1119/1.17850.

[64] R. Davis, D. S. Harmer and K. C. Hoffman, *Search for neutrinos from the sun*, *Phys. Rev. Lett.* **20** (May, 1968) 1205–1209, doi:10.1103/PhysRevLett.20.1205.

[65] T2K Collaboration Collaboration, K. Abe et al., *Evidence of electron neutrino appearance in a muon neutrino beam*, *Phys. Rev. D* **88** (Aug, 2013) 032002, doi:10.1103/PhysRevD.88.032002.

[66] O. S. Brüning, P. Collier, P. Lebrun, S. Myers, R. Ostojic, J. Poole et al., *LHC Design Report Vol.1: The LHC Main Ring*. CERN-2004-003-V1, CERN-2004-003, CERN-2004-003-V-1 in CERN Yellow Reports: Monographs. CERN, Geneva, 2004.

[67] CMS Collaboration, G. L. Bayatian et al., *CMS Physics: Technical Design Report Volume 1: Detector Performance and Software*, , Geneva, 2006.

[68] ATLAS Collaboration, G. Aad et al., *The ATLAS Experiment at the CERN Large Hadron Collider*, *JINST* **3** (2008) S08003, doi:10.1088/1748-0221/3/08/S08003.

[69] CMS Collaboration, S. Chatrchyan et al., *The CMS experiment at the CERN LHC*, *JINST* **3** (2008) S08004, doi:10.1088/1748-0221/3/08/S08004.

[70] LHCb Collaboration, A. A. Alves, Jr. et al., *The LHCb Detector at the LHC*, *JINST* **3** (2008) S08005, doi:10.1088/1748-0221/3/08/S08005.

[71] ALICE Collaboration, K. Aamodt et al., *The ALICE experiment at the CERN LHC*, *JINST* **3** (2008) S08002, doi:10.1088/1748-0221/3/08/S08002.

[72] TOTEM Collaboration, G. Anelli et al., *The TOTEM experiment at the CERN Large Hadron Collider*, *JINST* **3** (2008) S08007, doi:10.1088/1748-0221/3/08/S08007.

[73] LHCf Collaboration, O. Adriani et al., *The LHCf detector at the CERN Large Hadron Collider*, *JINST* **3** (2008) S08006, doi:10.1088/1748-0221/3/08/S08006.

[74] MoEDAL Collaboration, J. Pinfold et al., *Technical Design Report of the MoEDAL Experiment*, CERN-LHCC-2009-006, MoEDAL-TDR-001, 2009.

[75] *ECFA High Luminosity LHC Experiments Workshop: Physics and Technology Challenges. 94th Plenary ECFA meeting*, Nov, 2013. https://cds.cern.ch/record/1631032.

[76] CMS Collaboration, K. Klein, *The Phase-2 Upgrade of the CMS Tracker: Technical Design Report*, CERN-LHCC-2017-009, CMS-TDR-014, CERN, Geneva, Jun, 2017.

[77] F. Marcastel, *CERN's Accelerator Complex. La chaîne des accélérateurs du CERN*, Oct, 2013, https://cds.cern.ch/record/1621583, General Photo.

[78] K. Schindl, *The injector chain for the LHC*, Jan, 1999, http://cds.cern.ch/record/397574.

[79] CMS Collaboration, S. Dasu et al., *CMS TriDAS project: Technical Design Report, Volume 1: The Trigger Systems*, CERN-LHCC-2000-038, 2000.

[80] CMS Collaboration, G. L. Bayatian et al., *CMS Physics: Technical Design Report Volume 2: Physics Performance*, *J. Phys.* **G34** (2007) 995–1579, doi:10.1088/0954-3899/34/6/S01.

[81] T. Sakuma and T. McCauley, *Detector and Event Visualization with SketchUp at the CMS Experiment*, *J. Phys. Conf. Ser.* **513** (2014) 022032, [arXiv:1311.4942], doi:10.1088/1742-6596/513/2/022032.

[82] D. Sprenger, M. Weber, R. Adolphi, R. Brauer, L. Feld, K. Klein et al., *Validation of Kalman Filter alignment algorithm with cosmic-ray data using a CMS silicon strip tracker endcap*, *JINST* **5** (2010) P06007, [arXiv:1003.5460], doi:10.1088/1748-0221/5/06/P06007.

[83] CMS Collaboration, V. Khachatryan et al., *CMS Tracking Performance Results from early LHC Operation*, *Eur. Phys. J.* **C70** (2010) 1165–1192, [arXiv:1007.1988], doi:10.1140/epjc/s10052-010-1491-3.

[84] CMS Collaboration, S. Chatrchyan et al., *Description and performance of track and primary-vertex reconstruction with the CMS tracker*, *JINST* **9** (2014) P10009, [arXiv:1405.6569], doi:10.1088/1748-0221/9/10/P10009.

[85] CMS Collaboration, M. Hoch, "CMS pixel detector.", Dec, 2014, CMS-PHO-TRACKER-2014-001, https://cds.cern.ch/record/1977415.

[86] CMS Collaboration, V. Karimäki, M. Mannelli, P. Siegrist, H. Breuker, A. Caner, R. Castaldi et al., *The CMS tracker system project: Technical Design Report*, CERN-LHCC-98-006, CMS-TDR-5, Geneva, 1997.

[87] CMS Collaboration, D. A. Matzner Dominguez, D. Abbaneo, K. Arndt, N. Bacchetta, A. Ball, E. Bartz et al., *CMS Technical Design Report for the Pixel Detector Upgrade*, CERN-LHCC-2012-016, CMS-TDR-011, FERMILAB-DESIGN-2012-02, 2012.

[88] CMS Collaboration, M. Brice, "First half of CMS inner tracker barrel.", Oct, 2006, CERN-EX-0610026, https://cds.cern.ch/record/995912.

[89] CMS Collaboration, CERN. Geneva. LHC Experiments Committee, *The CMS electromagnetic calorimeter project: Technical Design Report*, CERN-LHCC-97-033, CMS-TDR-4, 1997.

[90] CMS Collaboration, P. Bloch, R. Brown, P. Lecoq and H. Rykaczewski, *Addendum to the CMS ECAL technical design report: Changes to the CMS ECAL electronics*, CERN-LHCC-2002-027, Geneva, 2002.

[91] *CMS ECAL Preshower and Endcap Engineering Design Review. v.2 - Preshower*, (Geneva), CERN, 2000. https://cds.cern.ch/record/539819.

[92] CMS Collaboration, G. L. Bayatian et al., *CMS Physics: Technical Design Report Volume 1: Detector Performance and Software*, CERN-LHCC-2006-001, Geneva, 2006.

[93] P. Adzic et al., *Energy resolution of the barrel of the CMS electromagnetic calorimeter*, *JINST* **2** (2007) P04004, doi:10.1088/1748-0221/2/04/P04004.

[94] CMS Collaboration, CERN. Geneva. LHC Experiments Committee, *The CMS hadron calorimeter project: Technical Design Report*, CERN-LHCC-97-031, CMS-TDR-2, 1997.

[95] CMS Collaboration, A. Penzo and Y. Onel, *The CMS-HF quartz fiber calorimeters*, *J. Phys. Conf. Ser.* **160** (2009) 012014, doi:10.1088/1742-6596/160/1/012014.

[96] B. S. Acharya, T. Aziz, S. Banerjee, S. Banerjee, H. S. Bawa, S. B. Beri et al., *The CMS Outer Hadron Calorimeter*, CMS-NOTE-2006-127, CERN, Geneva, Jun, 2006.

[97] CMS HCAL Collaboration, S. Abdullin et al., *Design, performance, and calibration of CMS hadron-barrel calorimeter wedges*, *Eur. Phys. J.* **C55** (2008) 159–171, doi:10.1140/epjc/s10052-008-0573-y.

[98] G. Bayatian et al., *Design, performance and calibration of the CMS forward calorimeter wedges*, *Eur. Phys. J.* **C53** (2008) 139–166, doi:10.1140/epjc/s10052-007-0459-4.

[99] CMS Collaboration, G. Acquistapace et al., *The CMS magnet project: Technical Design Report*, CERN-LHCC-97-10, 1997.

[100] A. Herve, *The CMS detector magnet*, *IEEE Transactions on Applied Superconductivity* **10** (March, 2000) 389–394, doi:10.1109/77.828255.

[101] CMS Collaboration, S. Chatrchyan et al., *Precise Mapping of the Magnetic Field in the CMS Barrel Yoke using Cosmic Rays*, *JINST* **5** (2010) T03021, [arXiv:0910.5530], doi:10.1088/1748-0221/5/03/T03021.

[102] CMS Collaboration, CERN. Geneva. LHC Experiments Committee: Technical Design Report, *The CMS muon project: Technical Design Report*, CERN-LHCC-97-032, CMS-TDR-3, 1997.

[103] CMS Collaboration, *Performance of the CMS Muon Detectors in 2016 collision runs*, CMS-DP-2016-046, Jul, 2016.

[104] CMS Collaboration, S. Chatrchyan et al., *Performance of the CMS Drift Tube Chambers with Cosmic Rays*, *JINST* **5** (2010) T03015, [arXiv:0911.4855], doi:10.1088/1748-0221/5/03/T03015.

[105] CMS Collaboration, C. Battilana, *The CMS muon system: status and upgrades for LHC Run-2 and performance of muon reconstruction with 13 TeV data*, *JINST* **12** (2017) C01048, doi:10.1088/1748-0221/12/01/C01048.

[106] C. Anderson, V. Barashko, S. Korenblit, A. Korytov and G. Mitselmakher, *Effect of gas composition on the performance of cathode strip chambers for the CMS endcap muon system*, CMS-NOTE-2004-033, 2004.

[107] CMS Collaboration, S. Chatrchyan et al., *Performance of CMS muon reconstruction in pp collision events at* $\sqrt{s} = 7$ *TeV*, *JINST* **7** (2012) P10002, [arXiv:1206.4071], doi:10.1088/1748-0221/7/10/P10002.

[108] CMS Collaboration, S. Chatrchyan et al., *The performance of the CMS muon detector in proton-proton collisions at sqrt(s) = 7 TeV at the LHC*, *JINST* **8** (2013) P11002, [arXiv:1306.6905], doi:10.1088/1748-0221/8/11/P11002.

[109] TOTEM Collaboration, G. Antchev et al., *First measurement of elastic, inelastic and total cross-section at* $\sqrt{s} = 13$ *TeV by TOTEM and overview of cross-section data at LHC energies*, arXiv:1712.06153.

[110] CMS Collaboration, A. Tapper and D. Acosta, *CMS Technical Design Report for the Level-1 Trigger Upgrade*, CERN-LHCC-2013-011. CMS-TDR-12, Jun, 2013.

[111] G. Hall, *A time-multiplexed track-trigger for the {CMS} hl-lhc upgrade*, *Nuclear Instruments and Methods in Physics Research Section A: Accelerators, Spectrometers, Detectors and Associated Equipment* **824** (2016) 292 – 295, doi:10.1016/j.nima.2015.09.075. Frontier Detectors for Frontier Physics: Proceedings of the 13th Pisa Meeting on Advanced Detectors.

[112] A. Zabi et al., *The CMS Level-1 Calorimeter Trigger for the LHC Run II*, *JINST* **12** (2017) C01065, doi:10.1088/1748-0221/12/01/C01065.

[113] CMS Collaboration, S. Cittolin, A. Rácz and P. Sphicas, *CMS: The TriDAS project. Technical design report, Vol. 2: Data acquisition and high-level trigger*, CERN-LHCC-2002-026, 2002.

[114] CMS Luminosity Physics Object Group, "CMS Luminosity - Public Results." https://twiki.cern.ch/twiki/bin/view/CMSPublic/LumiPublicResults, visited on 2018-09-14.

[115] CMS Collaboration, *CMS Luminosity Measurements for the 2016 Data Taking Period*, CMS-PAS-LUM-17-001, 2017.

[116] S. van der Meer, *Calibration of the Effective Beam Height in the ISR*, CERN-ISR-PO-68-31, 1968.

[117] G. Apollinari, I. Béjar Alonso, O. Brüning, P. Fessia, M. Lamont, L. Rossi et al., *High-Luminosity Large Hadron Collider (HL-LHC)*, CERN-2017-007-M, 2017. doi:10.23731/CYRM-2017-004.

[118] The CERN Large Hadron Collider: Accelerator and Experiments Collaboration, G. Apollinari, I. Béjar Alonso, O. Brüning, M. Lamont and L. Rossi, *High-Luminosity Large Hadron Collider (HL-LHC): Preliminary Design Report*, , Geneva, 2015. doi:10.5170/CERN-2015-005.

[119] CMS Collaboration, D. Contardo, M. Klute, J. Mans, L. Silvestris and J. Butler, *Technical Proposal for the Phase-II Upgrade of the CMS Detector*, CERN-LHCC-2015-010. LHCC-P-008. CMS-TDR-15-02, Geneva, Jun, 2015.

[120] L. Arnaudon et al., *Linac4 Technical Design Report*, CERN-AB-2006-084, CERN, Geneva, Dec, 2006.

[121] J. Jones, G. Hall, C. Foudas and A. Rose, *A pixel detector for level-1 triggering at slhc*, in *11^{th} Workshop on Electronics for LHC Experiments, Heidelberg, September 2005, CERN Report CERN-2005-011*, (Geneva), pp. 130–134, CERN, CERN, 2005, https://cds.cern.ch/record/873448.

[122] M. Pesaresi, *Development of a new Silicon Tracker for CMS at Super-LHC*, Ph.D. thesis, Imperial College London, 2010.

[123] M. Pesaresi and G. Hall, *Simulating the performance of a p_T tracking trigger for CMS*, *Journal of Instrumentation* **5** (2010) C08003, doi:10.1088/1748-0221/5/08/C08003.

[124] G. Hall, M. Raymond and A. Rose, *2-d pt module concept for the SLHC CMS tracker*, *Journal of Instrumentation* **5** (2010) C07012, doi:10.1088/1748-0221/5/07/C07012.

[125] D. Abbaneo, *Performance Requirements for the Phase-2 Tracker Upgrades for ATLAS and CMS*, *EPJ Web Conf.* **127** (2016) 00002, doi:10.1051/epjconf/201612700002.

[126] R. Aggleton, L. Ardila-Perez, F. Ball, M. Balzer, G. Boudoul, J. Brooke et al., *An FPGA based track finder for the L1 trigger of the CMS experiment at the High Luminosity LHC*, *Journal of Instrumentation* **12** (December, 2017) P12019.

[127] G. Fedi, *L1 track trigger for the CMS HL-LHC upgrade using AM chips and FPGAs*, *EPJ Web Conf.* **150** (2017) 00004, doi:10.1051/epjconf/201715000004.

[128] E. Bartz et al., *FPGA-Based Tracklet Approach to Level-1 Track Finding at CMS for the HL-LHC*, *EPJ Web Conf.* **150** (2017) 00016, [arXiv:1706.09225], doi:10.1051/epjconf/201715000016.

[129] K. Compton, S. Dasu, A. Farmahini-Farahani, S. Fayer, R. Fobes, R. Frazier et al., *The MP7 and CTP-6: multi-hundred Gbps processing boards for calorimeter trigger upgrades at CMS*, *Journal of Instrumentation* **7** (2012) C12024, doi:10.1088/1748-0221/7/12/C12024.

[130] P. V. C. Hough, *Method and means for recognizing complex patterns*, December, 1962, US Patent 3,069,654.

[131] C. Amstutz, F. A. Ball, M. N. Balzer, J. Brooke, L. Calligaris, D. Cieri et al., *An FPGA-Based Track Finder for the L1 Trigger of the CMS Experiment at the High Luminosity LHC*, in *2016 IEEE-NPSS Real Time Conference (RT)*, pp. 1–9, June, 2016, doi:10.1109/RTC.2016.7543102.

[132] R. Frühwirth, *Application of Kalman filtering to track and vertex fitting*, *Nucl. Instrum. Meth.* **A262** (1987) 444–450, doi:10.1016/0168-9002(87)90887-4.

[133] C. Amstutz, F. A. Ball, M. N. Balzer, J. Brooke, L. Calligaris, D. Cieri et al., *Online track reconstruction using kalman filters on fpgas*, in *2016 IEEE-NPSS Real Time Conference (RT)*, March, 2017.

[134] R. Aggleton et al., *A novel FPGA-based track reconstruction approach for the Level-1 trigger of the CMS experiment at CERN*, doi:10.23919/FPL.2017.8056825.

[135] CMS Collaboration, *L1 tracklet-based track finding and fitting*, CMS Detector Note CMS-DN 2014/043, 2014.

[136] G. R. Lynch and O. I. Dahl, *Approximations to multiple Coulomb scattering*, *Nucl. Instrum. Meth.* **B58** (1991) 6–10, doi:10.1016/0168-583X(91)95671-Y.

[137] A. Buckley et al., *General-purpose event generators for LHC physics*, *Phys. Rept.* **504** (2011) 145–233, [arXiv:1101.2599], doi:10.1016/j.physrep.2011.03.005.

[138] S. Höche, *Introduction to parton-shower event generators*, in *Proceedings, Theoretical Advanced Study Institute in Elementary Particle Physics: Journeys Through the Precision Frontier: Amplitudes for Colliders (TASI 2014): Boulder, Colorado, June 2-27, 2014*, SLAC-PUB-16160, pp. 235–295, 2015, arXiv:1411.4085.

[139] J.-C. Winter, F. Krauss and G. Soff, *A Modified cluster hadronization model*, *Eur. Phys. J.* **C36** (2004) 381–395, [arXiv:hep-ph/0311085], doi:10.1140/epjc/s2004-01960-8.

[140] CMS Collaboration, V. Khachatryan et al., *Event generator tunes obtained from underlying event and multiparton scattering measurements*, *Eur. Phys. J.* **C76** (2016) 155, [arXiv:1512.00815], doi:10.1140/epjc/s10052-016-3988-x.

[141] GEANT4 Collaboration, S. Agostinelli et al., *GEANT4: A Simulation toolkit*, *Nucl. Instrum. Meth.* **A506** (2003) 250–303, doi:10.1016/S0168-9002(03)01368-8.

[142] V. Lefébure, S. Banerjee and I. González, *CMS Simulation Software Using Geant4*, CMS-NOTE-1999-072, CERN-CMS-NOTE-1999-072, 1999.

[143] J. Alwall, R. Frederix, S. Frixione, V. Hirschi, F. Maltoni, O. Mattelaer et al., *The automated computation of tree-level and next-to-leading order differential cross sections, and their matching to parton shower simulations*, *JHEP* **07** (2014) 079, [arXiv:1405.0301], doi:10.1007/JHEP07(2014)079.

[144] S. Alioli, P. Nason, C. Oleari and E. Re, *A general framework for implementing NLO calculations in shower Monte Carlo programs: the POWHEG BOX*, *JHEP* **06** (2010) 043, [arXiv:1002.2581], doi:10.1007/JHEP06(2010)043.

[145] T. Sjöstrand, S. Ask, J. R. Christiansen, R. Corke, N. Desai, P. Ilten et al., *An Introduction to PYTHIA 8.2*, *Comput. Phys. Commun.* **191** (2015) 159–177, [arXiv:1410.3012], doi:10.1016/j.cpc.2015.01.024.

[146] CMS Collaboration, *Particle-Flow Event Reconstruction in CMS and Performance for Jets, Taus, and MET*, CMS-PAS-PFT-09-001, 2009.

[147] CMS Collaboration, *Commissioning of the Particle-Flow reconstruction in Minimum-Bias and Jet Events from pp Collisions at 7 TeV*, CMS-PAS-PFT-10-002, 2010.

[148] CMS Collaboration, A. M. Sirunyan et al., *Particle-flow reconstruction and global event description with the CMS detector*, *JINST* **12** (2017) P10003, [arXiv:1706.04965], doi:10.1088/1748-0221/12/10/P10003.

[149] T. Speer, K. Prokofiev, R. Frühwirth, W. Waltenberger and P. Vanlaer, *Vertex Fitting in the CMS Tracker*, CMS-NOTE-2006-032, CERN, Geneva, Feb, 2006.

[150] K. Rose, *Deterministic annealing for clustering, compression, classification, regression, and related optimization problems*, in *Proceedings of the IEEE*, vol. 86, pp. 2210 – 2239, 12, 1998.

[151] R. Fruhwirth, W. Waltenberger and P. Vanlaer, *Adaptive vertex fitting*, *J. Phys.* **G34** (2007) N343, doi:10.1088/0954-3899/34/12/N01.

[152] CMS Collaboration, *Primary vertex resolution in 2016*, CMS-DP-2016-041, Jul, 2016.

[153] CMS Collaboration, V. Khachatryan et al., *Performance of Electron Reconstruction and Selection with the CMS Detector in Proton-Proton Collisions at sqrts = 8 TeV*, *JINST* **10** (2015) P06005, [arXiv:1502.02701], doi:10.1088/1748-0221/10/06/P06005.

[154] W. Adam, R. Frühwirth, A. Strandlie and T. Todorov, *Reconstruction of Electron Tracks With the Gaussian-Sum Filter*, CMS-RN-2003-001, CERN-CMS-RN-2003-001, 2003.

[155] CMS Collaboration Collaboration, *Electron and photon performance in CMS with the full 2016 data sample*, CMS-DP-2017-004, March, 2017.

[156] G. P. Salam, *Towards Jetography*, *Eur. Phys. J.* **C67** (2010) 637–686, [arXiv:0906.1833], doi:10.1140/epjc/s10052-010-1314-6.

[157] M. Cacciari, G. P. Salam and G. Soyez, *The anti-k_t jet clustering algorithm*, *JHEP* **04** (2008) 063, [arXiv:0802.1189], doi:10.1088/1126-6708/2008/04/063.

[158] CMS Collaboration, V. Khachatryan et al., *Jet energy scale and resolution in the CMS experiment in pp collisions at 8 TeV*, *JINST* **12** (2017) P02014, [arXiv:1607.03663], doi:10.1088/1748-0221/12/02/P02014.

[159] C. Collaboration, *Jet algorithms performance in 13 TeV data*, .

[160] CMS Collaboration, *Jet energy scale and resolution performances with 13TeV data*, CMS-DP-2016-020, Jun, 2016.

[161] Particle Data Group Collaboration, J. Beringer et al., *Review of Particle Physics (RPP)*, *Phys. Rev.* **D86** (2012) 010001, doi:10.1103/PhysRevD.86.010001.

[162] CMS Collaboration, A. M. Sirunyan et al., *Identification of heavy-flavour jets with the CMS detector in pp collisions at 13 TeV*, *Submitted to: JINST* (2017) , [arXiv:1712.07158].

[163] CMS Collaboration, *Performance of missing energy reconstruction in 13 TeV pp collision data using the CMS detector*, CMS-PAS-JME-16-004, 2016.

[164] CMS Collaboration, S. Chatrchyan et al., *Missing transverse energy performance of the CMS detector*, *JINST* **6** (2011) P09001, [arXiv:1106.5048], doi:10.1088/1748-0221/6/09/P09001.

[165] A. Roodman, *Blind analysis in particle physics*, *eConf* **C030908** (2003) TUIT001, [arXiv:physics/0312102]. [,166(2003)].

[166] CMS Collaboration, *Search for resonant pair production of Higgs bosons decaying to two bottom quark-antiquark pairs in proton-proton collisions at 13 TeV*, CMS-PAS-HIG-16-002, 2016.

[167] ATLAS Collaboration, *Search for pair production of Higgs bosons in the $b\bar{b}b\bar{b}$ final state using proton-proton collisions at $\sqrt{s} = 13$ TeV with the ATLAS detector*, ATLAS-CONF-2016-017, 2016.

[168] CMS Collaboration, S. Chatrchyan et al., *Search for neutral Higgs bosons decaying to tau pairs in pp collisions at $\sqrt{s} = 7$ TeV*, *Phys. Lett.* **B713** (2012) 68–90, [arXiv:1202.4083], doi:10.1016/j.physletb.2012.05.028.

[169] CMS Collaboration, A. M. Sirunyan et al., *Extraction and validation of a new set of CMS PYTHIA8 tunes from underlying-event measurements*, arXiv:1903.12179.

[170] R. D. Ball et al., *Parton distributions with LHC data*, *Nucl. Phys.* **B867** (2013) 244–289, [arXiv:1207.1303], doi:10.1016/j.nuclphysb.2012.10.003.

[171] CMS Collaboration, F. Fiori, *CMS Tracker operational experience*, *PoS* **Vertex2016** (2017) 006, doi:10.22323/1.287.0006.

[172] CMS Collaboration, *Measuring Electron Efficiencies at CMS with Early Data*, CMS-PAS-EGM-07-001, Dec, 2008.

[173] CMS Collaboration Collaboration, *Muon Identification and Isolation efficiency on full 2016 dataset*, .

[174] CMS Collaboration, V. Khachatryan et al., *Measurement of the $t\bar{t}$ production cross section using events in the $e\mu$ final state in pp collisions at $\sqrt{s} = 13$ TeV*, *Eur. Phys. J.* **C77** (2017) 172, [arXiv:1611.04040], doi:10.1140/epjc/s10052-017-4718-8.

[175] A. Bodek, A. van Dyne, J. Y. Han, W. Sakumoto and A. Strelnikov, *Extracting Muon Momentum Scale Corrections for Hadron Collider Experiments*, *Eur. Phys. J.* **C72** (2012) 2194, [arXiv:1208.3710], doi:10.1140/epjc/s10052-012-2194-8.

[176] CMS Collaboration, V. Khachatryan et al., *Measurement of the differential cross section for top quark pair production in pp collisions at* $\sqrt{s} = 8$ *TeV*, *Eur. Phys. J.* **C75** (2015) 542, [arXiv:1505.04480], doi:10.1140/epjc/s10052-015-3709-x.

[177] CMS Collaboration, *Measurement of the top quark pair production cross section using eμ events in proton-proton collisions at* $\sqrt{s} = 13$ TeV *with the CMS detector*, CMS-PAS-TOP-16-005, 2016.

[178] CMS Collaboration, *Search for SUSY in same-sign dilepton events at* $\sqrt{s} = 13$ TeV, CMS-PAS-SUS-15-008, 2015.

[179] J. Butterworth et al., *PDF4LHC recommendations for LHC Run II*, *J. Phys.* **G43** (2016) 023001, [arXiv:1510.03865], doi:10.1088/0954-3899/43/2/023001.

[180] N. Wardle. Private Commnuications, 2018-2019.

[181] CMS Top Physics Analysis Group. Private Commnuication, 2017.

[182] CMS Collaboration, *Investigations of the impact of the parton shower tuning in Pythia 8 in the modelling of* $\mathrm{t\bar{t}}$ *at* $\sqrt{s} = 8$ *and 13 TeV*, CMS-PAS-TOP-16-021, 2016.

[183] A. Hocker et al., *TMVA - Toolkit for Multivariate Data Analysis*, arXiv:physics/0703039.

[184] J. H. Friedman, T. Hastie and R. Tibshirani, *Additive logistic regression: a statistical view of boosting*, *Annals of Statistics* **28** (1998) 2000.

[185] J. H. Friedman, *Greedy function approximation: A gradient boosting machine*, *Annals of Statistics* **29** (2000) 1189–1232.

[186] J. H. Friedman, *Stochastic gradient boosting*, *Computational Statistics & Data Analysis* **38** (Feb., 2002) 367–378, doi:10.1016/S0167-9473(01)00065-2.

[187] "Xgboost library documentation." https://xgboost.readthedocs.io/en/latest/.

[188] I. Guyon, J. Weston, S. Barnhill and V. Vapnik, *Gene selection for cancer classification using support vector machines*, *Machine Learning* **46** (Jan, 2002) 389–422, doi:10.1023/A:1012487302797.

[189] T. "Head, MechCoder, G. Louppe, I. Shcherbatyi, fcharras, ZéVinícius et al., *scikit-optimize/scikit-optimize v0.5.2*, doi:10.5281/zenodo.1207017.

[190] P. Vischia. Private Commnuication, 2017.

[191] "Higgs combination statistics tool."
https://cms-hcomb.gitbooks.io/combine/content/.

[192] L. Moneta, K. Belasco, K. S. Cranmer, S. Kreiss, A. Lazzaro, D. Piparo et al., *The RooStats Project*, *PoS* **ACAT2010** (2010) 057, [arXiv:1009.1003].

[193] RooStats Team Collaboration, G. Schott, *RooStats for Searches*, in *Proceedings, PHYSTAT 2011 Workshop on Statistical Issues Related to Discovery Claims in Search Experiments and Unfolding, CERN,Geneva, Switzerland 17-20 January 2011*, (Geneva), pp. 199–208, CERN, CERN, 2011, arXiv:1203.1547, doi:10.5170/CERN-2011-006.199, http://inspirehep.net/record/1093113/files/arXiv:1203.1547.pdf.

[194] G. Cowan, K. Cranmer, E. Gross and O. Vitells, *Asymptotic formulae for likelihood-based tests of new physics*, *Eur.Phys.J.* **C71** (2011) 1554, [arXiv:1007.1727], doi:10.1140/epjc/s10052-011-1554-0, 10.1140/epjc/s10052-013-2501-z.

[195] M. Baak, S. Gadatsch, R. Harrington and W. Verkerke, *Interpolation between multi-dimensional histograms using a new non-linear moment morphing method*, *Nucl. Instrum. Meth.* **A771** (2015) 39–48, [arXiv:1410.7388], doi:10.1016/j.nima.2014.10.033.